UNCLASSIFIED

AD NUMBER
ADB004531
LIMITATION CHANGES
TO: **Approved for public release; distribution is unlimited.**
FROM: **Distribution authorized to U.S. Gov't. agencies only; Test and Evaluation; APR 1975. Other requests shall be referred to Materials and Mechanics Research Center, ATTN: AMXMR-PL, Watertown, MA 02172.**
AUTHORITY
DARPA ltr, 19 Dec 1974

THIS PAGE IS UNCLASSIFIED

Best
Available
Copy

THIS REPORT HAS BEEN DELIMITED
AND CLEARED FOR PUBLIC RELEASE
UNDER DOD DIRECTIVE 5200.20 AND
NO RESTRICTIONS ARE IMPOSED UPON
ITS USE AND DISCLOSURE.

DISTRIBUTION STATEMENT A

APPROVED FOR PUBLIC RELEASE;
DISTRIBUTION UNLIMITED.

AD B004531

AD

AMMRC CTR 75-8

BRITTLE MATERIALS DESIGN, HIGH TEMPERATURE GAS TURBINE

Technical Report By:

Arthur F. McLean, Ford Motor Company, Dearborn, Michigan 48121
Eugene A. Fisher, Ford Motor Company, Dearborn, Michigan 48121
Raymond J. Bratton, Westinghouse Electric Corporation, Pittsburgh, Pa. 15235
Donald G. Miller, Westinghouse Electric Corporation, Pittsburgh, Pa. 15235

April, 1975

Interim Report Number 7, July 1, 1974 to December 31, 1974

Contract Number DAAG 46-71-C-0162

Sponsored by the Advanced Research Projects Agency

ARPA Order Number 1849

Project Code Number 1D10

Agency Accession Number DA OD 4733

DDC
RECEIVED
JUN 16 1975
B

Distribution limited to U.S. and NATO Government agencies, [redacted] only: Test and Evaluation data; April, 1975. Other requests for this document must be referred to the Director, Army Materials and Mechanics Research Center, ATTN: AMXMR-PL, Watertown, Massachusetts 02172

Prepared for

ARMY MATERIALS AND MECHANICS RESEARCH CENTER
Watertown, Massachusetts 02172

The findings in this report are not to be construed as an official Advanced Research Projects Agency, Department of the Army, or U.S. Government position, either expressed or implied, unless so designated by other authorized documents.

Mention of any trade names or manufacturers in this report shall not be construed as advertising nor as an official indorsement or approval of such products or companies by the United States Government.

DISPOSITION INSTRUCTIONS

Destroy this report when it is no longer needed. Do not return it to the originator.

AMMRC CTR 75-8

BRITTLE MATERIALS DESIGN, HIGH TEMPERATURE GAS TURBINE

Technical Report By:

Arthur F. McLean, Ford Motor Company, Dearborn, Michigan 48121
Eugene A. Fisher, Ford Motor Company, Dearborn, Michigan 48121
Raymond J. Bratton, Westinghouse Electric Corporation, Pittsburgh, Pa 15235
Donald G. Miller, Westinghouse Electric Corporation, Pittsburgh, Pa 15235

April, 1975

Interim Report Number 7, July 1, 1974 to December 31, 1974

Contract Number DAAG 46-71-C-0162

Sponsored by the Advanced Research Projects Agency

ARPA Order Number 1849

Project Code Number 1D10

Agency Accession Number DA OD 4733

Distribution limited to U.S. and NATO Government agencies [redacted] only: Test and Evaluation data; April, 1975. Other requests for this document must be referred to the Director, Army Materials and Mechanics Research Center, ATTN: AMXMR-PL, Watertown, Massachusetts 02172

Prepared for:

ARMY MATERIALS AND MECHANICS RESEARCH CENTER
Watertown, Massachusetts 02172

ABSTRACT

The "Brittle Materials Design, High Temperature Gas Turbine" program objective is to demonstrate successful use of brittle materials in demanding high temperature structural applications. A small vehicular gas turbine and a large stationary gas turbine, each using uncooled ceramic components, will be utilized in this iterative design and materials development program. Both the contractor, Ford Motor Company, and the subcontractor, Westinghouse Electric Corporation, have had in-house research programs in this area prior to this contract.

In the vehicular turbine project, a major program milestone, comprising a 100 hour durability test of the stationary ceramic hot flow path components in an engine was completed. In the fabrication of ceramic turbine rotors, significant improvement in bonding the components of the silicon nitride duo density rotor resulted when hot pressing of the shaped hub was combined with press bonding to the blade ring. Spin testing of seven hot pressed silicon nitride rotor hubs, with burst speeds ranging from 102,000 to 120,000 rpm, confirmed that this material was adequate for rotor requirements. A silicon carbide combustor tube has been successfully tested in a combustor rig for a total of 171 hours, including 20 hours at an outlet temperature of 2500°F. A redesigned ceramic flow path, Design D, was conceived using common one piece stators and common rotors in both first and second stage locations. Through variations in particle size distribution, it was found that injection molded reaction sintered silicon nitride of 2.7 gm/cm^3 density (84.5% of T.D.) could be made. The effect of oxidation on lower density forms of reaction sintered silicon nitride was evaluated.

In the stationary turbine project, static rig testing of hot pressed silicon nitride and silicon carbide stator vanes up to 2500°F was initiated. Cracks were observed visually on two of the four silicon carbide vanes during the third cycle, but the vanes remained functional. During the fifth cycle, the metal combustor basket imploded, throwing metal debris into the vanes, followed by a temperature excursion to 3000°F and a rapid quench to 600°F under choked flow conditions. Following this accident, it was found that all four silicon carbide vanes had been shattered. One of the four silicon nitride vanes was cracked, while the remaining three vanes were still intact, an encouraging example of ceramic material survival under unexpected catastrophic conditions. The static test rig is being modified and rebuilt for the continuation of 2500°F testing. Additional tensile strength and creep tests were performed on hot pressed silicon nitride.

FORWARD

This report is the seventh semi-annual technical report of the "Brittle Materials Design, High Temperature Gas Turbine" program initiated by the Advanced Research Projects Agency, ARPA Order Number 1849, and monitored by the Army Materials and Mechanics Research Center, under Contract Number DAAG-46-71-C-0162. This is an incrementally-funded six year program.

Since this is an iterative design and materials development program, design concepts and materials selection and/or properties presented in this report will probably not be those finally utilized. Thus all design and property data contained in the semi-annual reports must be considered tentative, and the reports should be considered to be illustrative of the design, materials, processing, and NDT techniques being developed for brittle materials.

The principal investigator of this program is Mr. A. F. McLean, Ford Motor Company, and the technical monitor is Dr. A. E. Gorum, AMMRC. The authors would like to acknowledge the valuable contributions in the performance of this work by the following people:

Ford Motor Company

N. Arnon, R. R. Baker, P. Beardmore, D. J. Cassidy, J. C. Caverly
H. A. Cikanek, D. A. Davis, G. C. DeBell, E. F. Dore, A. Ezis, W. A. Fate,
M. U. Goodyear, E. T. Grostick, D. L. Hartsock, P. H. Havstad, D. W. Huser,
R. A. Jeryan, C. F. Johnson, K. H. Kinsman, C. A. Knapp, J. T. Kovach,
J. G. LaFond, J. A. Mangels, W. E. Meyer, M. E. Milberg, W. M. Miller,
J. J. Mittman, T. G. Mohr, P. F. Nicholls, A. Paluszny, G. Peitsch,
N. P. Peters, J. J. Schuilies, J. R. Secord, K. H. Styhr, L. R. Swank,
W. Trela, J. Uy, T. J. Whalen, W. Wu

Westinghouse Electric Corporation

J. Allen, G. W. Bauserman, C. R. Booher, Jr., E. S. Diaz, A. N. Holden,
R. Kossowsky, T. Lam, F. F. Lange, S. Y. Lee, W. Malchman, A. M. Elshinnawy,
D. G. Miller, S. Mumford, T. J. Rahaim, S. C. Sanday, S. C. Singhal, J. P. Smed,
L. C. Szema, W. Van Buren, C. Visser, R. Weidenbacker, J. White, C. A. Andersson,
C. B. Brenneman, S. E. Gabrieles, B. Acchione, C. W. Carlson, R. K. Smith,
D. Wood

Army Material and Mechanics Research Center

E. M. Lenoe, R. N. Katz, D. R. Messier, H. Priest

TABLE OF CONTENTS

	Page No.
Title Page	i
Abstract	ii
Forward	iii
Table of Contents	iv
List of Illustrations	v
List of Tables	xv
1. Introduction	1
2. Introduction and Summary-Vehicular Turbine Project	3
2.1 Vehicular Turbine Project Plan	5
2.2 Progress and Status Summary-Vehicular Turbine Project	7
2.2.1 Ceramic Component Development	8
2.2.2 Materials Technology	12
2.3 Future Plans	15
3. Progress on Ceramic Component Development-Vehicular Turbine Project	19
3.1 Ceramic Rotor Development	19
3.1.1 Design and Analysis	21
3.1.2 Materials and Fabrication	30
3.1.3 Testing	41
3.2 Ceramic Stators, Rotor Shrouds, Nose Cones, and Combustors	49
3.2.1 Design and Analysis	50
3.2.2 Materials and Fabrication	56
3.2.3 Testing	58
3.3 Gas Bearings	67
3.3.1 Gas Bearing Design and Development	68
4. Progress on Materials Technology-Vehicular Turbine Project	71
4.1 Development of Improved Molded Silicon Nitride	73
4.2 Oxidation Resistance of Reaction Sintered Silicon Nitride	81
4.3 High Temperature Fracture Behavior of Silicon Nitride	85
4.4 Elastic Property Measurements	91
4.5 Development of Sialon Materials	93
4.6 Ultrasonic NDE	97
4.7 X-Ray Radiography	99
5. Introduction and Summary-Stationary Turbine Project	101
5.1 Stationary Turbine Project Plan	103
5.2 Progress and Status Summary-Stationary Turbine Project	105
5.2.1 Component Development	106
5.2.2 Materials Technology	109
5.3 Future Plans	113
6. Progress on Ceramic Component Development-Stationary Turbine Project	115
6.1 Stator Vane Development	115
6.1.1 Design	117
6.1.2 The Stress Analysis of Silicon Nitride Vanes	119
6.1.3 The Ceramic Insulator	129
6.1.4 Static Rig Tests	141
6.1.5 Vane Fabrication	154
6.1.6 Water Cooled Static Rig for 2500°F Testing	155
7. Progress on Material Technology-Stationary Turbine Project	157
7.1 Material Engineering Data	157
7.1.1 Tensile Tests of Si_3N_4	158
7.1.2 Flexural Tests of LAS	159
7.1.3 Creep in Si_3N_4	160
7.1.4 Flexural Creep Analysis	161
7.1.5 Low Cycle Fatigue in Hot Pressed Si_3N_4	170
7.2 Materials Science	171
7.2.1 Microstructure of Hot Pressed Silicon Nitride and Silicon Carbide	172
7.2.2 Gas-Solid Reactions	173
7.2.3 Non-Destructive Evaluation of Materials-Stationary Turbine Project	182
8. References	183

LIST OF ILLUSTRATIONS

		Page No.
Figure 2.1	Schematic View of the Vehicular Gas Turbine Engine Flowpath	5
Figure 2.2	Block Diagram Flow Chart of the Iterative Development Process	6
Figure 2.3	Schematic Cross-Section View of Design C and Design D Hot Flow Path Configurations	16
Figure 3.1	Heat Transfer Film Coefficients, First Stage Rotor Blade, at 55% Speed, 2390°R Inlet Temperature, and Radius of 1.7 Inches	24
Figure 3.2	Heat Transfer Film Coefficients, First Stage Rotor Blade, at 100% Speed, 2960°R Inlet Temperature, and Radius of 1.7 Inches	24
Figure 3.3	Heat Transfer Film Coefficients, First Stage Rotor Blade, at 55% Speed, 2390°R Inlet Temperature, and Radius of 1.994 Inches	24
Figure 3.4	Heat Transfer Film Coefficients, First Stage Rotor Blade, at 100% Speed, 2960°R Inlet Temperature, and Radius of 1.994 Inches	24
Figure 3.5	Heat Transfer Film Coefficients, First Stage Rotor Blade, at 55% Speed, 2390°R Inlet Temperature, and Radius of 2.294 Inches	25
Figure 3.6	Heat Transfer Film Coefficients, First Stage Rotor Blade, at 100% Speed, 2960°R Inlet Temperature, and and Radius of 2.294 Inches	25
Figure 3.7	Heat Transfer Film Coefficients, Second Stage Rotor Blade, at 100% Speed, 2960°R Inlet Temperature, and Radius of 1.7 Inches	25
Figure 3.8	Adiabatic Wall Temperature of First Stage Rotor Blade at Radius of 1.7 Inches	25
Figure 3.9	Adiabatic Wall Temperature of First Stage Rotor Blade at Radius of 1.994 Inches	26
Figure 3.10	Adiabatic Wall Temperature of First Stage Rotor Blade at Radius of 2.294 Inches	26
Figure 3.11	Adiabatic Wall Temperature of Second Stage Rotor Blade at Radius of 1.7 Inches	26
Figure 3.12	Assumed Hot Gas Circulation in Cavity Between First and Second Stage Rotors	28

LIST OF ILLUSTRATIONS

		Page No.
Figure 3.13	Film Coefficients vs Radius for the Cavity Between First and Second Stage Rotors	29
Figure 3.14	Hot Press Bonding Assembly	31
Figure 3.15	Microstructure of Bond Interface Between Hot Pressed Silicon Nitride Rotor Hub and Reaction Sintered Silicon Nitride Blade Ring (500 X)	32
Figure 3.16	Hot Press Bonding Assembly for Simultaneous Forming and Bonding a Silicon Nitride Rotor Hub to a Blade Ring	33
Figure 3.17	Sectioned Silicon Nitride Duo-Density Turbine Rotor	34
Figure 3.18	Microstructure of Bond Interface (250 X)	35
Figure 3.19	Wax Pattern (Right) and Completed Shell Mold (Left) for Slip Casting of Rotors	36
Figure 3.20	Shell Mold as Filled with Slip	36
Figure 3.21	Section of Silicon Nitride Test Sample Showing High Density Surface Layer (100 X)	37
Figure 3.22	Nitriding Rates at Various Temperatures of 95% Equivalent Silicon Nitride Density Slip Cast Samples at 10,000 psi Nitrogen Pressure	40
Figure 3.23	Hot Pressed Silicon Nitride Rotor Hub at Burst (102,800 rpm)	42
Figure 3.24	Large Section of Rotor Hub Recovered from Spin Pit After Burst Test, Indicating Suspected Area of Fracture Origin	42
Figure 3.25	Suspected Area of Fracture Origin of Rotor Hub (1000 X)	43
Figure 3.26	Maximum Principal Stress Contours (psi) of Rotor Hub at Burst Speed of 116,000 rpm	44
Figure 3.27	The Turbine Rotor Test Rig	45
Figure 3.28	First Set of Ceramic Rotors Mounted on Power Turbine Shaft	46
Figure 3.29	Heat Transfer Film Coefficients, First Stage Stator Vane, at 55% Speed, 2390°R Inlet Temperature, and Radius of 1.7 Inches	51
Figure 3.30	Heat Transfer Film Coefficients, First Stage Stator Vane, at 100% Speed, 2960°R Inlet Temperature, and Radius of 1.7 Inches	51

LIST OF ILLUSTRATIONS

		Page No.
Figure 3.31	Heat Transfer Film Coefficients, First Stage Stator Vane, at 55% Speed, 2390°R Inlet Temperature, and Radius of 1.95 Inches	51
Figure 3.32	Heat Transfer Film Coefficients, First Stage Stator Vane, at 100% Speed, 2960°R Inlet Temperature, and Radius of 1.95 Inches	51
Figure 3.33	Heat Transfer Film Coefficients, First Stage Stator Vane, at 55% Speed, 2390°R Inlet Temperature, and Radius of 2.2 Inches	52
Figure 3.34	Heat Transfer Film Coefficients, First Stage Stator Vane, at 100% Speed, 2960°R Inlet Temperature, and Radius of 2.2 Inches	52
Figure 3.35	Heat Transfer Film Coefficients, Second Stage Stator Vane, at 55% Speed, 2390°R Inlet Temperature, and Radius of 1.7 Inches	52
Figure 3.36	Heat Transfer Film Coefficients, Second Stage Stator Vane, at 100% Speed, 2960°R Inlet Temperature, and Radius of 1.7 Inches	52
Figure 3.37	Heat Transfer Film Coefficients, Second Stage Stator Vane, at 55% Speed, 2390°R Inlet Temperature, and Radius of 2.05 Inches	53
Figure 3.38	Heat Transfer Film Coefficients, Second Stage Stator Vane, at 100% Speed, 2960°R Inlet Temperature, and Radius of 2.05 Inches	53
Figure 3.39	Heat Transfer Film Coefficients, Second Stage Stator Vane, at 55% Speed, 2390°R Inlet Temperature, and Radius of 2.4 Inches	53
Figure 3.40	Heat Transfer Film Coefficients, Second Stage Stator Vane, at 100% Speed, 2960°R Inlet Temperature, and Radius of 2.4 Inches	53
Figure 3.41	Adiabatic Wall Temperature of First Stage Stator Vane at Radius of 1.7 Inches	54
Figure 3.42	Adiabatic Wall Temperature of First Stage Stator Vane at Radius of 1.95 Inches	54
Figure 3.43	Adiabatic Wall Temperature of First Stage Stator Vane at Radius of 2.2 Inches	54
Figure 3.44	Adiabatic Wall Temperature of Second Stage Stator Vane at Radius of 1.7 Inches	54

LIST OF ILLUSTRATIONS

		Page No.
Figure 3.45	Adiabatic Wall Temperature of Second Stage Stator Vane at Radius of 2.05 Inches	55
Figure 3.46	Adiabatic Wall Temperature of Second Stage Stator Vane at Radius of 2.4 Inches	55
Figure 3.47	Combustor Test Rig	59
Figure 3.48	"Refel" Silicon Carbide Combustor After Completion of 171 Hours of Testing	60
Figure 3.49	Molded Silicon Nitride Nose Cone After Completion of 100 Hour Cyclic Durability Test	63
Figure 3.50	Molded Silicon Nitride First Stage Stator After Completion of 100 Hour Cyclic Durability Test	63
Figure 3.51	Slip Cast Silicon Nitride Rotor Shrouds After Completion of 100 Hour Cyclic Durability Test	64
Figure 3.52	X-Ray Radiograph of Stator No. 430 Indicating Defect Which Initiated Failure	64
Figure 3.53	X-Ray Radiograph of Stator No. 428 Indicating Defects Which Initiated Failure	65
Figure 3.54	Oscilloscope Traces of High Speed Shaft Excursions	68
Figure 3.55	Compliant Foil Journal Bearing Test Rig	69
Figure 4.1	Relationship Between Volume Percent Filler of Injection Molding System and Final Silicon Nitride Density	74
Figure 4.2	Relative Viscosity as a Function of Percent Solids Content of a Monodispersed System [24]	74
Figure 4.3	Calculated Viscosity for Various Bimodel Suspensions vs Distribution Ratios and Concentrations [24]	75
Figure 4.4	Calculated Viscosity of Monomodel and Bimodel Suspensions vs Volume Fraction of Solids With a Volume Fraction of Fine Particles of 25% [24]	76
Figure 4.5	Various Particle Size Distribution Curves of Silicon Metal Powders	76
Figure 4.6	Optical Micrographs (500 X) of Molded Silicon Nitride at (a) Density of 2.25 gm/cm^3 (Type B) (b) Density of 2.55 gm/cm^3 (74D) and (c) 2.7 gm/cm^3 (75F)	78
Figure 4.7	Weight Gain vs Time for 2.2 gm/cm^3 Density Reaction Sintered Silicon Nitride at Several Temperatures [3]	81

LIST OF ILLUSTRATIONS

		Page No.
Figure 4.8	Weight Gain of Reaction Sintered Silicon Nitride of 2.2 gm/cm^3 Density vs Time at 1900°F	83
Figure 4.9	Effect of Oxidation for 200 Hours at 1900°F on the Thermal Expansion of 2.2 gm/cm^3 Reaction Sintered Silicon Nitride	83
Figure 4.10	Oxygen Concentration vs Time at Surface and Interior of 2.2 gm/cm^3 Density Silicon Nitride Oxidized at 1900°F	84
Figure 4.11	Weight Gain vs Density for Silicon Nitride Oxidized for 200 Hours at 1900°F	84
Figure 4.12	Temperature Dependence of Fracture Stress as Influenced by Fracture Initiating Flaw Size, Showing (inset) a Schematic of the Griffith Relationship of Fracture Stress, σ_f, to Crack Size, d.	85
Figure 4.13	Rationale for the Influence of Temperature T, and Strain Rate, $\dot{\varepsilon}$, on the Mechanical Resistance to Fracture of Brittle Materials	87
Figure 4.14	Loading Rate Dependence of Extent of Subcritical Crack Growth at 1300°C in Precracked Hot Pressed Silicon Nitride (Norton HS-130). Initial Flaw Size is Marked by Arrow	88
Figure 4.15	Loading Rate Dependence of Extent of Subcritical Crack Growth at 1350°C in Precracked Hot Pressed Silicon Nitride (Norton HS-130). Initial Flaw Size is Marked ACB and by Arrow	89
Figure 4.16	Extent of Subcritical Crack Growth at 1300°C in Stress-Rupture Type Tests of Precracked Specimens. Initial Flaw is Marked ABC in (c). (a) and (b) Failed Under Load at the Indicated Fraction of the Fast Fracture Strength and in the Indicated Time. (c) Was Unloaded After 40 Minutes at the Indicated Load and Broken at Room Temperature	89
Figure 4.17	X-ray Diffraction Pattern, Taken With CuK$_\alpha$ Radiation, of (a) A Typical Sialon Containing Extraneous Phase, and (b) Of a Poorly Sintered Sialon Lacking Extraneous Phase	95
Figure 4.18	Scanning Electron Micrographs of a Fracture Initiating Flaw in a Sialon Specimen Prepared Without Additives by Sintering for 15 Minutes in Argon at 1750°C	96
Figure 4.19	Longitudinal (V_L) and Transverse (V_T) Sonic Velocity vs Density of Silicon Nitride	97

LIST OF ILLUSTRATIONS

		Page No.
Figure 4.20	Acoustic Impedance vs Modulus of Elasticity of Silicon Nitride	98
Figure 4.21	Radiographs of As-Molded Second Stage Stator Vanes, Showing Flaws in All 74D Vanes and Seven of Ten Flaw-Free 74F Vanes	99
Figure 4.22	Radiograph of Outer Shroud of As-Molded First Stage Monolithic Stator Which is Free From Molding Flaws	100
Figure 5.1	30 MW Test Turbine Flow Path	103
Figure 5.2	Si_3N_4 Stator Vane Assemblies After Static Rig Testing At 2200°F (100 Cycles)	106
Figure 5.3	Interaction Between Properties And Design	109
Figure 6.1	W-251 Rotating Rig Test Turbine With Modifications Indicated	118
Figure 6.2	Initial And Boundary Conditions For End Cap Thermal Analysis (h - BTU hr^{-1} ft^{-2} °F, T - °F)	120
Figure 6.3	Calculated Variations In Heat Transfer Coefficients At Mid-Height Of Vane And On End Cap Surface vs Distance From The Leading Edge	120
Figure 6.4	Three-Dimensional Element Model Of The Second Generation Airfoil Under Equilibrium Conditions	121
Figure 6.5	Three-Dimensional Element Model Of The End Cap Under Equilibrium Conditions	122
Figure 6.6	Temperature And Stress Distributions For Second Generation Design Airfoil At 10th Second Of Flame Out From 2500°F Steady State Gas Temperature (Section 7a) (h: High-Low)	122
Figure 6.7	Temperature And Stress Distributions For Airfoil Section 3 At 10th Second Of Flame Out From 2500°F Steady State Gas Temperature (h: High-Low)	123
Figure 6.8	Temperature And Stress Distribution For Airfoil Section 6a At 10th Second Of Flame Out From 2500°F Steady State Gas Temperature ((a) h: High-Low, (b) h: High-Low, (c) h: High-High)	124
Figure 6.9	Stress Distribution During Cooling at 25°F/Sec From 2500°F Steady State Gas Temperature At 50th Second In Airfoil Section 6a	125
Figure 6.10	Temperature And Stress Distributions For End Cap Section 7e At 14th Second Of Flame Out From 2500°F Steady State Gas Temperature (h: High-Low)	125

LIST OF ILLUSTRATIONS

		Page No.
Figure 6.11 --	Temperature And Stress Distributions For End Cap Section 6e At 14th Second Of Flame Out From 2500°F Steady State Gas Temperature (h: High-Low)	126
Figure 6.12 --	Temperature And Stress Distributions For End Cap Section 3' At 14th Second Of Flame Out From 2500°F Steady State Gas Temperature (h: High-Low)	127
Figure 6.13 --	Stress Distribution During Cooling At 25°F/Sec From 2500°F Steady State Gas Temperature At 58th Second In End Cap Section 7e	127
Figure 6.14 --	Deformations Of The Airfoil End Cap Contact Surfaces At Steady State And During Transient	128
Figure 6.15 --	Ceramic Stator Vane Assembly With Insulators	130
Figure 6.16 --	Typical Insulator Failures In Cervit C140 LAS Material	130
Figure 6.17 --	One-Dimensional Radial Conduction/Convection/Radiation Heat Transfer Model - Steady State Condition	131
Figure 6.18 --	Two-Dimensional Finite Element Model Of End Cap - Insulator Combination	133
Figure 6.19 --	Gas/Air Temperature vs Time Profile For Insulator - End Cap Combination	134
Figure 6.20 --	Convection Coefficients vs Time Profiles For Shoe, Insulator, End Cap Combinations	135
Figure 6.21 --	Insulator Hot Gas Transient Thermal Response Of LAS	136
Figure 6.22 --	Insulator Heat Gas Transient Thermal Response Of Hot-Pressed Si_3N_4	137
Figure 6.23 --	Insulator Two-Dimensional Stress Model	138
Figure 6.24 --	Insulator Hot Gas Two-Dimensional In Plane Maximum Stress Response For LAS	139
Figure 6.25 --	Insulator Hot Gas Two-Dimensional Maximum Stress Response Of Hot-Pressed Si_3N_4	140
Figure 6.26 --	Static Test Rig For 2500°F Test Of Ceramic Vanes	141
Figure 6.27 --	Temperature Profile At 1200°F, Idle	142
Figure 6.28 --	Temperature Profile At 1800°F	142
Figure 6.29 --	Temperature Profile At 2300°F	143

LIST OF ILLUSTRATIONS

		Page No.
Figure 6.30	Temperature Profile At 2500°F	143
Figure 6.31	Typical Cycle For 2500°F Testing	144
Figure 6.32	Location Of Parts In 2500°F Static Rig Test Assembly	145
Figure 6.33	Combustor Failure From 2500°F Static Rig Tests	147
Figure 6.34	Silicon Nitride (Left) And Silicon Carbide (Right) Stator Vane Assemblies After 2500°F Static Rig Test (5 Cycles)	147
Figure 6.35	Ceramic Mixer-Inlet Side - 2500°F Static Rig Test	148
Figure 6.36	Ceramic Mixer-Outlet Side - 2500°F Static Rig Test	148
Figure 6.37	Typical Si_3N_4 Stator Vane Assembly After 2500°F Test (Cleaned)	149
Figure 6.38	Silicon Nitride Airfoil With Thermal Cracks After 2500°F Test	150
Figure 6.39	Silicon Nitride End Cap Inner #2 After 2500°F Test	151
Figure 6.40	Silicon Carbide End Cap Inner #4 After Static Rig Test At 2500°F	151
Figure 6.41	Silicon Carbide End Cap Outer #5 After Static Rig Test At 2500°F	152
Figure 6.42	Silicon Carbide End Cap Inner #6 After Static Rig Test At 2500°F	152
Figure 6.43	Insulators From 2500°F Static Rig Test (5 Cycles)	153
Figure 6.44	Water Cooled Rig For 2500°F Test of Ceramic Vanes	155
Figure 6.45	Water Cooled Exhaust Duct	156
Figure 7.1	Average Stress Strain Curve For Silicon Nitride At 2500°F	158
Figure 7.2	Flexural Test Results For Cervit C140 LAS Insulator Material At Room Temperature	159
Figure 7.3	Tensile Stress-Strain-Time Deformation Surface, Intersected By Lines Of Constant Stress (AB) And Constant Moment (AC And AD)	163
Figure 7.4	Constant Moment Line And Moment Relaxation Curves For A Calculated Example Where Deformation In Tension And Compression Are Equal, Time Dependent And Non-Linear	165
Figure 7.5	Total Strain Versus Time For A Calculated Example Where Deformation In Tension And Compression Are Equal, Time Dependent And Non-Linear	165

LIST OF ILLUSTRATIONS

		Page No.
Figure 7.6	Stress-Strain Distributions At Various Times During A Constant Moment Flexural Creep Test For A Calculated Example Where Deformation In Tension And Compression Are Equal, Time Dependent And Non-Linear	166
Figure 7.7	Creep Curves For The Uniaxial Constant Stress Test And The Flexural Constant Moment Test For A Calculated Example Where Deformation In Tension And Compression Are Equal, Time Dependent And Non-Linear	167
Figure 7.8	Constant Moment Line And Moment Relaxation Curves For A Calculated Example Where Deformation In Tension Was Time-Dependent And Non-Linear, And Deformation In Compression Was Linear Elastic	167
Figure 7.9	Total Strain Versus Time For A Calculated Example Where Deformation In Tension Was Time Dependent And Non-Linear And Deformation In Compression Was Linear Elastic	168
Figure 7.10	Stress-Strain Distributions At Various Times During A Constant Moment Flexural Creep Test For A Calculated Example Where Deformation In Tension Was Time Dependent And Non-Linear, And Deformation In Compression Was Linear Elastic	168
Figure 7.11	Creep Curves For The Uniaxial Constant Stress Test And The Flexural Constant Moment Test For A Calculated Example Where Deformation In Tension Was Time Dependent And Non-Linear, And Deformation In Compression Was Linear Elastic	169
Figure 7.12	Decomposition Pressure Of Nitrogen Over $Si_3N_4(s)$	174
Figure 7.13	Partial Pressures Of Various Volatile Species Over $Si_3N_4(s)$ In Nitrogen At 1 atm Pressure	175
Figure 7.14	Partial Pressure Of Various Volatile Species Over $Si_3N_4(s)$ In Nitrogen At 7.75 atm Pressure	175
Figure 7.15	Partial Pressures Of Various Volatile Species Over SiC(s) At 1600°K	176
Figure 7.16	Partial Pressures Of Various Volatile Species Over SiC(s) At 2000°K	176
Figure 7.17	Partial Pressures Of Various Volatile Species Over $SiO_2(s)$ At 1400°K (1127°C)	177
Figure 7.18	Partial Pressure Of Various Volatile Species Over $SiO_2(s)$ At 1600°K (1327°C)	178
Figure 7.19	Partial Pressures Of Various Volatile Species Over $SiO_2(s)$ At 1800°K (1527°C)	178

LIST OF ILLUSTRATIONS

	Page No.
Figure 7.20 -- Partial Pressures Of Various Volatile Species Over $SiO_2(\ell)$ At 2000°K (1727°C)	179
Figure 7.21 -- Partial Pressures Of Various Volatile Species Over $SiO_2(s,\ell)$ In Oxygen At 1 atm Pressure	179
Figure 7.22 -- Partial Pressures Of Various Volatile Species Over $SiO_2(s,\ell)$ In Oxygen At 10^{-8} atm Pressure	180
Figure 7.23 -- Pressures Of SiO(g) At The $Si_3N_4(s)$ - $SiO_2(s)$ And SiC(s) - $SiO_2(s)$ Interfaces	181

LIST OF TABLES

		Page No.
Table 3.1	Average Film Coefficients for Inter-Blade Channel Groove and Shrouds	26
Table 3.2	Average Film Coefficients for Inter-Blade Channel Groove and Shrouds	55
Table 3.3	Accumulated Test Time on "Refel" SiC Combustor	60
Table 3.4	Summary of Component Tests Over the ARPA Cycle Qualification Testing	62
Table 4.1	Moldability as a Function of Particle Distributions for Two Levels of Loading	77
Table 4.2	Physical Properties of Injection Molded Si_3N_4	78
Table 4.3	Flexural Creep Properties of High Density	79
Table 4.4	Summary of Elastic Properties of Some Turbine Ceramic Materials	91
Table 6.1	Insulator Material Stress Comparison	132
Table 6.2	End Cap Stress for Various Insulator Materials	132
Table 7.1	Creep of Pre-Oxidized Si_3N_4 (HS-130)	160
Table 7.2	Low Cycle Fatigue Properties of Silicon Nitride at 2300°F	170
Table 7.3	Chemical Analysis of Norton NC-203 Silicon Carbide	172

1. INTRODUCTION

As stipulated by the Advanced Research Projects Agency of the Department of Defense at the outset of this program, the major purpose is to demonstrate that brittle materials can be successfully utilized in demanding high temperature structural applications. ARPA's major program goal is to prove by a practical demonstration that efforts in ceramic design, materials, fabrication, testing and evaluation can be drawn together and developed to establish the usefulness of brittle materials for engineering applications.

The gas turbine engine, utilizing uncooled ceramic components in the hot flow path, was chosen as the vehicle for this demonstration. The progress of the gas turbine engine has been and continues to be closely related to the development of materials capable of withstanding the engine's environment at high operating temperature. Since the early days of the jet engine, new metals have been developed which have allowed a gradual increase in operating temperatures. Today's nickelchrome superalloys are in use, without cooling, at turbine inlet gas temperatures of 1800° to 1900°F. However, there is considerable incentive to further increase turbine inlet temperature in order to improve specific air and fuel consumptions. The use of ceramics in the gas turbine engine promises to make a major step in increasing turbine inlet temperature to 2500°F. Such an engine offers significant advances in efficiency, power per unit weight, cost, exhaust emissions, materials utilization and fuel utilization. Successful application of ceramics to the gas turbine would therefore not only have military significance, but would also greatly influence our national concerns of air pollution, utilization of material resources, and the energy crisis.

From the program beginning, two gas turbine engines of greatly different size were chosen for the application of ceramics. One is a small vehicular turbine of about 200 hp (contractor Ford) and the other is a large stationary turbine of about 30 MW (sub-contractor Westinghouse). One difference in philosophy between the projects is worth noting. Because the ceramic materials, fabrication processes, and designs are not fully developed, the vehicular turbine engine was designed as an experimental unit and features ease of replacement of ceramic components. Iterative developments in a component's ceramic material, process, or design can therefore be engine-evaluated fairly rapidly. This work can then parallel and augment the time-consuming efforts on material and component characterization, stress analysis, heat transfer analysis, etc. Some risk of damage to other components is present when following this approach, but this is considered out-weighed by the more rapid acquisition of actual test information. On the other hand, the stationary turbine engine is so large, so expensive to test, and contains such costly and long lead-time components which could be damaged or lost by premature failure, that very careful material and design work must be performed to minimize the possibility of expensive, time-consuming failures.

It should be noted that both the contractor and sub-contractor had in-house research programs in this area prior to initiation of this program.

Silicon nitride and silicon carbide had been selected as the primary material candidates. Preliminary design concepts were in existence and, in the case of the vehicular engine, hardware had been built and testing had been initiated.

At the out-set, the program was considered to be both highly innovative and risky. However, it showed promise of large scale financial and technological payoff as well as stimulation of the pertinent technical communities. The program is now in its fourth year and major accomplishments have been achieved.

This is the 7th semi-annual report of progress. Prior reports have been broken down into three major elements:

- Vehicular Turbine Project
- Stationary Turbine Project
- Materials Technology (applicable to both projects)

However, it is now apparent, that, at the current stage of the program, materials technology is no longer "general" but rather specifically related to the objectives of each project. In addition, the widespread interest from the turbine technology community centers on either the vehicular turbine project or the stationary turbine project. For these reasons, this report and subsequent reports on the program will be broken down into sections; each section will be complete in itself and will include its own introduction, again to be of more help to the reader. The two sections will be titled:

- Vehicular Turbine Project
- Stationary Turbine Project

2. INTRODUCTION AND SUMMARY-VEHICULAR TURBINE PROJECT

The principal objective of the Vehicular Turbine Project is to develop ceramic components and demonstrate them in a 200-HP size high temperature vehicular gas turbine engine. The entire hot flow path will comprise uncooled parts. The attainment of this objective will be demonstrated by 200 hours of operation over a representative duty cycle at turbine inlet temperatures of up to 2500°F. Successful completion of this program objective demonstrates that ceramics are viable structural engineering materials, but will also represent a significant breakthrough by removing the temperature barrier which has for so long held back more widespread use of the small gas turbine engine.

Development of the small vehicular regenerative gas turbine engine using superalloy materials has been motivated by its potentially superior characteristics when compared with the piston engine. These include:

- Continuous combustion with inherently low exhaust emissions
- Multi-fuel capability
- Simple machine - fewer moving parts
- Potentially very reliable and durable
- Low maintenance
- Smooth, vibration-free production of power
- Low oil consumption
- Good cold starting capabilities
- Rapid warm-up time

With such impressive potential, the small gas turbine engine using superalloys has been under investigation by every major on-highway and off-highway vehicle manufacturer in the world

In addition, the small gas turbine engine without exhaust heat recovery (i.e. non-regenerative) is an existing, proven type of power plant widely used for auxiliary power generation, emergency standby and continuous power for generator sets, pump and compressor drives, air supply units, industrial power plants, aircraft turboprops, helicopter engines, aircraft jet engines, marine engines, small portable power plants, total energy systems, and hydrofoil craft engines. While this variety of applications of the small gas turbine using superalloys is impressive, more widespread use of this type engine has been hampered by two major barriers, efficiency and cost. This is particularly so in the case of high volume automotive applications.

Since the gas turbine is a heat engine, efficiency is directly related to cycle temperature. In current small gas turbines, maximum temperature is limited not by combustion, which at stoichiometric fuel/air ratios could produce temperatures well in excess of 3500°F, but by the capabilities of the hot component materials.

Today, nickel-chrome superalloys are used in small gas turbines where blade cooling is impractical, and this limits maximum turbine inlet gas temperature to about 1800°F. At this temperature limit, and considering state-of-the-art component efficiencies, the potential overall efficiency of the small regenerative gas turbine is not significantly better than that of the gasoline engine and not as good as the Diesel. On the other hand a ceramic gas turbine engine operating at 2500°F will have fuel economies superior to the Diesel at significant weight savings.

The other major barrier is cost and this too is strongly related to the hot component materials. Nickel-chrome superalloys, and more significantly cobalt based superalloys which meet typical turbine engine specifications, contain strategic materials not found in this country and cost well over $5/lb.; this is excessively costly with respect to high volume applications such as trucks or automobiles. High temperature ceramics such as silicon nitride or silicon carbide, on the other hand, are made from readily available and vastly abundant raw materials and show promise of significantly reduced cost compared to superalloys, probably by at least an order of magnitude.

Thus, successful application of ceramics to the small gas turbine engine, with an associated quantum jump to 2500°F would not only offer all of the attributes listed earlier, but in addition offer superior fuel economy and less weight at competitive cost with the piston engine.

2.1 VEHICULAR TURBINE PROJECT PLAN

The vehicular turbine project is organized to design and develop an entire ceramic hot flow path for a high temperature, vehicular gas turbine engine. Figure 2.1 shows a schematic of this regenerative engine. Air is induced through an intake silencer and filter into a radial compressor, and then is compressed and ducted through one side of each of two rotary regenerators. The hot compressed air is then supplied to a combustion chamber where fuel is added and combustion takes place.

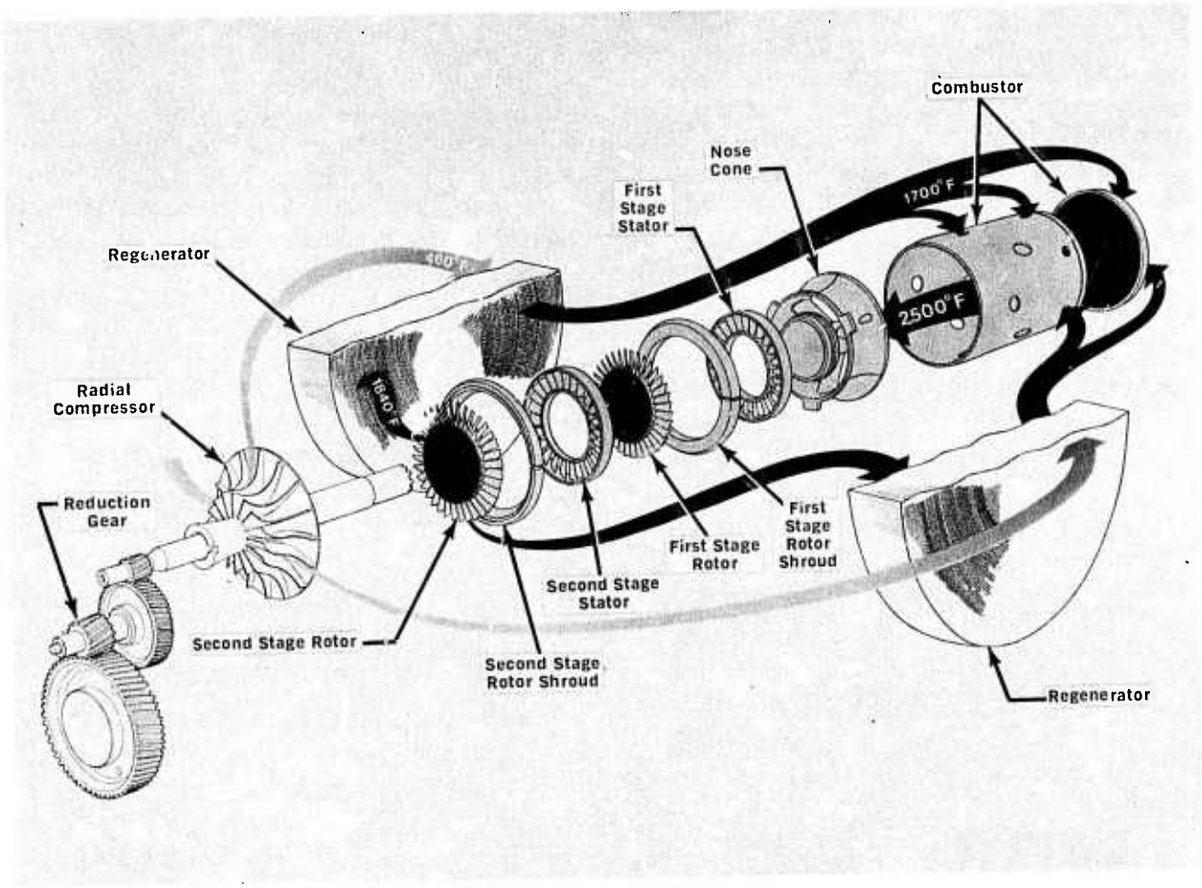

Figure 2.1 Schematic View of the Vehicular Gas Turbine Engine Flowpath

The hot gas discharging from the combustor is then directed into the turbine stages by a turbine inlet nose cone. The gas then passes through the turbine stages which comprise two turbine stators, each having stationary airfoil blades which direct the gas onto each corresponding turbine rotor. In passing through the turbine, the gas expands and generates work to drive the compressor and supply useful power. The expanded turbine exhaust gas is then ducted through the hot side of each of the two regenerators which, to conserve fuel, transfer much of the exhaust heat back into the compressed air. The hot flow path components, subject to peak cycle temperature and made out of superalloys in today's gas turbine, are the combustor, the turbine inlet nose cone, the turbine stators, the turbine tip shrouds, and the turbine rotors. These are areas where the use of ceramics could result in the greatest benefits, therefore these components have been selected for application in the vehicular turbine project.

Successful development of the entire ceramic flow path, as demonstrated in a high temperature vehicular gas turbine engine, will involve a complex iterative development. Figure 2.2 shows a block diagram flow chart, including the feedback loops, of the major factors involved, and serves to illustrate the magnitude of this complex and comprehensive iterative development program. Of particular importance is the inter-relationship of design, materials development, ceramic processes, component rig testing, engine testing, non-destructive evaluation and failure analysis. One cannot divorce the development of ceramic materials from processes for making parts; no more so can one isolate the design of those parts from how they are made or from what they are made. Likewise, the design of mountings and attachments between metal and ceramic parts within the engine are equally important. Innovation in the control of the environment of critical engine components is another link in the chain. Each of these factors has a relationship with the others, and to obtain success in any one may involve compromises in the others. Testing plays an important role during the iterative development since it provides a positive, objective way of evaluating the various combinations of factors involved. If successful, the test forms the credibility to move on to the next link in the development chain. If unsuccessful the test flags a warning and prompts feedback to earlier developments to seek out and solve the problem which has resulted in failure. Finally, all of the links in the chain are evaluated by a complete engine test, by which means the ultimate objective of the program will be demonstrated. It is important then to recognize that this is a systems development program--no single area is independent, but each one feeds into the total iterative system.

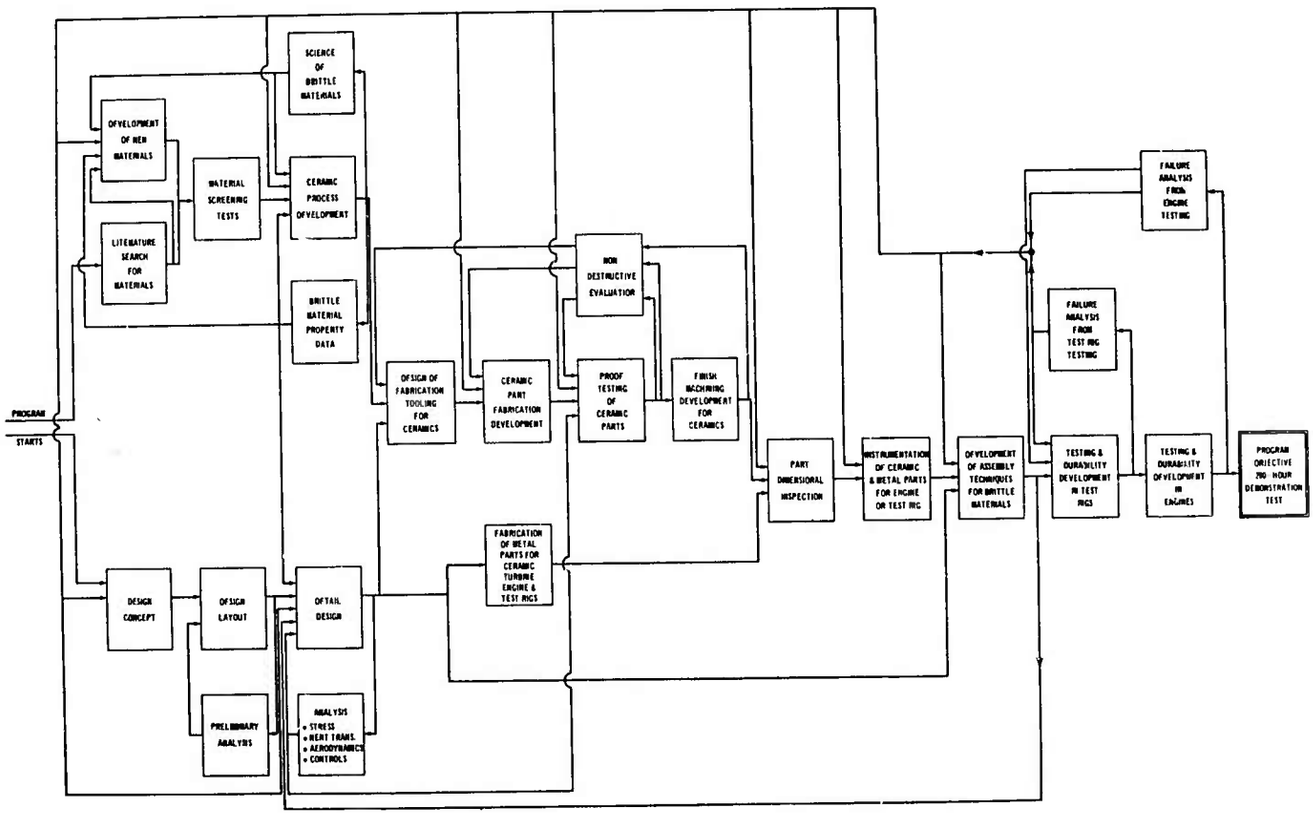

Figure 2.2 Block Diagram Flow Chart of the Iterative Development Process

2.2 PROGRESS AND STATUS SUMMARY - VEHICULAR TURBINE PROJECT

To meet the program objectives, the work has been divided into two major tasks:

1. Ceramic Component Development

2. Materials Technology

The progress and present status in each of these is summarized in Section 2.2.1 and 2.2.2.

2.2.1 CERAMIC COMPONENT DEVELOPMENT

Two categories of ceramic components are under development: rotating parts (i.e. ceramic rotors), and stationary parts (i.e. ceramic stators, rotor shrouds, nose cones, and combustors). In this iterative development, each component will pass through various phases comprising design and analysis, materials and fabrication, and testing.

Ceramic Rotors

Development of the ceramic turbine rotor is by far the most difficult task in the ARPA program. This is because of:

- The high centrifugal stresses associated with maximum rotor speeds of 64,240 rpm.
- The high thermal stresses associated with thermal shock and the high temperature gradients from the rotor rim to the rotor hub.
- The high temperature of the uncooled blades associated with turbine inlet gas temperatures of up to 2500°F.
- The very complex shape of the turbine rotor.
- The hostile environment associated with the products of combustion from a turbine combustor.

Progress and Status

- Fully dense Si_3N_4 first and second stage integral rotors were designed and analyzed (1,2,3,4).
- A method of attaching rotors was conceived and designed (1,2).
- The following approaches for making integral rotors were investigated but discontined:
  - Direct hot pressing of an integral Si_3N_4 rotor (1).
  - Ultrasonic machining of a rotor from a hot pressed Si_3N_4 billet (1,2,3).
  - Hot pressing an assembly of individually hot pressed Si_3N_4 blades (1,2).
  - Pseudo-isostatic hot pressing of an injection molded Si_3N_4 preform (1,2,3).
  - Hot pressing using comformable tooling of preformed Si_3N_4 blades and hub (2,3,4).
  - Fabrication of a dense SiC blade ring by chemical vapor deposition (1,2,3,4).
  - Electric discharge machining of a rotor from a hot pressed SiC billet (2,3,4).

Note: Numbers in parentheses refer to references listed in Section 8.

- A "duo-density" Si_3N_4 ceramic rotor was conceived and designed [3].

- Tooling to injection mold Si_3N_4 blade rings was designed and procured [3].

- Hundreds of blade rings were molded for bonding experiments, cold spin tests, and developing blade ring quality.

- Over two hundred hot press bonding of duo-density rotors were carried out. These have progressed from rotors with flat-sided hubs to current fully-contoured hubs made simultaneously with the hot press bonding operation. Prior severe blade ring distortion problems have been solved by using a blade fill to support the blade ring during bonding. In addition, the diffusion bond has improved to its current excellent quality as evidenced by microstructure examination. However, remaining problems are cracking of the blade ring during hot press bonding and inconsistency from run to run particular with regard to the degree and mode of rim cracking [4,5,6,7].

- Cold spin testing resulted in blade failures over a range of speeds, all lower than design speed. This emphasizes the need for three-dimensional blade stress analysis as well as development of a higher strength, better quality blade material. Cold spin testing of rotor hubs of hot pressed Si_3N_4 showed a characteristic failure speed of 115,965 rpm with a Weibull slope of 17.66 [4,5,6,7].

- A three dimensional model of the rotor blade along with heat transfer coefficients has been generated for three dimensional thermal and stress analysis [5,6].

- Development of better quality blade rings continues. X-ray radiography of green parts has proved effective in detecting major flaws. Slip cast Si_3N_4 test bars having a density of 2.7 gm/cm^3 show four point MOR of 40,000 psi, therefore processes to slip cast a rotor blade ring are under investigation as are methods of achieving 2.7 gm/cm^3 density with injection molded material [6,7].

- Thermal shock testing simulating the engine light-off condition was conducted on rotor blade rings for approximately 2,500 cycles without damage [5,6].

- A technique to evaluate probability of failure using Weibull's theories was developed and applied to ceramic rotors [5].

A test rig was designed and built to simulate the engine for hot spin testing of ceramic rotors. A set of low quality duo-density rotors was spin tested to 20% speed and 1950°F for a short time before failure, believed due to an axial rub [3,4,5,7].

Cold spin testing was conducted on a number of blade rings and segment of blade rings [4,5,6].

Ceramic Stators, Rotor Shrouds, Nose Cone, and Combustors

While development of the ceramic turbine rotor is the most diffcult task, parallel development of the stationary ceramic flow path components is necessary to meet the objective of running an uncooled 2500°F vehicular turbine engine. In addition, success in designing, making, and testing these ceramic components will have an important impact on the many current applications of the small gas turbine where stationary ceramics alone can be extremely beneficial. The progress and status of these developments is summarized below taking each component in turn.

Progress and Status

Ceramic Stators

- Early Design A first stage stators incorporating the turbine tip shrouds had been designed, made by assembling individual injection molded Si_3N_4 vanes, and tested, revealing short time thermal stress vane failures at the vane root [1].

- Investigations of a number of modified designs led to Design B where the rotor shroud was separated from the stator. Short time thermal stress vane failures at the vane root were eliminated [1].

- In the fabrication of stators, the starting silicon powder, the molding mixture and the nitriding cycle were optimized for 2.2 gm/cm^3 density material [2,3].

- Engine and thermal shock testing of first stage Design B stators revealed a longer term vane cracking at the vane mid-span. This led to modification of the vane cord, designated the Design C configuration, which solved the vane mid-span cracking problem [3,4].

- A remaining problem in first and second stage stators was cracking of outer shrouds, believed due to notch effect between adjacent vanes. To solve this, tooling for a one-piece first stage Design C stator was procured [4,5].

- The second stage stator could not be made in one piece due to vane overlap, so an "inverted channel" design was investigated to eliminate notches at the stator outside diameter. However, engine testing showed that axial cracking of the outer shroud remains a problem [3,4,5,6].

- Completed 50 hour duty-cycle engine test of the hot flow path components to 1930°F. The assembled first stage Design C stator was in excellent condition; some vanes in the second stage inverted channel stator had developed fine cracks [6].

- Completed 100 hour duty-cycle engine test of the hot flow path components without a second stage stator to 1930°F. The one piece first stage Design C stator successfully survived this test [7].

Ceramic Rotor Shrouds

- Separate first and second stage ceramic rotor shrouds, which are essentially split rings, evolved in the stator change from Design A to Design B [1].

- As a result of rig and engine testing, rotor shrouds made of cold pressed, reaction sintered Si_3N_4 were modified to have flat rather than conical side faces [2].

- Because of occasional cracking, cold pressing was replaced with slip casting for making higher density rotor shrouds, resulting in 2-3 times increase in strength [3].

- Slip casting of rotor shrouds solved the cracking problem but revealed a dimensional change problem as a function of operating time. This was solved by incorporation of nitriding aids and heat treatment cycles in the fabrication process which reduced instability to acceptable levels [4,5,6].

- Completed 50 hour duty cycle engine test of the hot flow path components to 1930°F, after which both first and second stage rotor shrouds were in excellent condition [6].

- Completed 100 hour duty-cycle engine test of the hot flow path components to 1930°F, after which both first and second stage rotor shrouds were in excellent condition [7].

- Further such testing of rotor shrouds to 245 hours showed them to remain crack free and in excellent condition [7].

Ceramic Nose Cones

- Early Design A nose cones had been designed, made from injection molded reaction sintered Si_3N_4, and tested [1].

- The nose cone was modified to Design B to accommodate Design B first stage stator. Several Design B nose cones were made and tested in rigs and engines [2].

- Voids in molding nose cones were minimized by preferentially heating tooling during molding [5].

- Circumferential cracking and axial cracking problems led to preslotted, scalloped nose cones designated Design C [3,4,5,6].

- Completed 50 hour duty-cycle engine test of the hot flow path components to 1930°F, after which the Design C nose cone was in excellent condition [6].

- Completed 100 hour duty-cycle engine test of the hot flow path components to 1930°F after which the Design C nose cone was in excellent condition [7].

- Further such testing of the nose cone to 221 hours showed it to remain crack free and excellent condition [7].

Ceramic Combustor

- To facilitate materials development, a combustor design was completed comprising a simple ceramic tube attached to a metal dome.

- Combustor tubes made of slip cast Si_3N_4 and various grades of recrystallized SiC (Crystar) cracked during light off tests in the combustor test rig [4].

- A combustor tube made of reaction sintered SiC (Refel) successfully survived 171 hours of rig testing simulating the engine duty cycle with 20 hours at 2500°F combustor outlet temperature [7].

2.2.2 MATERIALS TECHNOLOGY

Materials technology forms the basis for component development including component design, component fabrication, material quality in the component as-made, and evaluation by testing. There are three major categories under materials technology---materials engineering data, materials science, and non-destructive evaluation. Progress and present status in each of these areas is summarized below:

Materials Engineering Data

- Techniques were developed and applied for correlating the strength of simple ceramic disks with bend test specimens using Weibull probability theories [5].

- Elastic property data as a function of temperature was determined for various grades of silicon nitride and silicon carbide [2,3,4,5,6,7].

- The flexural strength vs temperature of several grades of SiC and Si_3N_4 was determined [3,4,5,6].

- The compressive strength vs temperature of hot pressed SiC and hot pressed Si_3N_4 was determined [4].

- Creep in bending at several conditions of stress and temperature was determined for various grades of reaction sintered silicon nitride [4,5,6].

- The specific heat vs temperature of 2.23 gm/cm^3 reaction sintered Si_3N_4 was measured, as were thermal conductivity and thermal diffusivity vs temperature for both 2.23 gm/cm^3 and 2.68 gm/cm^3 reaction sintered Si_3N_4 [4].

- Stress-rupture data was obtained for reaction sintered silicon nitride under several conditions of load and temperature [6].

Materials Science

- A technique was developed and applied to perform quantitative x-ray diffraction analyses of the phases in silicon nitride [2].

- An etching technique was developed and used for the study of the microstructure of several types of reaction sintered Si_3N_4 [2].

- The relationship of some processing parameters upon the properties of reaction sintered Si_3N_4 were evaluated [3,4,5,6].

- The oxidation behavior of 2.2 gm/cm^3 density Si_3N_4 was determined at several different temperatures. The effect of oxidation was found to be reduced when the density of reaction sintered Si_3N_4 increased [3,7].

- The relationship of impurities to strength and creep of reaction sintered silicon nitride was studied, and material was developed having considerably improved creep resistance [4,5,6].

Fractography and slow crack growth studies were performed on reaction sintered SiC [5] and hot pressed Si_3N_4 [6,7].

The development of sintered Sialon-type materials was initiated [7].

Non-Destructive Evaluation

- Ultrasonic C-scan techniques were developed and applied for the measurement of internal flaws in turbine ceramics [1,2,3,4].

- Sonic velocity measurements were utilized as a means of quality determination of hot pressed Si_3N_4 [2,3,5].

- A computer-aided-ultrasonic system was used to enhance the sensitivity of defect analysis in hot pressed Si_3N_4 [3,4,6].

- Acoustic emission was applied for the detection of crack propagation rate and the onset of catastrophic failure in ceramic materials [1,2,5,6].

- A method was developed and applied for the detection of small surface cracks in hot pressed Si_3N_4 combining laser scanning with acoustic emission [4].

- X-ray radiography was applied for the detection of internal defects in turbine ceramics [2,3,4,5].

- Hidden flaws in as-molded stators and rotor blade rings were located by x-ray radiography [5,6,7].

- A state-of-the-art summary of NDE methods as applied to the ceramic turbine programs was compiled [6].

2.3 FUTURE PLANS

It is clear from progress to date that an enormous amount of ground has been covered on all fronts with respect to identifying and solving the real problems in applying ceramic materials to gas turbine engines. Nonetheless, a large number of difficult problems remain before full success can be demonstrated on stationary flow path components and, in particular, on ceramic turbine rotors. To expedite solution of the really fundamental problems in ceramic design, an important decision with respect to future plans was recently made. This is discussed under Component Development below and involves a simplification of the hot flow path configuration.

Component Development

As summarized in paragraph 2.2.1, the latest first stage Design C stators are made in one piece, and, as a result, are made more readily and have greatly improved durability. However, cracking problems with the second stage stator persist, since a way to design and fabricate this stator in one piece has not been found. Therefore, it has been decided to modify the flow path configuration to use a one piece first stage stator in both the first and second stage locations.

In addition, considerable development remains to successfully and consistently fabricate duo-density rotors; minimizing the types of parts would provide a more intense effort on the real problems of producing good quality blade rings and good quality hot press bonds between the blade ring and hub. Therefore, as part of the flow path modification it was decided to use one basic rotor configuration, for both first and second stage locations. The preferred aerodynamic match selected was to use a second stage ceramic rotor machined to a smaller diameter to fit the first stage location, and another second stage ceramic rotor machined to fit the second stage location using the one piece stator. This will immediately reduce the amount of tooling required in the ceramic rotor project, and will, in addition, ease possible future tooling changes required to accommodate blade redesign based on three-dimensional stress analyses now underway. A further benefit is the somewhat reduced rotor stresses because of the smaller rotor diameters.

This revised flow path configuration has been designated Design D and is compared schematically with Design C in Figure 2.3. Although there is no appreciable change at part load, aerodynamic efficiency is lower at full power. However, this change will significantly enhance fabrication and durability development toward the 200 hour objective. Because of the compromise in aerodynamic efficiency, future plans will include design studies of an updated flow path configuration optimized for aerodynamic efficiency, ceramic manufacturing and durability.

In addition to adopting the new Design D flowpath, future plans on component development will focus on material and process improvement, and continued rig and engine testing. Technology will be researched to fabricate molded and/or slip cast higher density (2.7 gm/cm^3) Si_3N_4 components, in particular rotor blade rings and one-piece stators. Also more emphasis will be placed on producing parts in prototype quantities to facilitate assessing consistency both of making the part and of the part quality.

With regard to testing, ceramic rotors of higher density Si_3N_4 will be cold spin tested to evaluate part quality and material strength; this will lead to subsequent testing in the high temperature turbine rotor test rig. Two major test series are planned for the stationary ceramic components: the first is

PRECEDING PAGE BLANK-NOT FILMED

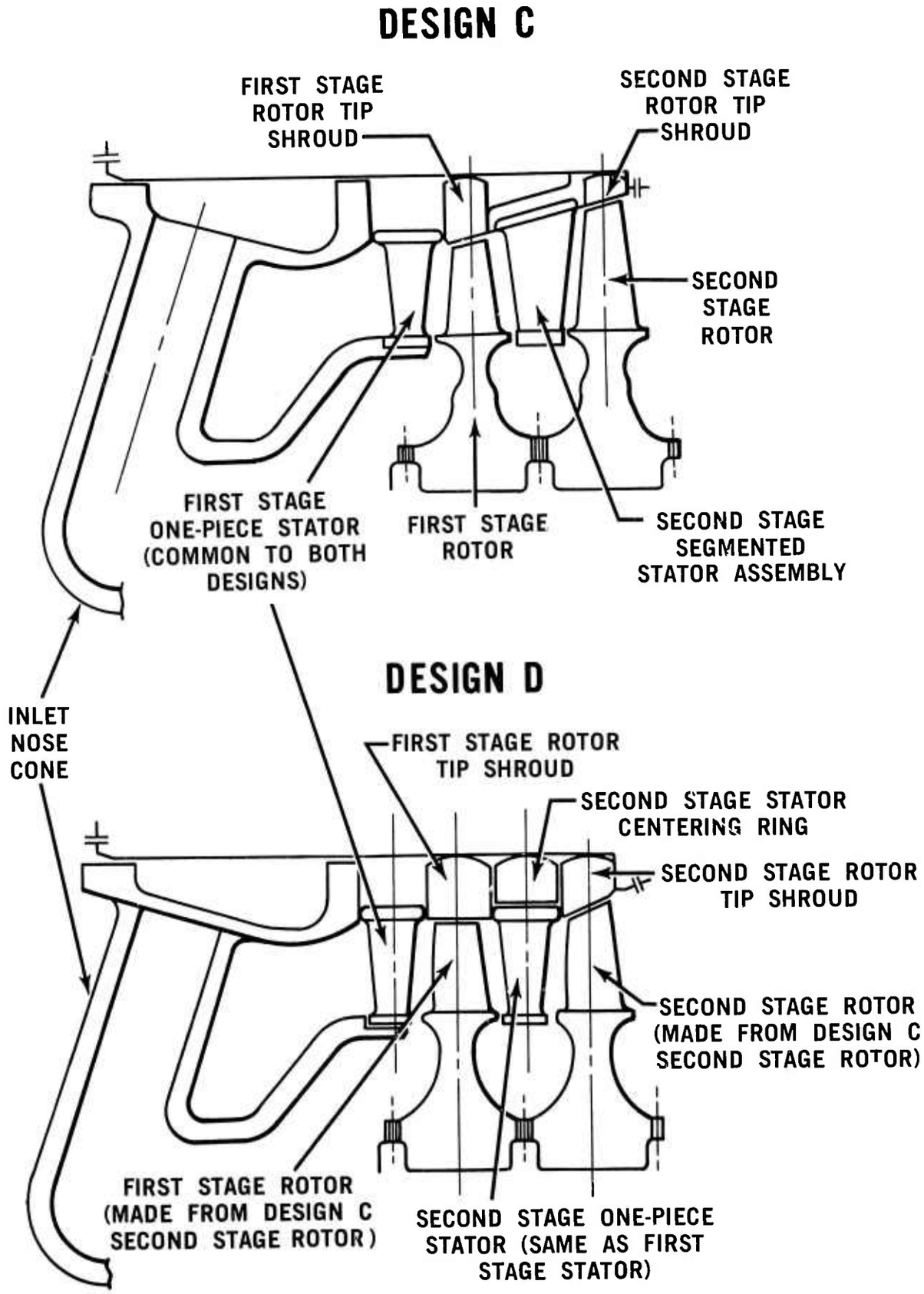

Figure 2.3 Schematic Cross-Section View of Design C and Design D Hot Flow Path Configurations

a 175 hour engine test over the ARPA duty cycle up to 1930°F (metal turbine rotors); the second is a test of the components up to 2500°F in a specially designed stationary flowpath test rig which does not incorporate rotating parts. Success in each of these phases of testing will provide the basis for building and testing engines with the entire ceramic flowpath including ceramic turbine rotors. Continued development of this complete system will then lead to the final program objective of completing a 200 hour engine durability test with ceramic temperatures up to 2500°F.

Material Technology

Feedback from engine and rig testing of stationary components made from reaction sintered Si_3N_4 indicates that improved durability could be expected if improvements in strength and oxidation resistance could be obtained. Therefore, major emphasis is being placed on the development of higher density injection molded Si_3N_4 for rotor blade rings, nose cones, and stators. Such material would be expected to have significantly improved strength and oxidation resistance; in addition, other means of improving oxidation resistance are being studied. Another area receiving major emphasis will be processing improvements in both molded and slip cast reaction sintered Si_3N_4. Integral with this effort will be the application and continued development of non-destructive evaluation techniques to assist in the elimination of flaws-in particular, those flaws which are found by testing to have a critical effect upon component life.

In the final stages of the program, increasing attention will be given to material characterization, including the higher density reaction sintered silicon nitride materials currently being developed. It is expected that materials engineering data will be compiled and statistically analyzed for those materials which are utilized for the 200 hour demonstration which constitutes the major program objective.

3. PROGRESS ON CERAMIC COMPONENT DEVELOPMENT-VEHICULAR TURBINE PROJECT

3.1 CERAMIC ROTOR DEVELOPMENT

SUMMARY

Two outside computer codes are being evaluated for use in three-dimensional analysis of turbine rotors, while modifications to in-house computer programs for such analyses continue.

To provide a set of boundary conditions for 3D thermal and stress calculations, heat transfer film coefficients were computed at 55 and 100 percent speed conditions for the first stage turbine rotor and 100% speed for the second stage rotor at one blade radius. Average values of film coefficients were computed for the rotor inter-blade channel and outer tip shroud.

Calculation of thermal stresses in the common profile disks has progressed with generation of the thermal boundary conditions.

Tests were conducted to determine the effectiveness of the installation tool used to preload the bolt assembly for the two turbine stages. The purpose of the tool is to minimize torsional stress in the bolt during pre-loading. The tool provides a means for pre-loading the bolt and transferring the load to the nut upon removal of the tool. Efficiency of this transfer was measured and found to be eighty percent.

A method of filling the cavities of a blade ring with slip cast silicon nitride material, prior to fabricating a duo-density wheel, was developed. The blade fill is required to back-up the blade ring during the bonding process to avoid damage to the blades from the high pressure loads applied.

Two methods of fabricating a duo-density turbine rotor have been under development. In one, a pre-hot pressed hub of silicon nitride is bonded to a machined blade ring. Quality of the bond achieved has been inadequate with incomplete bonding and distortion of the blade ring. The other method is designed to correct these conditions, and combines hot pressing of the hub to shape from silicon nitride powder with simultaneous press bonding of the hub to the blade ring. Excellent bonding, without blade ring distortion has been demonstrated with this second technique.

One method of making rotor blade rings is by a shell mold slip casting process under development at the Georgia Institute of Technology Experiment Station. Shell molds have been made for casting a monolithic rotor or a blade ring consisting of airfoil blades and supporting rim. Several slip castings have been made using materials with green densities sufficient to produce parts with both 2.7 gm/cm^3 and near-theoretical final density. However, removal of the shell mold after nitriding has so far resulted in blade damage because current molds have excessive strength.

The development of methods to use a high pressure nitrogen atmosphere to facilitate nitridation of high green density silicon compacts has continued at Battelle Memorial Institute with several test runs at pressures from 10,000 to 20,000 psi and various time-temperature schedules. Test samples with various green densities were prepared which simulated the turbine rotor cross section to be nitrided. The first autoclave run at 20,000 psi nitrogen pressure produced specimens severely reacted and distorted because of exudation of

PRECEDING PAGE BLANK-NOT FILMED

molten silicon caused by an uncontrolled exothermic reaction. In an attempt to prevent the uncontrolled reaction the process was varied by pre-nitriding the specimens, modifying the nitriding cycle pressure, time, and temperature, and changing the nitriding aids. However, successful nitriding of high green density silicon compacts has not been achieved to date, although the results obtained are encouraging enough to warrant continuation of the program.

Seven hot pressed silicon nitride rotor hubs were spun to failure in the cold spin pit for evaluation of strength and correlation with MOR bar test data. Burst speeds ranged from 102,000 to 120,000 rpm. The Weibull slope for the hubs, based on burst speed, was 17.66, with a characteristic speed of 115,965 rpm.

In order to check out the turbine rotor test rig, two hot pressed Si_3N_4 hubs (without blades) were run to 15% speed (10,125 rpm) and 1850°F. Following this, a set of ceramic turbine rotors of recognized low quality were spun to 12,848 rpm and 1950°F for a short time before failure, due to an axial rub. This test therefore revealed insufficient cold clearances.

An assessment of the current project status indicates that the primary approach for rotor development continues to be the duo-density Si_3N_4 concept. Significant improvement in bond quality has been achieved by hot pressing the hub and press bonding to the blade ring in one operation. Spin testing confirmed room temperature strengths of hot pressed rotor hubs; based on this, strength at temperature should be adequate for the rotor requirements. Full confirmation, however, must come from actual operational testing in a representative high temperature environment.

3.1.1 DESIGN AND ANALYSIS

Introduction

Development of in-house computer codes discussed in the last report [6] for three dimensional analysis of temperature and stress is continuing. Two additional finite element computer codes are discussed, along with associated model modifications.

Heat transfer coefficients for the first stage rotor at various operating conditions were calculated for typical blade sections. Convection coefficients for the second stage rotor at full speed operation were determined for a typical section.

Work was continued on the design of the common profile rotor disks, including a method of evaluating heat transfer in the interstage hub cavity.

Three Dimensional Analysis of Ceramic Rotors

The previous report [6] discussed development of the Ford version of the SAP [8] three dimensional stress analysis code. Further work is needed to complete modifications to allow analysis of repetitive structures [9], and apply this to the ceramic turbine rotor.

In the meantime, two alternate finite element computer codes are being investigated for three dimensional rotor analysis. These alternate codes, designated ANSYS [10] and NISA [11], are proprietary and are being made available from their owners on a royalty basis.

Both NISA and ANSYS utilize the frontal technique for equation solution whereas SAP makes use of the bandwidth technique. This basic difference requires the model of the rotor to be constructed differently for SAP analysis than for analysis by the alternate codes. ANSYS and NISA, however, have virtually identical input requirements, although there are differences between the two. The ANSYS code is limited to the eight noded brick for solid element analysis; this element incorporates Wilson's [12] incompatible displacement functions. NISA is available with 8, 20, and 32-noded solid elements, the higher order elements being used for rotor analysis. In addition, ANSYS has both steady state and transient heat transfer capability whereas NISA, to date, has steady state capability only. Material properties may be input as a function of temperature for both NISA and ANSYS stress analysis and for ANSYS heat transfer analysis, while the NISA heat transfer analysis accepts only constant material properties. Another major difference is that NISA is mounted on an in-house computer whereas ANSYS must be conducted on an outside computer.

As mentioned, both alternate codes are proprietary and can be used only on an as-is basis; therefore, they do not meet some of the special requirements of the total rotor analysis program. An example is their lack of output data in a form suitable for input directly to the Weibull strength analysis computer program. Therefore, work is continuing on the Ford version of the SAP code, which can be modified to suit the overall needs of ceramic rotor analysis.

Work is also continuing on the Ford TAP three dimensional heat transfer code to incorporate temperature-dependent material properties. A refinement of the analytical design process, discussed in the previous report, [6] was to

provide accurate three-dimensional analyses of mechanical and thermal loadings on ceramic structures. Utilizing the methods described in this approach, heat transfer film coefficients were computed at 55 percent speed and 100 percent speed conditions for the first stage rotor at three radii, representing three separate airfoil cross-sections of the blade. Also, film coefficients for the second stage rotor were computed at 100 percent speed at a given radius.

These data provide spatial variations of film coefficients from leading-to-trailing edge. Step-wise temporal variations are achieved at 55 percent and 100 percent speed conditions. The transient conditions between these steps are taken into account by using the 55 percent speed coefficients from light-off (time = 0) to 55 percent speed conditions. Likewise, the 100 percent speed film coefficients are employed to account for transients between 55 and 100 percent speed and for steady state conditions at 100 percent speed.

Average values of film coefficients for the rotor inter-blade channel and outer tip shroud were computed by an empirical method given by Zysina-Molozhen and Uskov [13]. These data, when combined with the airfoil film coefficients, may be mapped through interpolation and extrapolation to cover the full hot flow path wetted-surface area. As such, they constitute a set of boundary conditions for three dimensional as well as two dimensional rotor thermal and stress calculations and provide spatial and step-wise temporal variations which accurately simulate the critical engine running environment.

The method involves computation of initial flow angles, relative blade inlet velocities, and other flow parameters for all turbine stages for various radii throughout the flow path by use of a modified Ainley-Mathieson [14] computer program. This established both the relative and the total inlet and exit flow conditions for all radially distributed stream tubes for airfoils in both turbine stages. These data were used as input to the TSONIC [15] computer program which was utilized to determine the velocity distribution tangent to the airfoil surface. The velocity distribution adjacent to the boundary layer as computed by TSONIC and the accompanying total or free-stream conditions computed by the Ainley-Mathieson program were directly input to BLAYER [16], the boundary layer program. Output of BLAYER encompasses all principal boundary layer information. Film coefficients were obtained directly from a modified BLAYER which utilizes re gas conductivity for air at the film temperatures under consideration.

All vane airfoil boundary film coefficients were obtained directly from BLAYER except the stagnation point ($S/S_{max} = 0$) which was computed by a method of Cohen and Reshotko [17]. This empirical method, which is applicable to stagnation point heating on the leading edge of cylinders, was used as an approximation for leading edge heating on vanes. On page 58 of the last report [6], equations (1), (2), and (3), used in this empirical relationship, were inadvertently printed in error. These should be corrected to read:

$$h_s = \frac{k_w}{\sqrt{\nu_w}} \left(\frac{N_{n_u}}{\sqrt{N_{Rew}}} \right) \sqrt{C} \qquad (1)$$

$$C = \frac{2\mu_1}{r} \left(1 - 0.416\, M_1^{\,2} - 0.164\, M_1^{\,4}\right) \qquad (2)$$

$$N_{nu_c} = \left(0.032 + 0.014 \frac{\beta}{100}\right)\left(N_{Re_c}\right)^{0.8} \left(\frac{t}{b}\right)^{-0.175} \qquad (3)$$

Figures 3.1 through 3.6 show film coefficient predictions on the suction and pressure surfaces of the first stage rotor blades at radii of 1.7, 1.994 and 2.294 inches at 55% and 100% speed. These locations are indicated on the profile for the rotor blade inset in Figure 3.1. All suction surfaces of the first stage rotor exhibited both laminar and turbulent flow with the transition regime approximated with the dotted line. Transition between laminar and turbulent flow appeared to vary between S/S_{max} of 0.3 to 0.55, depending on flow rate, radial stream tube position and local surface angle.

All first stage rotor pressure surfaces exhibited both laminar and turbulent flow except the 55 percent speed case for radii of 1.994 and 2.294 inches. These flow regimes had been predicted earlier to be laminar only. Experimental data from work of Barnes and Edwards [18] appears to corroborate the prediction of turbulent flow observed on the first stage rotor pressure surfaces, since experimental values of turbulent flow were evident on similar pressure surfaces examined in that study. Prediction criteria for detecting turbulent flow transition is difficult, and there is much disagreement among methods presently available. However, it appears that the Schlichting-Ullrich-Granville [19,20,21] method built into BLAYER does an adequate job of predicting turbulence on turbomachinery blades.

Figure 3.7 shows heat transfer coefficients for the second stage rotor blade at a radius of 1.7 inches for 100 percent speed. This location is also indicated on the blade profile. The suction surface, unlike that of the first stage rotor, exhibited all laminar flow. The pressure surface exhibited both laminar and turbulent flow but transition occurred very far downstream at $S/S_{max} = 0.9$.

Figures 3.8 through 3.11 present adiabatic wall (or recovery) temperatures computed by BLAYER for the hot flow path cross-sections examined for the rotors in the course of this study. These temperatures are used with their corresponding film coefficients as indicated in the previous report [6].

Table 3.1 presents average film coefficients for first stage rotor inter-blade channels (or grooves) and outer tip shrouds. These data were computed by empirical methods [6,13].

When this work on the TAP three dimensional heat transfer code is completed, along with the SAP modifications for repetitive structures, these two finite element codes - used in conjunction with the Weibull statistical strength analysis code - will form a very useful package for the design of brittle materials in general and ceramic turbine rotors in particular.

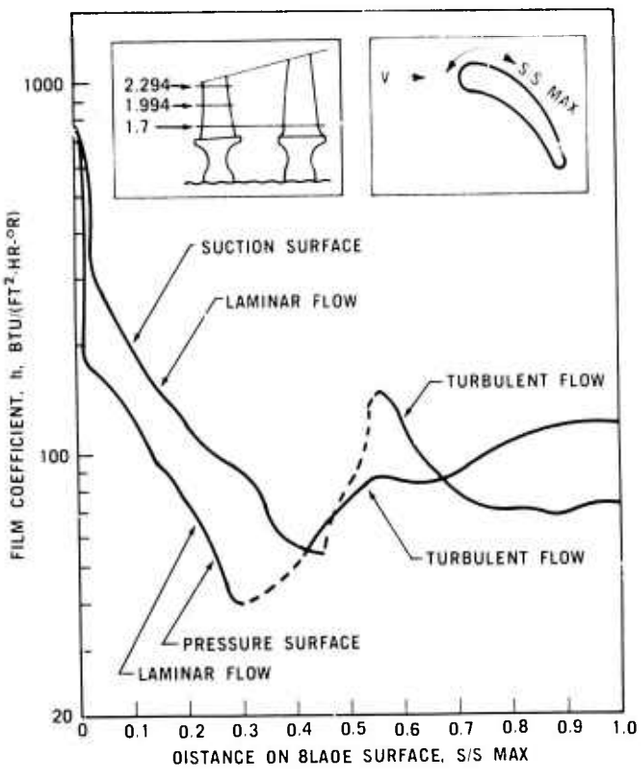

Figure 3.1 Heat Transfer Film Coefficients, First Stage Rotor Blade, at 55% Speed, 2390°R Inlet Temperature, and Radius of 1.7 Inches

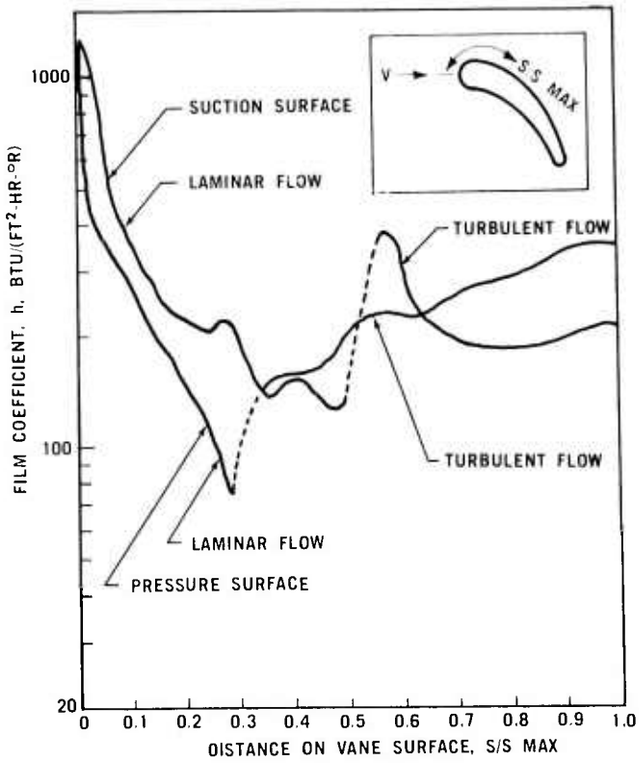

Figure 3.2 Heat Transfer Film Coefficients, First Stage Rotor Blade, at 100% Speed, 2960°R Inlet Temperature, and Radius of 1.7 Inches

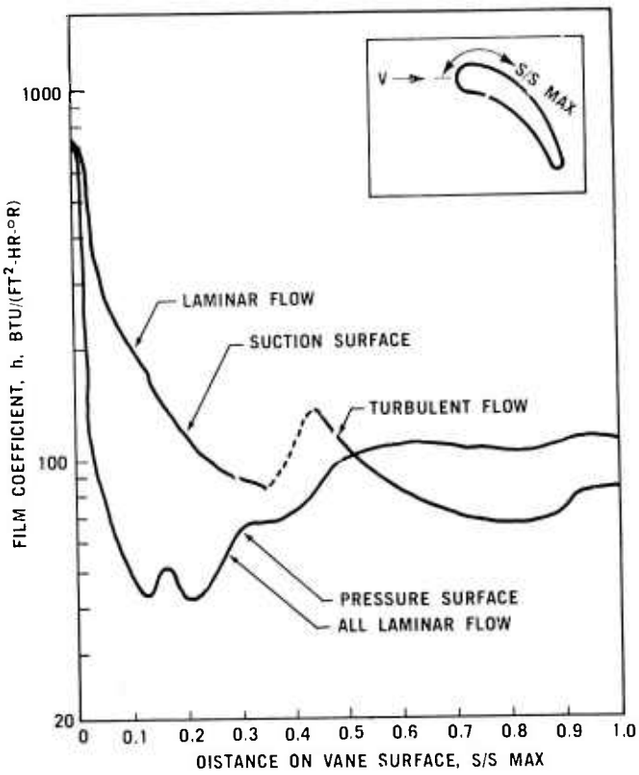

Figure 3.3 Heat Transfer Film Coefficients, First Stage Rotor Blade, at 55% Speed, 2390°R Inlet Temperature, and Radius of 1.994 Inches

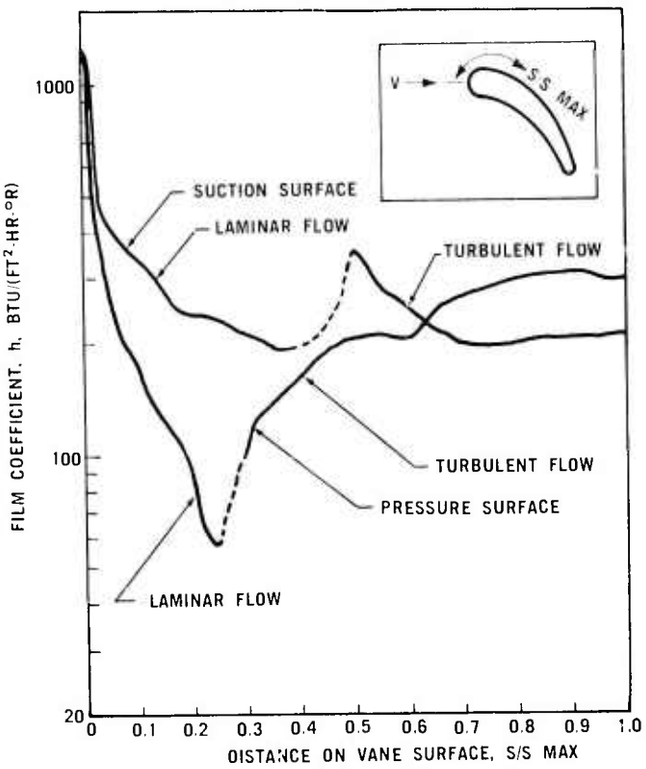

Figure 3.4 Heat Transfer Film Coefficients, First Stage Rotor Blade, at 100% Speed, 2960°R Inlet Temperature, and Radius of 1.994 Inches

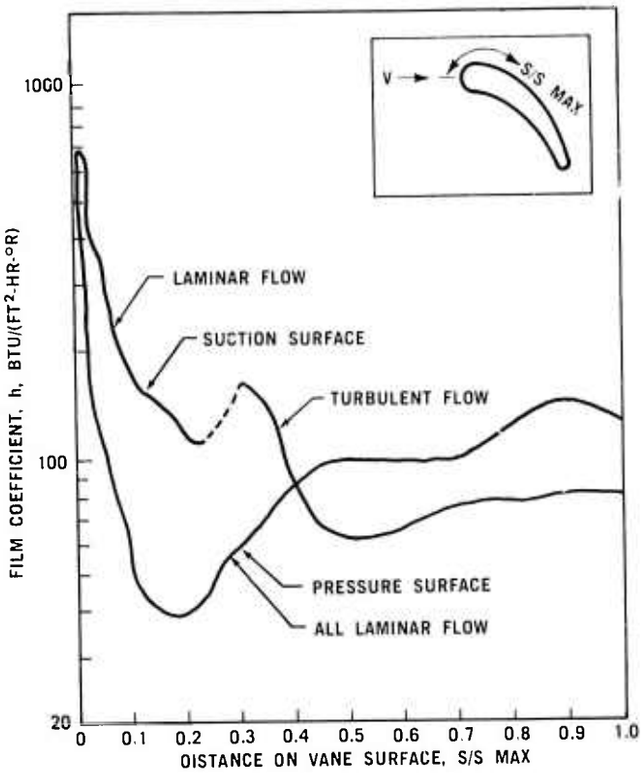

Figure 3.5 Heat Transfer Film Coefficients, First Stage Rotor Blade, at 55% Speed, 2390°R Inlet Temperature, and Radius of 2.294 Inches

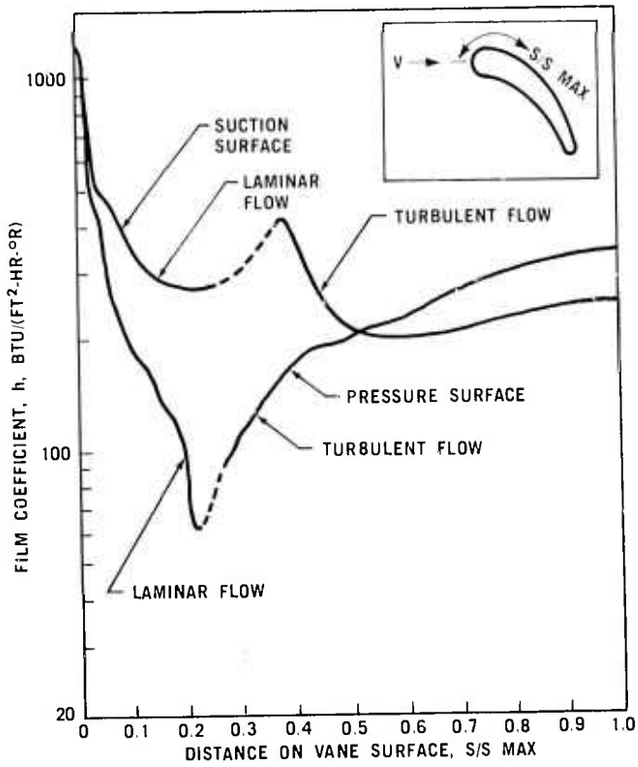

Figure 3.6 Heat Transfer Film Coefficients, First Stage Rotor Blade, at 100% Speed, 2960°R Inlet Temperature, and and Radius of 2.294 Inches

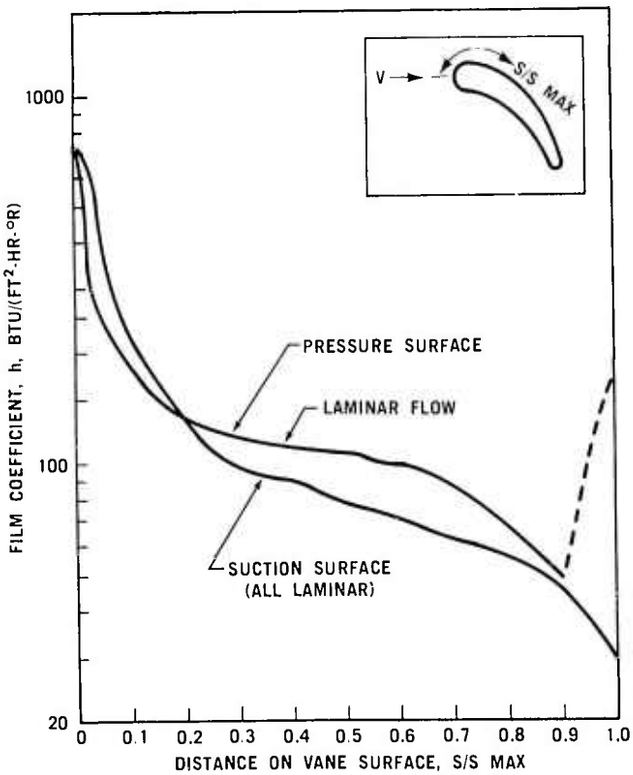

Figure 3.7 Heat Transfer Film Coefficients, Second Stage Rotor Blade, at 100% Speed, 2960°R Inlet Temperature, and Radius of 1.7 Inches

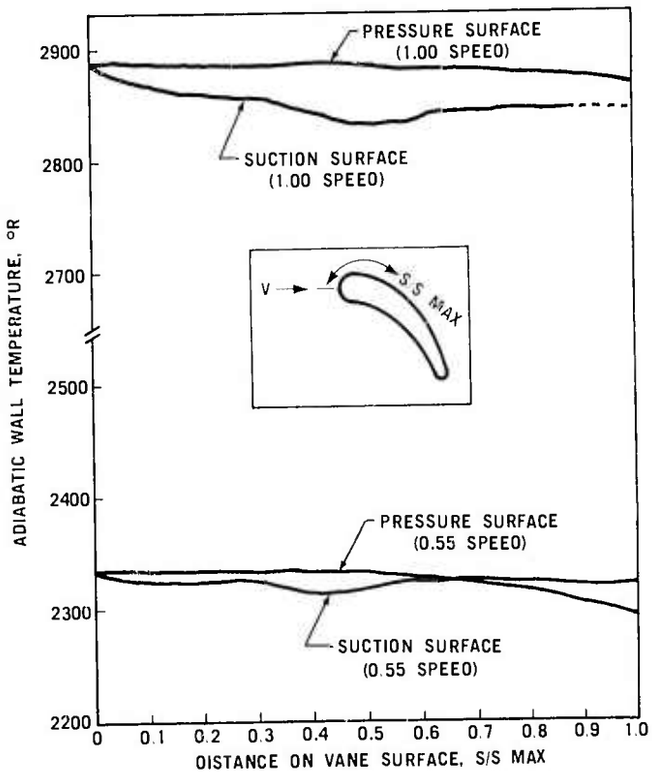

Figure 3.8 Adiabatic Wall Temperature of First Stage Rotor Blade at Radius of 1.7 Inches

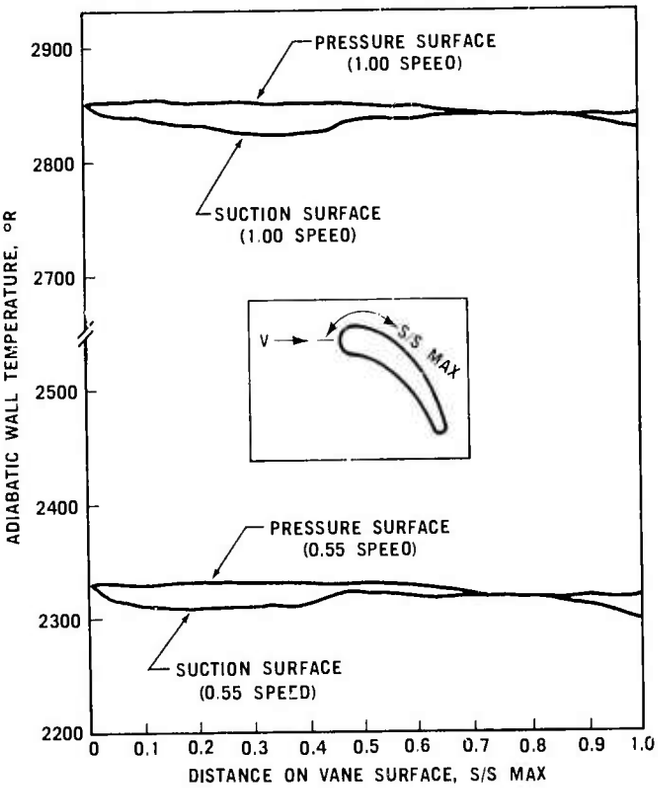

Figure 3.9 Adiabatic Wall Temperature of First Stage Rotor Blade at Radius of 1.994 Inches

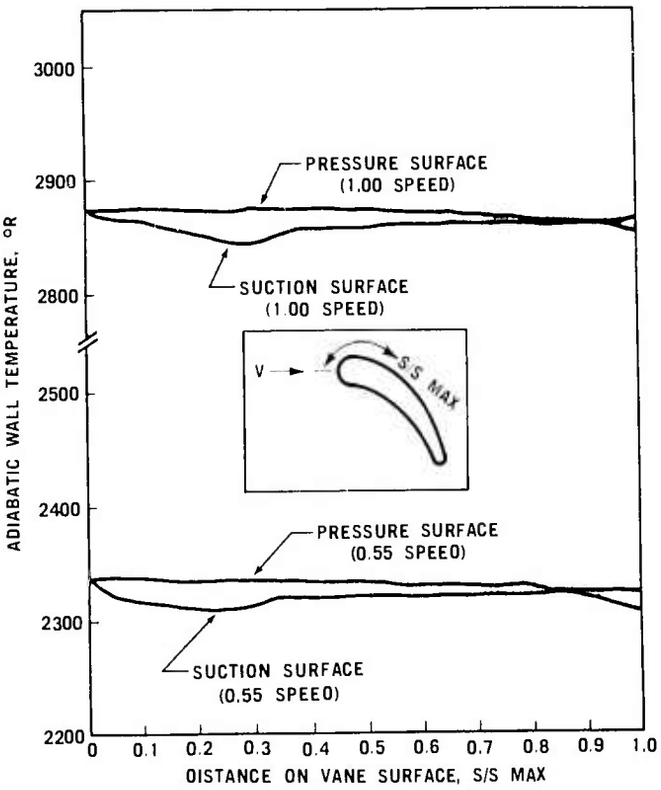

Figure 3.10 Adiabatic Wall Temperature of First Stage Rotor Blade at Radius of 2.294 Inches

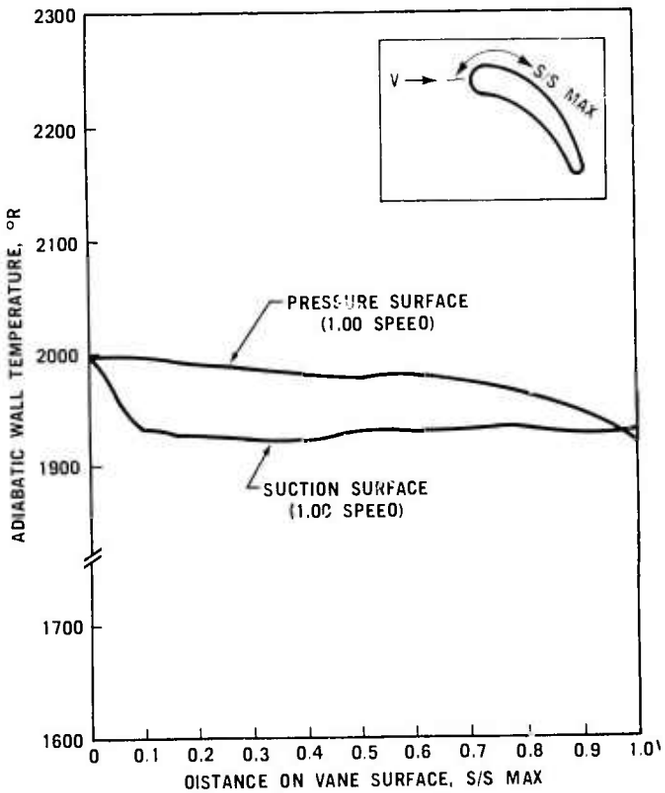

Figure 3.11 Adiabatic Wall Temperature of Second Stage Rotor Blade at Radius of 1.7 Inches

TABLE 3.1

AVERAGE FILM COEFFICIENTS FOR INTER-BLADE CHANNEL GROOVE AND SHROUDS

Average Convective Heat Transfer Film Coefficient Btu/(Ft^2-Hr-^{o}R)

	Outer Shroud		Inner Shroud or Channel	
Stage \ Speed	55%	100%	55%	100%
First Rotor	182	395	197	449

Thermal Stresses in Rotor Disks

The centrifugal stresses calculated for the common profile rotor disks were tabulated in the previous report [6]. The calculation of thermal stresses of the common profile disks is in progress, commencing with the generation of the thermal boundary conditions. The finite element grids used for the centrifugal stress analysis are also being used for the heat transfer analysis; these grids were shown in the last report [6].

In order to generate thermal boundary conditions for the common profile rotors, it was necessary to calculate the temperatures of the curvic couplings and the rotor attachment bolt using the thermal model of the assembly which includes the rotors and shaft. This finite element thermal model was shown in a previous report [3], and was modified to reflect the common profile rotor disks.

The gas flow in the common cavity between the first and second stage rotors is considered to be fed by the first stage rotor discharge. The assumed circulation is shown in Figure 3.12. Hot gas leaks into the cavity between the first stage rotor and the second stage stator. Some flows down the center of the cavity and up the faces of the disks, while the remainder crosses the bottom of the second stage stator platform; both streams exit between the second stage stator and rotor. Some of the gas is recirculated, but it is impossible to predict the amount. The gas entering the cavity has a calculated static temperature of 2150°F and a calculated static pressure of 34 psia at 100 percent speed with a turbine inlet temperature of 2500°F. The cavity gas is assumed to be circulating such that the heat transfer correlation for a free disk with radially uniform heat flux applies. The heat transfer correlation [22] used is

$$h = 0.25 \frac{k}{r} \left(\frac{\rho \omega r^2}{\mu}\right)^{0.80} \left(\frac{C_p \mu}{0.70 \quad k}\right)^{0.60} \qquad (4)$$

Where

k = thermal conductivity

r = radius

ρ = density

ω = angular velocity

μ = dynamic viscosity

C_p = specific heat

This is plotted in Figure 3.13 with the corresponding adiabatic wall temperature. The adiabatic wall temperature is based on a static temperature of 2150°F.

The heat transfer coefficients for the first and second stage rotor blades were shown earlier in this section. The heat transfer coefficients for the blade are not directly applicable to the two-dimensional finite element program, but are used with the fin efficiency of the blade to calculate an equivalent heat transfer coefficient that is utilized in two-dimensional thermal stress axisymetric analyses. The formula for this calculation has been given previously [1].

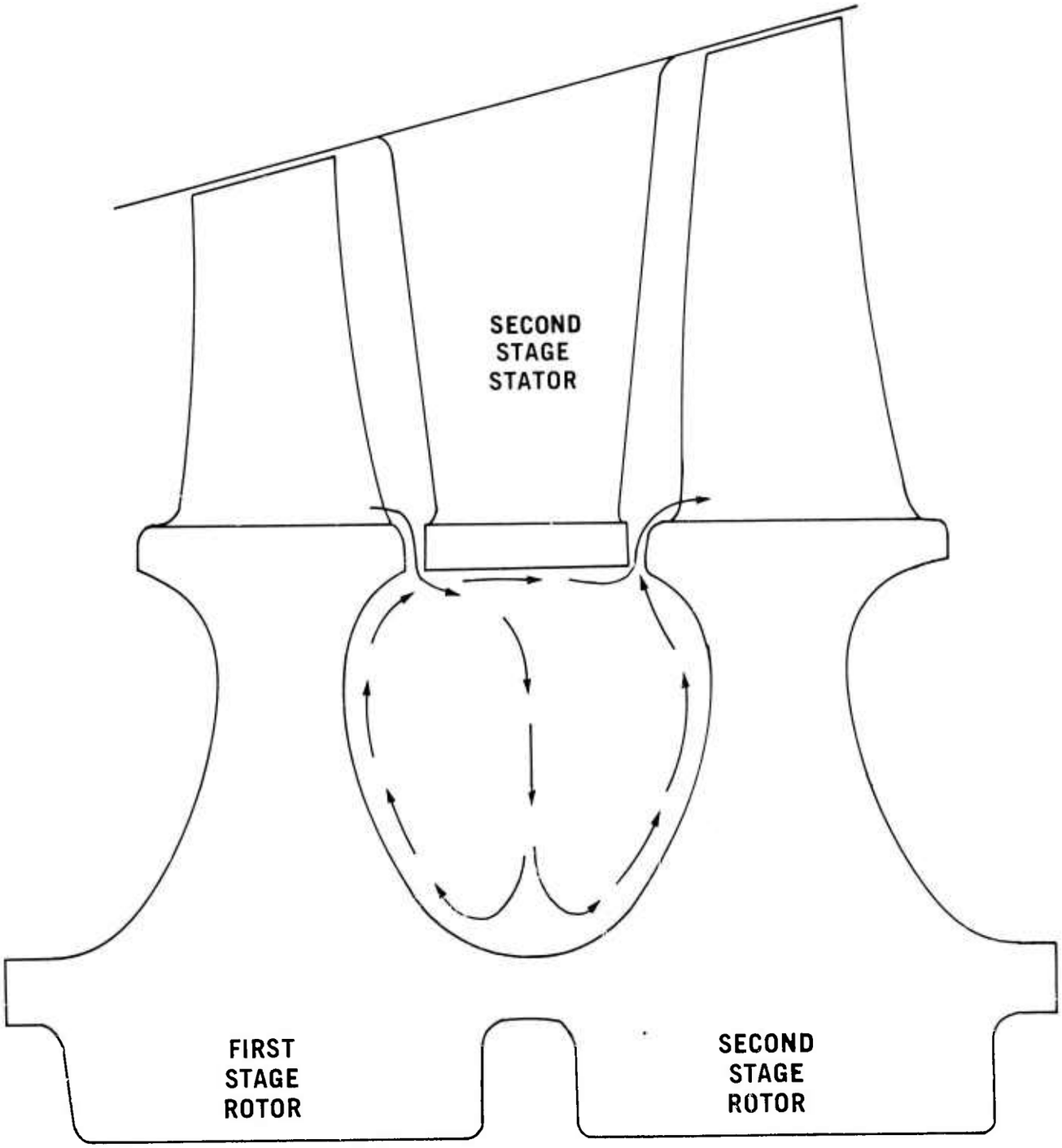

Figure 3.12 Assumed Hot Gas Circulation in Cavity Between First and Second Stage Rotors

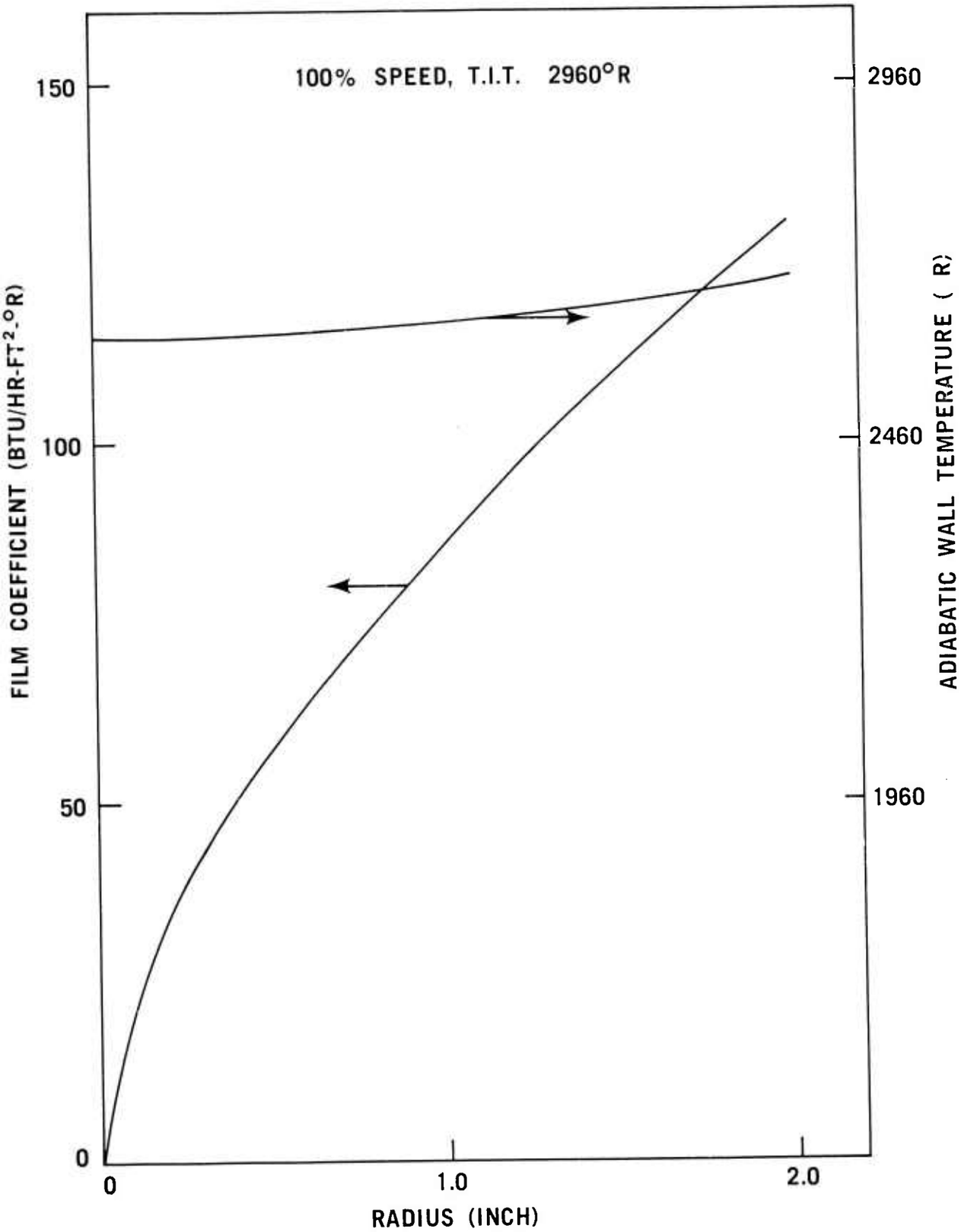

Figure 3.13 Film Coefficients vs Radius for the Cavity Between First and Second Stage Rotors

3.1.2 MATERIALS AND FABRICATION

Introduction

The primary in-house effort on fabrication of ceramic turbine rotors continues to be expended on the silicon nitride duo-density rotor. Blade fill reinforcement and restraint systems have been developed and simultaneous hot pressing of contoured hubs and hub-to blade ring bonding has been accomplished.

The development of slip casting of silicon nitride shapes by a modified investment casting technique has been extended to complete rotor blade rings in an effort to obtain higher strength reaction sintered parts for improved hot-press bonding. Remaining problems are removal of the shell mold after forming and complete nitriding of the blade ring.

A process for nitriding silicon shapes which were slip cast to very high densities, such that the resulting material approaches theoretical density, is under development.

Duo-Density Silicon Nitride Rotors

The duo-density concept is one of several techniques being investigated for fabricating a ceramic turbine rotor. In this concept, the high strength of the hot-pressed Si_3N_4 is utilized in the hub region where stresses are highest but temperatures are moderate and, therefore, creep problems are minimized. Reaction sintered Si_3N_4, which can be readily formed into complex airfoil blade shapes by injection-molding, is utilized for the blades. The blades are generally exposed to the higher temperatures but lower stress levels than the turbine rotor disk.

Work on the duo-density approach during this reporting period was directed toward further developing the graphite wedge hot pressing system [5,6] as the fabrication technique for bonding the reaction sintered Si_3N_4 blade ring and hot-pressed hub together. The blade ring assembly was injection molded in one piece from silicon metal powder and subsequently nitrided to form Si_3N_4 having a density of 2.2 gm/cm^3. Since the thin rim of the blade ring has insufficient strength to support the applied pressure during hot press bonding, a "double" blade fill" technique [6] was devised. This technique consists of first filling the space or cavities between the blades with slip cast silicon and subsequently nitriding to Si_3N_4. The Si_3N_4 blade cavity inserts are independent of one another. A second blade fill of slip-cast silicon is applied, entirely encasing both the turbine blades and blade cavity inserts and is subsequently converted to Si_3N_4. Boron nitride is used to prevent the various blade fill materials from bonding to each other and to the turbine blades. The theoretically dense Si_3N_4 contoured hub region was fabricated by hot-pressing AME alpha Si_3N_4 powder with 2 to 5 w/o MgO added. The MgO is a densification aid which enables the alpha Si_3N_4 powder to be hot-pressed to theoretical density. The bond surfaces of all component parts were machined to remove any oxide or reaction surface layers just prior to hot-press bonding.

Two press bonding fabrication techniques were the subject of development work during this reporting period. One technique [5] consisted of first hot-pressing a contoured Si_3N_4 hub followed by press bonding the Si_3N_4 hub and blade ring together. The other technique, although similar, involves both hot-pressing the contoured hub and hot-press bonding the hub to the blade ring in one operation. Figure 3.14 illustrates the hot-press bonding rig used for the first technique. The inside diameter of the blade ring and outside

diameter of the dense Si_3N_4 hub are machined to within a 0.001 inch slip fit and assembled in the hot-pressing rig. Graphite foil is used throughout to minimize surface reactions and sticking. A compression rig [5] is used to independently apply and control the pressure on both the outside graphite wedge system and inside hub component. The graphite wedge system is used to restrain and prevent deformation of the blade ring during hot-press bonding.

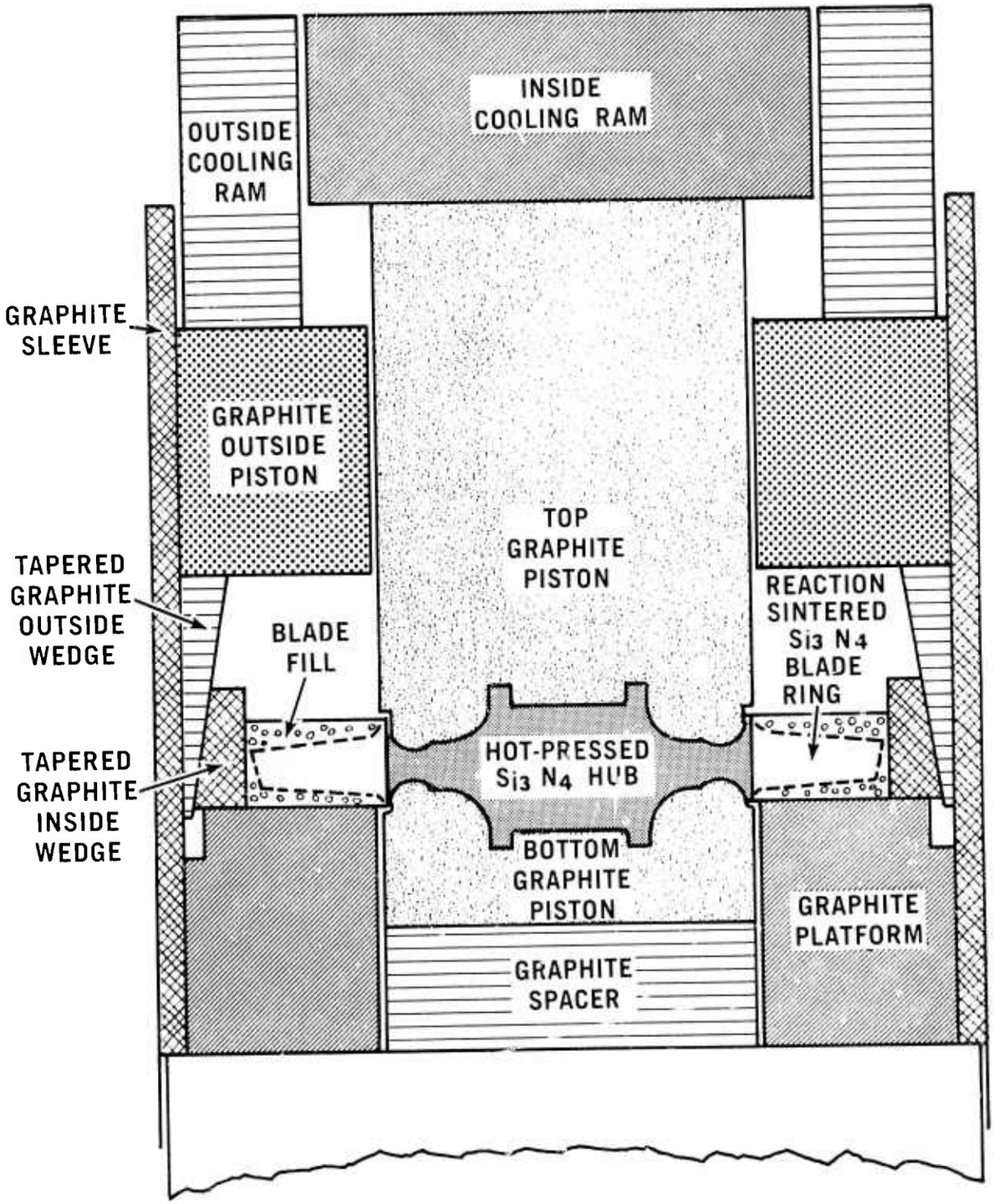

Figure 3.14 Hot Press Bonding Assembly

The rotor assembly is hot-press bonded at 1750°C and 2500 psi for 2 hours. In an effort to improve bonding, the magnesium oxide additive in the hot pressed hub was increased from 2 to 5 w/o. Preliminary microprobe analysis indicated magnesium diffusion across the bond interface. Although not verified as yet by vacuum spin testing, it is assumed that stronger and more uniform bonds will result by increasing the MgO concentration in the Si_3N_4 powder from 2 to 5 w/o. This should not affect the performance of the Si_3N_4 turbine rotor as the projected temperatures in the hub region are below the critical temperature at which creep becomes a significant problem. In addition, the 5 w/o MgO concentration eliminated the slight density variations previously experienced in the Si_3N_4 contoured hubs and was needed to consistently insure complete densification of the curvic region in the hub. Figure 3.15 shows a typical bond interface which is at the turbine blade radial centerline axis. Although excellent bonding was produced near the blade centerline axis, bonding at the outer extremities of the rim was only fair to poor. This is a result of insufficient pressure applied to the bond interface at these extremities due to the shape of the contoured graphite piston in this region. In addition, slight convex bowing of the blade rim was observed due to the higher concentration of pressure in this area.

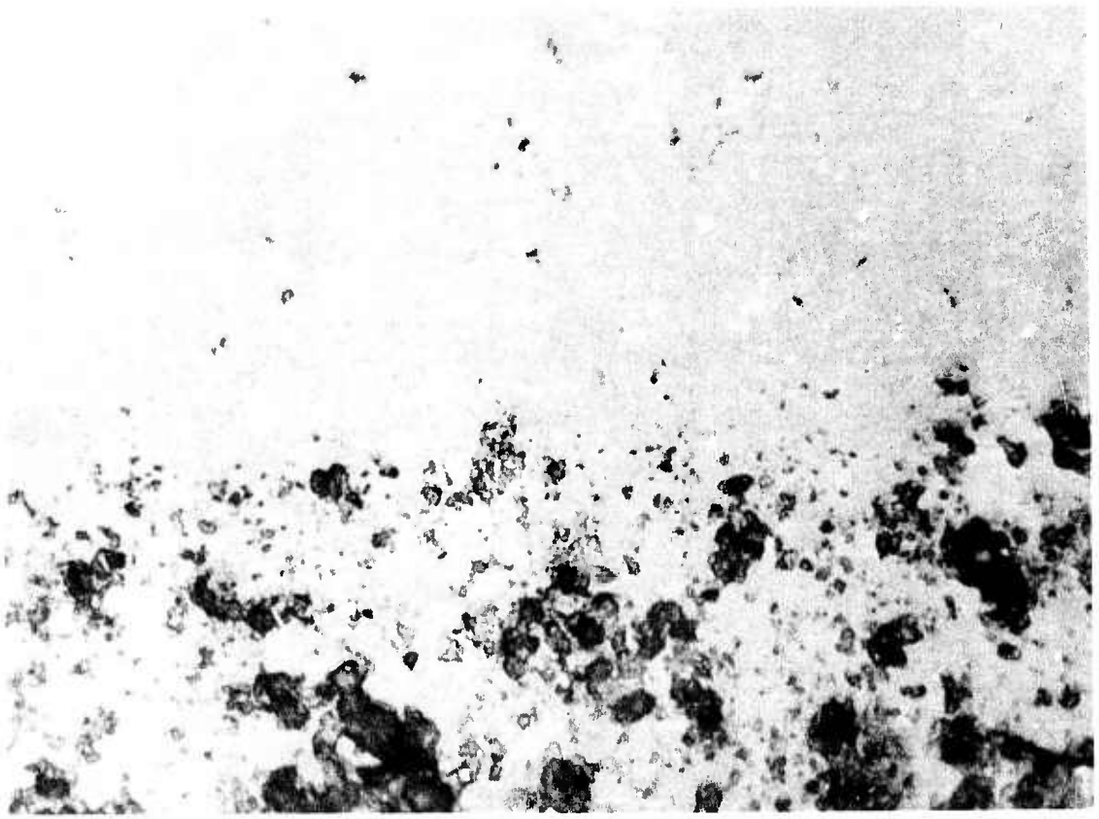

Figure 3.15 Microstructure of Bond Interface Between Hot Pressed Silicon Nitride Rotor Hub and Reaction Sintered Silicon Nitride Blade Ring (500 X)

Small variations in the hot-press bonding rig design have eliminated many of the previously experienced cracking problems. The excessive circumferential cracking problem was essentially eliminated by using the same graphite contoured pistons to hot-press the hub and hot-press bond the hub to the blade ring. This eliminated slight dimensional variations between the hub and pistons that were responsible for the circumferential cracking during bonding.

To improve the bonding over the entire interface, the hot-press bonding rig was altered slightly to enable the simultaneous hot-pressing and hot-press bonding of the Si_3N_4 hub to the blade ring. The hot-press bonding rig for this operation is shown in Figure 3.16. In the previously described hot-press bonding technique, the Si_3N_4 hub was hot-pressed to theoretical density at 4000 to 5000 psi pressure prior to the bonding cycle. However, the reaction sintered blade ring could not withstand this pressure. It was found that complete densification at much lower pressures (2000 to 2500 psi) could be achieved if magnesium nitrate rather than MgO was used as the densification additive. The magnesium nitrate was dissolved in the alcohol used to wet ball-mill the AME Si_3N_4 powder, thus producing a more uniform distribution. The magnesium nitrate was added to produce a concentration equivalent to 2 w/o MgO.

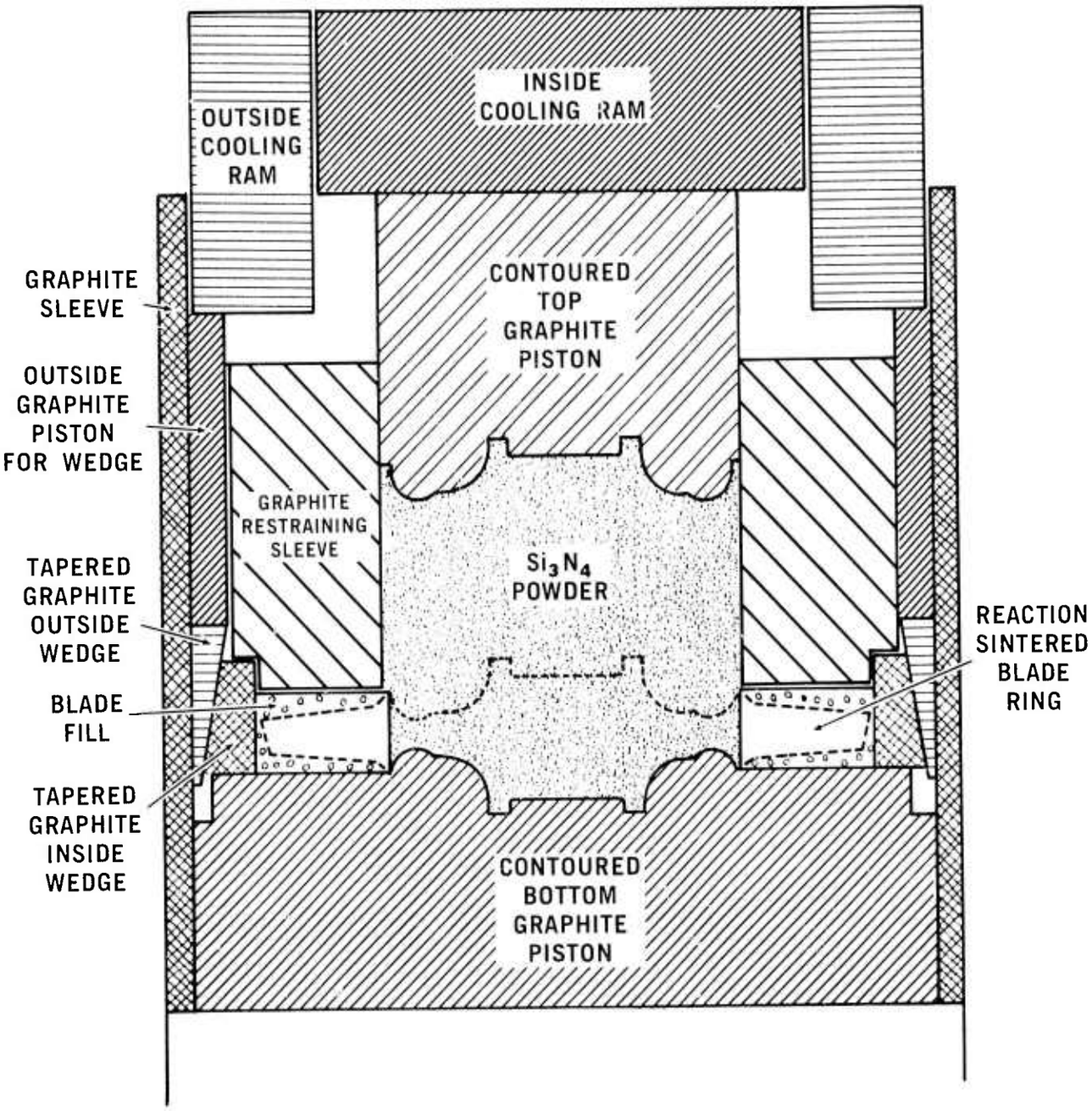

Figure 3.16 Hot Press Bonding Assembly for Simultaneous Forming and Bonding a Silicon Nitride Rotor Hub to a Blade Ring

As previously described, the blade ring assembly was prepared with the blade fill material and machined. The encased blade ring was assembled in the hot-press bonding rig as shown in Figure 3.16. The graphite wedges were again used to restrain and hold the blade ring in place. A pre-determined amount of processed AME Si_3N_4 powder containing magnesium nitrate was loaded into the cavity of the graphite restraining sleeve. A typical procedure involves hot-pressing the Si_3N_4 powder at 1750°C and 2500 psi for 2 hours to theoretical density and simultaneously bonding to the blade ring. Figures 3.17 and 3.18 show a sectioned Si_3N_4 turbine rotor and a typical bond interface, respectively, for a rotor fabricated by this technique. Bonding is considered excellent as evidenced by the microstructure. Bonding over the entire length of the rim was also achieved. In addition, the slight convex bowing of the blade rim previously encountered has not been observed when using this fabrication technique.

The major problem encountered is the inconsistent fracture of the graphite restraining sleeve. Fracture of this sleeve results in fracture of the turbine rotor. Several die assembly designs are being evaluated to enable more consistent press bonding without fracture.

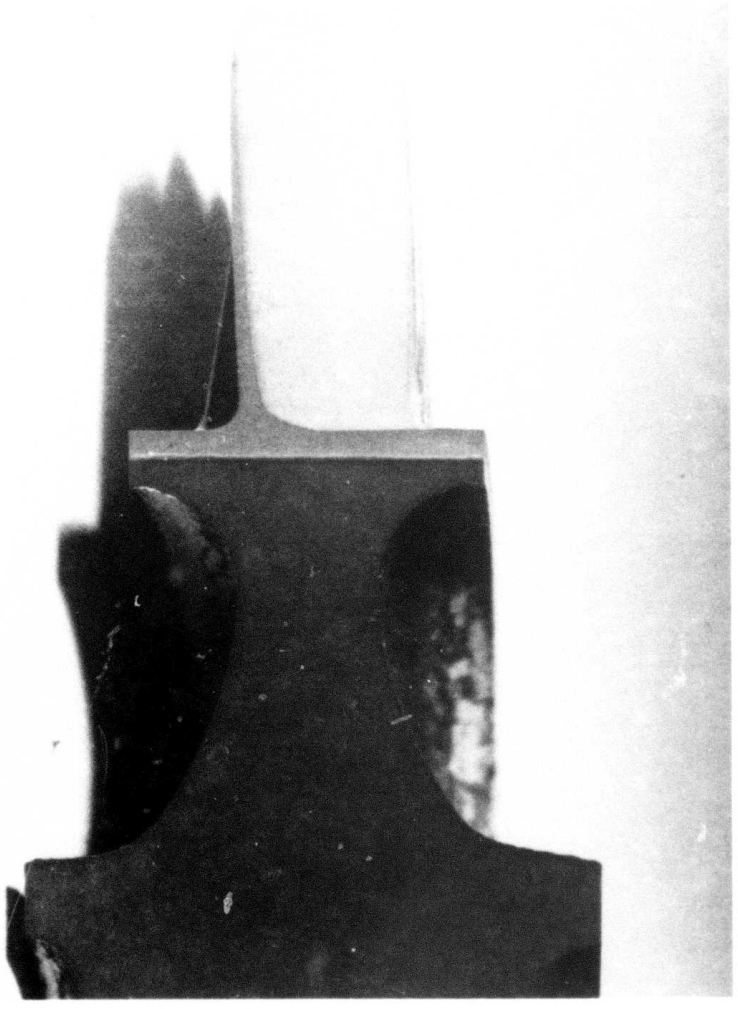

Figure 3.17 Sectioned Silicon Nitride Duo-Density Turbine Rotor

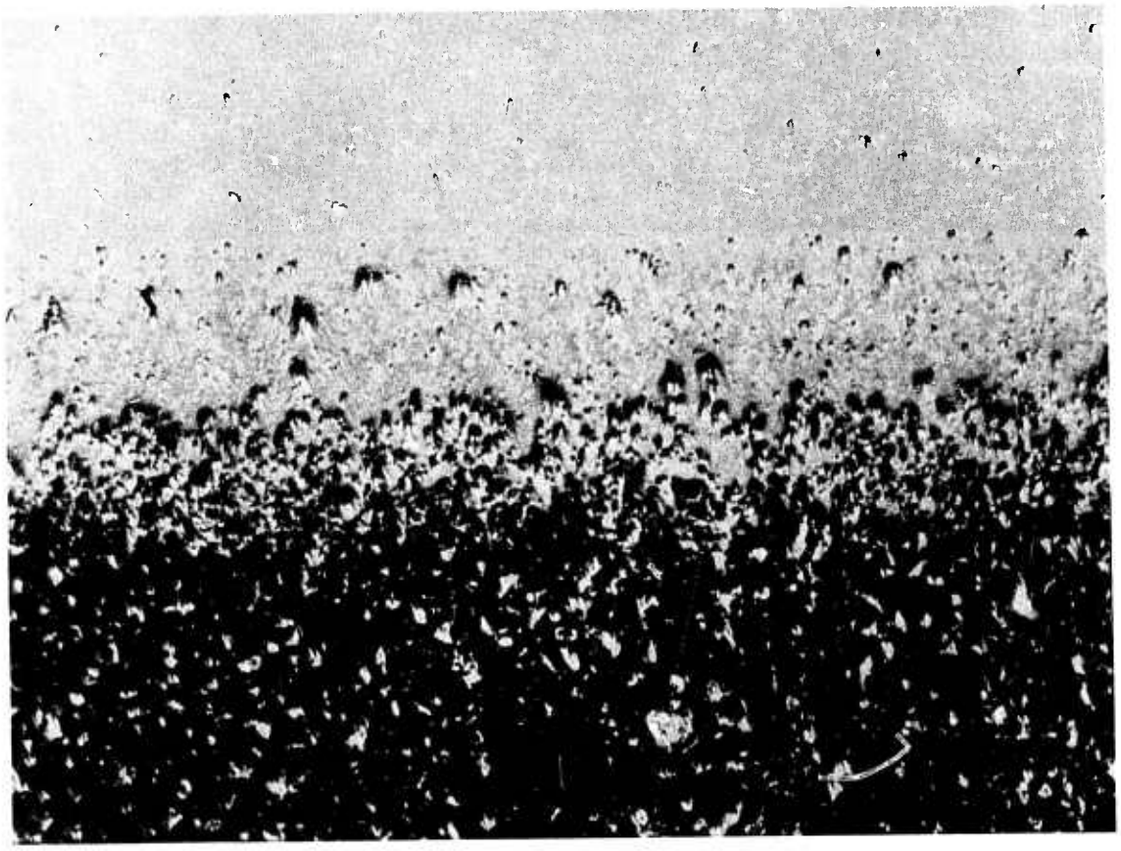

Figure 3.18 Microstructure of Bond Interface (250 X)

Monolithic Turbine Rotors

It has been previously reported [5,6] that a program had been initiated at the Georgia Institute of Technology Experiment Station directed at the development of investment casting techniques for forming precision cast ceramic shapes. Single airfoil blades and rotor segments of three adjacent blades were successfully cast from silicon slip in experimental fused silica shell molds and the shell mold subsequently removed after the shape had been nitrided to Si_3N_4.

The effort has been extended to complete rotor shapes in each of two designs; 1) a second stage rotor complete with contoured hub plus additional stock for the grinding of the curvic coupling and 2) a second stage rotor blade ring having airfoil blades and supporting rim structure but containing no central hub. Recent emphasis has been on the latter configuration, which is intended for use in duo-density Si_3N_4 rotors having a hot-pressed Si_3N_4 contoured hub.

Figure 3.19 is a photograph of a wax turbine rotor blade ring pattern (right) molded as one piece. On the left is a completed shell mold, made from such a wax pattern, photographed after the wax pattern had been removed and the silica mold air-fired to achieve strength adequate for casting and handling and to remove any residual traces of wax. Figure 3.20 shows such a mold after filling with silicon casting slip by a centrifugal casting method whereby all blade cavities are forcibly filled and a common blade ring formed in a shape suitable for the duo-density press bonding method. Such blade rings have been formed using both a casting slip which may be conventionally nitrided to 2.7 gm/cc density Si_3N_4 and a high density casting slip which when nitrided would yield near theoretical density.

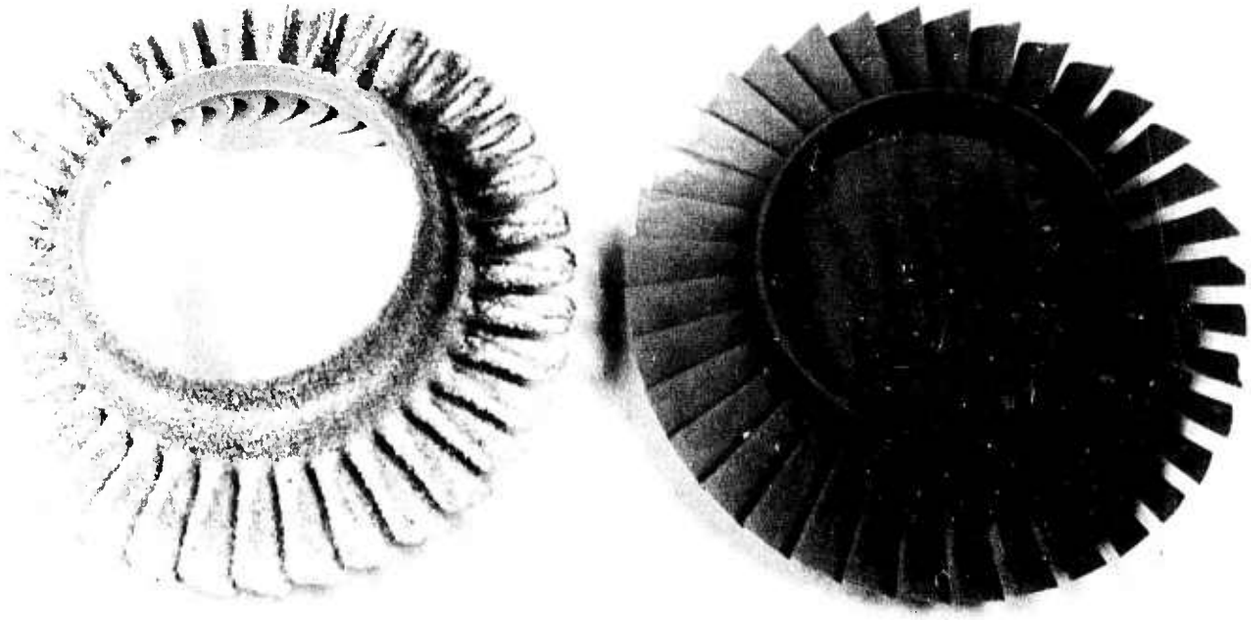

Figure 3.19 Wax Pattern (Right) and Completed Shell Mold (Left) for Slip Casting of Rotors

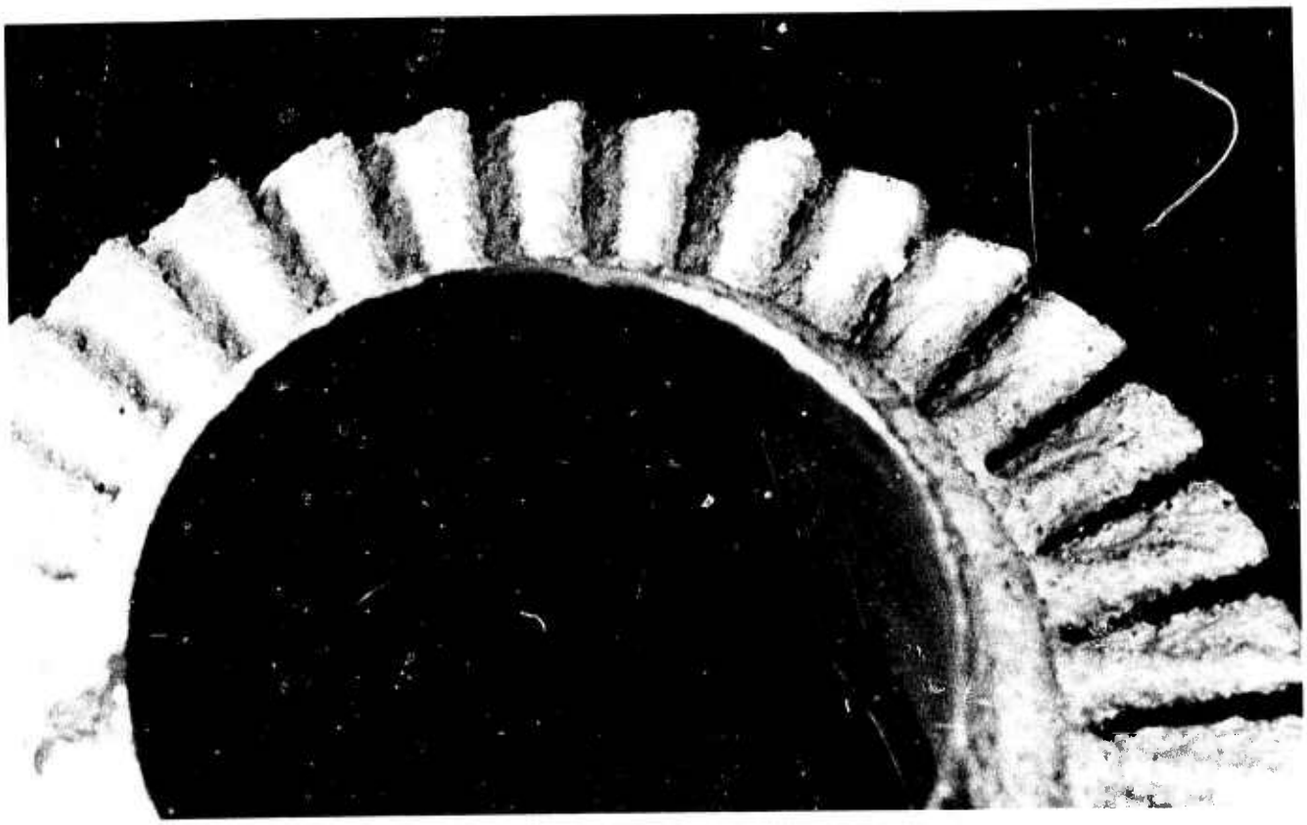

Figure 3.20 Shell Mold as Filled with Slip

Current silica shell molds have exhibited too high a fired strength for complete removal of the mold after nitriding without some blade damage. Experiments directed at weaker molds after nitriding are in progress.

High Pressure Nitriding of Reaction Sintered Silicon Nitride

Since near theoretical density is required to meet the high stress conditions in the hub region of silicon nitride turbine rotors, work has been directed toward the duo-density turbine rotor concept incorporating a hot pressed hub bonded to a molded blade ring. However, if high density reaction sintered Si_3N_4 could be made with sufficient strength to satisfy all the stress conditions of the turbine rotor, the fabrication of monolithic Si_3N_4 turbine rotors would be simpler than a duo density rotor and the blades would be stronger.

To increase the density of reaction-sintered Si_3N_4 components, the green density of the silicon compacts must correspondingly increase. Silicon metal compacts have been slip-cast to a density of 1.91 gm/cm^3, equivalent to 3.18 gm/cm^3 density when fully converted to Si_3N_4. Experience has shown that complete nitriding cannot be accomplished for a silicon compact having a green density greater than 1.6 gm/cm^3 (equivalent to 2.7 gm/cm^3 Si_3N_4) under conventional ambient pressure nitriding conditions.

Preliminary work has shown that high density slip-cast silicon test bars nitrided under standard conditions at one atmosphere of nitrogen resulted in a high density Si_3N_4 surface layer approximately 0.030 inches thick with little nitriding at the interior. The surface layer of such a nitrided test bar is shown in Figure 3.21. It appeared that the high density Si_3N_4 surface layer sealed off the interior and thus prevented penetration of nitrogen gas to the interior.

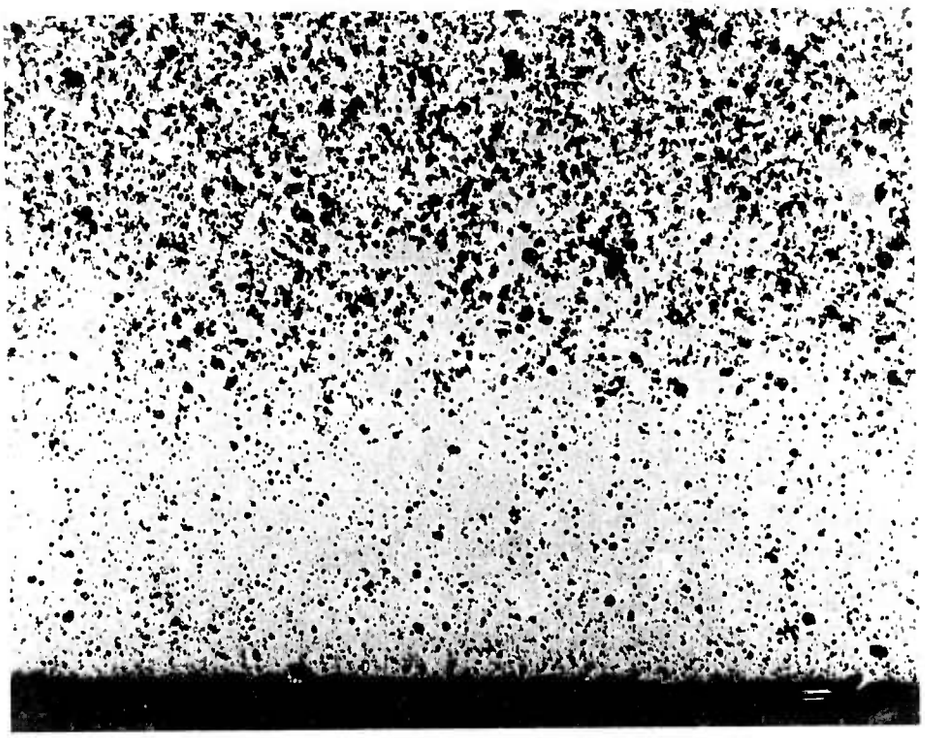

Figure 3.21 Section of Silicon Nitride Test Sample Showing High Density Surface Layer (100 X)

The gas permeability in porous structures is a function of pore size, pore volume, and gas pressure gradient. The pore size and pore volume of slip cast silicon compacts are governed by the starting material size distribution and powder packing efficiency to obtain the desired final Si_3N_4 density and thus are relatively fixed. A technique which would increase the accessability of the nitrogen gas to the inner structure in both the initial and final sintering stages would provide a means of achieving a fully reacted, high density material. Therefore, a program has been undertaken with Battelle Memorial Institute to investigate the potential of using a high pressure nitrogen atmosphere to enhance the nitriding of high density silicon compacts.

The high temperature, high pressure autoclave facility at Battelle has the capability of exerting gas pressures up to 50,000 psi on specimens of various shapes and sizes. The program plan was to determine the effect of nitrogen pressures on the degree of nitriding and the resultant final density. Pressures of 10,000 to 30,000 psi were to be utilized in conjunction with the current Ford atmospheric reaction-sintering time-temperature cycle. This cycle consisted of 24 hours each at temperatures of 2000°F, 2300°F, and 2660°F. Samples were prepared from silicon powder at various density levels from 74 to 82 percent of theoretical (74% dense silicon, if fully nitrided would be converted to Si_3N_4 at 90% of theoretical, 82% dense silicon would be equivalent to 100% dense Si_3N_4). Several specimens contained CaF and Fe_2O_3 as nitriding aids. The samples were nitrided in unsealed molybdenum cans and the nitrogen gas was cleaned by passing through a "getter" prior to specimen contact to remove traces of oxygen.

The first autoclave cycle was run at 20,000 psi nitrogen pressure. The specimens from the first run were severely reacted and distorted. Metallographic examination of these specimens revealed incomplete nitriding with large amounts of porosity apparently resulting from the exudation of molten silicon from the structure. At sometime during the cycle, the exothermic reaction became prematurely uncontrollable, causing temperatures to exceed the melting point of the silicon metal before a supporting nitride structure had formed within the specimen. At 20,000 psi nitrogen pressure, the runaway exothermic reaction appeared to have begun at about 1200°C (2192°F), which is a lower temperature than normally observed during nitriding at atmospheric pressure.

Several of these specimens did retain their shape and did develop internal patches of high density silicon nitride. However, the thermal runaway caused acceleration of the reaction kinetics and loss of control of the reaction. If high pressure nitriding is to be developed into a viable process, the optimum time-temperature nitriding cycle at a selected pressure(s) must be determined. The major consideration at any pressure will be to maximize reaction rate and final density without initiating a thermal runaway due to the exothermic nitriding reaction.

It is postulated that an entirely new set of kinetic relationships are in effect under high-pressure nitriding conditions. To optimize the high-pressure nitriding technique, it was concluded that increased pre-nitriding at both lower temperatures and pressures may permit better control over the exothermic reaction. In addition, by reducing the pressure to 10,000 psi, considerable cost advantage would be realized both in terms of operating costs and future capital equipment expenditures. Therefore, the program was redirected toward increasing the degree of nitriding at both lower temperatures and pressures.

Slip cast silicon cylinders were prepared at density levels equivalent to 90, 95, and 100 percent Si_3N_4. In addition, silicon samples were prepared containing 1 and 3 w/o iron oxide at 93 and 98 percent equivalent Si_3N_4 density levels, respectively. The program plan was to evaluate the degree of nitriding under 10,000 psi nitrogen pressure in the 900°C (1652°F) to 1350°C (2462°F) temperature range for times ranging from 5 to 15 hours. Figure 3.22 illustrates typical reaction curves for 95% equivalent Si_3N_4 density level silicon specimens for several autoclave cycles. Complete nitriding corresponds to a 67 percent weight gain. The results showed less than 2% nitriding at temperatures up to 1150°C (2102°F). Increasing the temperature to 1175°C (2327°F), not illustrated in Figure 3.22, caused the exothermic reaction to occur, resulting in exuded silicon metal. In an attempt to increase the reaction temperature to 1200°C and avoid the exotherm, the heating rate was decreased by a factor of 3-1/2 (from 2 to 7 hours to temperature). At 1200°C (2192°F), approximately 16% nitriding was obtained in the pure silicon metal specimen in 15 hours, while the iron oxide-containing specimens achieved about 18% nitriding in the same period. Nitriding times in excess of 10 hours did not produce significant improvements as indicated by the relatively level reaction curves. Thus, nitriding temperatures in excess of 1200°C are required to completely convert the silicon to Si_3N_4 under 10,000 psi pressure; however, as nitriding temperatures increase, it becomes more difficult to control the exothermic reaction and exudation of silicon metal.

Several samples that were high pressure nitrided at 1200°C for 15 hours to about 16-18 percent were rerun at 10,000 psi nitrogen pressure in the autoclave at 1350°C (2462°F) for 5 and 15 hours. The results of these autoclave cycles are summarized in Figure 3.22 and are indicated by the square data points. Nitriding of approximately 40 percent was obtained for silicon specimens containing 3% iron oxide, which would be 95% dense if completely nitrided. The higher nitriding temperature of 1350°C produced a significant increase in the degree of nitriding, and iron oxide additions appear to be more effective at higher temperatures. No exudation of silicon metal was observed. This nitriding temperature is 100°C lower than the 1460°C (2660°F) nitriding temperature used in the standard atmospheric nitriding cycle. Again, longer times at temperature and pressure had little, if any, effect on nitriding.

Although the results to date are incomplete, they are encouraging. Further effort will be concentrated on evaluating the effect of nitriding temperatures in excess of 1350°C. From the work to date several conclusions appear evident, which are:

1) High pressures do not lower the reaction temperature but appear to increase the reaction kinetics at a particular temperature.

2) Temperatures in excess of 1350°C (2462°F) are required to completely nitride 95 percent equivalent dense Si_3N_4 silicon compacts.

3) Temperatures of about 1200°C (2192°F) will initiate an uncontrollable exothermic reaction under 10,000 psi nitrogen pressure unless significant nitridation (15-20 percent) is achieved beforehand.

4) Green density level does not excessively effect the nitriding rate at high pressures, as there was little difference noted in the 90, 95, and 100 percent equivalent Si_3N_4 density level silicon specimens.

5) Iron oxide appears to increase the nitriding rate and the amount of nitriding obtained, especially at the higher temperatures.

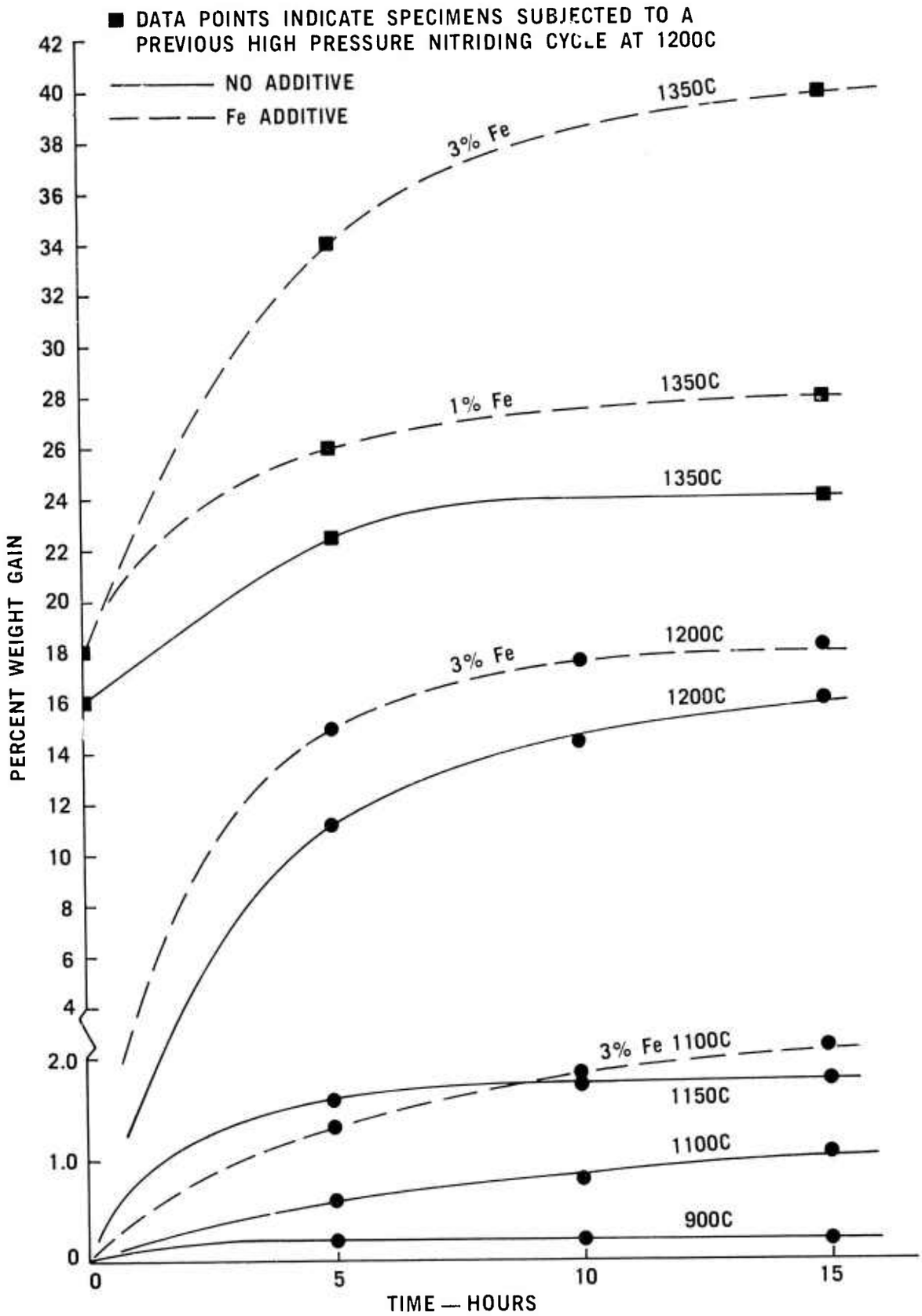

Figure 3.22 Nitriding Rates at Various Temperatures of 95% Equivalent Silicon Nitride Density Slip Cast Samples at 10,000 psi Nitrogen Pressure

3.1.3 TESTING

Spin testing of ceramic turbine rotor components has continued during this reporting period. A test group of seven hot-pressed Si_3N_4 rotor hubs, made under the same conditions, were spun to failure for strength evaluation. While analysis of the results is incomplete, relatively low scatter is indicated.

Shakedown testing of the turbine rotor test rig was completed using metal rotors. The initial testing of ceramic turbine rotors ended in failure, believed caused by inadequate clearance between the rotors and the stators.

Further testing of the rotor bolt attachment tool was conducted, and design improvements are discussed.

Testing of Hot-Pressed Si_3N_4 Rotor Hubs

Ten hot-pressed Si_3N_4 rotor hubs, similar to those used in fabricating duo-density rotors, were processed for strength evaluation testing. A single batch of 5% MgO - AME Si_3N_4 powder mixture was used to hot press the hubs. Care was taken to fabricate these parts under as nearly identical conditions as possible.

Seven of the ten test hubs were selected for destructive spin pit testing. Two others were set aside to be used as rotor spacers in the turbine wheel test rig, and the third was sectioned for the determination of modulus of rupture (MOR) data for statistical analysis. Correlation of the MOR data and rotor hub burst data is currently in progress.

The seven rotor hubs for spin testing were radiographically and dimensionally inspected prior to testing. No subsurface flaws were detected by x-ray. Small dimensional variations were noted with typical hub contours varying by 0.010 inches. A minimal amount of grinding was required prior to testing. The platform width was ground to 0.700 inches and the curvic coupling faces were ground to 1.230 inches. The center bore (0.50 inch) was held to ± 0.0005 inches. A diamond plated formed grinding tool was used to round off each end of the center bore. All other surfaces were as pressed. The resulting hub was similar to, although larger in diameter than those used in press bonding in order to minimize finish machining.

The test procedures adapted for this test have been described in detail [2]. All hubs were tested to destruction, and photographs at burst speed were obtained in most cases. A typical hub burst is shown in Figure 3.23. A cross-section of one hub after burst is shown in Figure 3.24. Cracks radiate from a central location near the center bore. This is typical of several of the larger pieces recovered from the spin pit; it is impossible to tell from the photographs at burst if the larger sections are associated with the origination of the burst. A series of photomicrographs up to 1000X (Figure 3.25) did not reveal anything unusual in this region. Burst speeds ranged from 102,880 to 120,710 rpm. The Weibull slope for hub burst speed was 17.66 with a characteristic speed of 115,965 rpm. Characteristic speed is the Weibull scale parameter of the distribution and is always equal to the speed at 63.2% failure on the Weibull curve. This indicates a high degree of consistency in this particular batch of rotor hubs. This Weibull modulus should not be confused with the material strength modulus reported elsewhere.

Figure 3.23 Hot Pressed Silicon Nitride Rotor Hub at Burst (102,800 rpm)

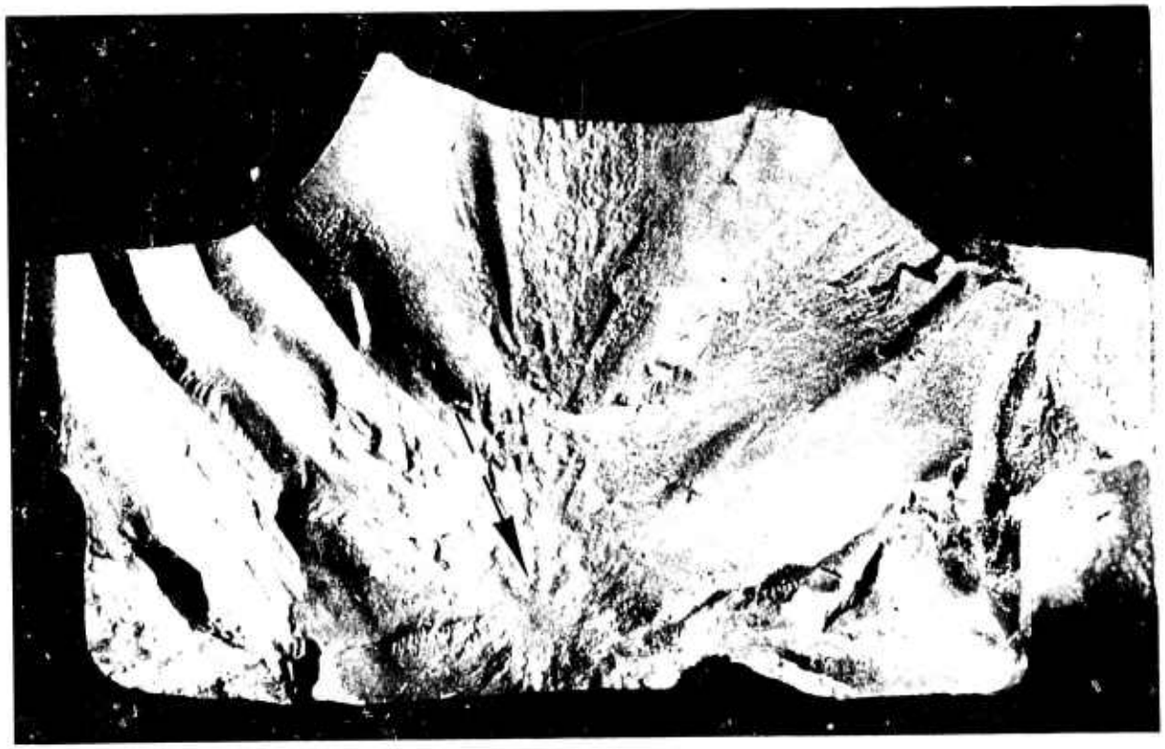

Figure 3.24 Large Section of Rotor Hub Recovered from Spin Pit After Burst Test, Indicating Suspected Area of Fracture Origin

Figure 3.25 Suspected Area of Fracture Origin of Rotor Hub (1000 X)

A finite element stress analysis was performed for a typical hub at burst speed. The resulting maximum principal tensile stress contours are shown in Figure 3.26. Stress concentrations are seen at the center bore and neck regions of the hub. The maximum tensile stress is indicated at the bore. However, the relatively small volume of material under high stress may make the center bore less critically stressed than the neck. Completion of the MOR correlation study and the hub Weibull analysis should resolve this question. These calculated strengths are comparable to previously reported average tensile strengths, and are encouraging in excess of calculated bore stresses in the complete duo density rotor [4].

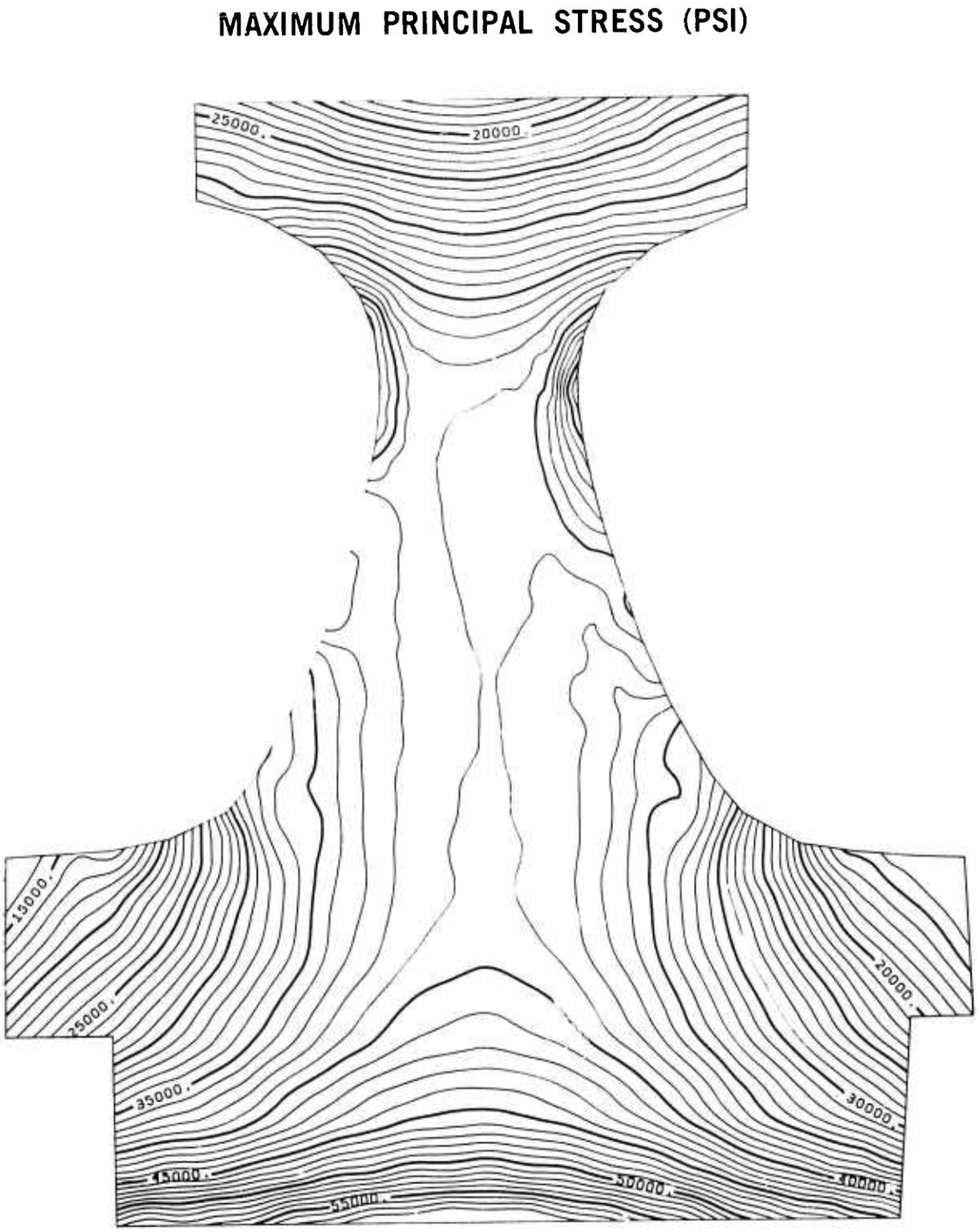

Figure 3.26 Maximum Principal Stress Contours (psi) of Rotor Hub at Burst Speed of 116,000 rpm

Testing in the Turbine Rotor Test Rig

Shakedown of the turbine rotor test rig (TRTR), shown in Figure 3.27, was completed with metal turbine rotors at a turbine inlet temperature of 1930°F, and a speed of 32,000 rpm or 50% of design speed.

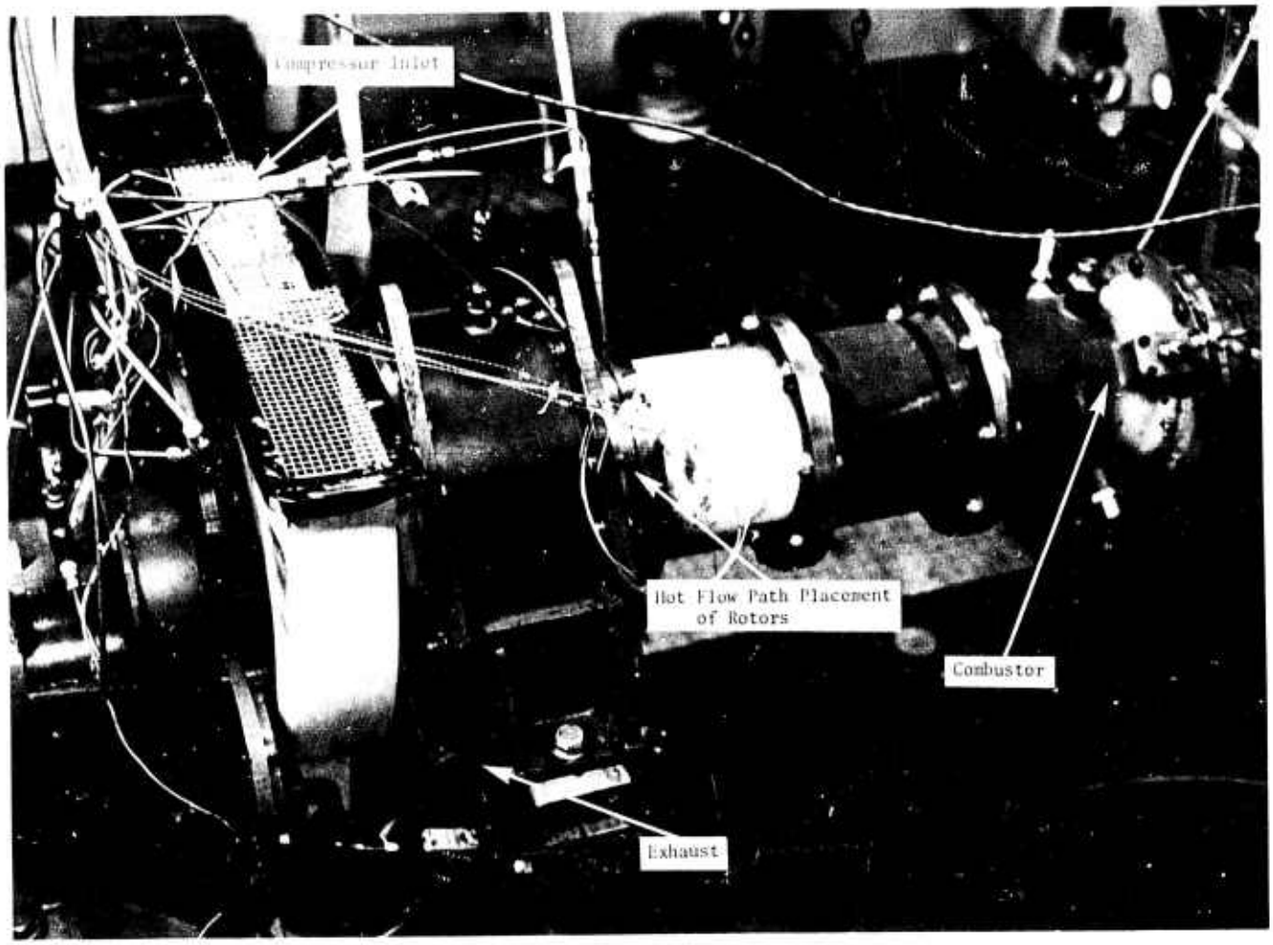

Figure 3.27 The Turbine Rotor Test Rig

Following this checkout, the rig was rebuilt with two hot pressed Si_3N_4 rotor hubs without blades (spacers) utilizing the previously described [2] folded bolt attachment hardware. This initial shakedown of the ceramic attachment design performed flawlessly through three thirty minute cycles from room temperature to 1850°F inlet temperature (0-15% design speed). Higher temperatures were not possible in this configuration due to backflow of hot exhaust gases through the compressor, as a result of running without turbine blades. Post-testing examination of the test hardware indicated the curvic coupling had allowed the required radial motions between metal and ceramic components. The rotor bolt had not taken a permanent set indicating design cooling air flows were adequate.

Prior to the next build, a set of ceramic turbine rotors were qualified to 20,000 rpm in the vacuum spin pit. Radiographic and visual inspection indicated this set of rotors were not of high quality and would therefore be tested at low temperature and speed. Figure 3.28 shows the two ceramic rotors mounted to the turbine shaft prior to buildup. The rig was rebuilt using the qualified ceramic rotors, a set of metal stators, and all other test hardware previously used in the initial ceramic shakedown test. Axial clearances between stators and rotors were held to 0.015 inches to minimize hot gas leakage between the two rotor stages.

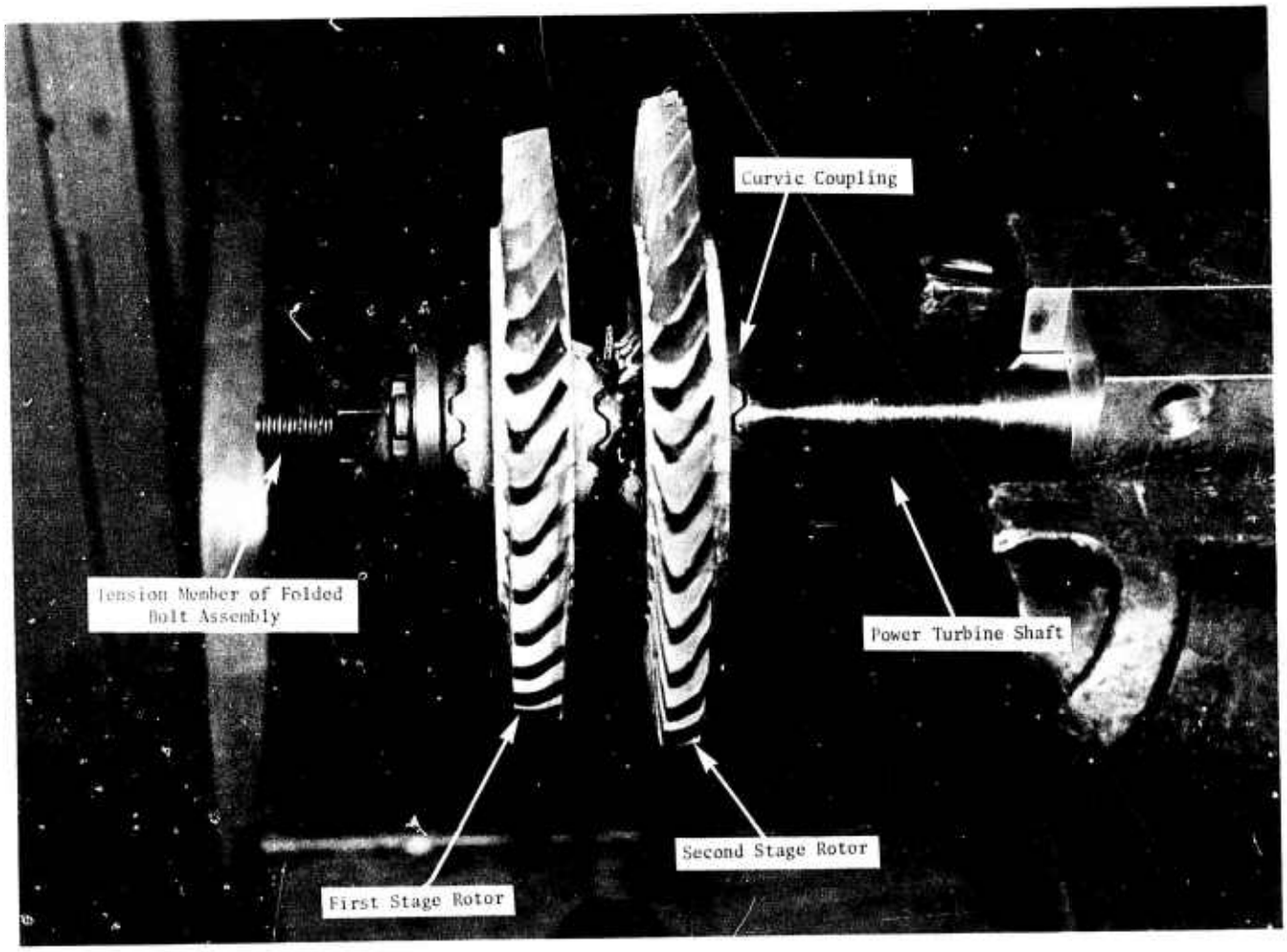

Figure 3.28 First Set of Ceramic Rotors Mounted on Power Turbine Shaft

After startup, a speed of 12,848 rpm and a turbine inlet temperature of 1950°F was reached and held for five minutes when failure occurred. The ceramic rotors failed, with severe damage to other components of the rig. This failure has been attributed to insufficient cold clearances between the rotors and the stators, causing an axial rub after thermal equilibrium was reached. This test was considered significant for the following reasons:

(1) The combustor light-off with a set of ceramic rotors was accomplished without incident.

(2) The test objective, the attainment of 1950°F and 20% engine speed, was accomplished.

The TRTR is being rebuilt in preparation for testing higher strength turbine rotors in 1975.

Ceramic Rotor Attachment

Tests were conducted to evaluate the effectiveness of the installation tool used to preload the folded bolt during assembly of the turbine. The tool is designed to stretch the bolt to the required preload while introducing essentially zero torsional stress, and utilizes a conventional method for producing controlled clamping load in a bolt where torsional stress of any magnitude would be undesirable. Operation of the tool was described in a previous report [5].

The tool was initially designed using the principle that rotation would only occur at the lubricated needle bearings and that relative motion between the threaded puller and the tension member of the bolt would not occur. Initial evaluation indicated that a lower than expected coefficient of friction of the threaded end of the tension member did in fact permit rotation to occur. The puller body was redesigned to include a retractable spring-loaded pin lock engaging a slot across the end of the tension member. Parts were modified and additional testing confirmed that this was a workable solution which would permit evaluation of the tool at the design (3900 pound) clamping load level.

Load was applied through the tool to produce the required preload in the bolt, as indicated by a calibrated strain gaged load ring. Holding this load, the engine nut on the tension member was tightened using the tool until the load ring output indicated that the nut had accepted a small portion of the load. At this point the tool was removed and the strain (and preload) induced in the folded bolt was expected to remain. The efficiency of this load transfer from fixture to rotor nut was checked by accurately measuring the extension of the tension member caused by the induced load. Length measurements taken under controlled conditions before and after stretch indicated that this efficiency of transfer was approximately eighty percent but was repeatable.

Further testing is planned to determine whether this loss of load is due to thread deformation when the full load is applied to the rotor nut or whether radial looseness in the nut thread is a contributing factor. If the exact cause cannot be determined, the load applied by the tool can be artificially increased to produce the desired load in the bolt so long as the efficiency of transfer remains repeatable.

3.2 CERAMIC STATORS, ROTOR SHROUDS, NOSE CONES, AND COMBUSTORS

SUMMARY

Work continued on the three-dimensional heat transfer and thermal stress analyses of first and second stage stators. Heat transfer film coefficients were computed for second stage stators at 55% and 100% speed conditions. Additional heat transfer film coefficients were determined for the first stage stator at the 100% speed condition.

First stage stators of higher density (2.55 gm/cm^3) silicon nitride were injection molded with outer shrouds free of detectable defects, using changes in gating configurations to improve quality. Several stators were transfer molded from silicon carbide using the one-piece first stage stator tooling. Fabrication of slip cast Si_3N_4 rotor shrouds continued with no additional development work. Thermal shock rig testing of low density (2.2 gm/cm^3) one-piece first stage stator vanes resulted in failures in 800 to 1000 cycles at a maximum cycle temperature of 2300°F. Higher density (2.55 gm/cm^3) vanes were crack free after 3000 cycles at the same peak temperature.

A ceramic combustor made from "Refel" reaction sintered silicon carbide was tested for 171 hours over a cyclic test sequence. This combustor survived the test, which included 20 hours at a combustor outlet temperature of 2500°F.

Successful completion of the 100 hour engine durability test for hot flow path ceramic components was accomplished during this reporting period. The ceramic components consisted of a nose cone, a one piece first stage stator, first and second stage turbine rotor shrouds, and a spacer to replace the second stage stator. The test consisted of 17 cold starts, 14 hot starts, and 100 one-hour cycles during which the speed was automatically varied to follow the test cycle with a flat steady-state temperature schedule of 1930°F. All components survived 100 hours without structural failure. The nose cone and both shrouds remained crack free after over 200 such hours of cyclic durability. The first stage stator had no vane cracks, although two outer shroud cracks occurred at 103 hours.

As an overall assessment, the development of ceramic stators, rotor shrouds and nose cones has achieved a major milestone - one hundred hours of demonstrated engine durability. Cracking of the first stage stator outer shroud beyond 100 hours occurred at locations containing known defects; processing and material improvements should increase the life of this component. In addition, the nose cone and rotor shrouds of present configuration have achieved 200 hours durability at 1930°F. To enhance future fabrication and durability development, at some expense to aerodynamic efficiency, a Design D flow path configuration will be adopted, comprising common stators and common rotors in both first and second stage locations. In addition, study of an updated flow path configuration, optimized for aerodynamic efficiency, ceramic manufacturing, and durability, will be carried out, culminating in a design layout.

PRECEDING PAGE BLANK-NOT FILMED

3.2.1 DESIGN AND ANALYSIS

Introduction

In generating input for three dimensional stress and heat transfer analyses of stators, convective heat transfer coefficients for both first and second stage stator vanes were determined along with the adiabatic wall temperatures for the respective vane sections. The coefficients are given for various airfoil sections at 55 and 100 percent speeds and temperatures.

Stator Stress and Heat Transfer Analysis

The methodology for three-dimensional heat transfer and thermal stress analysis was elucidated in the last report [6] and was discussed briefly in Section 3.1.1 of this report.

Stator analytical progress to date includes a complete set of heat transfer film coefficients computed by programs TSONIC and BLAYER. These data include convective film coefficient distributions on airfoil cross-sections at radii of 1.7, 1.95, and 2.2 inches for the first stage stator and at radii of 1.7, 2.05 and 2.4 inches for the second stage stator. These locations are indicated on vane profiles inset into Figures 3.29 and 3.35 respectively. Coefficients for both stators were computed at 55 percent and 100 percent speeds in order to cover the range of engine running conditions. Estimates of convective film coefficients on the inner and outer shrouds between blades were also computed. By cross-plots or extrapolation of these combined data, the full three dimensional wetted-surface can be mapped to simulate all the critical engine running environments. These coefficients are used in a manner similar to that used for rotors, as discussed in Section 3.1.1 of this report.

Figures 3.29 through 3.34 present film coefficients as a function of dimensionless surface distance S/S_{max} at speeds of 55 and 100 percent for both suction and pressure surfaces of the first stage stator vane. Pressure surfaces exhibited entirely laminar flow during these conditions. From the stagnation point ($S/S_{max} = 0$) to the dotted curve, the suction surface also exhibited laminar flow. Transition from laminar to turbulent flow is shown by the dotted curve. From the end of the transition regime to S_{max}, turbulent flow was predicted on the suction surface boundary layer.

Figures 3.35 through 3.40 show heat transfer film coefficients computed on the pressure and suction surfaces of the second stage stator vanes for 55 percent and 100 percent speed conditions. Suction and pressure surfaces, in all cases, exhibited both laminar and turbulent flow regimes. Transition (indicated by the broken curves) on suction and pressure surfaces generally occurred between an S/S_{max} of 0.25 to 0.50. Physical phenomenon and transition criteria are discussed in Section 3.1.1 of this report and in the last report [6]

Figures 3.41 through 3.46 show the adiabatic wall temperatures computed by BLAYER for first and second stage stator vane surfaces. These data are used per the recommendations of Section 3.1.1 of this report and the last report [6].

Table 3.2 presents average film coefficients for first and second stage stator inner and outer shrouds. These data were also computed by empirical methods discussed in the last report [6] and are used according to recommendations presented therein.

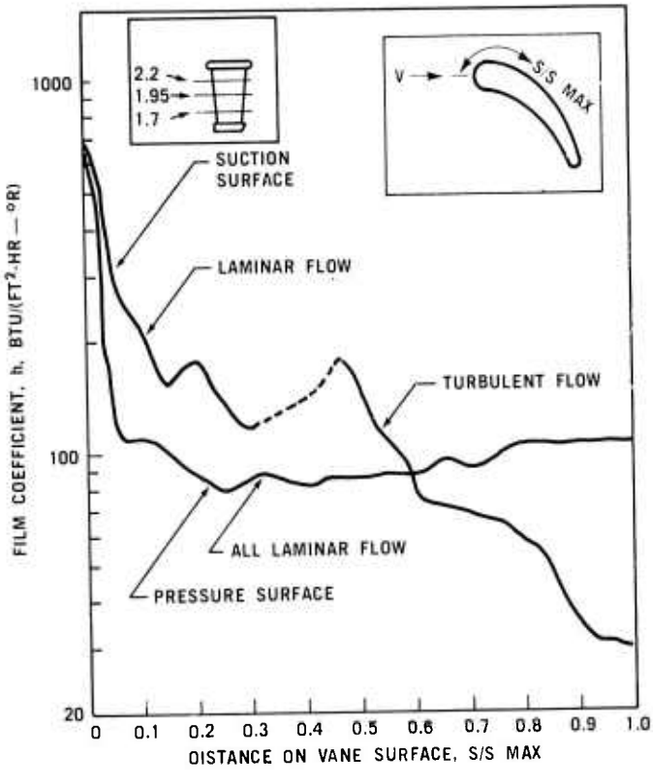

Figure 3.29 Heat Transfer Film Coefficients, First Stage Stator Vane, at 55% Speed, 2390°R Inlet Temperature, and Radius of 1.7 Inches

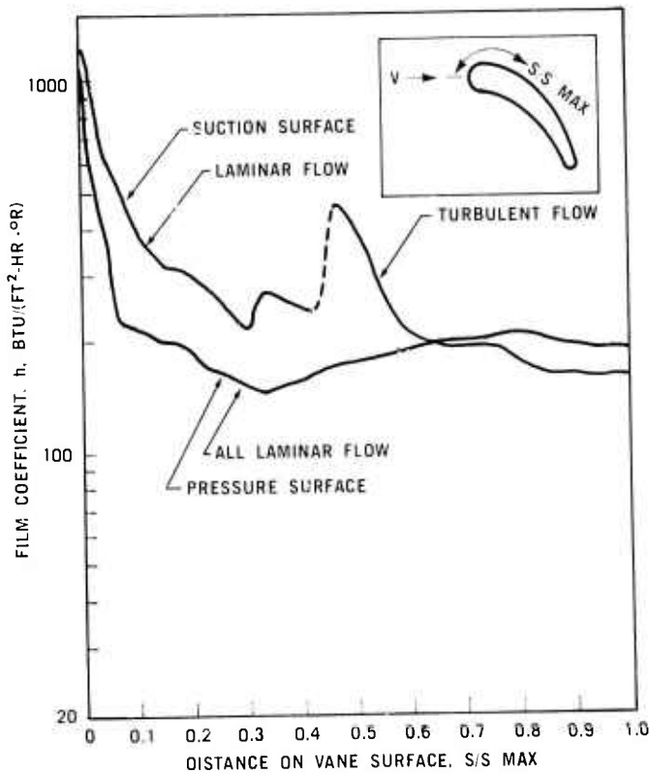

Figure 3.30 Heat Transfer Film Coefficients, First Stage Stator Vane, at 100% Speed, 2960°R Inlet Temperature, and Radius of 1.7 Inches

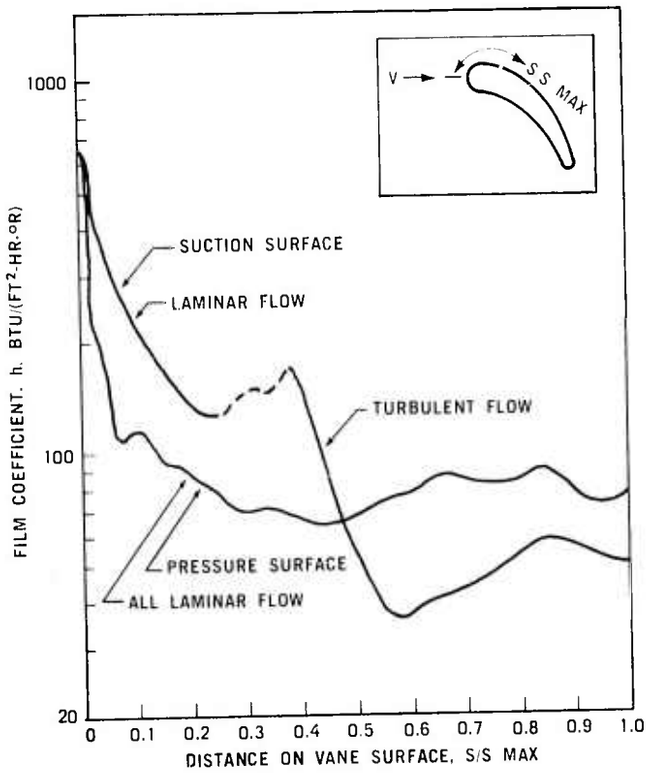

Figure 3.31 Heat Transfer Film Coefficients, First Stage Stator Vane, at 55% Speed, 2390°R Inlet Temperature, and Radius of 1.95 Inches

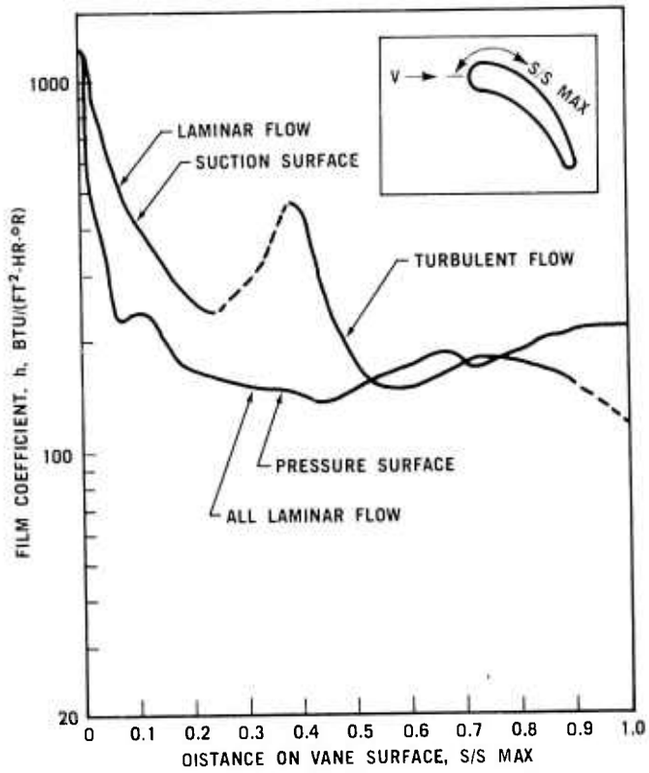

Figure 3.32 Heat Transfer Film Coefficients, First Stage Stator Vane, at 100% Speed, 2960°R Inlet Temperature, and Radius of 1.95 Inches

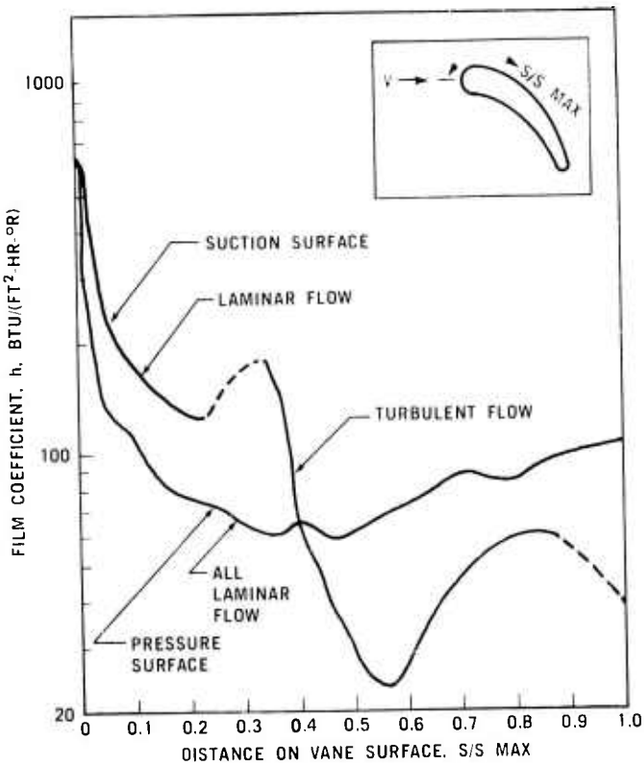

Figure 3.33 Heat Transfer Film Coefficients, First Stage Stator Vane, at 55% Speed, 2390°R Inlet Temperature, and Radius of 2.2 Inches

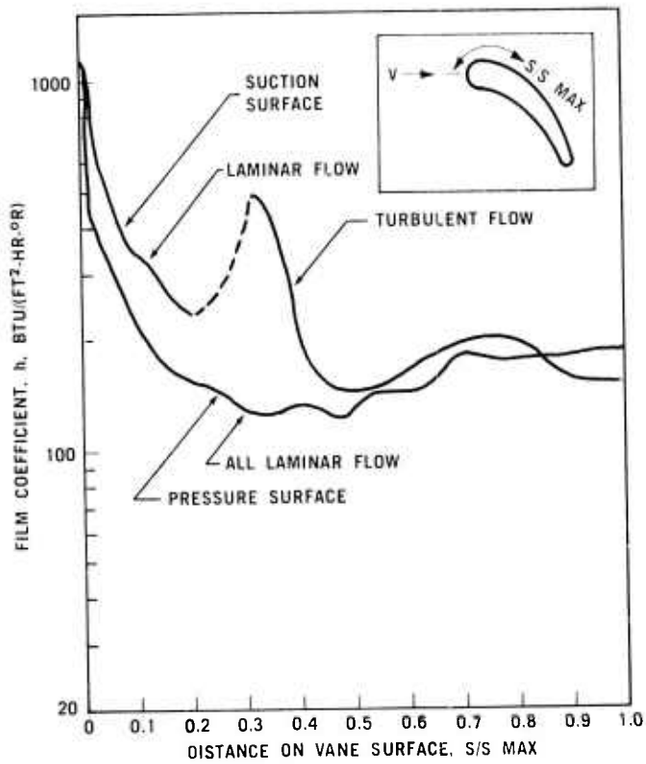

Figure 3.34 Heat Transfer Film Coefficients, First Stage Stator Vane, at 100% Speed, 2960°R Inlet Temperature, and Radius of 2.2 Inches

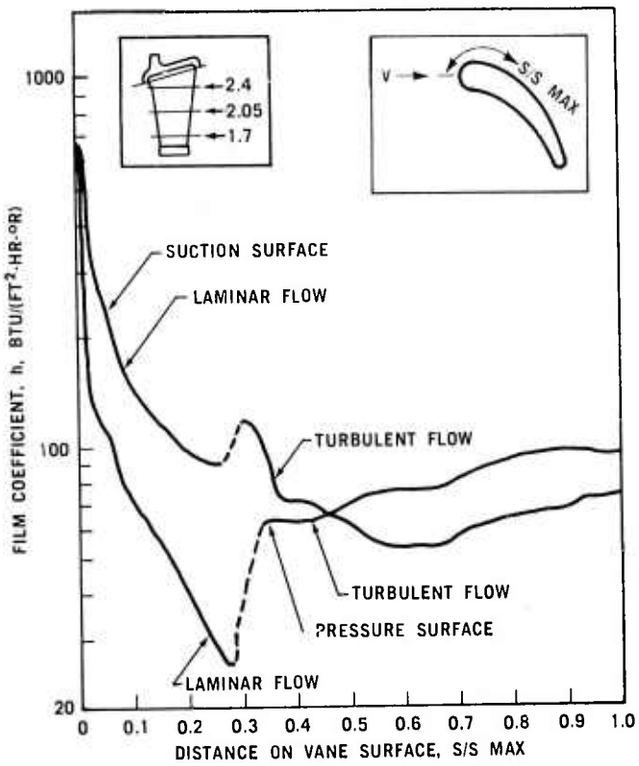

Figure 3.35 Heat Transfer Film Coefficients, Second Stage Stator Vane, at 55% Speed, 2390°R Inlet Temperature, and Radius of 1.7 Inches

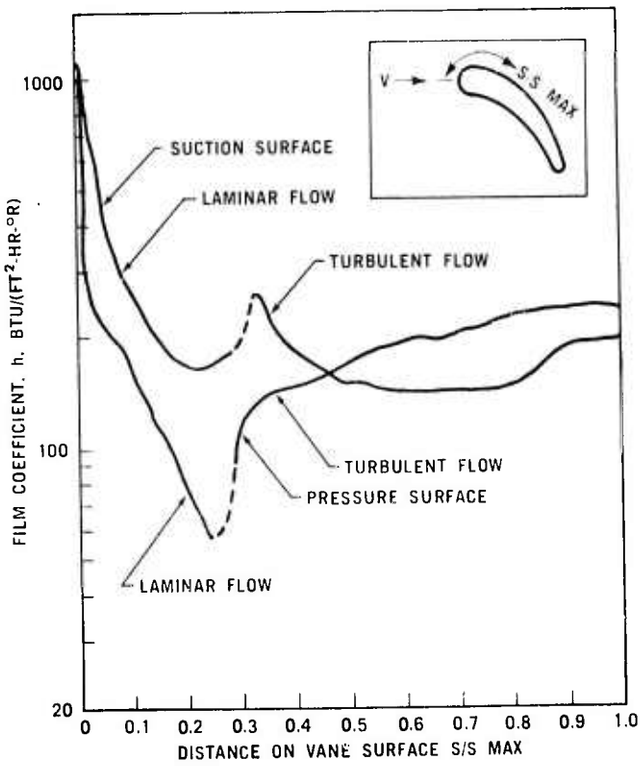

Figure 3.36 Heat Transfer Film Coefficients, Second Stage Stator Vane, at 100% Speed, 2960°R Inlet Temperature, and Radius of 1.7 Inches

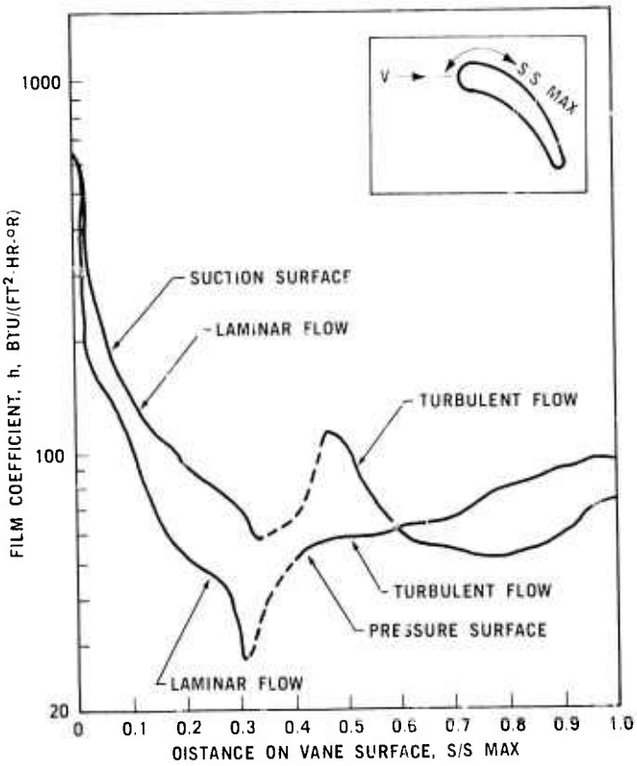

Figure 3.37 Heat Transfer Film Coefficients, Second Stage Stator Vane, at 55% Speed, 2390°R Inlet Temperature, and Radius of 2.05 Inches

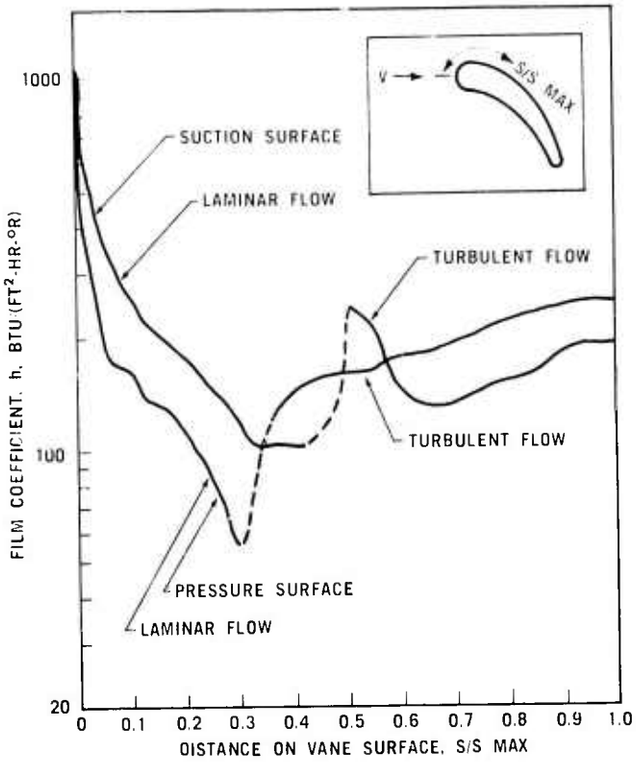

Figure 3.38 Heat Transfer Film Coefficients, Second Stage Stator Vane, at 100% Speed, 2960°R Inlet Temperature, and Radius of 2.05 Inches

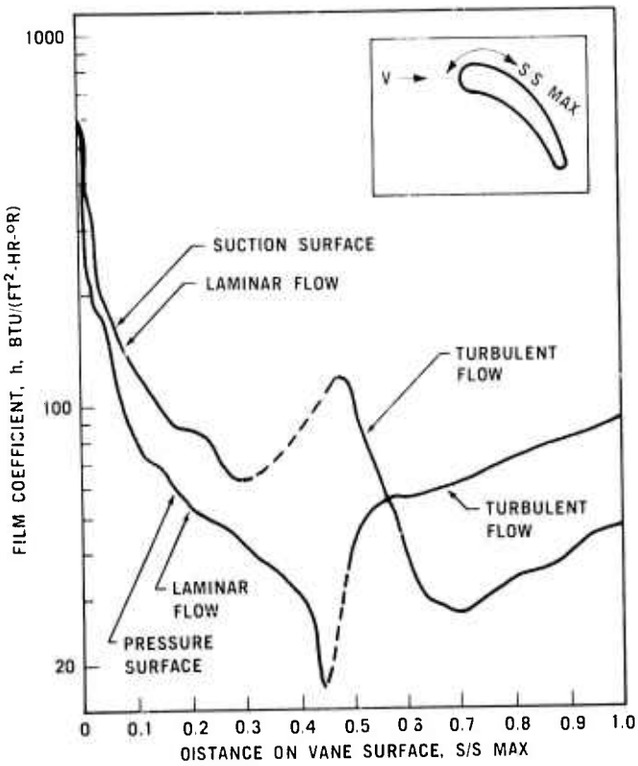

Figure 3.39 Heat Transfer Film Coefficients, Second Stage Stator Vane, at 55% Speed, 2390°R Inlet Temperature, and Radius of 2.4 Inches

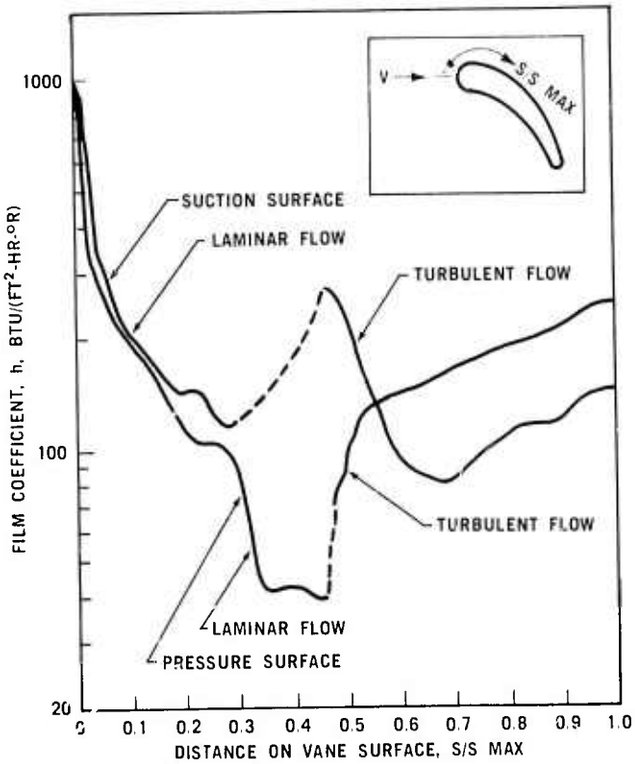

Figure 3.40 Heat Transfer Film Coefficients, Second Stage Stator Vane, at 100% Speed, 2960°R Inlet Temperature, and Radius of 2.4 Inches

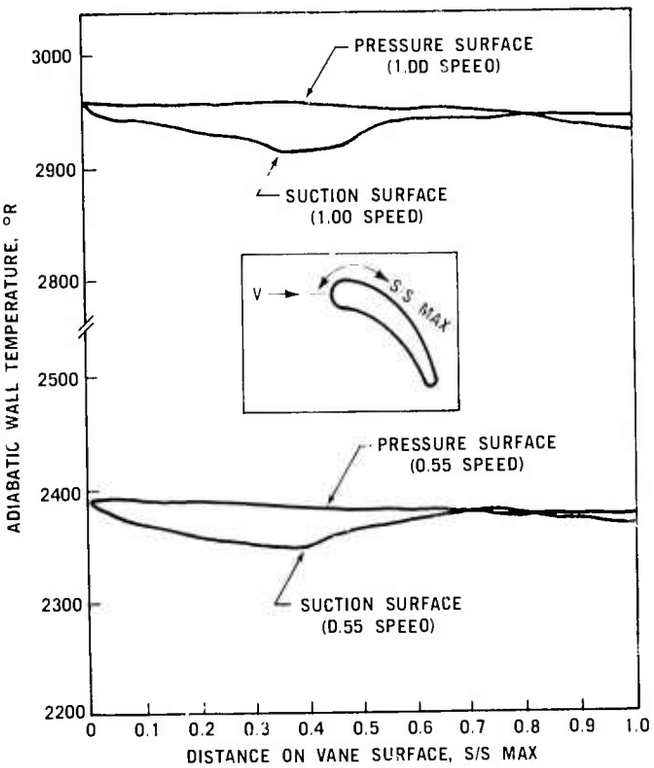

Figure 3.41 Adiabatic Wall Temperature of First Stage Stator Vane at Radius of 1.7 Inches

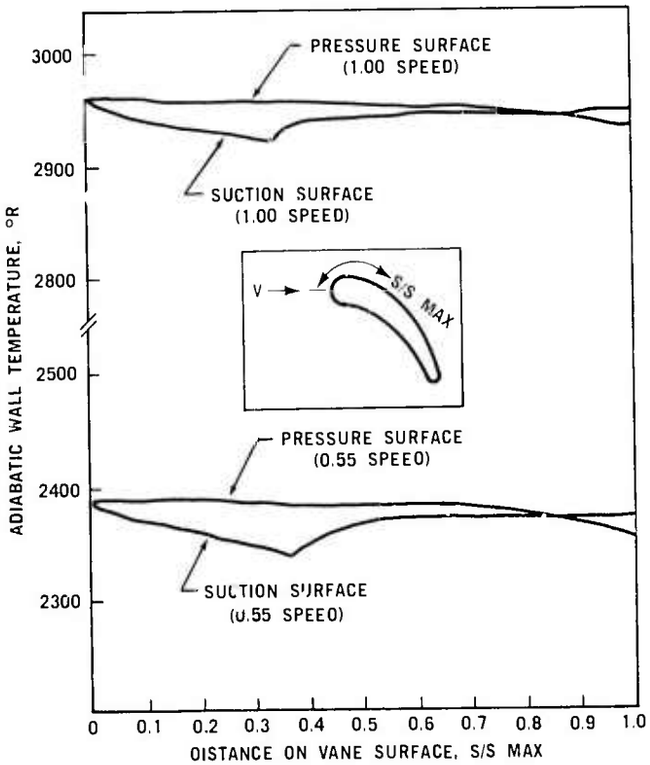

Figure 3.42 Adiabatic Wall Temperature of First Stage Stator Vane at Radius of 1.95 Inches

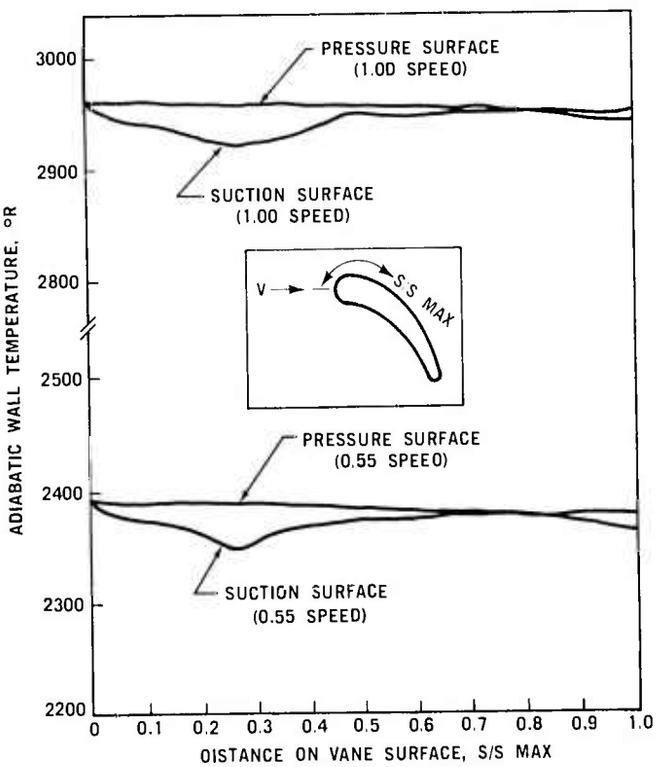

Figure 3.43 Adiabatic Wall Temperature of First Stage Stator Vane at Radius of 2.2 Inches

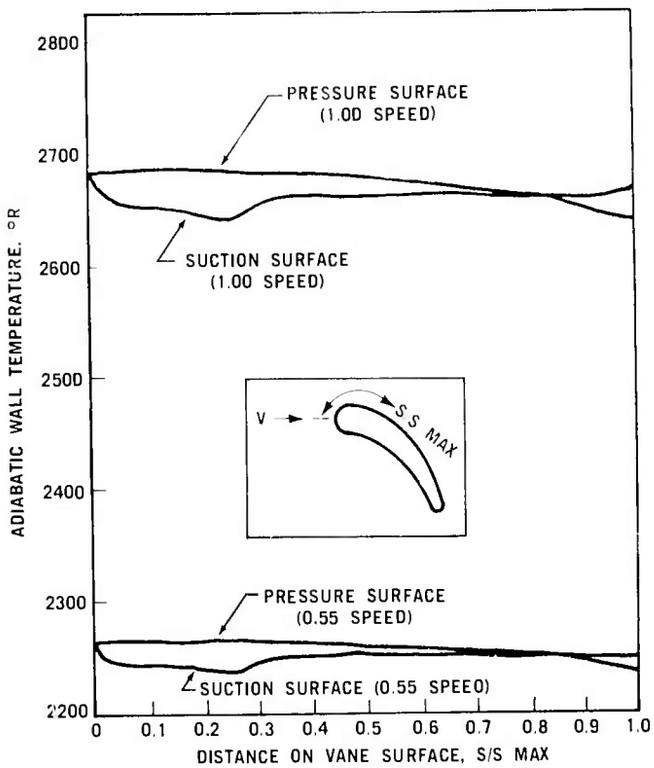

Figure 3.44 Adiabatic Wall Temperature of Second Stage Stator Vane at Radius of 1.7 Inches

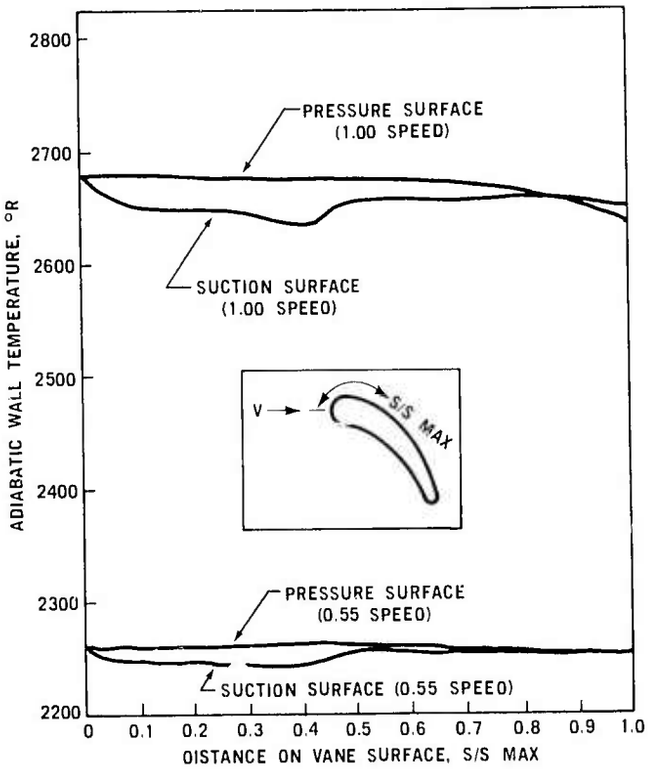

Figure 3.45 Adiabatic Wall Temperature of Second Stage Stator Vane at Radius of 2.05 Inches

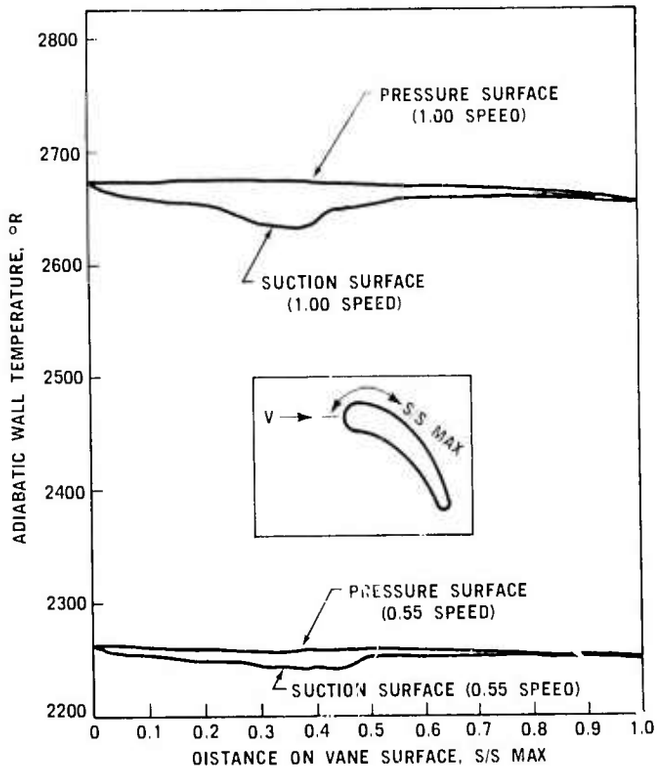

Figure 3.46 Adiabatic Wall Temperature of Second Stage Stator Vane at Radius of 2.4 Inches

TABLE 3.2

AVERAGE FILM COEFFICIENTS FOR
INTER-BLADE CHANNEL GROOVE AND SHROUDS

	Average Convective Heat Transfer Film Coefficient Btu/(Ft^2- hr-^{o}R)			
	Outer Shroud		Inner Shroud or Channel	
Speed / Stage	55%	100%	55%	100%
First Stator	150	374	157	391
Second Stator	143	314	158	355

3.2.2 MATERIALS AND FABRICATION

Introduction

Work during this reporting period was directed toward fabricating flaw-free one-piece first stage stators using a silicon metal powder injection molding composition yielding reaction sintered Si_3N_4 of 2.55 gm/cm^3 density. Stators previously fabricated and discussed in the last report [6] were of 2.2 gm/cm^3 density. In addition, some work was done on transfer molding a reaction sintered SiC material, developed by Ford Motor Company on another program. The transfer molding process was used because this composition utilizes thermoset polymers which cannot be handled on available injection molding equipment.

Silicon Nitride Stator Fabrication

During this reporting period, development of a higher density one-piece first stage stator was continued. Higher density parts (2.55 gm/cm^3) have been molded which have no identifiable cracks or voids when inspected by x-ray radiography and a low power microscope. Absence of internal voids in the outer shroud represents a marked improvement over previous injection molded one-piece stators. These earlier one-piece stators which were engine tested (refer to Section 3.2.3 of this report) were noted to have failed through the outer shroud in a region containing cold shut (knit) lines. The cold shut lines were caused by material cooling at a surface as it advanced through the die cavity. When two cooled surfaces contact as the part fills out, they fail to knit, leaving a crack-like defect.

In an effort to eliminate cold shut and internal voids, new gating configurations were evaluated. Gating the material into the tool using a sprue bushing with 25 gates yielded 25 well defined knit lines. Changing to a 5 runner gate reduce the well defined knit lines to 5 and diminished the other 20 knit lines to a level barely visible. A single runner gate with a reduced area at the cavity entrance yielded a component having no knit lines. The mechanism which controlled knit line formation seemed to relate to the shear put into the material during injection. Greater shear forces yielded a more homogeneous part and produced a flaw free component, although mold release was a problem due to increased surface abrasion during injection of the entire shot through one vane cavity. Other gating systems and new mold releases are being evaluated to eliminate part release problems.

Silicon Carbide Stator Fabrication

The first stage one-piece stator tooling was adapted for transfer molding a special reaction bonded silicon carbide, developed under a separate in-house program. Components were molded of several compositions incorporating slight variations. Some of the components molded had completely filled the die cavity and appeared visually perfect. These components are presently being processed and results of their testing will be reported at a later date. In addition several individual SiC stator segments were processed for thermal shock testing, as reported in Section 3.2.3 of this report.

Two major problems became evident during silicon carbide moldings: (1) tooling wear, and (2) excessive flash. Both problems, although possible to eliminate with tooling changes, make molding of silicon carbide stators slow and difficult.

Rotor Shroud Fabrication Development

A heat-treat process for producing slip cast Si_3N_4 rotor shrouds was discussed in the previous report [6]. This process was successfully used to produce rotor shrouds having gap and diameter stability after exposure to engine operating stresses and temperatures. No further development work was carried out on rotor shroud fabrication during this reporting period. Engine testing results of rotor shrouds produced by this process are given in Section 3.2.3 of this report.

3.2.3 TESTING

Introduction

The stationary hot flow path components include the combustor, turbine inlet nose cone, first and second stage stators, and first and second stage rotor shrouds. In order to evaluate these components, three different types of test rigs were used. The Combustor Test Rig was used for combustor evaluation, the Thermal Shock Test Rig was used for initial testing of stator vane designs and materials, and Engine Test Rigs were used to evaluate and demonstrate the durability of the nose cone, stators, and shrouds over the prescribed duty cycle.

Thermal Shock Rig Testing

During this reporting period, testing was performed on 2.55 gm/cm^3 silicon nitride one-piece first stage stator vanes. Preliminary results showed that the higher density material was superior to the 2.2 gm/cm^3 silicon nitride at 2300°F. The operation of the thermal shock test rig has been discussed in previous reports [3,4,5,6].

Simultaneous thermal shock testing of one-piece first stage stator vanes made of both density materials resulted in the low density vanes failing at 800 to 100[illegible] cycles at 2300°F and no failures of the high density vanes. During this testing, a visual difference in heating rate was observed between the high density and low density vanes. Starting at room temperature, the low density vane heated more rapidly than the high density vane. Temperature measurements with an infrared pyrometer verified that a temperature difference of 200°F existed at steady state. The low density vane stabilized at 2300°F and the high density vane at 2100°F. This temperature difference was compensated during additional testing of high density material. Heat input was increased and quench air increased to yield a 2300°F part temperature and a 600°F/sec down-shock. Subsequent testing of high density stator vanes subjected eight test samples to 2300°F part temperatures and 600°F/sec downshock with no failures in 3000 cycles.

Transfer molded reaction sintered silicon carbide stator segments were also tested in thermal shock. The fabrication of these stators was discussed in Section 3.2.2 of this report. In all, eight three-vane segments from one-piece first stage stators were evaluated. This included testing of segments of two types of Ford silicon carbide for 1000 cycles at 2300°F. All samples survived without failure, although a fine crack approximately 1/8 inches long developed at the leading edge of one vane.

Ceramic Combustor Testing

Evaluation of ceramic combustors has been conducted by subjecting prototype components to a series of tests simulating engine conditions. The results of these tests were reported previously [4,6], and showed that dense, high strength, reaction bonded silicon carbide was the best candidate. During the previous reporting period [6], a combustor made of "Refel" SiC was successfully evaluated for 50 hours over a cyclic durability test representative of the prescribed engine duty cycle. During this reporting period the cyclic d ability testing of the same "Refel" combustor continued toward the 200 hour milestone.

The "Refel" SiC combustor was tested in the Combustor Test Rig shown in Figure 3.47. This rig provides a simulation of the operating conditions that a combustor will experience in an engine, and its features were described in some detail in the last report [6].

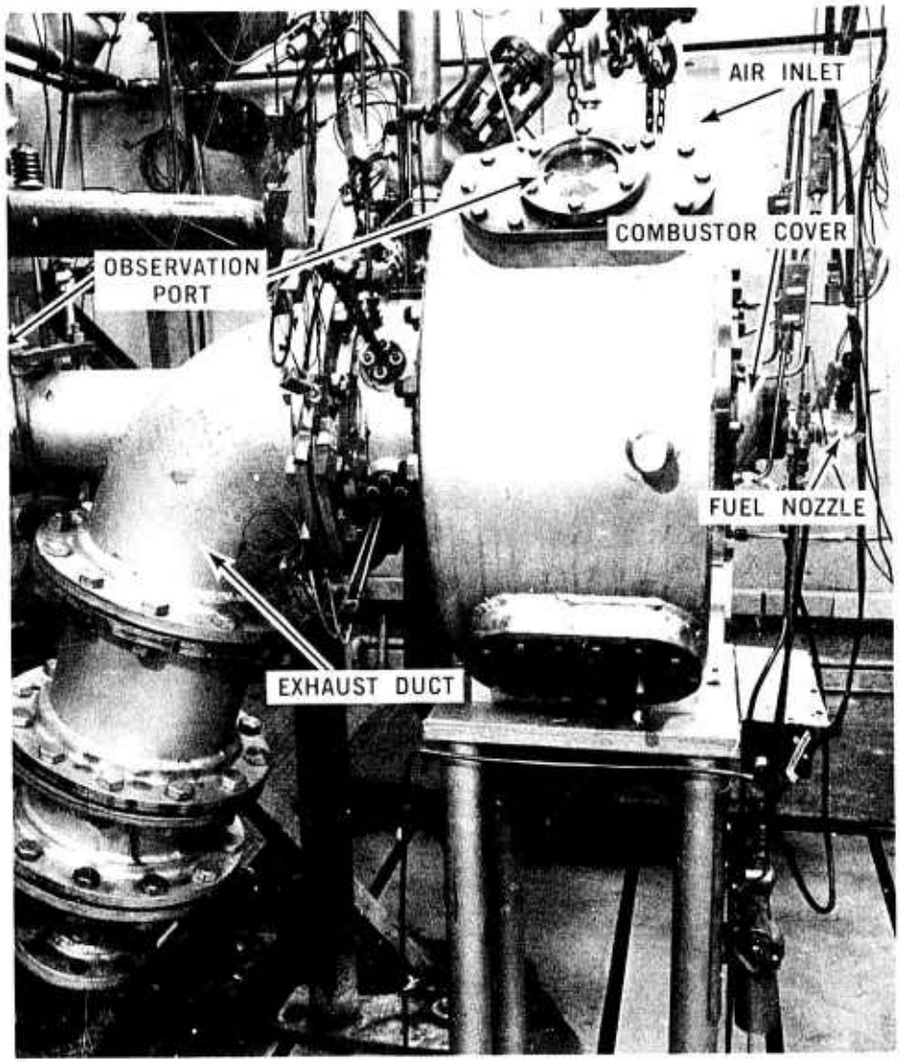

Figure 3.47 Combustor Test Rig

The "Refel" silicon carbide combustor used for the testing reported previously [6] was used again for continuation of the durability testing. The total time accumulated on this combustor and the operating temperatures are listed in Table 3.3. Since the Combustor Test Rig is not equipped with an automatic control system, the length of each cycle through the simulated engine speed conditions was extended to 10 hours as a matter of expediency. The normal duty cycle would be completed in one hour.

This combustor was also subjected to 16 additional cold lights, making a total of 56 cold lights since testing was started. A photograph of the "Refel" combustor, taken after completion of 56 cold lights and 171 hours of testing, is shown in Figure 3.48. Visual inspection and a check using fluorescent dye penetrant confirmed that there was no cracking. The combustor showed no sign of any visual change as compared to its appearance before testing.

TABLE 3.3

ACCUMULATED TEST TIME
ON "REFEL" SiC COMBUSTOR

Speed %	Time	Combustor Outlet Temperature °F
55	83 hours	1930
59	40 hours, 15 minutes	1930
69	10 hours, 55 minutes	1930
77.5	8 hours, 45 minutes	1930
86.5	8 hours, 5 minutes	1930
100	20 hours	2500
TOTAL	171 hour	

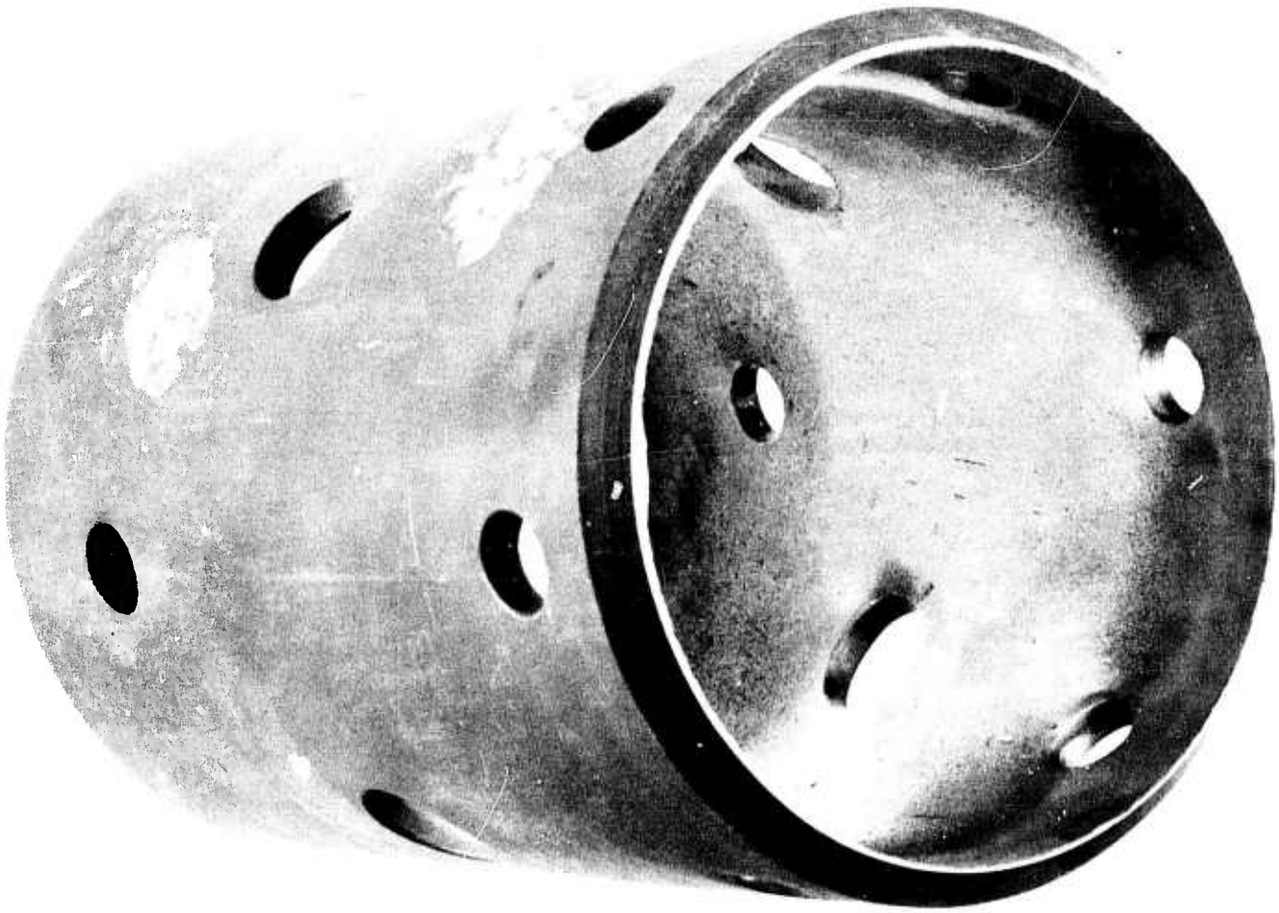

Figure 3.48 "Refel" Silicon Carbide Combustor After Completion of 171 Hours of Testing

Because of the success of this test, the "Refel" type of silicon carbide continues to be considered as the leading candidate material for use in ceramic combustors. The test will be continued, using the same combustor, until 200 hours of cyclic durability have been completed. Additional testing on more combustors will be performed in order to ascertain the reliability of the material in this design.

Hot Static and Dynamic Testing of Stators, Shrouds, and Nose Cones

The evaluation of the turbine inlet nose cone, first and second stage stators, and first and second stage rotor tip shrouds continues in Engine Test Rigs. These components are evaluated over a cycle known as the ARPA duty cycle that was presented in detail in the previous report [6] but will be partially reviewed again.

Initially, each component is qualified by subjecting it to 10 cold lights followed by immediate engine shutdown. This is done with the rotors removed from the rig to minimize the risk of damage to other components. This is referred to as qualification testing. Following this, the components are subjected to engine durability testing. This testing is done with rotors installed in the engine. The durability cycle using metal rotors is such that, every hour, engine speed is varied automatically in steps from 55% to 87% while turbine inlet temperature is maintained at 1930°F. The evaluation is conducted in 15 hour segments and, during each segment, the components are subjected to 2 hot shutdowns followed by 2 hot lights.

Table 3.4 shows the results of engine testing on ceramic stationary components performed to date. The top line indicates the target values established for each component. The balance of the table summarizes test data for all ceramic components which have both passed the qualification test and been subjected to engine durability testing over the ARPA duty cycle.

In reviewing the data, two significant events should be noted. The first event, described in the last report, was a 50 hour durability run, in which all of the components were in excellent condition after the test, except for the second stage stator which did exhibit some fine trailing edge vane cracks.

The second event was a 100 hour component durability test to meet a major milestone of the program. The objective was to complete a minimum of 100 hours of duty cycle testing on each component. The components used in this test were as follows: a turbine inlet nose cone of injection molded silicon nitride of 2.2 gm/cm^3 density, a first stage stator of the new one-piece design made from injection molded Si_3N_4 at 2.55 gm/cm^3 density, and first and second stage rotor tip shrouds of slip cast Si_3N_4 of 2.7 gm/cm^3 density. A 2.7 gm/cm^3 slip cast silicon nitride spacer was used in lieu of a second stage stator because persistent cracking problems had previously occurred on both second stage stators and early first stage stators, made by assembling and bonding individual vanes. A way had been found to make the first stage stator in one piece, and one of them was scheduled for the 100 hour evaluation test. However, a way to make second stage stators in one piece had not been found because of the desired blade overlap for aerodynamic reasons. Therefore, so as not to jeopardize the 100 hour test, it was decided to run the durability test without a second stage stator. More importantly, success in testing a one-piece first stage stator would give emphasis to the development of a suitable one-piece second stage stator.

TABLE 3.4

SUMMARY OF COMPONENT TESTS OVER THE ARPA CYCLE

QUALIFICATION TESTING

Component and Serial Number	ENGINE STATIC Lights Cold	ENGINE STATIC Shutdowns Cold	ENGINE STATIC Shutdowns Hot	ENGINE STATIC Hours	CYCLIC TESTING Lights Cold	CYCLIC TESTING Lights Hot	CYCLIC TESTING Shutdowns Cold	CYCLIC TESTING Shutdowns Hot	CYCLIC TESTING Hours	COMPONENT STATUS*
Target	10	9	1	.2	14	26	-	40	200	S
Nose Cone										
102	10	9	1	.2	44	36	21	59	221.5	S
103	19	17	2	.4	1	2	0	3	50.5	F,O
130	-	-	-	-	5	3	2	6	24.5	F,H
First Stator										
372	10	9	1	.2	1	2	0	3	50.5	S,C
428	-	-	-	-	17	14	6	25	103	F,C
430	10	9	1	.2	14	13	6	21	61.5	F,C
Second Stator										
5	10	9	1	.2	1	2	0	3	50.5	F,V
First Shroud										
24	19	17	2	.4	1	2	0	3	50.5	S
111	13	12	1	.2	61	41	34	68	245	S
Second Shroud										
38	19	17	2	.4	1	2	0	3	50.5	S
106	10	9	1	.2	61	41	34	68	245	S

* S-Serviceable
F-Failed
O-Failure occurred in testing other than the ARPA duty cycle
H-Part failed during handling
D-Cracked Shroud
V-Vanes (s) failure

At the completion of the 100 hours of duty cycle testing, the turbine inlet nose cone, shown in Figure 3.49, was in good shape and was crack free. In fact, this nose cone has achieved a total cyclic test time of 221.5 hours.

The first stage one-piece stator completed the 100 hour component durability objective. A complete inspection after 94 hours showed this component to be crack free, both in the 25 vanes and the outer shroud. Rig performance data taken at 95, 98 and 101 hours showed no change in the test data, and the test was terminated at the end of the work shift, at which point the stator had accumulated 103 hours. Subsequent inspection revealed two axial outer shroud cracks, as

shown in Figure 3.50, but no cracks in the 25 stator vanes. The axial outer shroud cracks are similar to a crack which occurred at 61.5 hours in a similar cyclic test of another Si_3N_4 monolithic stator (No. 430).

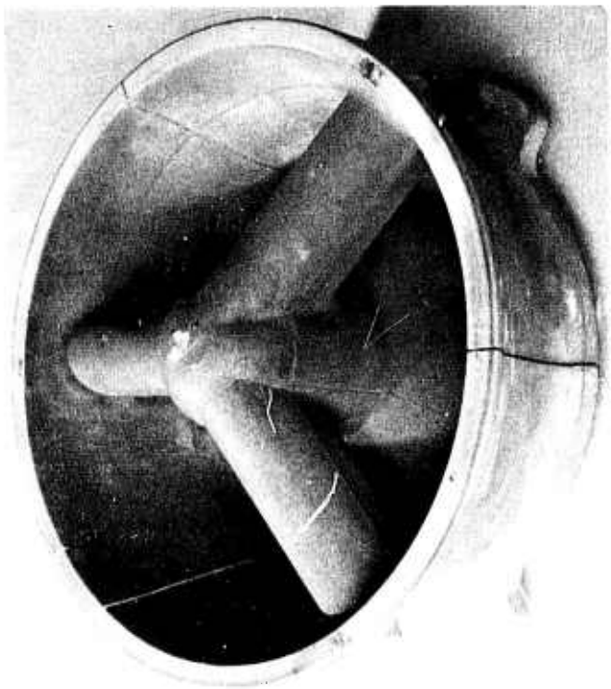

Figure 3.49 Molded Silicon Nitride Nose Cone After Completion of 100 Hour Cyclic Durability Test

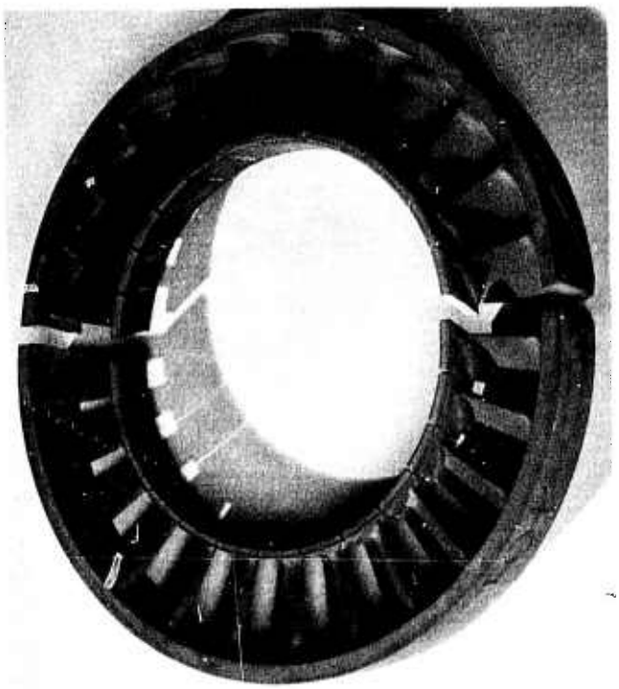

Figure 3.50 Molded Silicon Nitride First Stage Stator After Completion of 100 Hour Cyclic Durability Test

Both the first and second stage rotor tip shrouds, Figure 3.51, successfully completed the 100 hour durability objective and are crack free and in very good condition. In fact, both shrouds have each achieved a total duty cycle test time of 245 hours.

The stators tested during this period had been evaluated for defects by x-ray radiography in the as-molded condition, using procedures described in the last report [6]. Figure 3.52 is the as-molded radiograph of stator No. 430, which

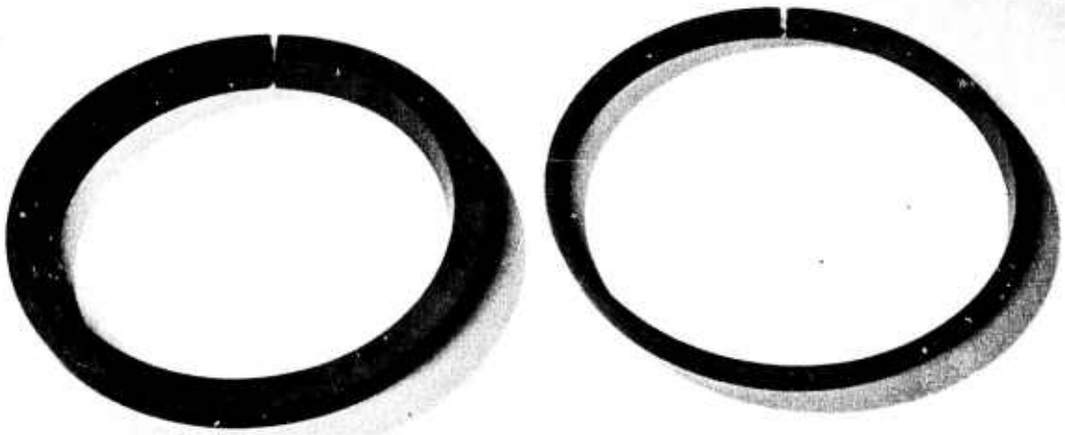

Figure 3.51 Slip Cast Silicon Nitride Rotor Shrouds After Completion of 100 Hour Cyclic Durability Test

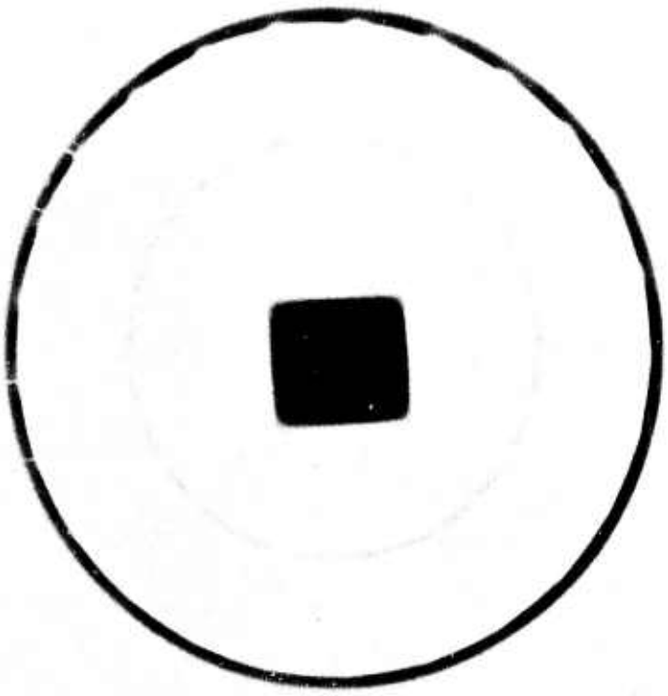

Figure 3.52 X-Ray Radiograph of Stator No. 430 Indicating Defect Which Initiated Failure

developed one crack in the outer shroud after 61.5 hours of cyclic testing. The arrow in the radiograph indicates the defect - in this case an axial knit line of low density - which apparently caused this crack. Likewise, Figure 3.53 is the as-molded radiograph of stator No. 428, which exhibited two outer shroud cracks after 103 hours of cyclic testing. Arrows indicate the defects which were located at the failure points. This information is very informative, and has been used as the basis for deciding that future one-piece stators of 2.55 gm/cm^3 density should contain no detectable defects in the outer shroud in order to be acceptable for rig and engine use.

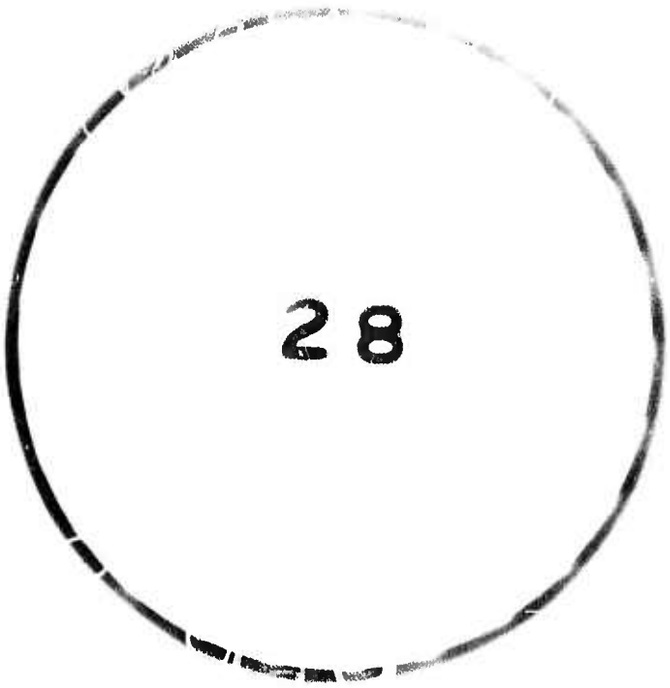

Figure 3.53 X-Ray Radiograph of Stator No. 428 Indicating Defects Which Initiated Failure

The results of this duty cycle testing of stators, nose cones and rotor shrouds are very encouraging. While further improvements in the stator are needed, it is clear that fabrication in one piece has resulted in an important step forward. This illustrates once again the iterative nature of the ceramic turbine development program; since the second stage stators as originally designed could not be made to survive reliably, a change to the one-piece design is indicated. For this reason, as well as the desire to concentrate resources on ceramic rotor development, a major decision has been made with respect to the remainder of the program. This decision is to utilize a first stage stator in both the first and second stage locations. At the same time, the second stage rotor, with different machined dimensions, will-be used for both the first and second stage rotor locations. This flow path configuration has been designated Design D. Changing to this configuration will greatly enhance fabrication and durability development, although a loss in turbine efficiency will be realized at full speed. In order not to lose sight of high efficiency, a separate study will culminate in a design layout of Design E flow path configuration by the end of the ARPA program. In this configuration, the first stage stator, first stage rotor, second stage stator, and second stage rotor will all be different and optimized for aerodynamic efficiency, ceramic manufacturing, and durability.

3.3 GAS BEARINGS

SUMMARY

A 3-leaf compliant foil gas bearing system has been tested in a dynamic simulator test rig. A severe resonance problem was encountered around the second critical speed (45,000 rpm) of the system. Insufficient damping is suspected as the cause. Immediate plans call for modification of system components, including bearings, to alleviate the resonance problem and for a detailed mapping of system dynamic responses near the resonant conditions.

A bearing test aparatus, designated for testing and development of individual bearings and high temperature bearing coatings, has been designed and is ready for procurement.

PRECEDING PAGE BLANK-NOT FILMED

3.3.1 GAS BEARING DESIGN AND DEVELOPMENT

Introduction

Testing of the first generation single leaf HYDRESIL [23] foil bearing system in a dynamic simulator test rig has been previously reported [6]. Because of assembly and fabrication problems, a second generation, three leaf HYDRESIL foil bearing was designed and is being tested. Tests to date indicate that the three leaf bearing has less damping capacity than the single leaf bearing, therefore, a compromise system must be designed which can be easily assembled and fabricated and which has adequate damping capacity to avoid resonance problems.

Testing

The three leaf second generation HYDRESIL foil bearings [6] have been tested in the dynamic simulator test rig. Bearing temperatures were monitored. Bearing deflections and rotor shaft excursions were also monitored at various axial stations by a capacitance displacement instrumentation system. The capacitance probes provide both a vertical and a horizontal signal at each station. The signals are combined and displayed on oscilloscopes as Lissajous diagrams of shaft whirling motion. A high speed Visicorder is being installed to provide permanent records of test runs and to aid in the diagnosis of failures.

Testing of both generation bearings has established that the rotor bearing system has regions of resonance occurring at 21,000 rpm and at 45,000 rpm. The rotor bearing system with single leaf foil bearings was able to pass successfully through these two resonance regions. The rotor bearing system having three leaf foil bearings passes through the first resonance region but will not pass through the second resonance region. The system is stable up to 42,500 rpm, but upon increasing speed to 45,000 rpm, whirling of the journal goes out of bounds (0.004 inches in diameter) as indicated in Figure 3.54. This condition has been repeated in a number of tests and is believed to be caused by insufficient damping.

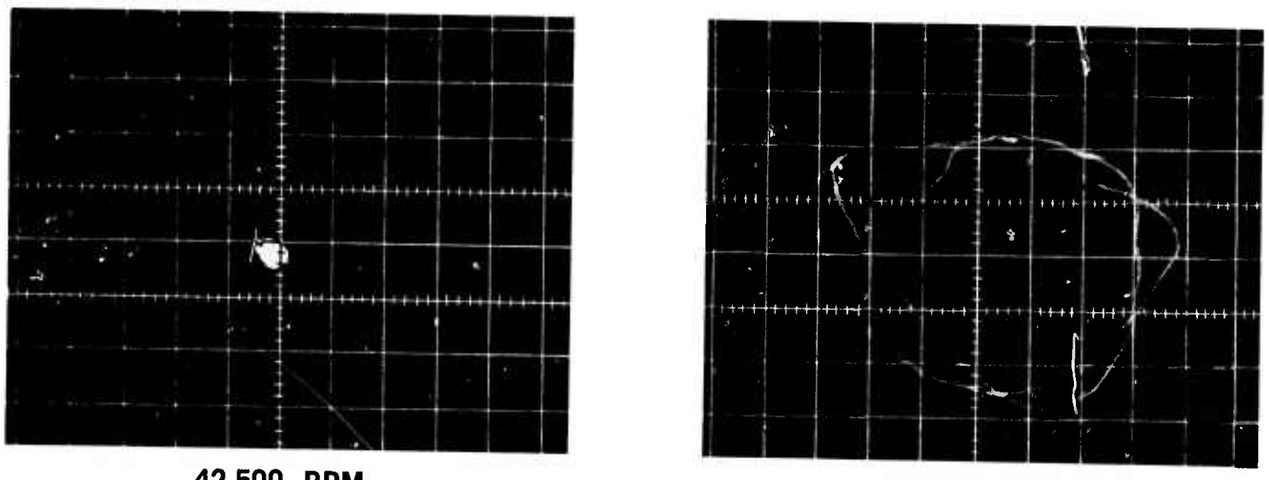

42,500 RPM 44,000 RPM

TURBINE END COMPLIANT FOIL BEARING LOCATION

SCALE 1 DIV. = .001 INCH

Figure 3.54 Oscilloscope Traces of High Speed Shaft Excursions

In spite of excessive whirling, the compliant foil bearings have only incurred slight damage. Some of the corrugations are flattened due to the induced loading which occurs during excessive whirling. The foil blanket also shows a slight scuffing over the corrugations due to intermittent loss of minimum air film.

Compliant Foil Journal Bearing Test Rig

A compliant foil journal bearing test rig has been designed and is shown schematically in Figure 3.55. The rig will be used to evaluate candidate foil bearing materials and surface treatments and to investigate journal-bearing sliding compatibility and high temperature corrosion resistance.

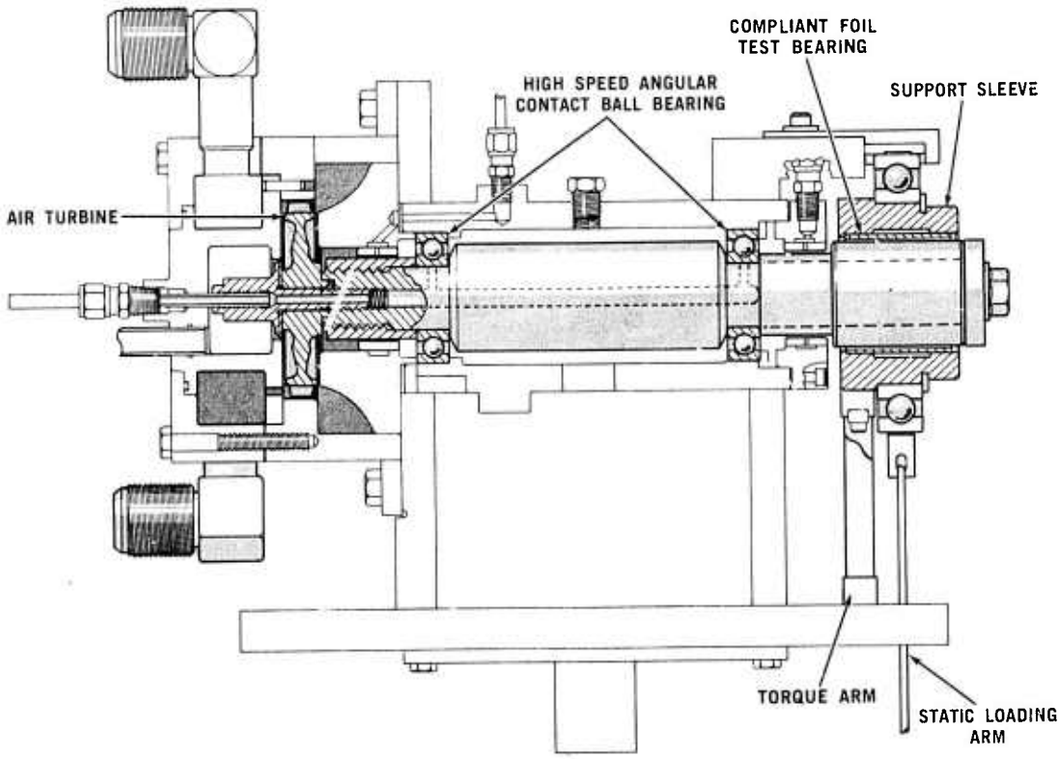

Figure 3.55 Compliant Foil Journal Bearing Test Rig

The rig consists of a single shaft mounted on two high speed preloaded angular contact ball bearings and driven by an air turbine capable of 70,000 rpm. The test bearing is overhung on the other end of the support shaft and is pressed into a support sleeve that is free to rotate as the bearing rides on the shaft journal. A thin cantilevered beam is strain gaged and attached to the support sleeve for measurement of torque between the test bearing and journal. Static weights are attached to the bearing sleeve to simulate bearing loading conditions. The components of this rig have been detailed and are ready for procurement.

In the development and application of non-destructive evaluation techniques to materials and components, the room temperature ultrasonic velocity of silicon nitride was found to vary linearly with density over the range of 2.3 - 3.18 gm/cm^3. A linear relationship also exists between acoustic impedance and modulus of elasticity in silicon nitride. X-ray radiography of as-molded second stage stator vanes played a major role in refining molding materials and molding parameters. A marked increase in the yield of flaw free molded parts resulted when these parameters were applied to the fabrication of engine components.

4. PROGRESS ON MATERIALS TECHNOLOGY - VEHICULAR TURBINE PROJECT

SUMMARY

Materials technology is a very important portion of the systems approach employed in this project for the development of high temperature gas turbine engines. The generation of ceramic material property data, in progress since the beginning of the project, has been instrumental in component design modifications and failure analysis. As testing and fabrication experience was gained, improvements in materials have also been made. The properties of these improved materials are determined and fed back into design modifications and failure analysis, thus closing the loop. The work on determining material properties and material improvements for the vehicular ceramic turbine project, is reported in this section.

Reaction sintered Si_3N_4 components, made by the injection molding process, are inlet nose cones, stators, and rotor blade rings for use in the duo-density process. While testing has shown that nose cones molded from 2.2 gm/cm^3 density material have been generally satisfactory, improved materials are needed for stators and rotor blade rings. Development work has resulted in molded Si_3N_4 of 2.55 gm/cm^3 density, which was followed by the attainment of 2.7 gm/cm^3 density. While further work is needed to finalize the 2.7 gm/cm^3 density material and to obtain property data, this material should be far superior to the earlier 2.2 gm/cm^3 density molded Si_3N_4.

Work reported previously [3] indicated that porous reaction sintered Si_3N_4 oxidized more rapidly at temperatures around 1900°F than at higher temperatures, primarily because the self-protecting oxide film is not sufficiently formed at 1900°F. Data shows that 2.2 gm/cm^3 density Si_3N_4 is seriously oxidized after 200 hours at 1900°F, exhibiting a loss in strength from 17,000 psi before oxidation to 10,000 psi after oxidation. An increase in thermal expansion rate was also found after this exposure. While work continues to quantify and solve this problem, encouraging preliminary test results on 2.7 gm/cm^3 density Si_3N_4 indicate that successful development of this material will substantially diminish the oxidation problem as well as provide stronger material.

Fracture mechanics technology, as applied to ceramic materials for gas turbine engines, is being utilized in order to develop a broad understanding of the behavior of these materials. Work presented in this section describes the mechanism of slow crack growth in materials also exhibiting some high temperature plasticity, using hot pressed silicon nitride as the model system.

A relatively new class of oxygen-nitrogen ceramics named Sialon have been proposed as candidate materials for high temperature ceramic turbine engines. The results of a preliminary investigation of pressureless sintered Sialon materials is included in this section. This work was concerned with composition studies and phase analysis of Sialon materials, with the objective of attaining high strengths. To date, only modest strengths (MOR of 35,000 psi) have been achieved using a composition of 60% Si_3N_4 and 40% Al_2O_3.

PRECEDING PAGE BLANK-NOT FILMED

4.1 DEVELOPMENT OF IMPROVED MOLDED SILICON NITRIDE

Introduction

The development of injection molded Si_3N_4 before the start of this contract resulted in a material with a density of 2.2 - 2.3 gm/cm^3 and a 4 point bend strength of 17,000 psi. Testing of prototype turbin engine components made from this material has shown marginal results, so efforts to improve the quality of this type of Si_3N_4 have been in progress. Developments in nitriding techniques [5] have indicated that the strength can be increased to 26,000 psi without increasing density; however, these techniques were not readily applied to engine components. Oxidation experiments were carried out on this improved material at 1900°F for 120 hours, with weight gains of approximately 8.7%, which is similar to the weight gain of standard material of the same density. Refer to Section 4.2 of this report for a further discussion of oxidation of Si_3N_4.

Further improvements in properties could be achieved by increasing the density of the injection molded material. Slip cast Si_3N_4 with a density of 2.6 - 2.7 gm/cm^3 has a strength of 40,000 psi, improved creep resistance and higher thermal conductivity than the 2.3 gm/cm^3 density injection molded Si_3N_4. The higher density Si_3N_4 should also yield improvements in oxidation resistance. By developing an injection molded Si_3N_4 with a density of 2.5 to 2.7 gm/cc a material will be available that should have similar properties to the slip cast Si_3N_4 along with the fabrication advantages of injection molding.

High Density Molded Silicon Nitride

Higher density injection molded Si_3N_4 can be obtained by increasing the amount of the silicon metal powder relative to the organic binder system. Figure 4.1 shows the volume percentage of filler (silicon + 3% Fe_2O_3) necessary to obtain the final nitrided Si_3N_4 density. The use of 3% Fe_2O_3 as a nitriding aid was discussed previously [5]. It is possible to obtain this relation knowing the specific gravity of the starting materials and the 1.61 conversion factor normally experienced for weight gain upon nitriding. Since there is no volume change on either binder removal or nitriding this relationship is valid.

The viscosity of a filled organic system change rapidly when solids are added above the 50 volume percent level, as shown in Figure 4.2. However, this viscosity relationship can be drastically altered by blending two or more different particle size distributions of the solid filler material as shown in Figure 4.3. At low filler concentrations, the viscosity is independent of particle size. However, at the 60 volume percent concentration, the viscosity can be reduced by almost two orders of magnitude by the use of the proper blend of particle size distributions. This curve also shows that for a bimodal blend of powders between 70 and 75% loading, the minimum viscosity can be obtained using 65% coarse powder and 35% fine powder. Figure 4.4 also shows the effect of the particle size on viscosity. This figure shows that for a blend of two distributions, (25% fine/75% coarse) the mean particle size ratio (R12) is critical for obtaining minimum viscosities. The choice of an optimum particle distribution of silicon powder is the basis for the development work undertaken to achieve the high density injection molded Si_3N_4.

PRECEDING PAGE BLANK-NOT FILMED

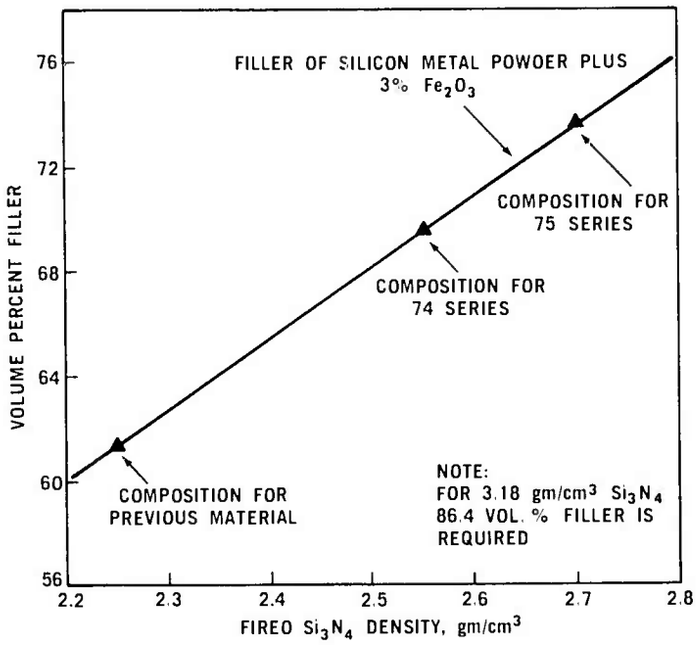

Figure 4.1 Relationship Between Volume Percent Filler of Injection Molding System and Final Silicon Nitride Density

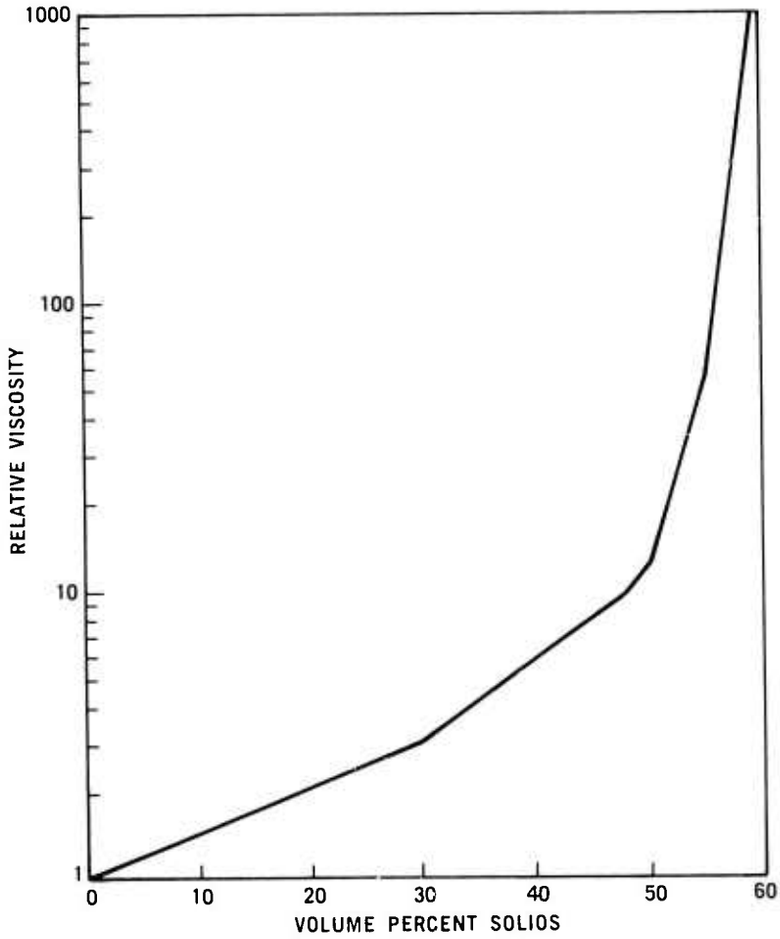

Figure 4.2 Relative Viscosity as a Function of Percent Solids Content of a Monodispersed System [24]

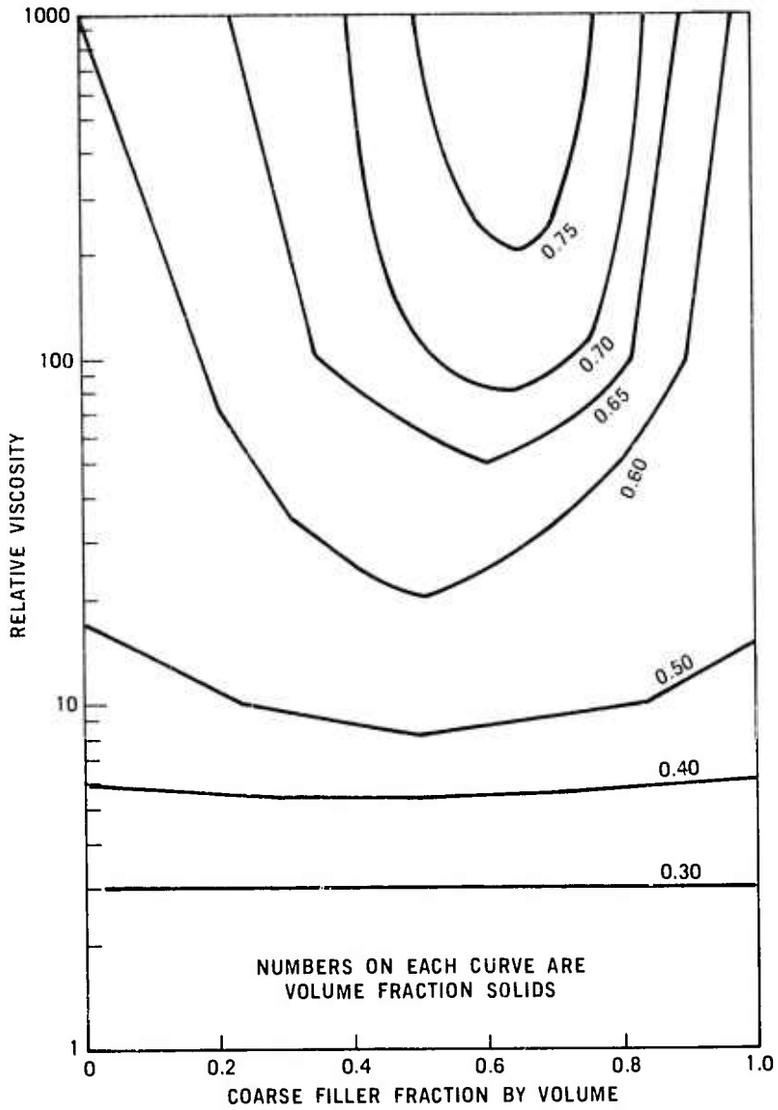

Figure 4.3 Calculated Viscosity for Various Bimodel Suspensions vs Distribution Ratios and Concentrations [24]

The particular particle size distributions used in this work are shown in Figure 4.5. The D, P, and P materials were obtained by dry ball milling silicon powder feed stock for various periods of time. Material P required 142 hours of ball milling. The A material was obtained by air classification of the silicon feed stock, with an upper cut point of 40 μm.

The powders were mixed into the injection molding batches listed in Table 4.1. The 74 series yields Si_3N_4 of 2.55 gm/cm^3 density, while the 75 series results in material of 2.7 gm/cm^3 density. Moldability tests were then conducted for each material This test consisted of injecting the materials under controlled temperatures and pressures into the second stage stator vane die. The moldability was qualitatively determined to be either poor, fair or good. The blades were then subjected to x-ray radiography to determine the presence of internal molding flaws. Refer to Section 5.2 of this report for radiography results. The yield of good parts was determined by the number of flaw free parts divided by the total number of parts. These parameters, along with pertinent comments, are also shown in Table 4.1.

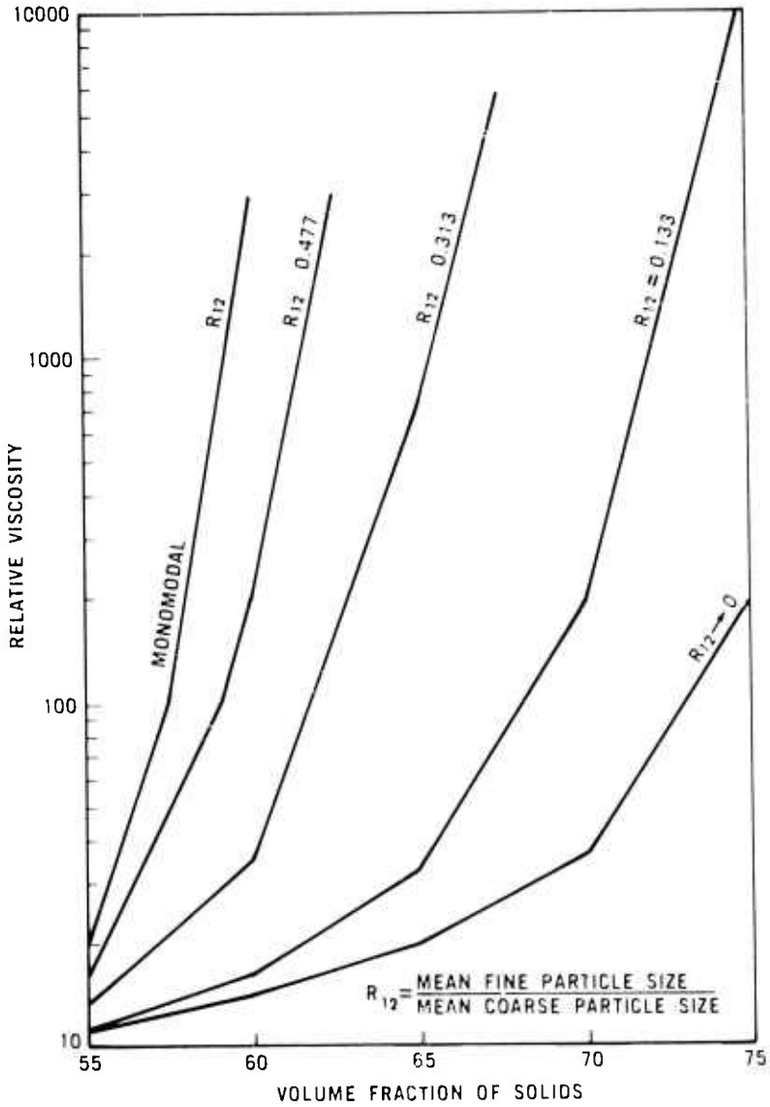

Figure 4.4 Calculated Viscosity of Monomodel and Bimodel Suspensions vs Volume Fraction of Solids With a Volume Fraction of Fine Particles of 25% [24]

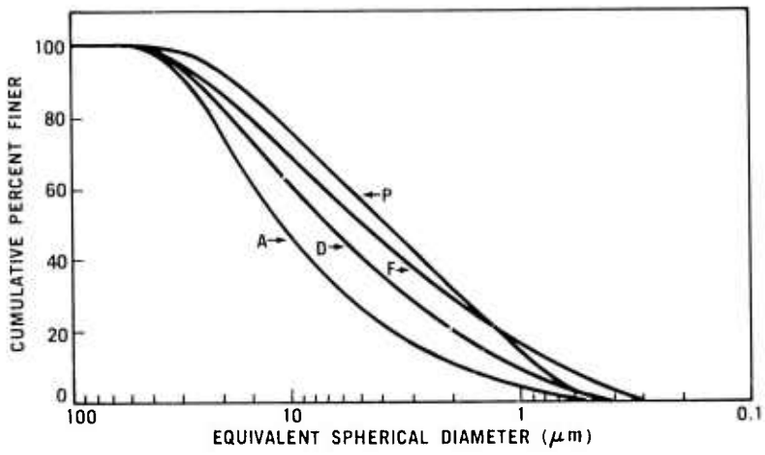

Figure 4.5 Various Particle Size Distribution Curves of Silicon Metal Powders

TABLE 4.1

MOLDABILITY AS A FUNCTION OF PARTICLE DISTRIBUTIONS FOR TWO LEVELS OF LOADING

Mat'l	Volume % Loading	Particle Distribution	R12(65C/35F)	Moldability	Yield of Good Parts	Comments
74A	69 1/2	A	0.175	Poor	21%	Thixotropic
74D	69 1/2	D	0.15	Fair/Good	20-50%	Reproducible from batch to batch
74F	69 1/2	F	0.112	Good	70%	Currently in use for all molded components, reproducible from batch to batch
75A	73 1/2	A	0.175	Would not mold	-	Very thixotropic-organic would separate
75D	73 1/2	D	0.15	Poor	-	Thixotropic
75F	73 1/2	F	0.112	Fair/Good	24%	-
75P	73 1/2	P	0.13	Good	75%	Will use for molding trials of 2.7 gm/cm^3 density monolithic stators

The most meaningful result shown in Table 4.1 is the fact that the yield of good parts increases as the starting particle size distribution becomes finer and broader. This is the result to be expected based upon the predictions of Farris [24]. As previously shown in Figure 4.4, the viscosity decreases as the size ratio between blends (R12) decreases. If the distributions shown in Figure 4.5 are divided into coarse and fine fractions, size ratios can be obtained for each distribution in Table 4.1. As shown, the size ratios generally decrease as the distribution become broader, consequently yielding more fluid molding compositions and higher quality components. The exception is the P distribution which is generally finer than the F distribution over most of the particle size range, but has fewer particles below 1 micron in diameter.

Material 74F has been used for molding of nose cones and one piece stators during this reporting period. The results of rig testing of some of these stators was discussed in Section 3.2.3 of this report. Since improved properties could be expected at the 2.7 gm/cm^3 density level, the 75 P material will be used for molding trials of one-piece stators in the near future.

Nitriding Parameters and Physical Properties

The most promising nitriding cycle for the higher density injection molded material discussed in Section 4.1 is based upon a cycle developed by Messier and Wong at AMMRC. This cycle consists of stepwise increases in temperature up to 2550°F and is based on nitriding kinetics. Specifically the cycle is: 20 hours at 1300°F, 3 hours at 2282°F, 20 hours at 2415°F, 7 hours 2510°F and 20 hours 2552°F. Other cycles were tried but this cycle consistently gave the best weight gains and the highest strength figures. The weight gains observed for the 74 series material (2.55 gm/cc density) were 60 to 61% while the 75 series (2.7 gm/cc density) were 59 to 60%. Neither structure shows an abnormal amount of free silicon as exhibited in Figure 4.6. Also shown in Figure 4.6 are the changes in microstructure as the density is increased from 2.3 gm/cm^3 to 2.7 gm/cm^3.

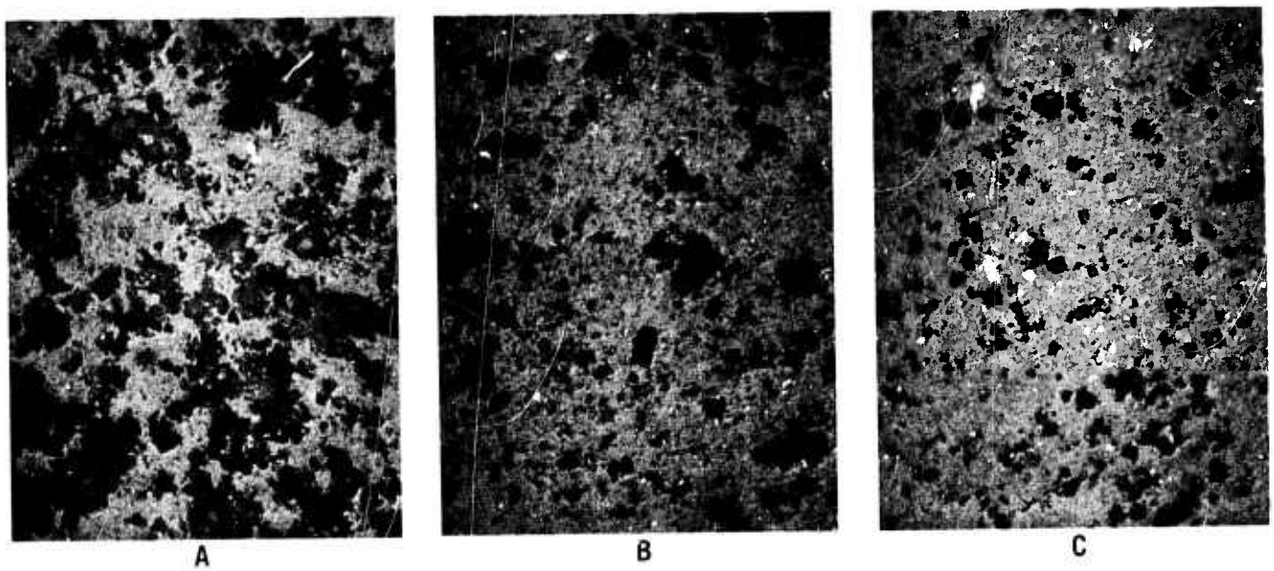

Figure 4.6 Optical Micrographs (500 X) of Molded Silicon Nitride at (a) Density of 2.25 gm/cm^3 (Type B) (b) Density of 2.55 gm/cm^3 (74D) and (c) 2.7 gm/cm^3 (75F)

An anomaly was noted in the strength results presented in Table 4.2. The MOR results for the 74A averaged on the high end of the predicted band. The 74D results were on the low end of the band, while the average results for the 74F were significantly below the predicted range. It seems that as the starting particle size of the silicon is made finer and the distributions broadened, the strength decreases. This is opposed to current thinking, which is that the finer the particle size of silicon the smaller the inherent flaws in the Si_3N_4 and the higher the strength. Experiments are currently in progress to investigate this phenomenon and determine the cause for these low strength values.

TABLE 4.2

PHYSICAL PROPERTIES OF INJECTION MOLDED Si_3N_4

Mat'l	Measured density	Ave MOR*	Anticipated MOR From Slip Cast Data
74A	2.52/2.58	38 ksi	32-40 ksi
74D	2.52/2.58	33 ksi	32-40 ksi
74F	2.52/2.58	27 ksi	32-40 ksi
75F	2.68/2.72	35 ksi	40-48 ksi

* MOR values are based on the following conditions:

1/8 x 1/4 x 1 1/3" samples, as nitrided surfaces
3/8 x 1 1/8" test fixture, 4 point loading
0.02 in/min loading rate

Preliminary bend creep results were obtained on the 74A injection molded Si_3N_4. The data presented in Table 4.3 shows that the creep resistance of this class of materials is as good as the slip cast material of similar composition. More testing will be performed to obtain the creep and stress rupture parameters for the 74 series and 75 series materials.

TABLE 4.3

FLEXURAL CREEP PROPERTIES OF HIGH DENSITY

(2.55 gm/cm^3 INJECTION MOLDED Si_3N_4

Mat'l	Temp	ATM	Stress	Test Duration	$\dot{\varepsilon}_s$ in/in/hr
74A	2300°F	Air	10 ksi	117 hours	1.6×10^{-6}
	2300°F	Air	20 ksi	90 hours	1.6×10^{-6}
	2300°F	Air	25 ksi	35 hours	1.7×10^{-6}
	Failed when loaded to 35 ksi				

4.2 OXIDATION RESISTANCE OF REACTION SINTERED SILICON NITRIDE

Introduction

Earlier studies of the oxidation characteristics of reaction sintered Si_3N_4 at several temperatures indicated that oxidation rate varied inversely with temperature. This effect is illustrated in Figure 4.7, which is reproduced from the third report [3], showing a relatively high weight gain at 1890°F. Samples tested at this temperature did not exhibit any visible protective coating, leading to the conclusion that internal oxidation was proceeding at a more rapid rate than was the case when a glassy coating was initially formed by oxidation at higher temperatures. Since almost all of the engine and rig testing of silicon nitride turbine components is taking place at temperatures around 1900°F, pending the development of ceramic turbine rotors, a more detailed investigation of the oxidation of silicon nitride at 1900°F was started. While most of this work was done using injection molded reaction sintered Si_3N_4 of 2.2 - 2.3 gm/cm^3 density, some testing was performed using the higher density materials discussed in Section 4.1 of this report.

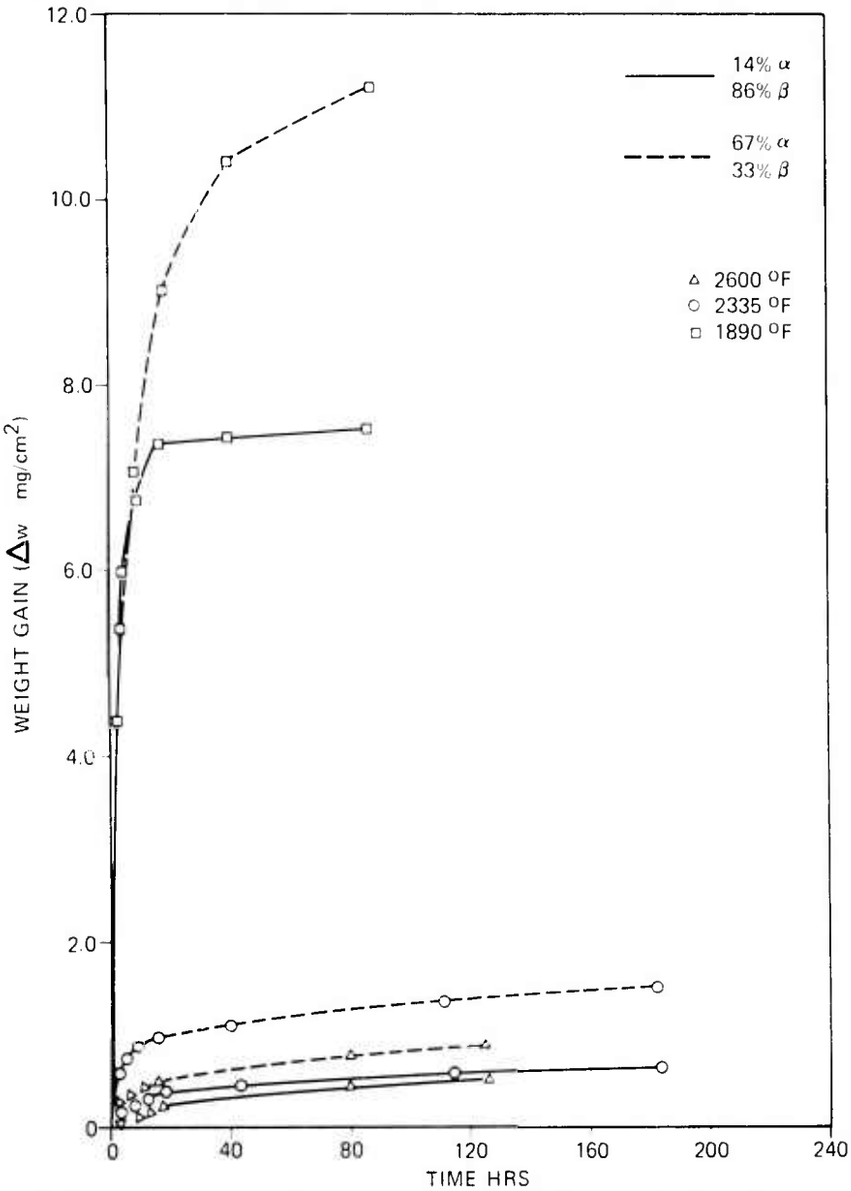

Figure 4.7 Weight Gain vs Time for 2.3 gm/cm^3 Density Reaction Sintered Silicon Nitride at Several Temperatures [3]

PRECEDING PAGE BLANK-NOT FILMED

Evaluation of Oxidation of Reaction Sintered Silicon Nitride

From thermodynamic data [25], the tendency of silicon nitride to oxidize to beta cristobalite (SiO_2) at the test conditions is readily apparent from the following reaction at 1900°F:

$$Si_3N_4 + 3\ O_2 \rightarrow 3\ SiO_2\ \text{(B Cris.)} + 2\ N_2.$$

The free energy is - 411,275 K_{cal}/mole. This is a very large driving force favoring the oxidation of silicon nitride, i.e., intrinsically, silicon nitride is prone to oxidation. The fact that silicon nitride has very good oxidation resistance in practice is due to the same mechanism operative in stainless steel and aluminum, i.e., the oxidation product protects the material from continued rapid oxidation.

Similar calculations for other reaction products of silicon nitride and oxygen indicated that the above is the most likely reaction to take place, barring kinetics problems, since the free energies of the other reactions are either positive or smaller negative numbers. In addition, similar calculations at other temperatures showed that the tendency for the above reaction decreases with temperature. However, the kinetics are generally more favorable at the higher temperatures.

The oxidation of silicon nitride into beta cristobalite produces a 78% increase in volume and 29% increase in weight. Experimentally, a low density material of 2.2 gm/cc density, when subjected to 200 hours at 1900°F in air, loses 25% silicon nitride and picks up 14.7 weight percent oxygen. This is equivalent to 27 weight % or 35 volume % of silica (which is mostly β cristobalite at 1900°F but inverts to α cristobalite when cooled to room temperature) for an overall weight gain of 6.5%.

The rate of weight gain is shown in Figure 4.8 for small test bars (1/8 inch by 1/4 inch by 1-1/4 inches long) of injection molded reaction sintered 2.2 gm/cm^3 density Si_3N_4 over a 200 hour test in still air at 1900°F. These bars were made from low calcium silicon metal of less than 40μ particle size with 1% Fe_2O_3 added as a sintering aid and were sintered in nitrogen with 1% added hydrogen. Other samples of this same material were heated in both argon and nitrogen for 200 hours at 1900°F with no change in weight, indicating that the weight gain in air is indeed due to oxidation.

Strength measurements at room temperature, taken on these bars before oxidation, resulted in an average four point modulus of rupture of 17,000 psi. After oxidation for 200 hours at 1900°F, this strength decreased to 10,000 psi, indicating a serious degradation in strength had occurred. Figure 4.9 illustrates a positive change in thermal expansion which resulted from the oxidation treatment, further evidence of changes in material properties.

Analytical investigations on both oxidized and unoxidized samples revealed a large increase in silica content, primarily α cristobalite, as identified by x-ray diffraction. Very little silicon oxynitride was found in either samples, nor was there any significant change in alpha/beta ratio.

Another experiment was performed, using the same injection molded material, to determine the relative rate of oxidation between the surface and the center of the test bars. As shown in Figure 4.10, the surface oxidized at a higher rate initially, and still contained more oxygen than the interior after 200

hours at 1900°F. However, the extrapolation indicated in Figure 4.10 shows that the oxygen content would equalize in about 300 hours.

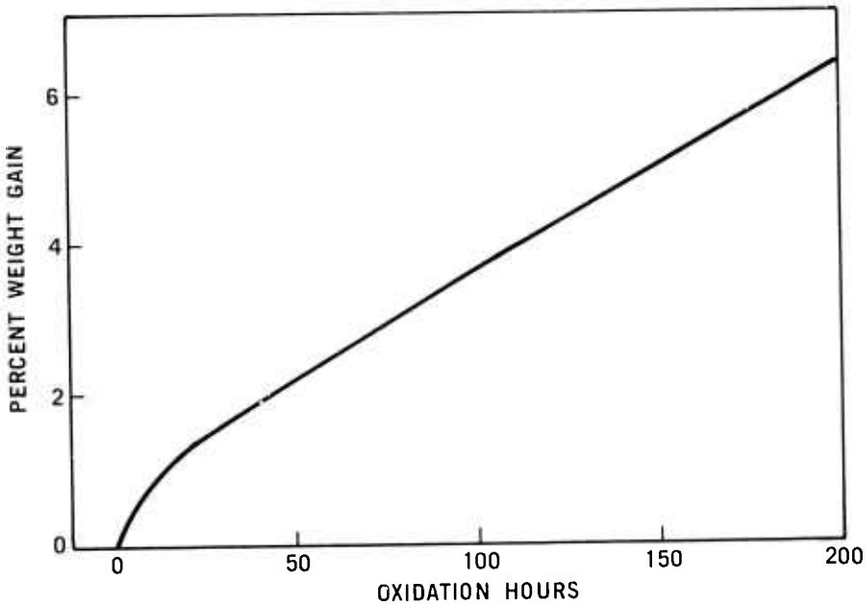

Figure 4.8 Weight Gain of Reaction Sintered Silicon Nitride of 2.2 gm/cm^3 Density vs Time at 1900°F

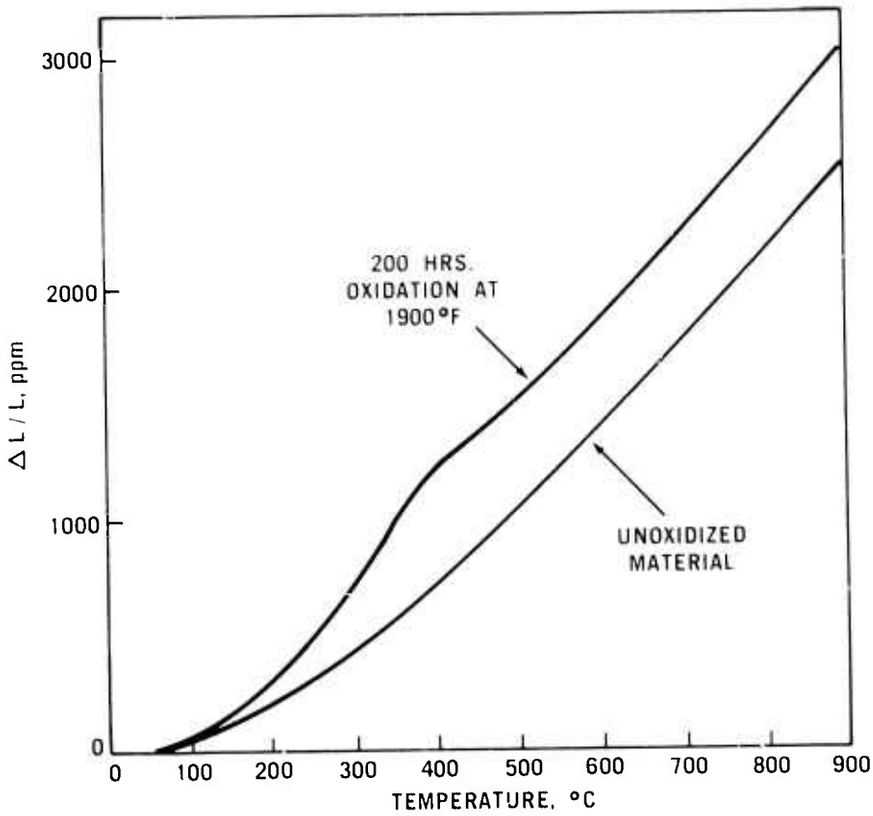

Figure 4.9 Effect of Oxidation for 200 Hours at 1900°F on the Thermal Expansion of 2.2 gm/cm^3 Reaction Sintered Silicon Nitride

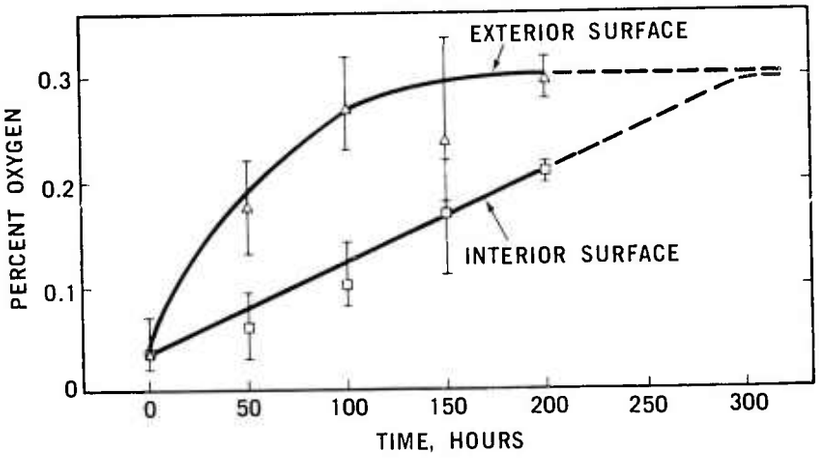

Figure 4.10 Oxygen Concentration vs Time at Surface and Interior of 2.2 gm/cm^3 Density Silicon Nitride Oxidized at 1900°F

Samples of higher density injection molded Si_3N_4, described in Section 4.1 of this report, were also oxidized for 200 hours at 1900°F. The results of the weight gain after 250 hours are plotted comparatively in Figure 4.11, and show an encouraging decrease in weight gain as density increases. Also encouraging is the finding that the 2.7 gm/cm^3 density material suffered no loss in strength after this treatment.

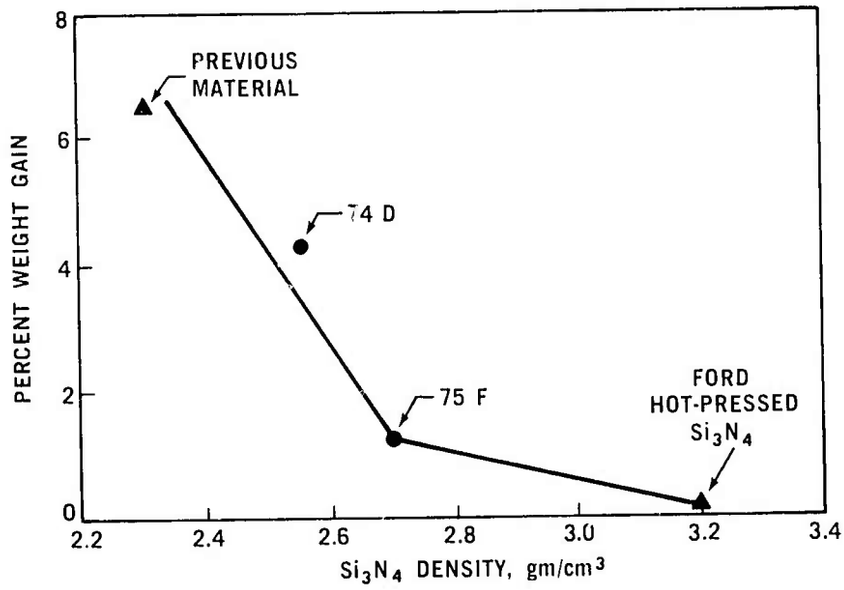

Figure 4.11 Weight Gain vs Density for Silicon Nitride Oxidized for 200 Hours at 1900°F

Further work to define and solve the oxidation problem of porous reaction sintered Si_3N_4 is in progress, and consists of a more detailed study of the high density material plus evaluating the effects of preoxidation at higher temperatures, as suggested by work discussed earlier [3], and development and testing of various coatings to limit the transport of oxygen into the interior of the material.

4.3 HIGH TEMPERATURE FRACTURE BEHAVIOR OF SILICON NITRIDE

Introduction

The technique of studying the fracture behavior of turbine ceramics using purposely introduced flaws of controlled size and geometry continues to be applied as described previously [6]. Work on hot pressed Si_3N_4 has been extended to include fractographic observations of time dependent fracture behavior. Those results include a schematic description of the response to applied load of a precracked brittle material in a regime where time dependent physical processes influence the ultimate load bearing ability of the material.

Time-Temperature Dependent Fracture Behavior

The influence of flaw size on fracture strength is schematically illustrated in Figure 4.12. The encircled letters refer to three different flaw sizes - B and C emplaced in a fracture specimen in a controlled manner, and A serving to indicate the smaller, naturally occurring flaws of uncontrolled morphology. The temperature dependence of fracture strength for these three flaw sizes in hot pressed silicon nitride (Norton HS-130) appears in Figure 4.12. The overall shape of this dependence and the mechanisms involved have been described earlier [6]. The difference in shape of curve (A) compared to (B) and (C) indicates a profound influence on the fracture process of the high stress supported by the small natural flaws. Smaller cracks support a higher stress and consequently lead to onset of viscosity (diffusion) controlled fracture processes at a lower temperature. The temperature dependent fracture behavior of specimens carrying the intermediate size fracture initiating flaw is a consistent illustration of this fact. At crack size (B) the fracture strength lies higher than for (C), the onset of diffusive processes influencing fracture occurs at a lower temperature, and the relative stress advantage (peak height) is smaller.

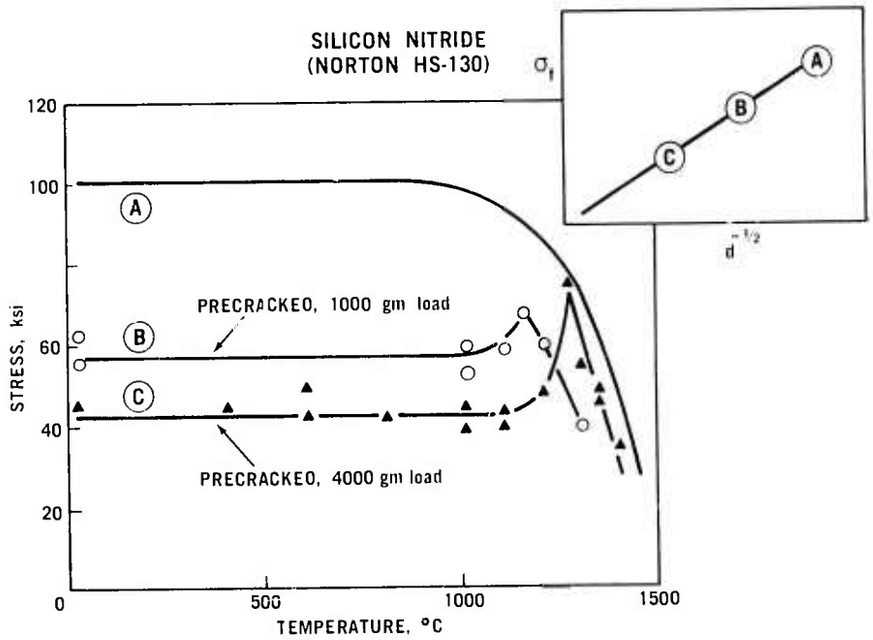

Figure 4.12 Temperature Dependence of Fracture Stress as Influenced by Fracture Initiating Flaw Size, Showing (inset) a Schematic of the Griffith Relationship of Fracture Stress, σ_f, to Crack Size, d.

It is well established [26-29] that viscosity (diffusion, plasticity) influenced fracture processes are a dominant feature of the mechanical behavior of hot pressed silicon nitride and numerous other brittle materials which are candidates for structural application. Such materials are strain rate sensitive. This effect typically appears as creep deformation and commonly adopts the mechanistic process of subcritical crack growth.

In the case of an emplaced semicircular crack perpendicular to the maximum tensile stress in the surface of a flexure test bar [6], the stress state at any point along the crack rim will be a function of position crack velocity and a nonlinear function of displacement (d) as the crack enlarges at a temperature in the viscosity controlled fracture regime. The response to two imposed strain rates is shown schematically in Figure 4.13a. The ability of the material to respond to the imposed strain by viscous accommodation is established by the relevant diffusivity, plotted at two temperatures in Figure 4.13b. In the case of hot pressed silicon nitride (Norton HS-130) the viscosity (diffusivity) of the glassy grain boundary film is the strength controlling factor.

Superposition of the diffusivity at two temperatures upon two enforced strain rates (Figures 4.13a and b) results in the plot in Figure 4.13c. Using this representation, the crack size corresponding to the limit of slow crack growth (and the onset of catastrophic or fast fracture) is found at the intersection of the imposed crack velocity with the upper limit of the ability of the material to accommodate (through thermally activated means) the mechanical processes at the crack tip. Thus a crack of original size d_o may grow to size d_1 or d_2 (Figure 4.13d), depending upon the combination of imposed strain rate and temperature of the test.

These considerations contribute to an understanding of the fracture mechanisms which lead to the temperature dependence of fracture strength shown in Figure 4.13e, representing the behavior of hot pressed silicon nitride, or Figure 4.13f, typical of the behavior of many other brittle ceramic materials. At low temperatures, the ability of the material to accommodate deformation at the crack tip by thermally activated molecular motion (diffusional processes) usually does not match the relatively higher rate of imposed strain. In that regime, the fracture behavior (strength and mechanism) is taken as essentially loading-rate independent over a wide range because the diffusion aided processes are essentially frozen. At relatively high temperatures, thermally activated processes are competitive over a significant range of crack tip velocities (Figure 4.13c) at the imposed strain rate. In this regime, cracks enlarge "slowly" until the rate of enlargement exceeds the rate of accommodation by the operative thermally activated mechanism. At this critical crack size, the general Griffith criteria for onset of catastrophic failure (fast fracture) is fulfilled for a specific combination of strain rate and temperature. Under given conditions of strain rate, the extent of subcritical crack growth would be expected to be larger the higher the temperature. The load bearing ability, of course, decreases inversely with the extent of subcritical crack growth and is very sensitive to strain rate. At intermediate temperatures, the existance of significant subcritical crack growth depends strongly on the operative strain rate. Therefore, within this temperature regime, it is particularly important that engineering judgment should not be based entirely on flexural tests typically run at relatively high strain rates.

The processes described schematically above have been demonstrated to occur in hot pressed silicon nitride (Norton HS-130) in two ways. First, precracked flexural bars were loaded to failure at different loading rates, there-

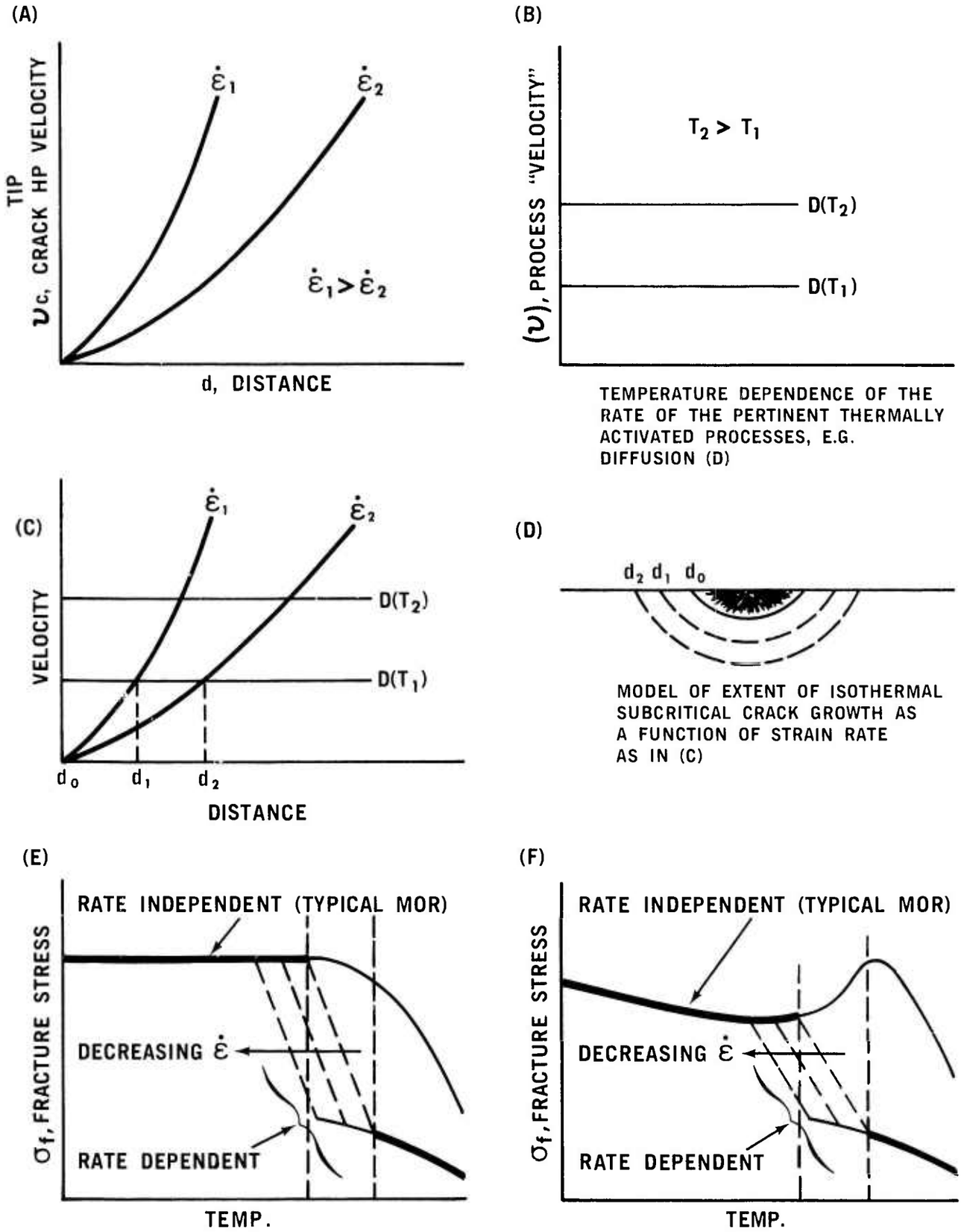

Figure 4.13 Rationale for the Influence of Temperature T, and Strain Rate, $\dot{\varepsilon}$, on the Mechanical Resistance to Fracture of Brittle Materials

by allowing fracture stress to remain the free variable. The extent of subcritical crack growth prior to catastrophic failure, as a function of loading rate, is shown fractographically in Figure 4.14 for tests at 1300°C, and in Figure 4.15 based on more limited data at 1350°C. The decreasing extent of subcritical crack growth at progressively higher loading rates is consistent with the higher measured fracture strength in these specimens. Comparison of these results at equivalent loading rates (i.e., Figure 4.14c and Figure 4.15a) provides a striking demonstration of the effect of even a modest increase in temperature. The other approach is to establish the fracture load and allow the time to failure to be the free variable (conventionally known as a stress rupture test) at a given temperature. Fractographic results of tests of this type performed at 1300°C are shown in Figure 4.16. Comparison of the extent of subcritical crack growth prior to catastrophic failure under load at 90% and 73% of the normal flexural test strength (i.e. MOR) is shown in Figures 4.16a and b.

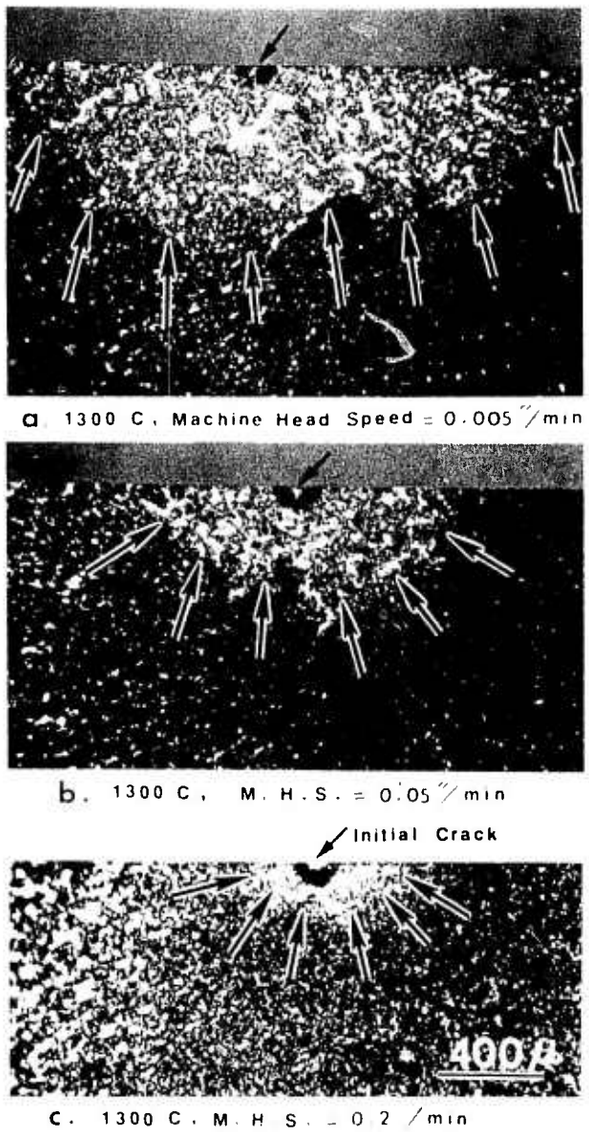

Figure 4.14 Loading Rate Dependence of Extent of Subcritical Crack Growth at 1300°C in Precracked Hot Pressed Silicon Nitride (Norton HS-130). Initial Flaw Size is Marked by Arrow

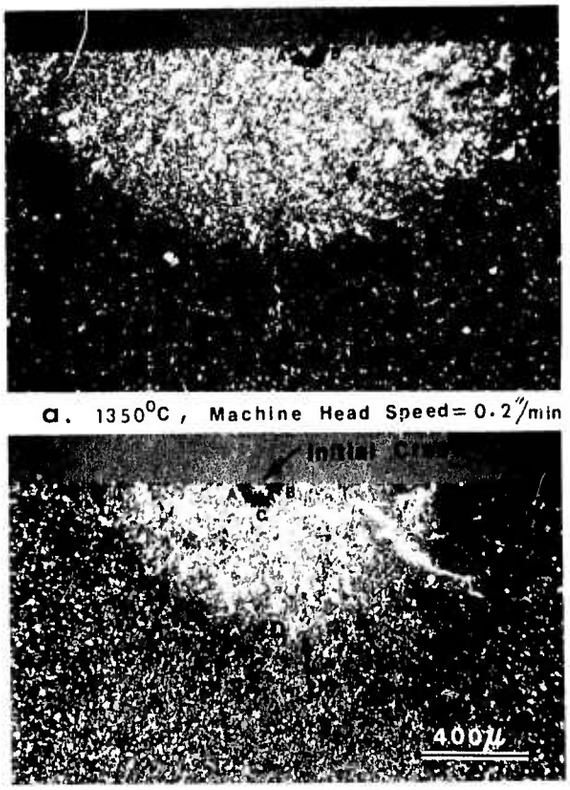

a. 1350°C, Machine Head Speed = 0.2″/min

b. 1350 C, M. H. S. = 0.5″/min

Figure 4.15 Loading Rate Dependence of Extent of Subcritical Crack Growth at 1350°C in Precracked Hot Pressed Silicon Nitride (Norton HS-130). Initial Flaw Size is Marked ACB and by Arrow

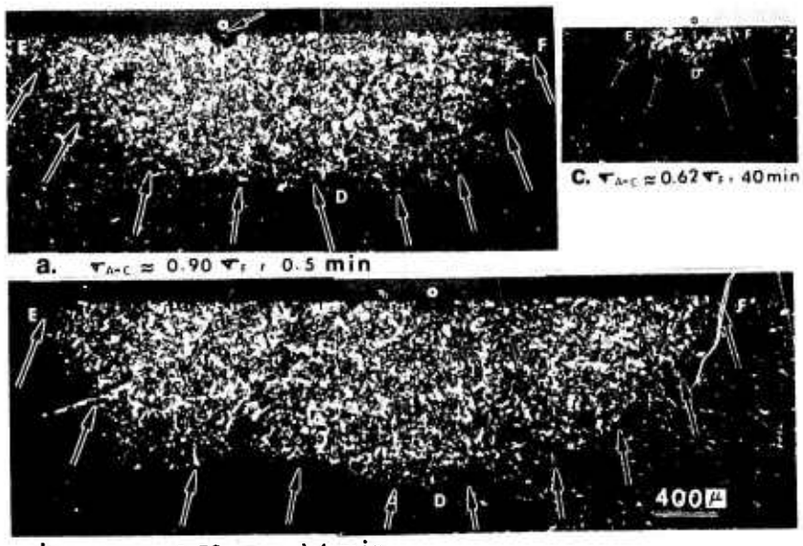

a. $\sigma_{A-C} \approx 0.90\ \sigma_f$, 0.5 min

c. $\sigma_{A-C} \approx 0.62\ \sigma_f$, 40 min

b. $\sigma_{A-C} \approx 0.73\ \sigma_f$, 1.4 min

Figure 4.16 Extent of Subcritical Crack Growth at 1300°C in Stress-Rupture Type Tests of Precracked Specimens. Initial Flaw is Marked ABC in (c). (a) and (b) Failed Under Load at the Indicated Fraction of the Fast Fracture Strength and in the Indicated Time. (c) Was Unloaded After 40 Minutes at the Indicated Load and Broken at Room Temperature

The time to failure (stress accommodation rate) is proportionally longer and the extent of subcritical crack growth is greater at the lower values of applied stress. At a load of 62% of the fast fracture strength (Figure 4.16c), the preplaced crack had only begun to enlarge after 40 minutes of applied load. In this case the sample was unloaded and then broken by a conventional flexural test procedure at room temperature to mark the extent of crack growth. Had the test been continued at 1300°C, the time to failure would have been much longer and the size of the crack much larger.

These results demonstrate on a fractographic and mechanistic basis the engineering significance of a systematic study of time dependent (strain rate sensitive) fracture behavior in brittle materials, particularly those that must withstand long periods under stress at high temperatures.

4.4 ELASTIC PROPERTY MEASUREMENTS

Room temperature elastic constants have been measured for a variety of silicon carbide and Sialon samples. Refer to Section 4.5 of this report for information on the Sialon materials. Results, obtained using pulsed MHz ultrasonic methods described earlier [2], are summarized in Table 4.4. Elastic modulii are believed accurate to within 4%.

For high density SiC, there is reasonable agreement among shear modulus values obtained by various investigators. This is not the case for Young's modulus where values reported for high density material range from 56.3 Mpsi [30] to 63.7 Mpsi [2]. Thus, the Young's modulus of SiC may be very impurity or structure sensitive.

TABLE 4.4

SUMMARY OF ELASTIC PROPERTIES OF SOME TURBINE CERAMIC MATERIALS

Material	Supplier	Processing	Density (gm/cm^3)	Young's Modulus (10^6 psi)	Shear Modulus (10^6 psi)	Poisson's Ratio
SiC	Norton	Hot pressed	3.28	58.3	28.5	0.025
SiC	UKAEA (Refel)	Reaction bonded	3.06	47.9	21.5	0.117
SiC	Ford	Reaction bonded	3.14	52.8	22.1	0.193
Sialon	Ford	Slip cast	2.89	26.9	10.8	0.241
Sialon	Ford	Slip cast	3.11	29.7	11.4	0.310

4.5 DEVELOPMENT OF SIALON MATERIALS

K. H. Jack [31] and a number of other workers have suggested that a high strength ceramic with properties similar to those of hot pressed silicon nitride might be prepared from an intimate mixture of silicon nitride and alumina by pressureless sintering. The obvious attraction of avoiding hot pressing has led to the investigation of this ceramic system in a number of laboratories. The new material, now generally called by the acronym Sialon, is believed to be a solution of Al_2O_3 in Si_3N_4, having the same structure as that of β Si_3N_4 with a somewhat larger unit cell; presumably the aluminum and oxygen atoms substitute for the silicon and nitrogen atoms, respectively. There is some uncertainty as to the solubility limit of Al_2O_3 in Si_3N_4 because one or more extraneous phases of unestablished composition are often formed along with the Sialon.

Although most of the studies of Sialon reported to date used samples prepared by hot pressing, the Sialon materials discussed herein were prepared by pressureless sintering. The chief characteristic sought in this study was high modulus of rupture in 4-point bending at room temperature. In addition, attention was given to phase composition (as indicated by x-ray diffraction patterns), microstructure, and, to some extent, density. Somewhat less importance was attached to the density than was the case in other Sialon investigations because it is difficult to know the theoretical density of a material of uncertain composition which often contains unknown phases. In addition, the sintered Sialon's which had reasonable strength also had densities nearly equal to those of a few hot pressed samples prepared in a preliminary study.

The material in this investigation were prepared from a mixture of 60% by weight of Si_3N_4 and 40% by weight Al_2O_3, nearly equimolar. The choice of the nearly equimolar mixture as a starting point resulted from the report by Oyama [32] that a broad minimum in thermal expansion occurred near this composition.

Experimental Procedure

Starting materials were standard AME Si_3N_4 powder which was ball milled in benzene to a 2-3 μm particle size, high purity AME Si_3N_4 powder, and Plessey high purity Si_3N_4 powder. Specimens were prepared by both cold pressing and slip casting. For cold pressing, starting materials were weighed, ball milled in benzene for mixing, and dried and pressed into bars at 20,000 psi. No binders were used. When high purity AME Si_3N_4 was used, the ball milling was continued for 7 days. For slip casting, the starting materials were weighed and then ball milled with an alginate suspension. The slip was de-aired and cast into plaster molds.

Sintering was done in a Tocco induction furnace. Specimens were placed in a BN crucible within a molybdenum susceptor contained in an alumina crucible. The space between the susceptor and the alumina crucible was packed with BN powder insulation. The entire assembly was dried at 400°F before sintering. After the assembly was placed in the induction furnace, the furnace was evacuated and then back filled with A or N_2 at one atmosphere pressure. A flow of 1 cubic foot per minute was maintained throughout the sintering run. The gas passed through a purification chain before entering the furnace. In general, the desired sintering temperature (1550°C to 1750°C) was attained in 1 to 1-1/2 hours and maintained automatically. The furnace was allowed to cool naturally after shutdown. Temperature was measured with a thermocouple inside the BN crucible.

PRECEDING PAGE BLANK-NOT FILMED

Room temperature modulus of rupture (MOR) was measured using a 4-point bend test. Specimens were 1/4 x 1/8 x 1 inch long with the surfaces ground to a 45 μm finish. Density was measured using standard ceramic immersion techniques. All x-ray diffraction patterns were obtained with a Norelco diffractometer using monchromatic CuK_α radiation. For microstructure studies, polished specimens were prepared by mounting and polishing with a 1 μm diamond paste. If desired, these samples were then etched with a hot solution containing 30 parts by volume HF, 25 H_2O_2 and 5 HNO_3. Fracture surfaces, and some etched polished sections, were examined with a scanning electron microscope.

Results

One group of test samples, sintered at 1750°C for 15 minutes in a nitrogen atmosphere, attained a reasonably high average MOR (35,000 psi). A material whose x-ray pattern indicated that it contained no extraneous phase, and which was extremely weak and poorly sintered, was obtained by sintering in argon at 1670°C for 3 hours. In general though, the materials contained extraneous phase and those fired in argon at 1750°C had average MORs around 20,000 psi or less, while those fired at lower temperatures were very weak. Figure 4.17a shows the x-ray pattern of a typical Sialon containing extraneous phase, and Figure 4.17b of the poorly sintered material containing no extraneous phase.

The use of high purity AME or Plessey silicon nitrides did not lead to improved materials and sintering at temperatures below 1700°C led to weak specimens.

When the fracture initiating flaw could be identified in the typical 20,000 psi materials, it was found to be a pore about 50 μm in diameter near the surface. Figure 4.18 shows such a pore in a fracture surface as seen with the scanning electron microscope.

Work is in progress to evaluate the effects of additives to the 60-40 compositions and others, and additional property data will be generated preparatory to application of the best composition for turbine engine components.

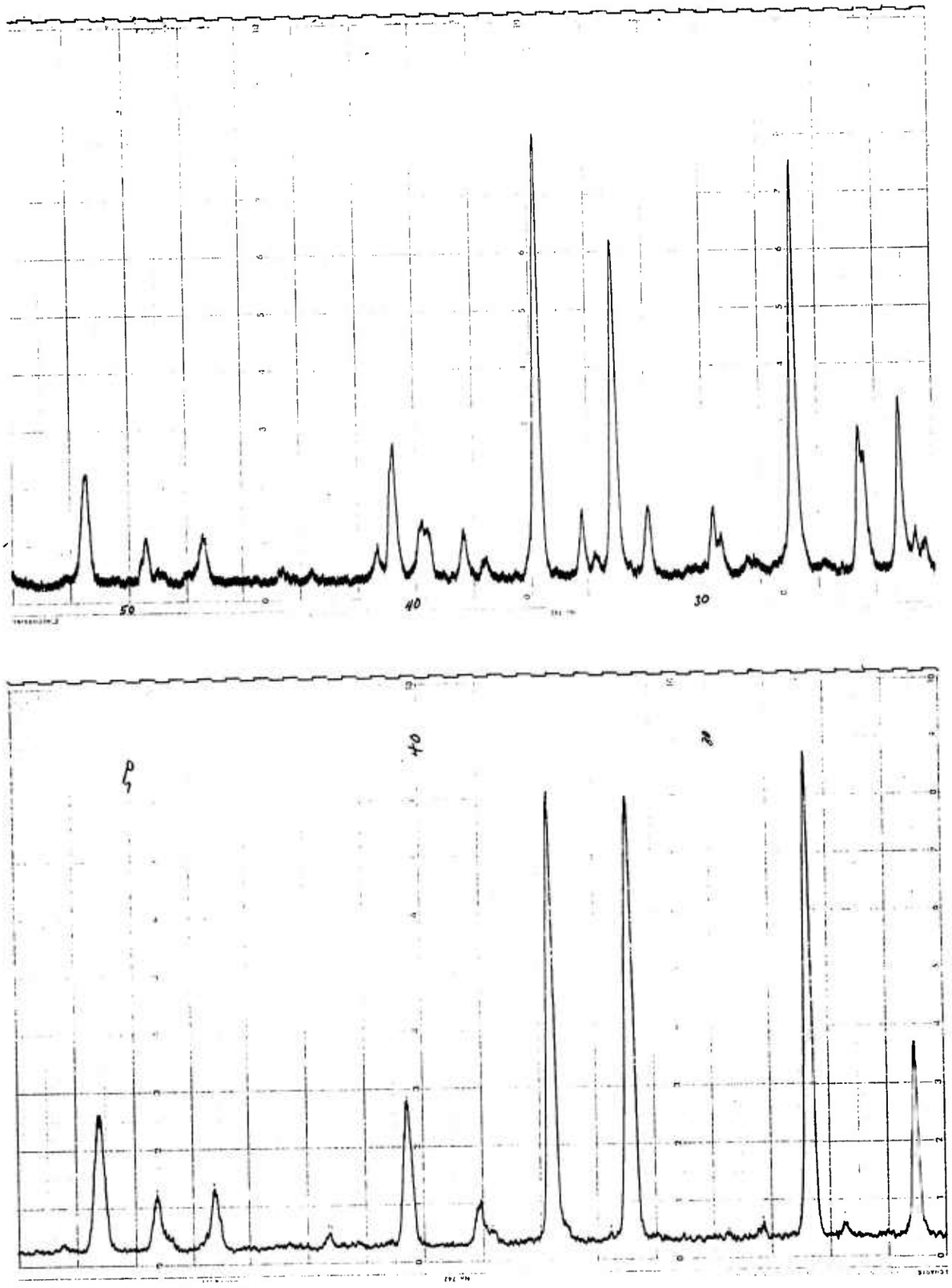

Figure 4.17 X-ray Diffraction Pattern, Taken With CuK_{α} Radiation, of (a) A Typical Sialon Containing Extraneous Phase, and (b) Of a Poorly Sintered Sialon Lacking Extraneous Phase

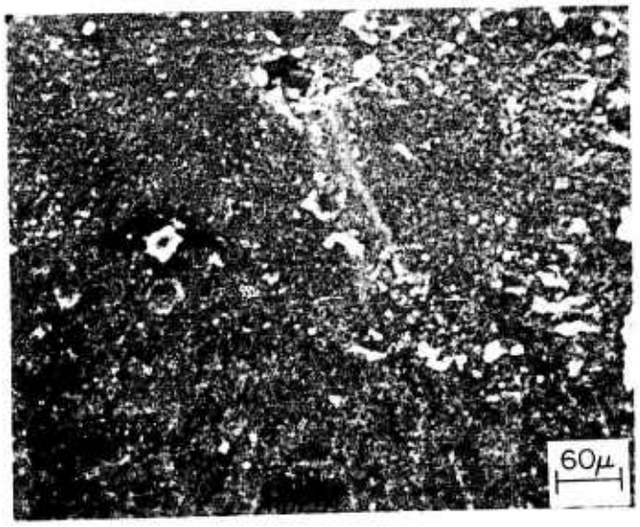

Figure 4.18 Scanning Electron Micrographs of a Fracture Initiating Flaw in a Sialon Specimen Prepared Without Additives by Sintering for 15 Minutes in Argon at 1750°C

4.6 ULTRASONIC NDE

Introduction

In addition to using ultrasonic techniques to detect subsurface flaws, silicon nitride sonic velocities were determined and correlated to density. This data was also used to calculate the modulus of elasticity and Poisson's ratio. Measuring material velocity provides a means of monitoring specific fabrication processes to assure that optimum material properties are obtained.

Silicon Nitride

The sonic velocities, in longitudinal and transverse directions, were measured in silicon nitride specimens representing various material densities. This data is shown in Figure 4.19. Commercially obtained transducers operating at rated 5 MHz frequencies and a Magnaflux PS-902 pulse ultrasonic unit were used in conjunction with an oscilloscope to accurately determine the transit time of ultrasonic waves propagating through the material. The sonic velocities were then calculated using the transit time and the measured material path.

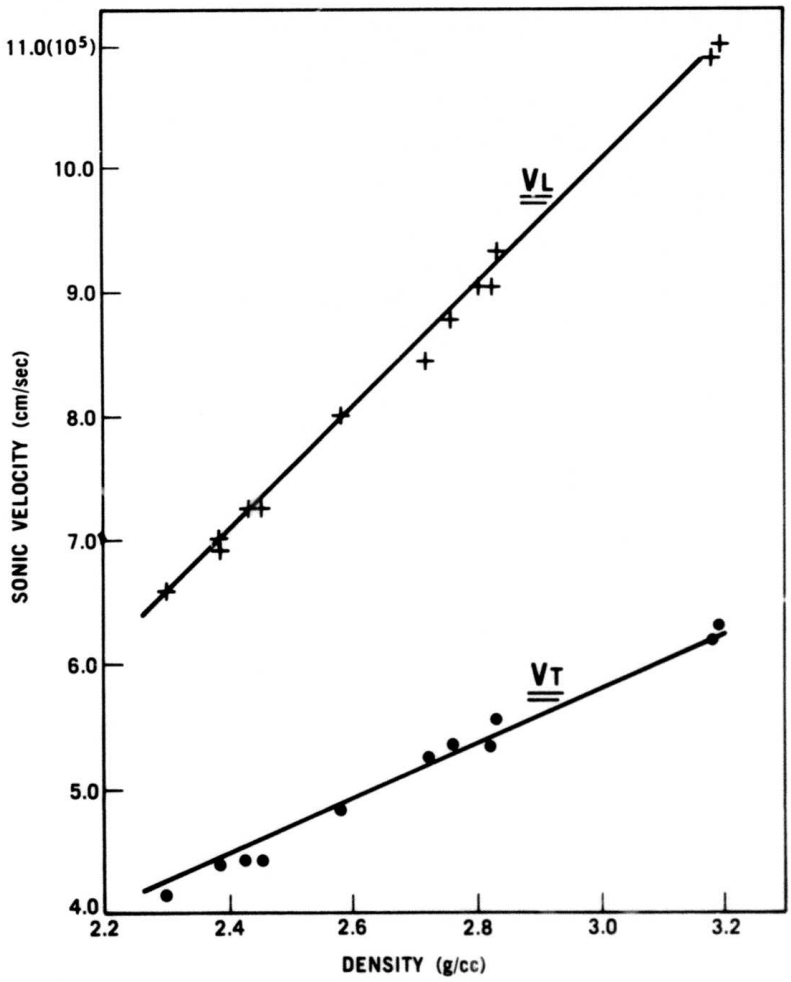

Figure 4.19 Longitudinal (V_L) and Transverse (V_T) Sonic Velocity vs Density of Silicon Nitride

The delayed sweep capability of the oscilloscope and an RF display of the ultrasonic signals results in accurate, consistent measurements of transit time. This measurement was obtained using multiples of the round-trip ultrasonic pulse and the same corresponding point on successive RF pulses, disregarding the initial ultrasonic pulse.

Acoustic impedance is defined as the product of longitudinal sonic velocity and material density. A linear relationship is shown to exist between acoustic impedance and modulus of elasticity in silicon nitride, as shown in Figure 4.20 This curve covers the range of density in silicon nitride obtained from processes such as injection molding, slip casting and hot pressing.

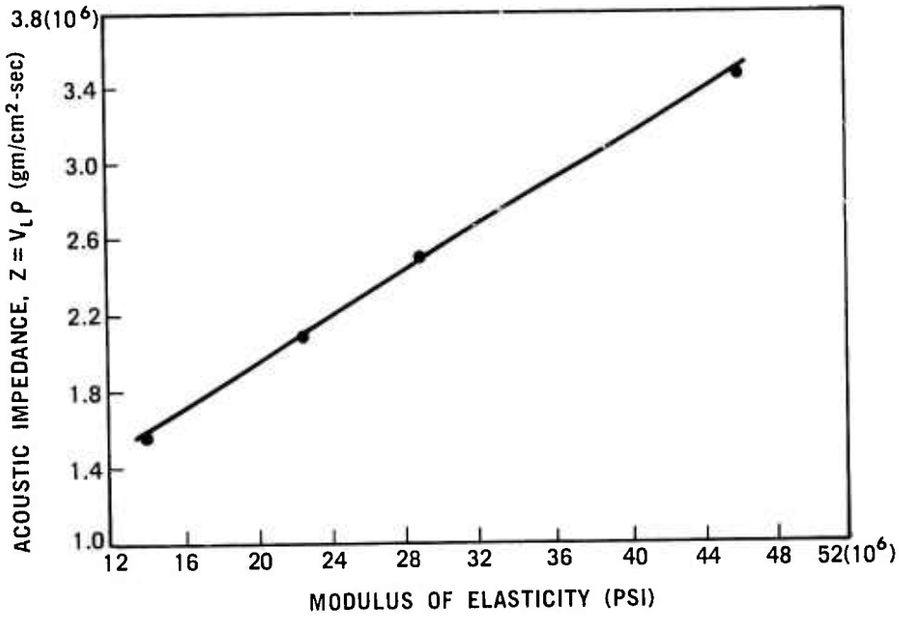

Figure 4.20 Acoustic Impedance vs Modulus of Elasticity of Silicon Nitride

4.7 X-RAY RADIOGRAPHY

Introduction

X-ray radiography is the primary NDE method used to determine the quality of as-molded turbine engine components. The usefulness of applying this NDE method to as-molded parts was previously established [6] and efforts were directed at upgrading the quality of all molded components. While optimization of molding parameters was the initial objective, this work provided insight into a material rheological problem which contributed to the low yield of flaw free components. Subsequent starting material changes and the establishment of optimum molding parameters have resulted in an improved yield of specific parts free from subsurface flaws detectable by radiographic methods.

Material and Process Optimization

Combining radiography with the molding parameter study of higher density reaction sintered silicon nitride materials for Design C second stage stator vanes provided a means of rapidly identifying the effect of the change upon component quality. A discussion of the development of higher density Si_3N_4 appears in Section 4.1 of this report. This study culminated in a high yield of parts free from molding flaws using a material having a nitrided density of 2.55 gm/cm^3. Figure 4.21 provides a comparison of the quality of Design C vanes as-molded before and after both material and process optimization. As shown, the 74D series vanes have numerous subsurface flaws running the length of the vanes between the inner shroud and the base. These x-ray indications are essentially segregated porosity, and are the result of the way the material flows in the vane tooling. The material enters the cavity at the lower left corner, fills a portion of the vane profile and the inner shroud, and then folds back into the vane cavity on the left side. The low density regions therefore outline the interface of the material as it flows back upon itself.

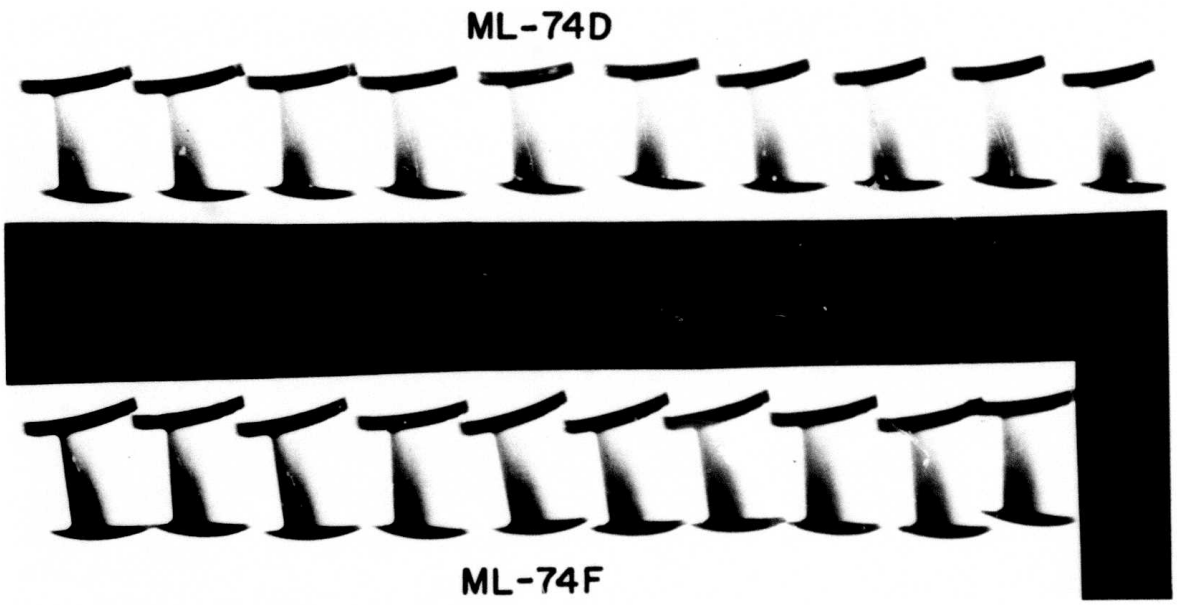

Figure 4.21 Radiographs of As-Molded Second Stage Stator Vanes, Showing Flaws in All 74D Vanes and Seven of Ten Flaw-Free 74F Vanes

The 74F series of vanes shows the effect of changes made to decrease the viscosity of the material. This results in a much improved yield (7 out of 10) of flaw free parts and, as shown, changes the flaw morphology from long stringer types to voids which are well rounded. Vanes having such defects would not, however, be used in a stator assembly. Further work is in progress to eliminate these remaining small voids.

First Stage Stators

Previous efforts to mold high density one-piece first stage stators, flaw free by x-ray, were unsuccessful. Flaws of varying severity were always detected in the outer shrouds of these components. Failures during engine testing have been correlated with subsurface flaws, detected by x-ray radiography, in the outer shroud. A discussion of this correlation appears in Section 3.2.3 of this report.

Using the molding data obtained during the second stage stator vane study, it was possible to injection mold first stage stators completely flaw free as measured by x-ray. Figure 4.22 is a radiograph of a first stage one-piece as-molded stator with no detectable molding flaws. This stator was made of higher density material, yielding Si_3N_4 of 2.55 gm/cm^3 density.

15

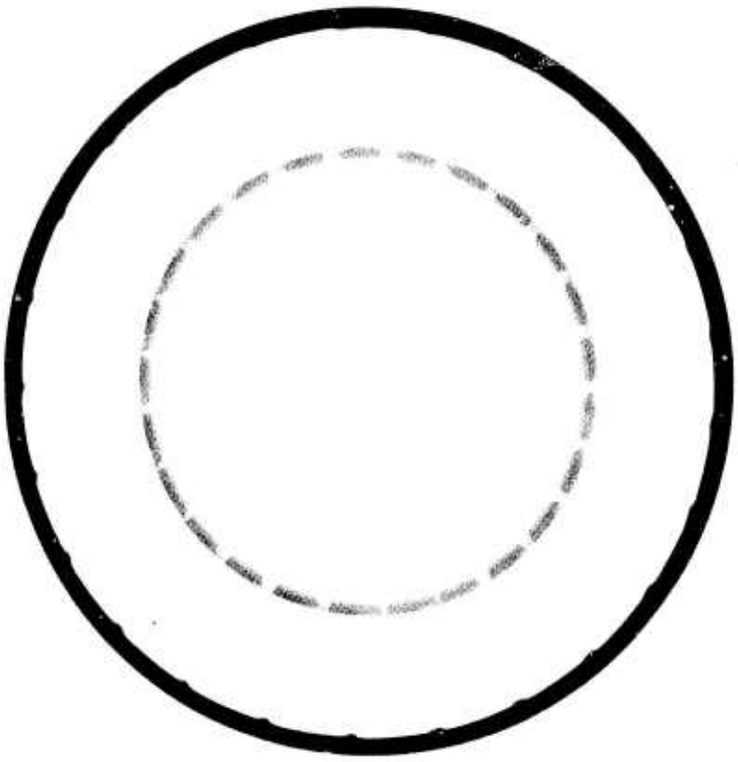

Figure 4.22 Radiograph of Outer Shroud of As-Molded First Stage Monolithic Stator Which is Free From Molding Flaws

5. INTRODUCTION AND SUMMARY-STATIONARY TURBINE PROJECT

The principal objective of the Stationary Gas Turbine Project is to demonstrate the use of uncooled ceramic first stage stator vanes operating at a peak inlet temperature of 2500°F in a 30 MW size test turbine. Successful completion of this program objective will demonstrate that ceramic materials are viable engineering materials that can be used in demanding high temperature structural applications. While working toward the turbine demonstration, very significant developments have been made in the areas of brittle material design technology, materials science and technology, materials fabrication, and component testing. The baseline technology developed on the ARPA Program thus becomes the keystone to further component and engine developments that will provide high performance gas turbines and, potentially, huge benefits to both the military and domestic sectors of the nation.

Gas turbine power generation is an existing, proven technology in this country, which today has the lowest capital cost per KW of installed capacity of any fossil fuel system. Currently the major use of these units is in electrical power generation to meet peaking power requirements. Available in sizes ranging from 19 to 70 megawatts, these units are applicable to DOD installations that require on-site power generation or the units may be mounted on barges to supply remote locations that have access to natural water ways. As a prime mover in ship propulsion, the heavy duty gas turbine is gaining considerable attention because of the potential for lower cost and improved ship performance and reliability.

Receiving renewed attention today, primarily as a result of the present "fuel" crisis, is the use of the combined cycle for electrical power generation. The combined cycle is a gas turbine-steam turbine system capable of using a wide variety of fuels including coal derivatives.

The major thrust of gas turbine technology will be the improvement of their overall efficiency in converting fuel to electrical energy. This efficiency is directly related to the maximum temperature at which gases can be allowed to enter the turbine. Current inlet temperatures are in the range of 1900° to 2000°F. When present day gas turbines are operated in conjunction with steam turbines via waste heat boilers in combined cycle operation, the present overall efficiency reaches 40-42% making the combined cycle plants competitive for intermediate load power generation. This can be raised significantly to 50% by improving the gas turbine system to allow operating temperatures of 2500°F. At this efficiency, the combined cycle installations are competitive for base load power generation. Herein lies the important role of ceramics because they provide the only direct materials approach to reaching 2500°F turbine inlet temperature where this high efficiency can be achieved. In addition, the excellent hot corrosion-erosion resistance of ceramics such as Si_3N_4 and SiC is expected to provide the required long-term reliability even when low grade dirty fuels are used.

5.1 STATIONARY TURBINE PROJECT PLAN

The Stationary Turbine Project is organized to design a turbine one stage at a time with ceramic components. Figure 5.1 shows a longitudinal section of the Westinghouse 30 MW turbine. In this simple cycle machine, air is induced through a large intake silencer and filtered into an 18-stage axial compressor before entering the combustor housing. The combustor housing supplies air at 650°F to combustion cans assembled in a circumferential array. Air is mixed with fuel and ignited in the primary combustion zone. The gas passes downstream through the combustor section, mixing with secondary air. Flow continues from the combustion section, through the transition zone, and enters the power turbine at the gas temperature. The hot gases expand through the three-stage turbine section and are either exhausted through a stack or ducted into a reheat boiler as part of a combined cycle power generating unit.

The first stage stator vane (see Fig. 5.1) is receiving the greatest attention on the ARPA program since it represents the hottest material application, the location where combustion products first impinge. Solving the design problems with this inlet stator vane also develops the needed analytical tools and opens the door to the design of other ceramic parts for turbines.

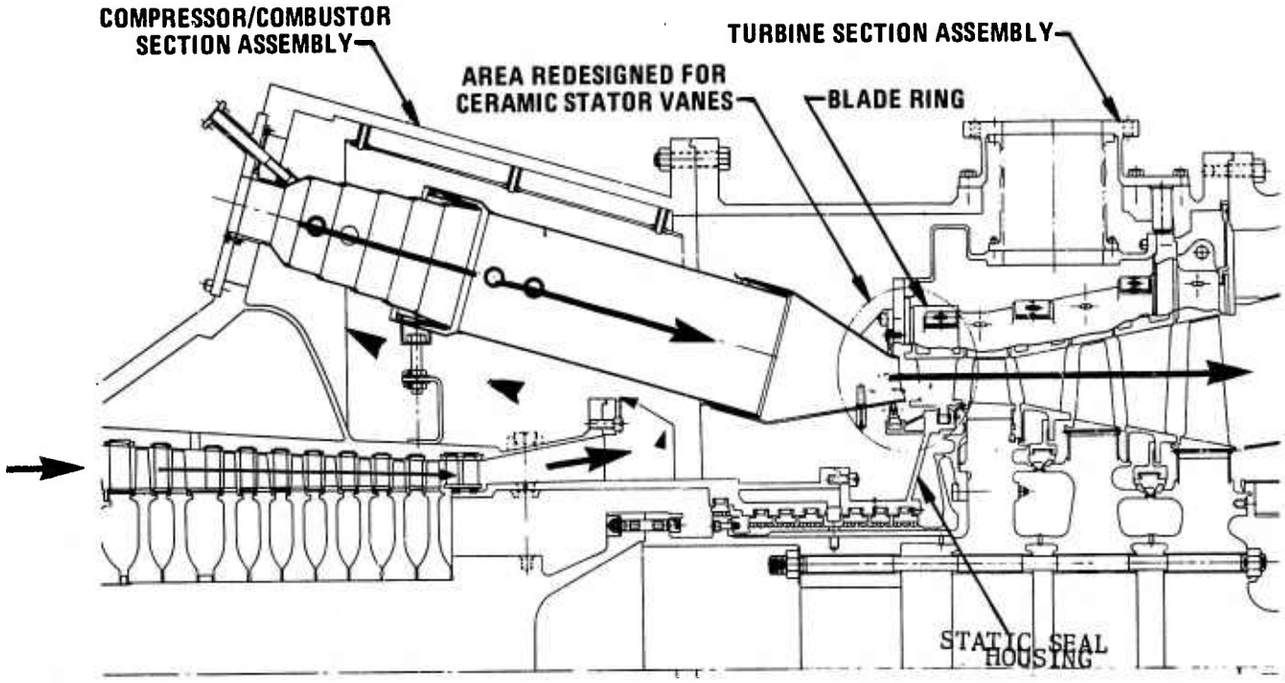

Figure 5.1 30 MW Test Turbine Flow Path

PRECEDING PAGE BLANK-NOT FILMED

Currently, the ceramic turbine concepts are developed and designed for a 30 MW frame size machine. Once feasibility and a performance base is achieved the utilization on larger production machinery becomes a matter of adaptation and scale up. This practice is especially important because material selection and optimum design depend upon several interrelated areas of knowledge such as physical properties, mass flow characteristics, heat transfer rates under steady state as well as transient condition to say nothing about the complex development of mechanical and thermal stress patterns in all components. To do the fundamental work on more than one basic unit would be far too costly and time consuming.

5.2 PROGRESS AND STATUS SUMMARY-STATIONARY TURBINE PROJECT

To meet the program objective, the work has been divided into two major task areas subdivided as follows:

1. Component Development
   (a) Design
   (b) Fabrication
   (c) Testing
2. Material Technology
   (a) Material Engineering Data
   (b) Material Science
   (c) Non-Destructive Evaluation

The present status is summarized according to Task in Sections 5.2.1 and 5.2.2.

5.2.1 COMPONENT DEVELOPMENT

Component Development is concerned with the design and analysis of the first stage stator vane, fabrication of the first stage stator vane design iterations, and the testing of first stage stator vanes in the static rig and advance test turbine. Turbine modification and the design of ceramic rotor blades are also considered here.

Design

A novel, power-generation, size ceramic stator vane has evolved from a unique sandwich type multiple component concept. The concept utilizes a three-piece vane that is insulated, cushioned, and supported in such a manner as to minimize critical steady state and thermal stresses which would otherwise preclude the use of brittle materials in an industrial turbine.

The foremost problem in designing and using brittle materials for engineering applications is to avoid areas of stress concentration. To do this, the stresses in critical volume elements of a component must be known. Two-dimensional finite elements for stress analysis (such as triangles) are adequate for analyzing most of the stresses in the three-piece stator vane. Interfacial contact stresses and stresses developed in rotor blades, however, cannot be represented in two dimensions, and, therefore, require a more sophisticated three-dimensional finite element program for resolution. The ARPA program has helped produce this valuable tool.

Status

- A novel 3-piece, uncooled, simply-supported, ceramic stator vane assembly was selected and designed.[1,2,3,4]

- To minimize stresses, the cross-sectional size of the ceramic vane selected is only half that of the metal vane counterpart.[2]

- Critical stresses of the 3-piece ceramic vane assembly have been evaluated for both transient and steady state conditions expected during turbine operation at 2500°F.[2,3,4,5]

- A full scale kinematic model was built to show that the stator vane assembly was functional when subjected to differential motions well in excess of design limits.[3]

- Detailed design of stator vane assembly, including the compressive spring loading system and the ceramic/metal insulation system was completed.[2,3]

- 3-D finite element code (WISEC) has been completed except for creep and contact stress analysis.[2,3,4,5,6]

- Preliminary analysis of ceramic rotor blade using 3-D finite element code has been completed.[4,5,6]

- Design emphasis and stress analysis is currently focused on stator vane assembly for test turbine demonstration.

Fabrication

Fabrication is perhaps the most important phase in the successful application of ceramics to gas turbines. Only fully dense, high-strength Si_3N_4 and SiC were selected for industrial gas turbine components. Currently, these materials are made commercially by a process of hot-pressing, whereby powder is consolidated by the simultaneous application of pressure and temperature. The ARPA program has provided the first full-scale power generation size ceramic vanes fabricated from hot-pressed Si_3N_4 and SiC. These were made to Westinghouse specifications by the Norton Company of Worcester, Massachusetts and their suppliers, by hot-pressing billets and then using diamond grinding tools and tracer milling machines to produce the stator vane geometry. This particular fabrication route has been followed in the ARPA program in order to assure the availability of components for testing.

Status

- Over 40 prototype vane sets for testing have been successfully fabricated by hot-pressing and machining.[3,4,5,6]

- 100 vane sets are on order for completion of 2500°F static rig tests and for the test turbine demonstration.

- The 100 vane sets on order differ from prototype designs in that airfoils will be tapered and twisted and end cap cavities are shallower for improved aerodynamic performance.[6]

Testing

A very important step in the ARPA program to develop ceramic vanes is to check the design and materials by testing full scale parts under realistic conditions. The plan is to test in a highly instrumented static rig first at 2200°F and then 2500°F under conditions that nearly duplicate real gas turbine conditions. This will be followed by full scale turbine testing in a Westinghouse 30 MW frame size test turbine modified for this purpose.

Status

- Design and construction of the instrumented static rig was completed after considerable delays due to procurement and start-up problems.[3,4]

- 2200°F static rig testing was successfully completed using Si_3N_4 vane assemblies (Fig. 5.2).[5]

- 2500°F static rig testing was initiated and then terminated temporarily due to rig damage caused by a combustor failure and failure of ceramic ducting.

- Initial 2500°F tests have demonstrated that Si_3N_4 ceramics are tougher than SiC as evidenced by

  - Ability of Si_3N_4 to withstand impact of flying metal from imploded combustor basket.

- Ability of Si_3N_4 to withstand extreme thermal shock from 3000°F to 600°F almost instantaneously.
- Complete failure of SiC vanes under the same conditions experienced by Si_3N_4.

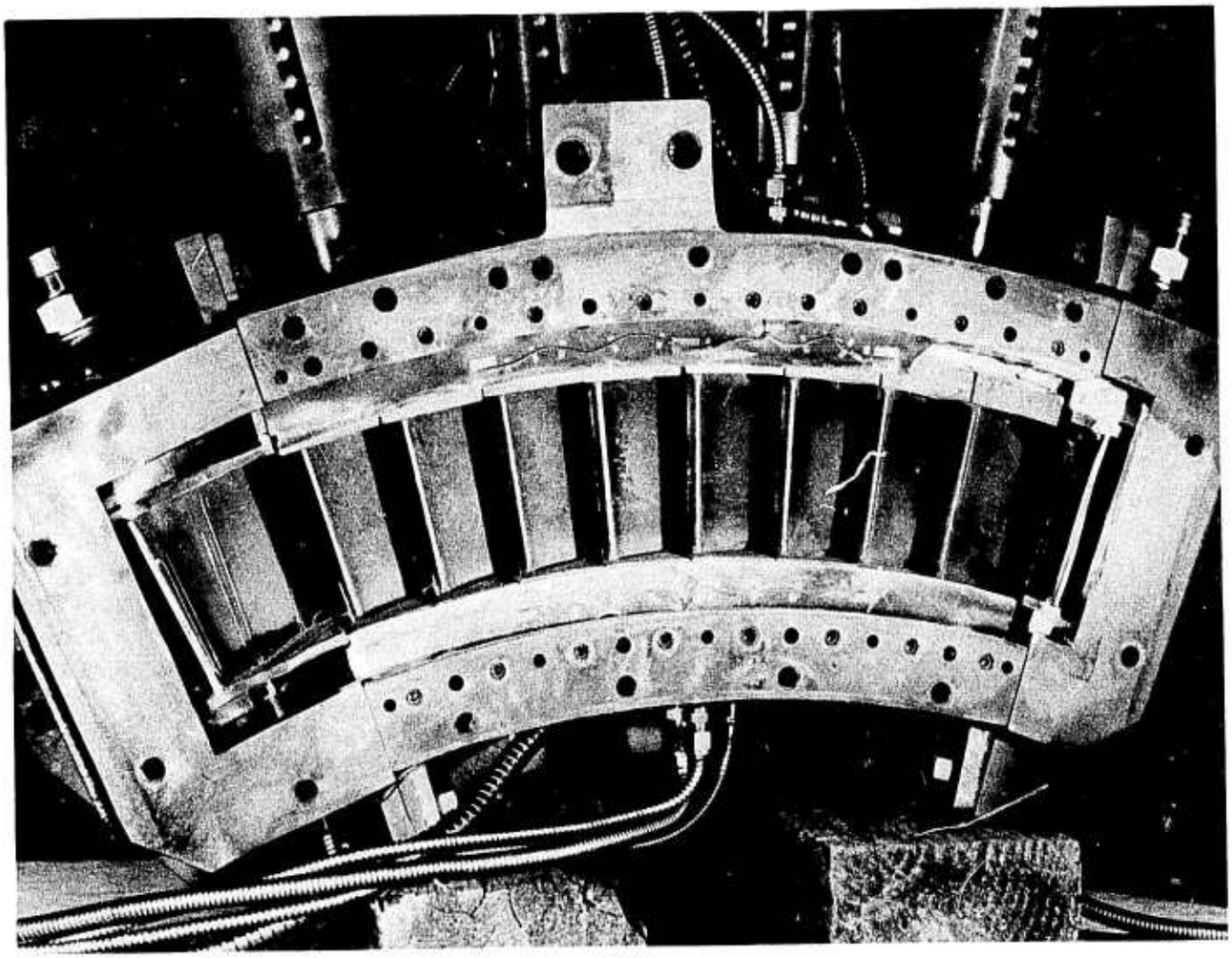

Figure 5.2 Si_3N_4 Stator Vane Assembles After Static Rig Testing At 2200°F (100 Cycles)

- The static rig has been re-modified for 2500°F operation using water-cooled metal ducting and a highly cooled metal combustor.

- 2500°F static rig testing is rescheduled for completion by July, 1975; vane delivery from Norton for these tests are scheduled for May, 1975.

- Design and layout drawings for the test turbine modifications have been prepared. Further design and procurement activity for the advanced test turbine has been deferred until completion of the 2500°F static rig tests.

5.2.2 MATERIALS TECHNOLOGY

Materials technology has been the basic building block for design technology, fabrication technology and testing. The sub-tasks consist of Materials Engineering Data, Materials Science, and Non-Destructive Evaluation of Materials. The plan has been to continue this phase throughout the program in order to properly evaluate material improvements and design changes that are natural evolutions in a focused engineering program.

Material Engineering Data

Design technology is highly dependent upon the thermal, physical and mechanical properties of the materials being used. A substantial effort has been expended to collect engineering property data for commercial hot-pressed Si_3N_4 and SiC to make the design code more comprehensive. The interaction between properties and design is shown in Fig. 5.3. Since the present design code uses an elastic-to-fracture criterion for stator vane ceramics and since the transient stresses are much larger than steady state stresses, reliable thermal properties have been extensively measured. Both established and new testing procedures have been utilized to evaluate the physical and mechanical properties of gas turbine ceramics at temperatures up to 2500°F.

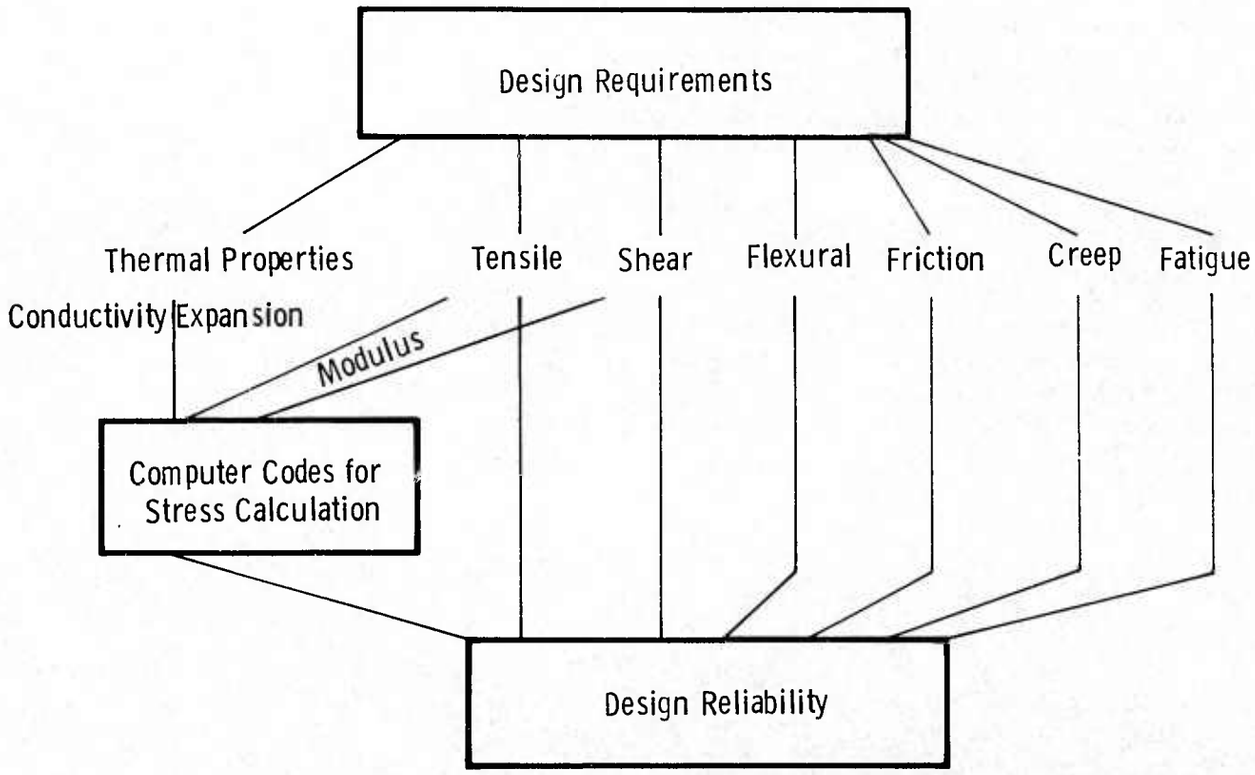

Figure 5.3 Interaction Between Properties And Design

Status

- Thermal properties have been characterized from RT to 2500°F for hot-pressed Si_3N_4 (Norton HS-130) and hot-pressed SiC (Norton NC-203).[3,4]

- Flexural strength, tensile strength, shear strength, friction behavior, high cycle fatigue and elastic properties have been characterized from RT to 2500°F for both HS-130 Si_3N_4 and NC-203 SiC.[2,3,4,5,6]

- Creep, stress rupture, low cycle fatigue, and corrosion-erosion behavior are continuing to be evaluated because these relate to reliability and require longer term evaluation. Data will continue to be available to 2500°F.[3,4,5,6]

- Fracture mechanics studies as related to high temperature behavior has been initiated in order to assess component reliability and assign a practical fracture criterion for engineering use.

- Statistical treatment of engineering properties continues to be conducted as data become available.[2,3,4]

Materials Science

The purpose of detailed investigations into materials science is to develop an understanding of material behavior which will lead to improvements. This is of particular importance since the ceramic materials being utilized in turbine engines are relatively new and appear capable of considerable improvement. The material science subjects isolated for detailed investigation have been defined by the engineering requirements of the system and thereby relate mainly to the commercial materials being used. They contribute to better control of the fabrication process and better properties, and tend to extent the useful life of the ceramic materials through property improvements.

The value of the material science work has already been demonstrated by the property improvements that have been made since the onset of the ARPA program. By discovering that certain impurities and foreign inclusions were detrimental to the strength of hot-pressed Si_3N_4 above 1800°F and learning how to process starting powders to achieve a desired microstructure, strength at 2550°F has improved by 400%.

Status

- Identification of microstructural details of commercial hot-pressed Si_3N_4 (Norton HS-110 and 130) and hot-pressed SiC (Norton NC-203) completed.[1,2,3,4]

- Correlations between properties, microstructure, and fabrication processing for HS-130 Si_3N_4 and NC-203 SiC completed.[3,4,5,6]

- Statistical chemical analysis of Norton HS-130 Si_3N_4 and NC-203 SiC completed.[6]

- Analysis of thermodynamic data for Si_3N_4 and SiC completed.[1,2]

- Static oxidation kinetics of HS-130 Si_3N_4 and NC-203 SiC completed.[3,4,5]

- Simultaneous oxidation-sulfidation kinetic studies in progress.[6]

Non-Destructive Evaluation

Microstructural uniformity is the key to reliable structural ceramics for gas turbine engine applications. The objectives of NDE are to identify and classify microstructural defects and relate these to the component fabrication process. The ultimate goal is to define meaningful inspection methods that can be used to accept/reject components prior to installation in the engine. Procedures utilizing ultrasonics, X-ray radiography, dye penetrants, and acoustic emission are currently being applied to ceramic systems for evaluation purposes.

Status

- Suitability of dye penetrants for detecting surface connected porosity and surface cracks has been established for ceramic gas turbine components.[5]

- Sensitivity of commercial techniques in ultrasonic A&C scanning to low density inclusions and segregated voids in hot-pressed Si_3N_4 and SiC has been established.[5,6]

- Detection limits and sensitivity by ultrasonic inspection has been established for hot-pressed ceramic turbine components.[5,6]

- Feasibility of applying acoustic emission to proof testing of ceramic components has been established.[4]

- Detection limits and sensitivity by X-ray radiographic inspection has been established for hot-pressed ceramic turbine components.[5,6]

- NDE of ceramic turbine components is continuing.

5.3 FUTURE PLANS

In November 1974, ARPA announced its intention to extend the ceramic turbine program beyond the originally planned 1976 completion date in order to compensate for very tight timing schedules on key tests, and for reduced technical effort in FY 74 and 75 resulting from funding reductions. The future plans for the Stationary Turbine Project are briefly discussed.

Component Development

Component development will continue but much of the emphasis will shift to advance turbine design and modification since the actual turbine test of ceramic stator vanes represents the climax of the six year program as now planned.

Design

The design task on stator vane development will focus on stress analysis of the vanes and vane assembly to be used in the test turbine demonstration. Coolant flow analysis will also be conducted on the vane-metal support structure. This work will continue through FY 76.

Fabrication

Vane fabrication will continue through FY 76 so that stator vanes will be available in sufficient quantities for the test turbine demonstration. These vanes will be made from Norton NC-132 silicon nitride and possibly silicon nitride hot-pressed with yttria providing the latter material proves superior in screening tests.

Testing

The greatest effort throughout the remainder of the program will be in the testing phase of full-scale components. Present status indicates that the static rig testing of silicon nitride stator vane assemblies should be complete by July 1975. Following this, emphasis will be placed upon completing all the tasks leading up to the test turbine demonstration which is scheduled for completion at the end of the ARPA program. These tasks include installation and check-out of the test turbine, completion of design modifications, procurement of turbine parts and instrumentation, completion of the turbine rebuild, check-out of the turbine with ceramic parts and advanced metal blading, and finally the test turbine demonstration consisting of 100 cycles of operation to 2500°F.

Material Technology

The Material Engineering Data and Materials Science tasks of the project will continue as a support function throughout the project. Efforts will be limited, however, to those specific areas required for the test turbine demonstration. The properties of remnant materials from stator vanes, insulators, etc., will be verified to insure that the test hardware meet specified standards. Improved commercial vane materials, in particular, Y_2O_3-doped Si_3N_4, will be characterized as will selected insulator materials in order to guarantee the highest component performance, durability, and reliability when used in the test turbine. Post-test evaluation of components and non-destructive evaluation of components before and after testing will continue.

6. PROGRESS ON CERAMIC COMPONENT DEVELOPMENT - STATIONARY TURBINE PROJECT

6.1 STATOR VANE DEVELOPMENT

SUMMARY

Design efforts have continued through the first half of this reporting period with the major effort directed toward design modifications of the rotating test turbine. This is the 30 MW-frame size turbine planned for demonstrating 100 duty cycles using uncooled ceramic nozzle guide vanes at a peak temperature of 2500°F. Layout and detailed design drawings have been prepared for 23 different parts, sub-assemblies and assemblies. Further design modification work and procurement of parts has been deferred until the completion of the 2500°F static rig test.

The stator vane design currently planned for the test turbine demonstration at the present time is a modification of the first generation design; i.e., a tapered and twisted airfoil with tenons representing a torroidal shape superimposed upon the airfoil cross-sectional geometry. This design is referred to as "advanced turbine stator vane design".

The second generation vane design will not be tested in the advanced turbine. Further stress analysis suggests that maximum principal stresses exceed the strength capabilities of candidate ceramics and program limitations do not permit confirmation of this design via static rig testing.

The latest results of 2 and 3-dimensional finite element stress analyses are reported for the stator vane assembly designs being investigated. Two conditions of shutdown from 2500°F are discussed. In addition, a contact stress analysis is presented that deals with differential displacements at the airfoil-end cap interface, a problem that is common to all versions of the three-piece stator vane design concept.

The previously reported damage[6] to the static rig, which occurred in the ceramic duct and mixer section during the initial calibration and shakedown test at 2300°F, was repaired to permit 2500°F operation. Testing was initiated in September using an eight-vane assembly that consisted of four hot-pressed silicon nitride and four hot-pressed silicon carbide vanes. During the third cycle of testing, at least two of the silicon carbide vanes appeared cracked, but remained functional. These tests were terminated during the fifth cycle when the combustor basket imploded throwing metal debris into the vanes and causing a temperature excursion to 3000°F and rapid quench to 600°F under choked flow conditions. Even after this dramatic test of endurance, the silicon nitride vanes remained functional. The silicon carbide vanes, however, were totally shattered, and the combustor, ceramic duct and ceramic mixer section of the rig were damaged beyond repair. The static rig has been rebuilt with a redesigned combustor, a water-cooled metal duct and a spray-cooled mixer section. All instrumentation has been repaired or replaced to permit heat transfer tests while awaiting delivery of vanes for 2500°F testing from Norton. 2500°F testing is scheduled to resume in June using silicon nitride stator vane assemblies of the "advanced turbine" design.

PRECEDING PAGE BLANK-NOT FILMED

Westinghouse has approved the machining process and airfoil qualification procedures for the fabrication of 100 stator vane assemblies for the test turbine demonstration. A similar review and approval of airfoil tenon and end cap machining practice has been scheduled for February. Norton has agreed to deliver 10 silicon nitride stator vane assemblies for the 2500°F static rig testing by May, 1975. Yttria-doped silicon nitride billets were ordered for initial evaluation. Stator vane assemblies may be fabricated from the best yttria compositions as part of the 100 vane order providing that the material is properly qualified.

6.1.1 DESIGN

Introduction

The large size of the Westinghouse stationary power turbine permits a ceramic stator vane design which is particularly well suited to brittle materials. A three-piece vane assembly has been selected to minimize stress and simplify fabrication. This replaces the more conventional geometry in which the airfoil is integral with the shrouds. The use of silicon nitride or silicon carbide stator vanes is intended to increase the service temperature of the resultant machine from 1955°F, average turbine inlet temperature at reserve power to a peak of 2500°F without a need to cool the first stage stator row.

Design activity has continued through the first half of this report period with the major effort directed toward design modifications of the rotating turbine. Layout and detailed drawings have been prepared for parts, sub-assemblies, and assemblies. Further design modification work and procurement of parts for the advanced test turbine have been deferreduntil the completion of the 2500°F static rig tests.

The Rotating Test Turbine

Layout drawings and design specifications have been prepared for the modification of the W251 test turbine rotating rig. An average turbine inlet temperature of 2300°F was selected for the design to meet the 2500°F peak temperature requirement on the first stage stator vanes. Since only the first stage vanes will be made from ceramic materials, considerable attention has been given to the cooling of metal components downstream and the cooling air supply.

Completed drawings are identified in accordance with associated assemblies and sub-assemblies in the turbine longitudinal of Fig. 6.1. The turbine cylinder or blade ring, which is represented normally as horizontally joined half cylinders enclosing all three stages of the power turbine, has been split and flanged to form upstream and downstream segments. Silicon nitride and/or silicon carbide stator vanes and support structures, including insulator blocks and spring loaded metal shoes, are contained within inner and outer support rings, which are bolted to the static seal housing and the upstream portion of the segmented turbine cylinder, respectively. The first stage rotor and all subsequent downstream stages remain within the downstream segment of the blade ring, remembering that the test rig differs from an actual power generating turbine in that the entire third stage is removed. Work in excess of that required to drive the compressor is expended against an eddy current brake and there is no generator coupled to the shaft of the test turbine.

The ceramic vane assemblies, insulators, seals, and support structure which constitute the first stage stator vane row of the turbine test rig will be the same design as those used for static rig tests.[2] A full compliment of 80 vanes will be tested in the turbine, however, rather than the cascade of 8 vanes which comprises the test configuration in the static rig.[4] Results of static rig testing at 2500°F to date and a stress analysis of the second generation design tentatively preclude the testing of silicon carbides or the second generation design, respectively, from full turbine testing. Silicon nitride vanes

of advanced turbine design[5,6] will be tested exclusively. The array may include some vane assemblies hot-pressed with yttria if an evaluation of properties so indicates.

The test turbine was removed from its foundation and moved to a storage location pending the rebuilding phase that will start in FY 76. Present plans call for the installation of the turbine in the new developmental laboratory and a check out of all auxiliaries, starting equipment, and control functions before the cover is opened for rebuilding. By doing this, only essential parts of the turbine, rather than the entire machine, need be transported to a plant facility for modification.

Continuation of the advanced turbine design task has been deferred until July, 1975.

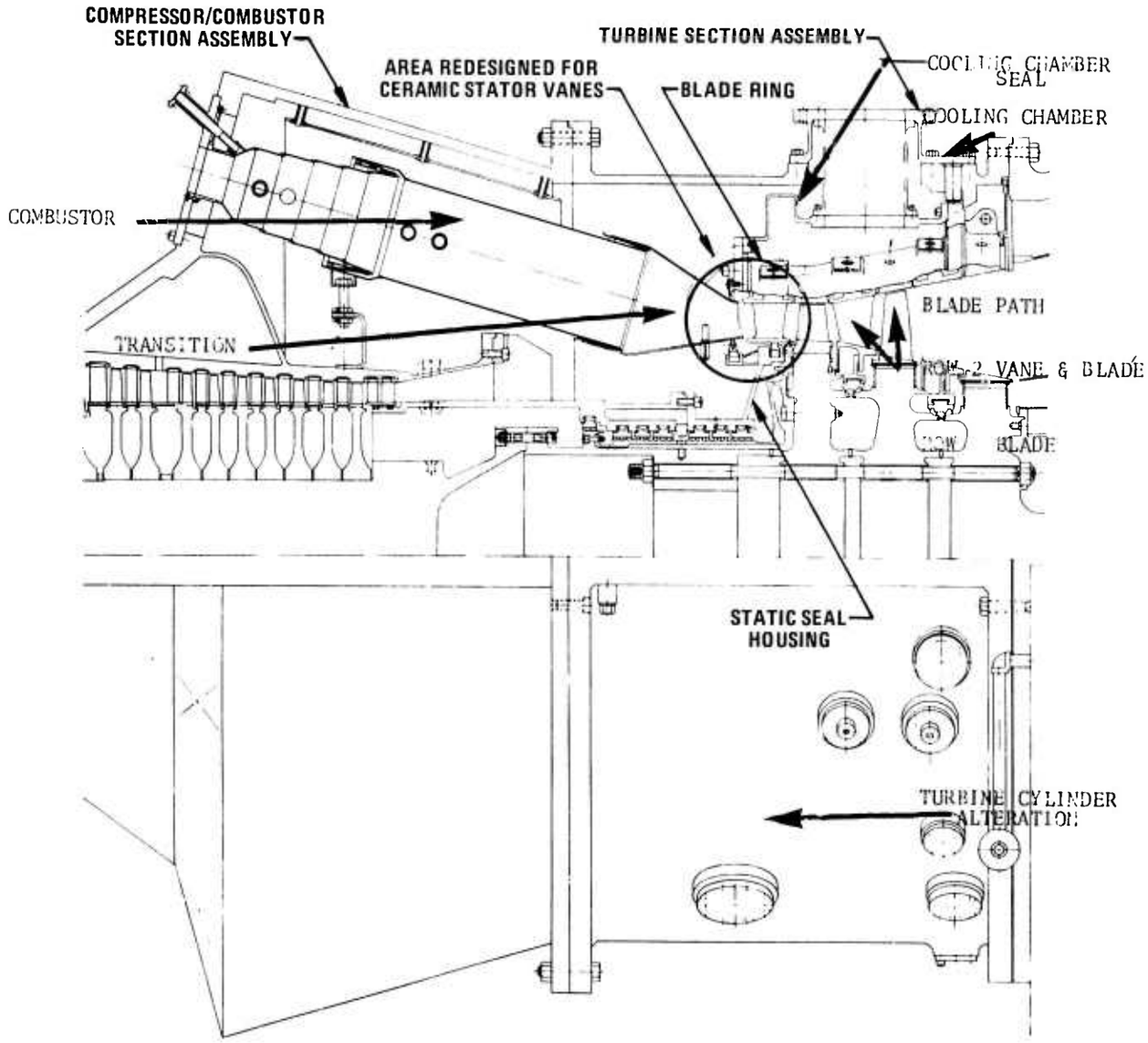

Figure 6.1 W-251 Rotating Rig Test Turbine With Modifications Indicated

6.1.2 THE STRESS ANALYSIS OF SILICON NITRIDE VANES

Introduction

The three dimensional stress analysis of the second-generation design stator vane assemblies was repeated to include the asymmetric condition of the tapered-twisted airfoil and the interaction of the end cap. Only the outer end cap was considered because principal stress maxima occurred there rather than in the inner end cap where the overall stress distribution should be proportionate but lower. The case of interference to cause high contact stresses along the mating surfaces of the end cap and airfoil was also developed for the second generation stator vane at a steady state temperature of 2500°F. Since the end cap geometry of the first, second, and advanced turbine design are similar, the analytical results presented here may be applied to all three end cap designs.

Analytical Results for Two Conditions of Shutdown from 2500°F

The qualifying assumptions are similar to those stated previously in that the silicon nitride is considered to be homogeneous, isotropic, and elastic at all temperatures and rates. The contact force between the airfoil tenon and the end cap and the gas load are considered negligible. The steady state condition is that of the static rig at 2500°F with gas temperature profiles extrapolated from data at 1800°F and 2300°F (see Fig. 6.29 under 2500°F Static Rig Testing). Transient thermal analyses were performed for two shutdown conditions, i.e., (1) flame out (∿ 350°F/sec), and (2) controlled at 25°F/sec.

The initial and boundary conditions for the end cap thermal analysis are superimposed upon the actual end cap geometry in Fig. 6.2. Heat transfer data for the airfoil and outer end cap are presented in Fig. 6.3. The three dimensional element models for the second generation design airfoil and an end cap that is common to all designs appear as Figs. 6.4 and 6.5, respectively.

Temperature and stress contours for the airfoil at midplane, section 3 (Fig. 6.4) and section 62 (Fig. 6.4) are shown in Figs. 6.6, 6.7 and 6.8, respectively. Under flame out conditions from 2500°F, the maximum principal stress at midplane reaches 72,300 psi at the 10th second. A stress concentration and a high stress gradient are apparent near the upper and lower tenon of Fig. 6.7. This results from the arbitrary use of a lower value for the heat transfer coefficient over the airfoil contact surface. The maximum principal stress in the airfoil occurs on the pressure side near the trailing edge. If the value of h is not reduced at the contact surface, but rather is considered to be exposed as part of the entire airfoil surface, the maximum principal is reduced approximately 5% from 127,300 psi (Fig. 6.8b) to 120,100 psi (Fig. 6.8c). Changes in the heat transfer coefficient at the contact surface has the effect of changing both the location of the maximum stress and the stress distribution. If the cool down rate is reduced to 25°F/sec, the maximum principal stress, occurring after 50 seconds, diminishes to 71,800 psi when Fig. 6.9 is compared with Fig. 6.8c using similar distributions for h.

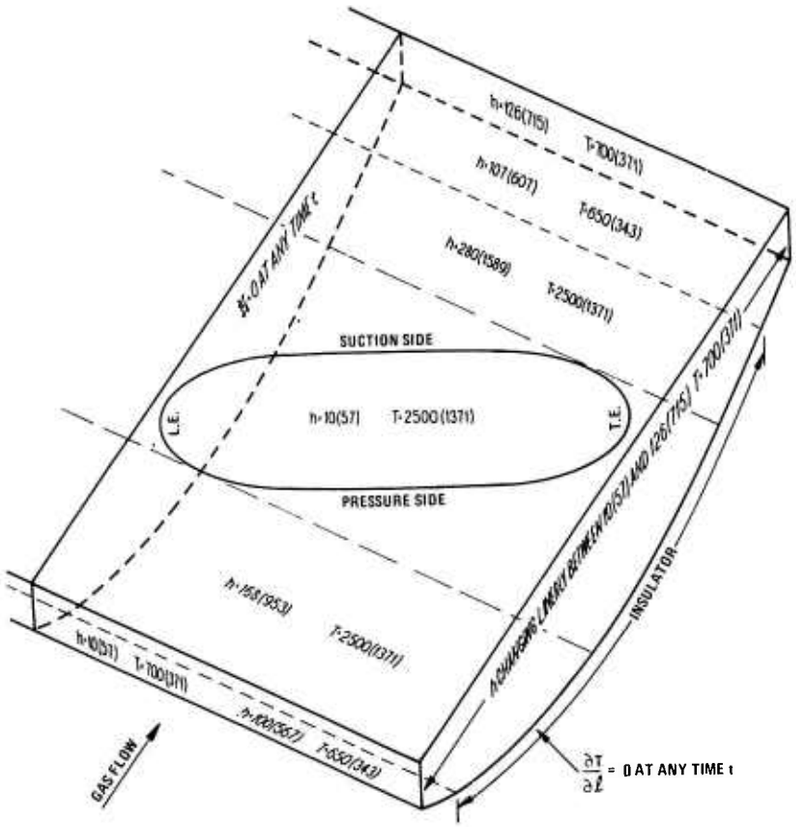

Figure 6.2 Initial And Boundary Conditions For End Cap Thermal Analysis (h - BTU hr^{-1} ft^{-2} °F, T - °F)

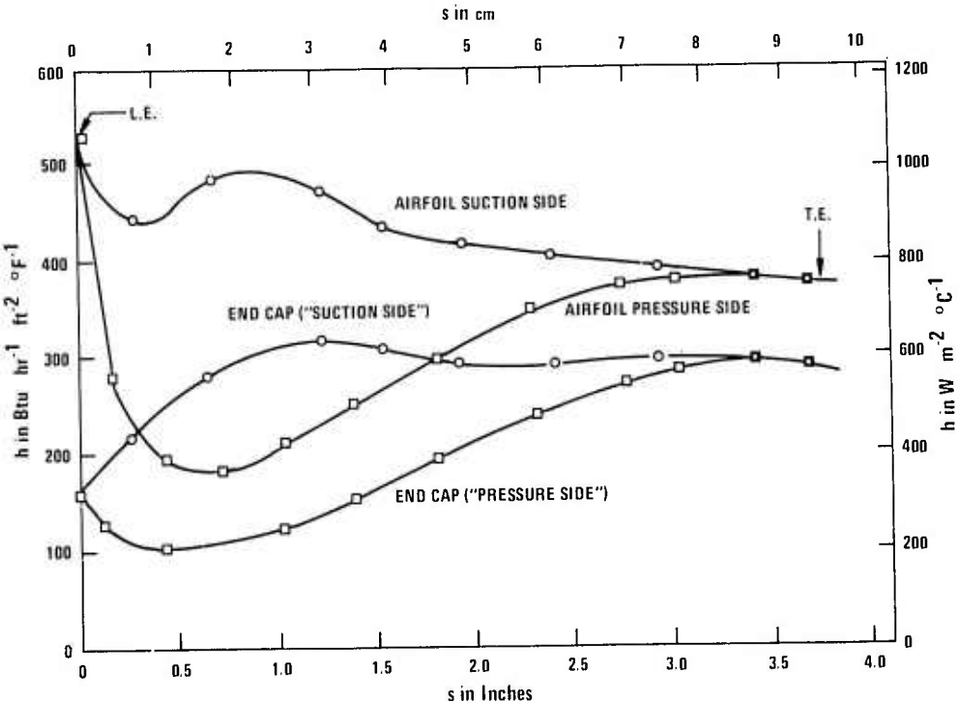

Figure 6.3 Calculated Variations In Heat Transfer Coefficients At Mid-Height Of Vane And On End Cap Surface vs Distance From The Leading Edge

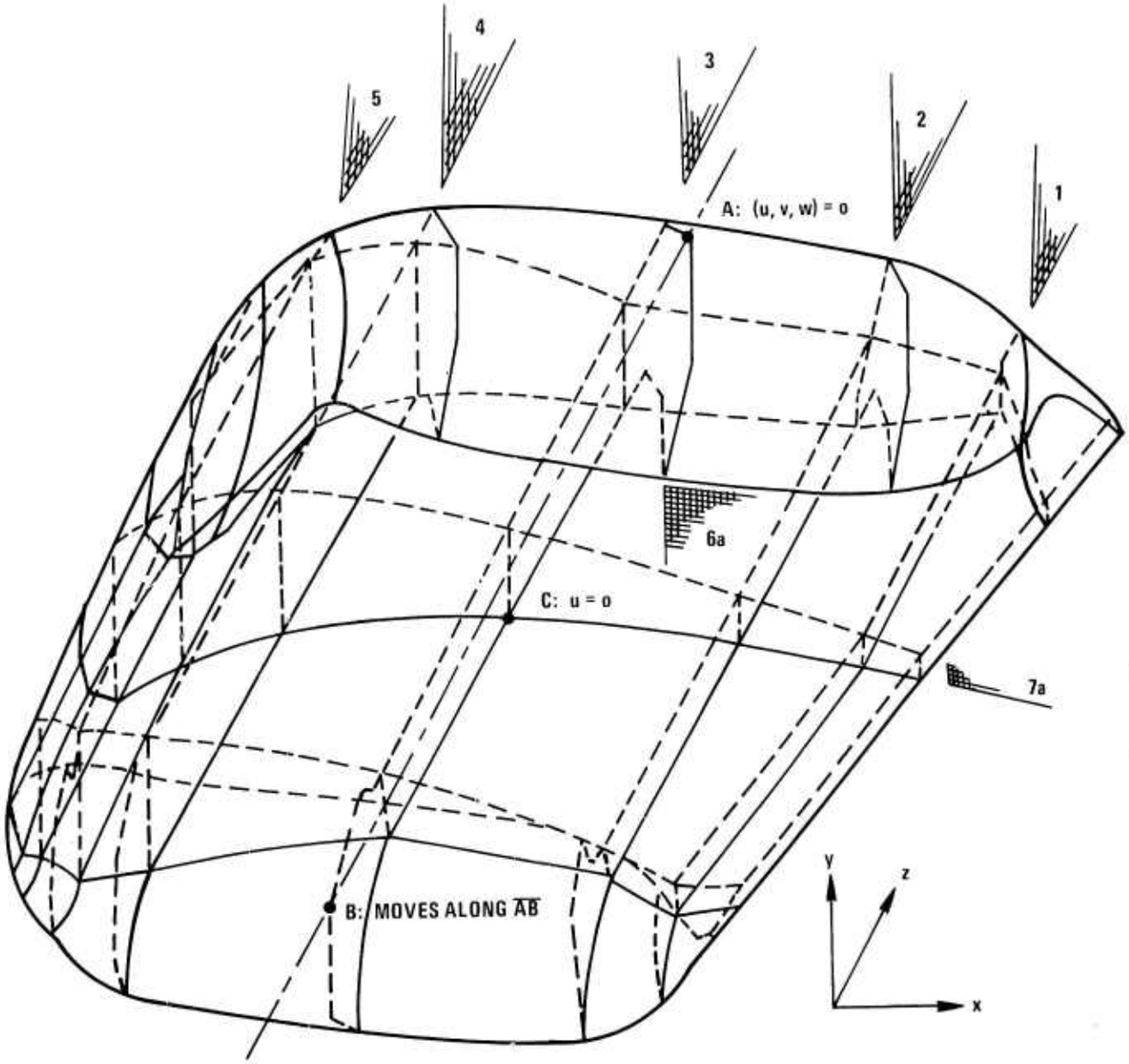

Figure 6.4 Three-Dimensional Element Model Of The Second Generation Airfoil Under Equilibrium Conditions

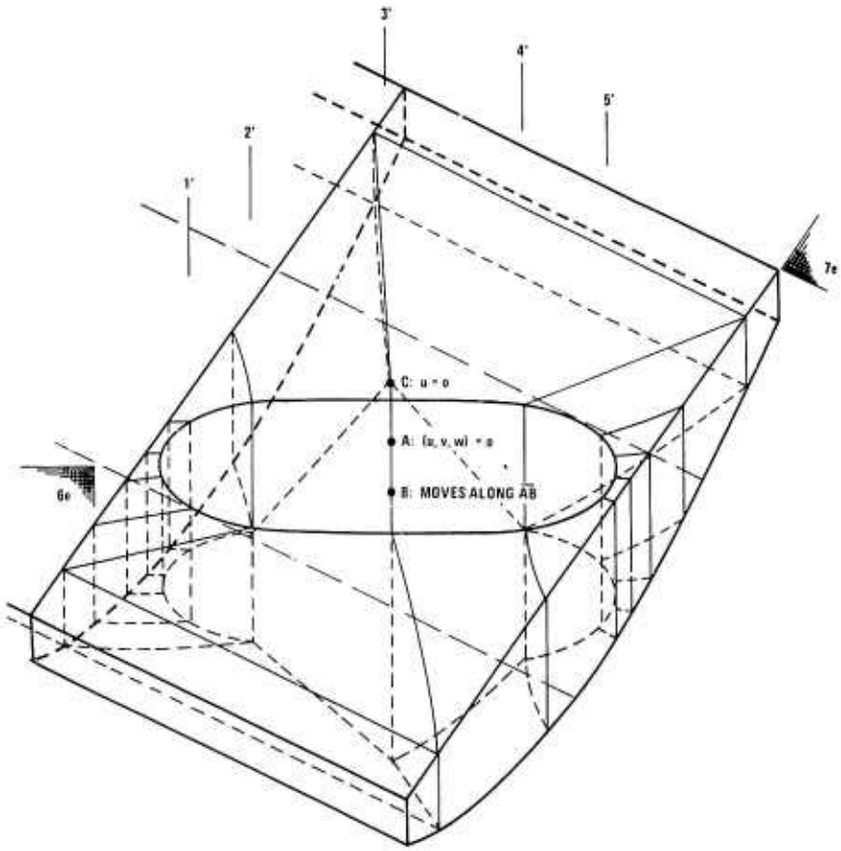

Figure 6.5 Three-Dimensional Element Mode' Of The End Cap Under Equilibrium Conditions

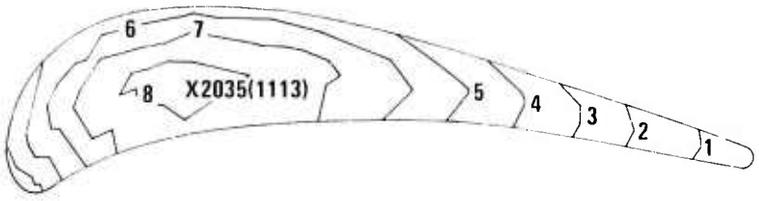

NO.	TEMP °F	(°C)
1	900	482
2	1050	565
3	1200	649
4	1350	732
5	1500	816
6	1650	899
7	1800	982
8	1950	1066

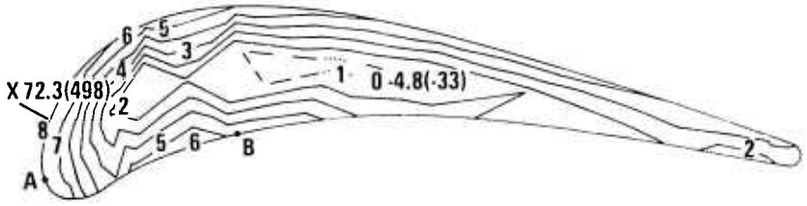

NO.	STRESS ksi	(MPa)
1	0	0
2	10	69
3	20	138
4	30	207
5	40	276
6	50	345
7	60	414
8	70	483

Figure 6.6 Temperature And Stress Distributions For Second Generation Design Airfoil At 10th Second Of Flame Out From 2500°F Steady State Gas Temperature (Section 7a) (h: High-Low)

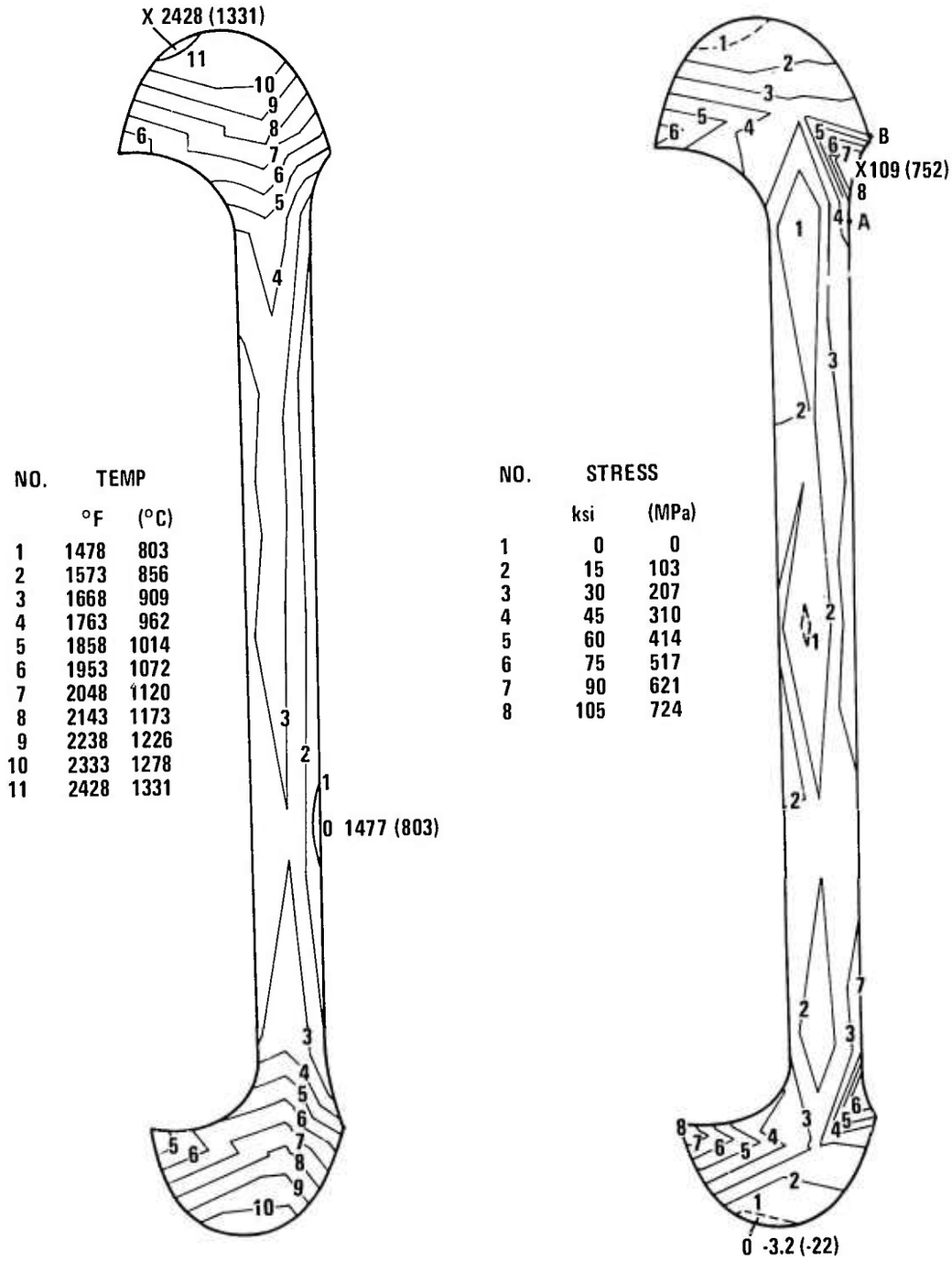

Figure 6.7 Temperature And Stress Distributions For Airfoil Section 3 At 10th Second Of Flame Out From 2500°F Steady State Gas Temperature (h: High-Low)

NO.	TEMP °F	(°C)
1	1425	774
2	1520	827
3	1615	879
4	1710	932
5	1805	985
6	1900	1038
7	1995	1091
8	2090	1143
9	2185	1196

NO.	STRESS ksi	(MPa)
1	15	103
2	30	207
3	45	310
4	60	414
5	75	517
6	90	621
7	105	724
8	120	827

NO.	STRESS ksi	(MPa)
1	0	0
2	15	103
3	30	207
4	45	310
5	60	414
6	75	517
7	90	621
8	105	724
9	120	827

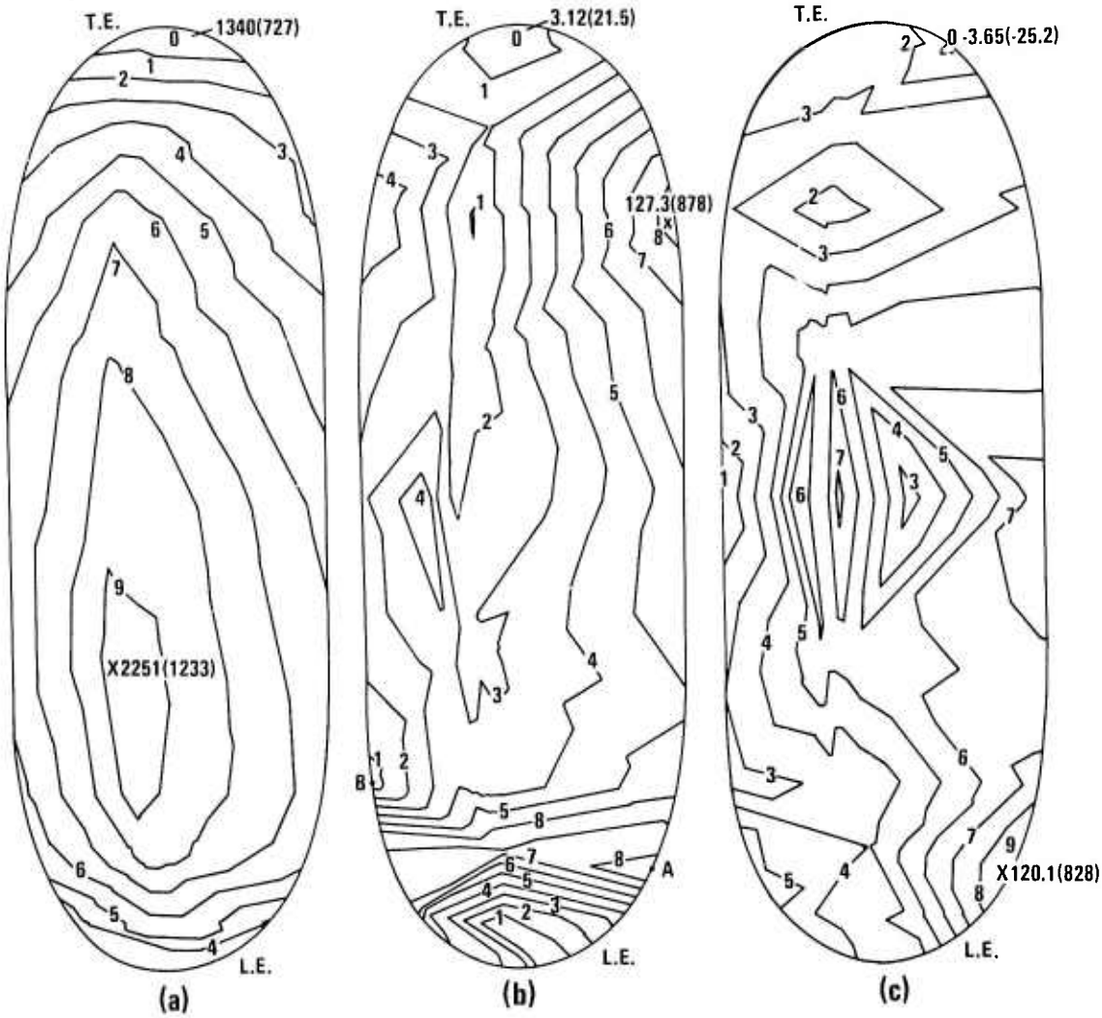

Figure 6.8 Temperature And Stress Distribution For Airfoil Section 6a At 10th Second Of Flame Out From 2500°F Steady State Gas Temperature ((a) h: High-Low, (b) h: High-Low, (c) h: High-High)

For the flame out condition, a maximum principal stress of 123,000 psi occurs at the inner surface of the outer end cap on the suction side near the leading edge of the airfoil after 14 seconds (Fig. 6.11). The three dimensional aspects of the temperature and stress distributions in the end cap can be obtained from Figs. 6.10, 6.11 and 6.12. Figure 6.13 describes the state of stress in the end cap resulting from cool down at 25°F/sec. A maximum principal stress of 92,900 psi now occurs within the end cap cavity.

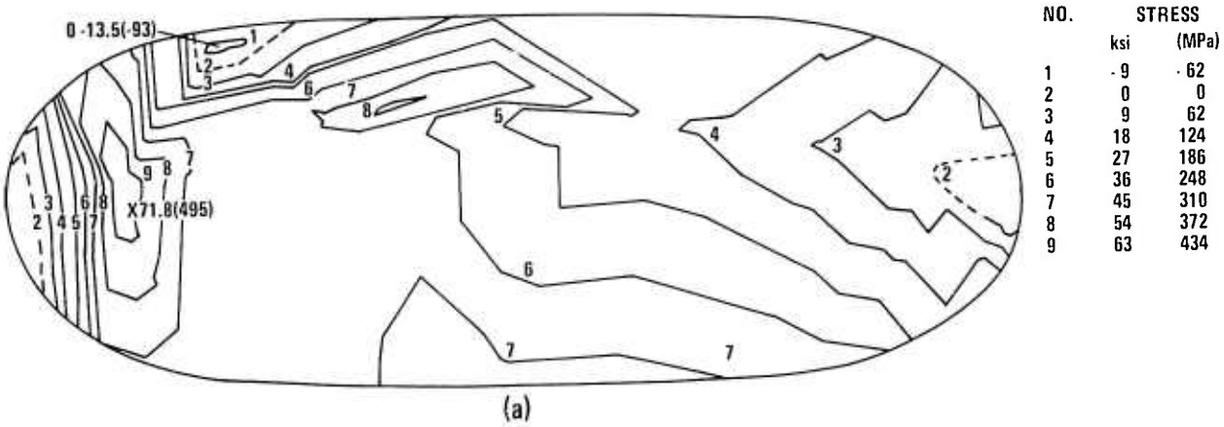

Figure 6.9 Stress Distribution During Cooling At 25°F/Sec From 2500°F Steady State Gas Temperature At 50th Second In Airfoil Section 6a

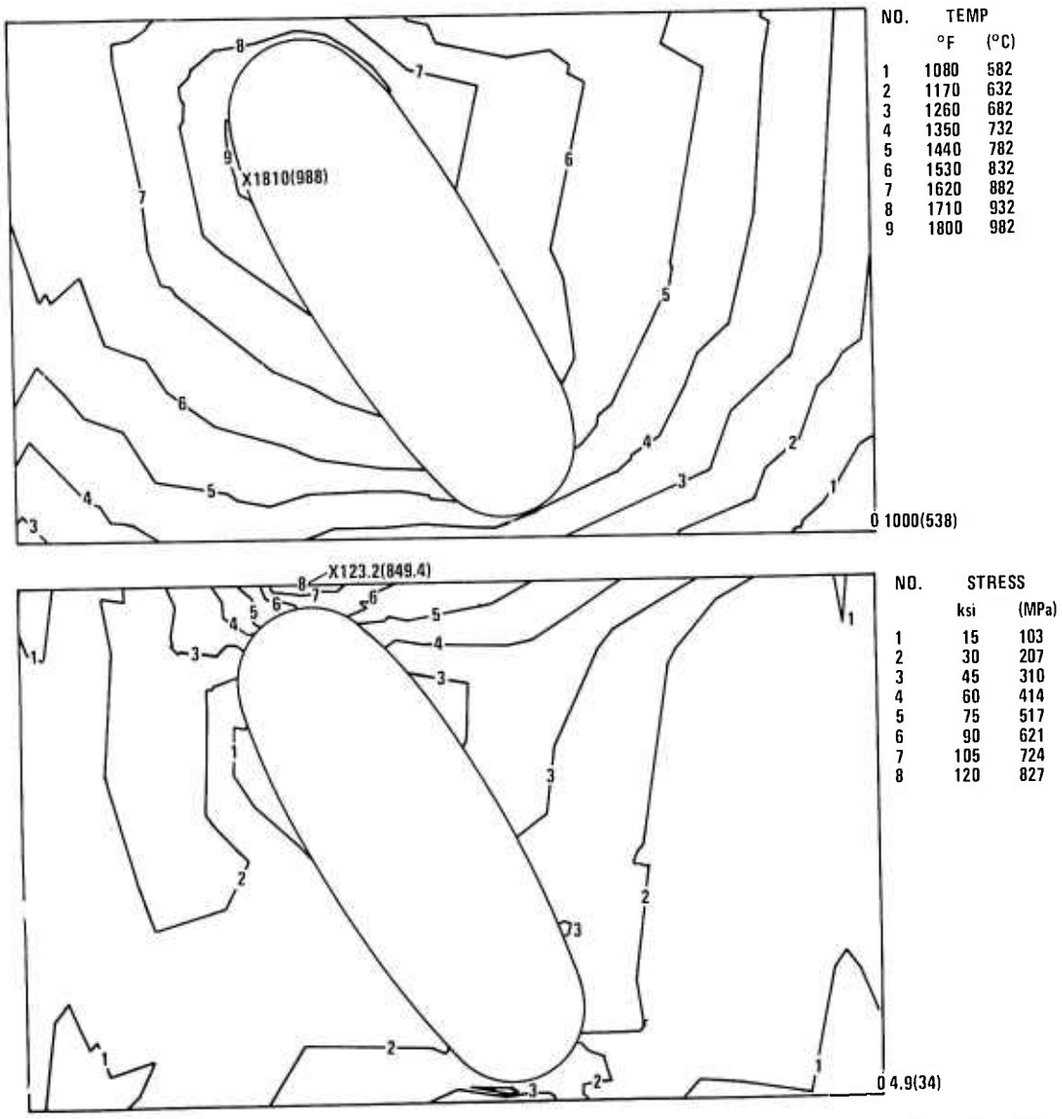

Figure 6.10 Temperature And Stress Distributions For End Cap Section 7e At 14th Second Of Flame Out From 2500°F Steady State Gas Temperature (h: High-Low)

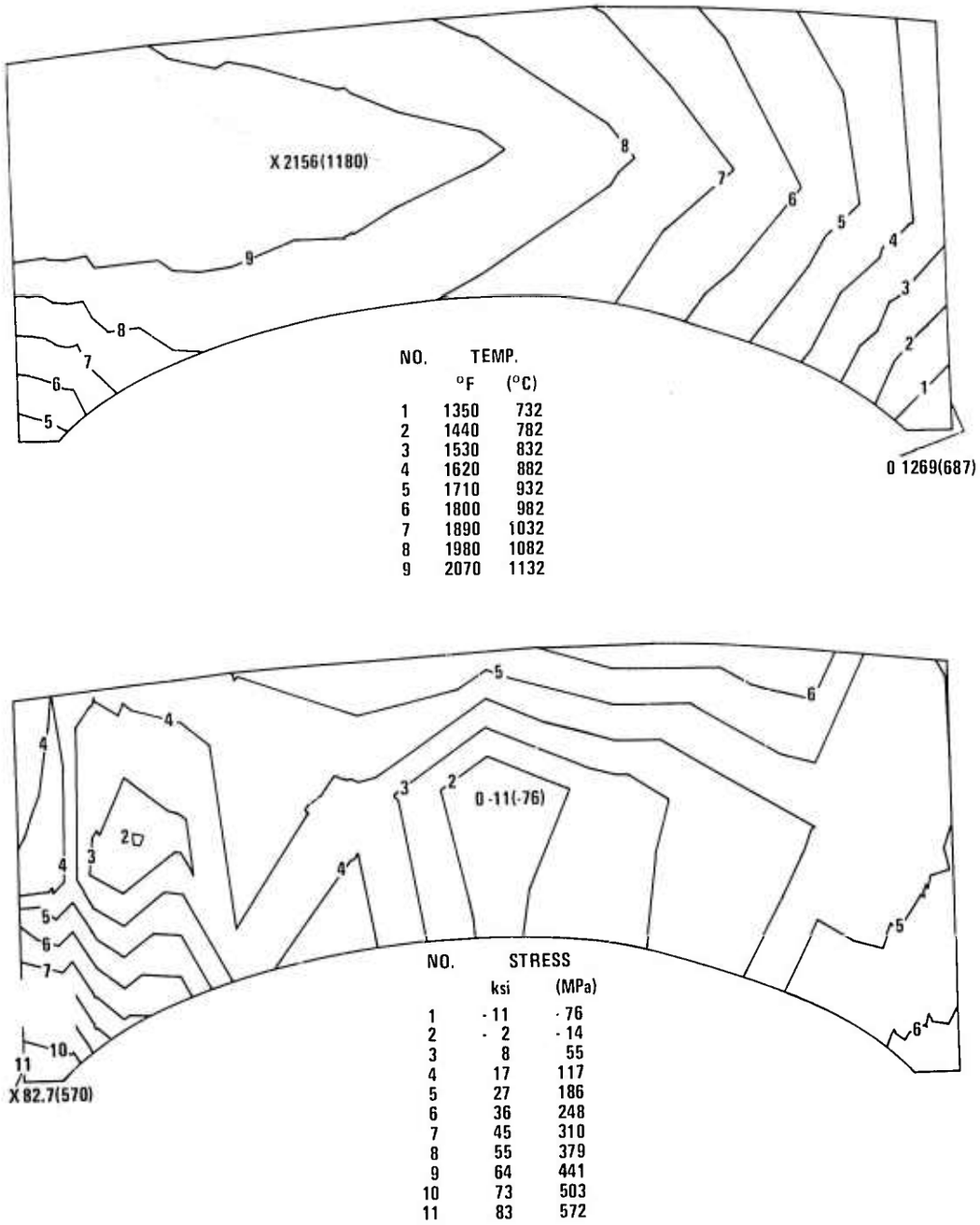

Figure 6.11 Temperature And Stress Distributions For End Cap Section 6e At 14th Second Of Flame Out From 2500°F Steady State Gas Temperature (h: High-Low)

These 3 dimensional stress analyses confirm a supposition that the states of stress in the second generation design airfoil under all conditions of flame out or controlled shutdown are much higher than those generated in the first generation design. Furthermore, the maximum principal stresses in the second generation design are expected to exceed the engineering strength of Si_3N_4, whereas the first generation and advanced turbine stator vane design are expected to survive multiple cycles in a controlled shutdown mode of peaking type service. The second generation design airfoil will be given no further consideration.

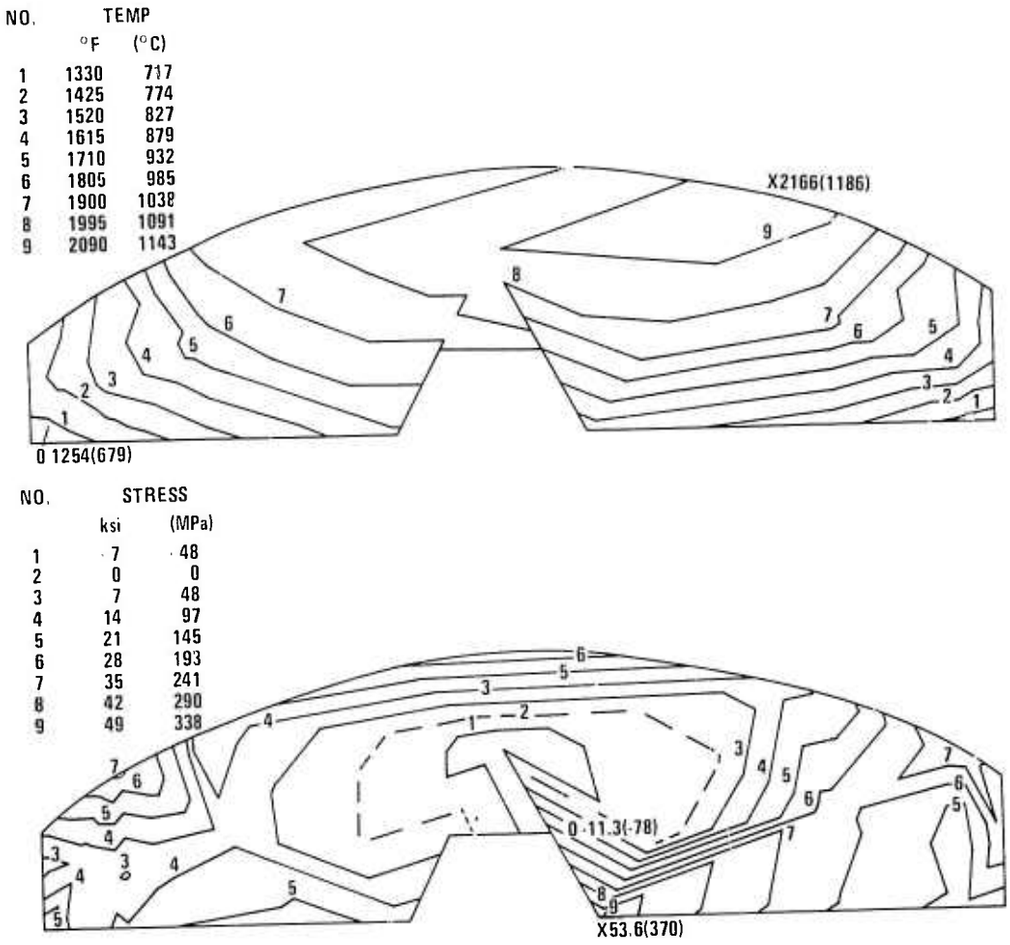

Figure 6.12 Temperature And Stress Distributions For End Cap Section 3' At 14th Second Of Flame Out From 2500°F Steady State Gas Temperature (h: High-Low)

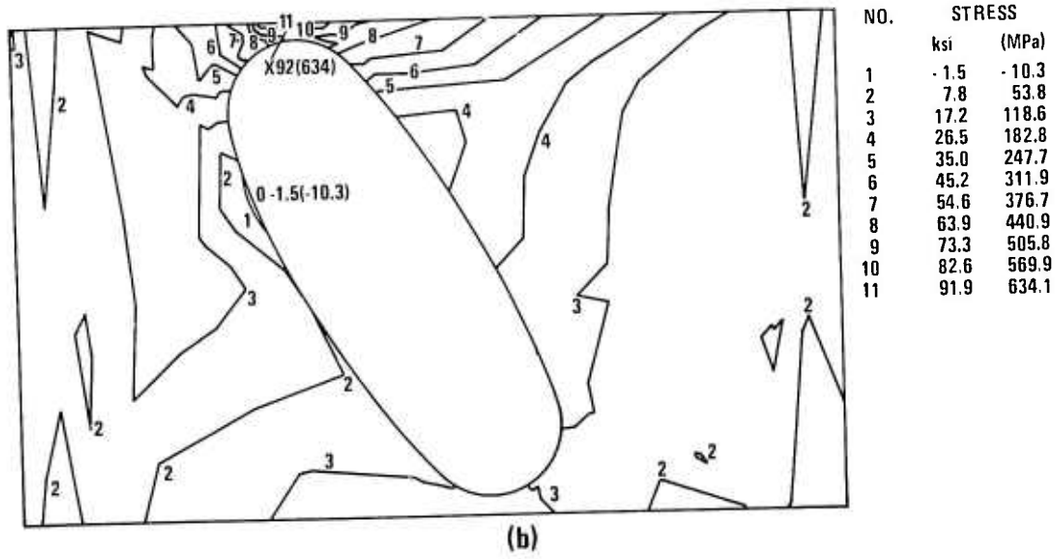

Figure 6.13 Stress Distribution During Cooling At 25°F/Sec From 2500°F Steady State Gas Temperature At 58th Second In End Cap Section 7e

Contact Stress Analysis

The airfoil-end cap interface of all versions of the three piece stator vane assembly is designed for partial area contact with the remaining portion of the mating surfaces in close proximity. Maximum clearances are specified at room temperature such that the contact stresses due to the axial spring load, which holds the assembly together, and the gas load remain low. However, differential deformation of the mating geometries can either reduce the contact area below that required to maintain acceptable contact stress levels or create interference, thus changing the contact points altogether thereby increasing the possibility of producing large bending and/or torsional stresses. The displacement components in the y-direction at four points, A, B, C and D, on the contact surface are shown in Fig. 6.14 with the second generation design stator vane used as a typical example. "Steady state" and "transient" displacements are defined as the distance a point moves from its original room temperature position to its position at steady state temperature or position at any transient temperature with respect to time. The transient chosen here occurs after 50 seconds under controlled shutdown conditions at 25°F/sec cooling rate.

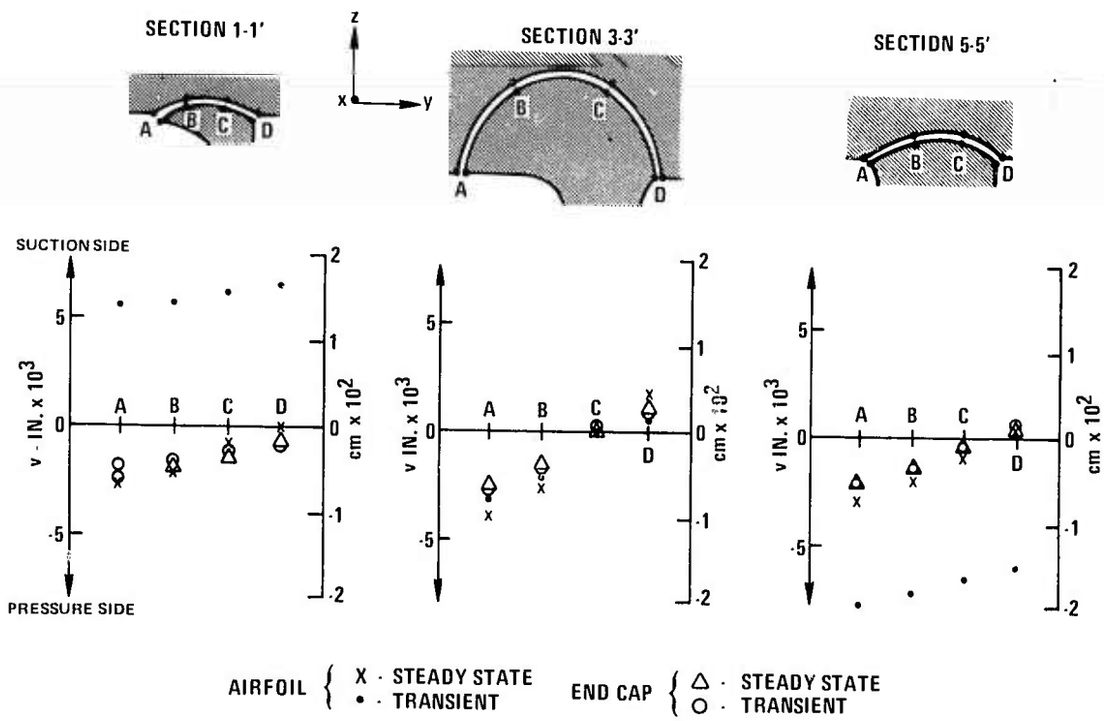

Figure 6.14 Deformations Of The Airfoil End Cap Contact Surfaces At Steady State And During Transient

The u and w displacements, in the x and y directions, respectively, are similar for the airfoil and end cap in both the steady state and transient cases calculated. They are not expected to create contact problems. The displacements v in the y-direction are also small and similar in magnitude in the airfoil and end cap for the steady state case.

While the transient displacements of Section 1', 3' and 5' (Fig. 6.14) of the end cap remain small, the transient displacements in the airfoil become large, i.e., important. Section 3, at the mid-chord stays at the same location while Section 5, near the leading edge, displaces toward the pressure side; and Section 1, near the trailing edge, displaces toward the suction side. The displacements calculated at the 10th second of a flame out transient from 2500°F for the airfoil have not been plotted because the corresponding displacements for the end cap have not been calculated. It should be mentioned, however, that the v displacements for this case are nearly three times those for the transient discussed above for Sections 1 and 5; they remain the same for Section 3.

The displacements in the y direction may create large contact stresses in as-yet-undetermined locations, and high bending and torsional stresses. These may also cause fretting at the interface surfaces.

Because of manufacturing considerations and a request from the vendor, the resulting radial difference between the mating surfaces at the airfoil tenon-end cap cavity interface is currently specified as 0.002 inches, minimum and 0.012 inches, maximum.

6.1.3 THE CERAMIC INSULATOR

Introduction

Ceramic insulators are used at both the inner and outer end cap positions to lower thermal gradients and support end cap pairs as shown in Fig. 6.15. Materials must be hard, durable to fretting type stresses, moderately strong in tension (> 10,000 psi), resistant to thermal shock (low elastic modulus and thermal expansion coefficients) and exhibit low thermal conductivity. Lithium alumina silicate (LAS) was selected initially and evaluated in static rig tests at 2200°F where it failed. Transient thermal cracks were observed at the upstream circumferential edges of all LAS insulators tested (Fig. 6.16). Cracking observed at downstream circumferential edges was attributed to edge loading. Evidence of fusion indicated that exposure temperatures locally had exceeded 2100°F, the slumping temperature of the LAS.

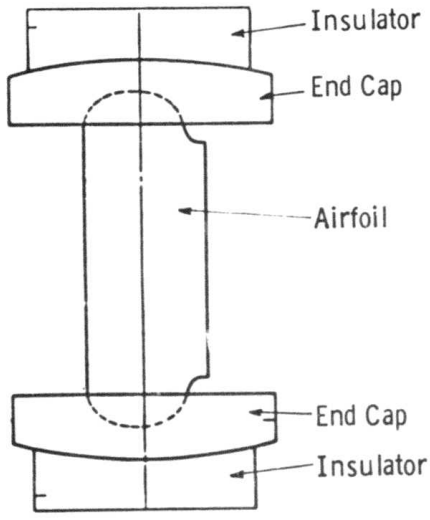

Figure 6.15 Ceramic Stator Vane Assembly With Insulators

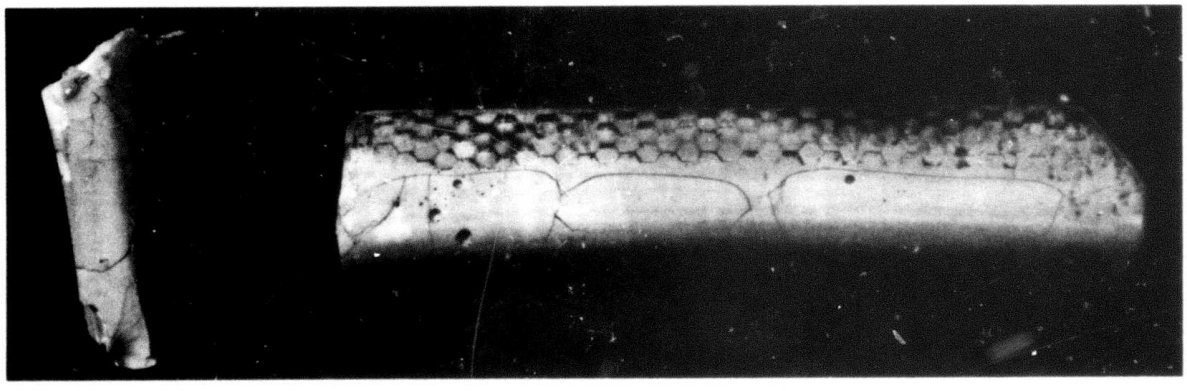

Figure 6.16 Typical Insulator Failures In Cervit C140 LAS Material

Selection of Alternate Insulator Materials

A qualitative, one-dimensional, steady state heat transfer and stress analysis was used initially to compare potential insulator materials. The heat transfer model appears in Fig. 6.17. Results were calculated from the simplified thermal stress equation for a clamped plate subjected to a uniform linear temperature gradient difference (T_1-T_2) as follows:

$$\sigma_t = \frac{\alpha E (T_1 - T_2)}{2(1-v)} \qquad (1)$$

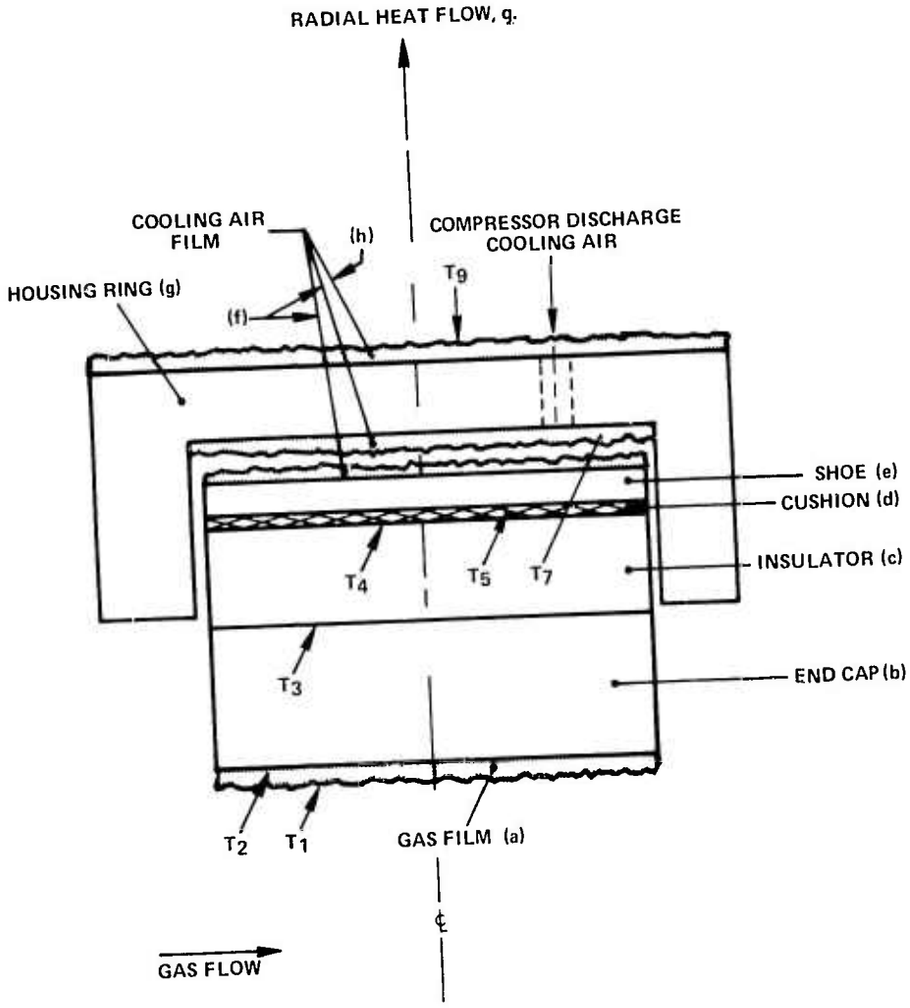

Figure 6.17 One-Dimensional Radial Conduction/Convection/Radiation Heat Transfer Model - Steady State Condition

Six candidate materials are compared in Table 6.1 where calculated stresses are based on average physical and thermal properties of the materials as supplied by vendor data. LAS rates best as long as the maximum temperature does not exceed 1800-1900°F where permanent changes in the material's properties occur. LAS can sustain the largest ΔT at the lowest stress level in the insulator and Si_3N_4 end cap (Table 6.2), whereas hot-pressed silicon carbide sustains the lowest ΔT with the highest stress in the Si_3N_4 end cap (Table 6.2). Other materials are ranked between. On a strength to stress basis, LAS is 5.54 times as good as "M"-boron nitride which has the desired temperature capability and a strength 2.24 times that required by peak stress standards.

TABLE 6.1
INSULATOR MATERIAL STRESS COMPARISON

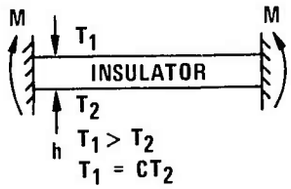

$$\sigma_T = \frac{\alpha E(T_1 - T_2)}{2(1-\nu)}$$

MATERIAL	PROPERTIES							STRESS		
	K $\frac{\text{BTU-IN}}{\text{HR-FT}^2\text{-°F}}$	T_1-T_2 ① °F	$\frac{T_1+T_2}{2}$ ① °F	E PSI x10^6	α IN/IN/°F X10^{-6}	ν	MOR PSI	σ_T PSI	$\frac{MOR}{\sigma_T}$	R.F.
1. LAS	12.0	1229	1425	12.5	0.15	0.28	20,000	1610	12.4	1.00
2. H.P. Si_3N_4	155.0	327	1363	41.0	1.70	0.23	100,000	14,800	6.75	1.84
3. H.P. SiC	395.0	147	1351	64.0	2.50	0.23	75,000	15,250	4.94	2.52
4. "A" BN	120.0	399	1368	9.0	1.35	0.23	11,000	3140	3.51	3.54
5. R.S. Si_3N_4	61.2	631	1384	18.5	1.65	0.23	28,500	12,500	2.28	5.44
6. "M" BN	55.0	672	1387	13.0	1.10	0.23	14,000	6240	2.24	5.54

R.F. = RATING FACTOR $= \left(\frac{MOR}{\sigma_T}\right)_{LAS} \div \left(\frac{MOR}{\sigma_T}\right)_{MTL}$ T GAS = 2250°F

① T_1-T_2 FROM 1-D HEAT TRANSFER ANALYSIS T AIR = 650°F

TABLE 6.2
END CAP STRESS FOR VARIOUS INSULATOR MATERIALS

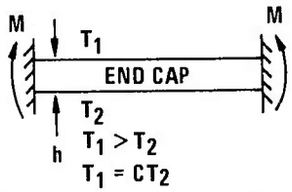

$$\sigma_T = \frac{\alpha E(T_1 - T_2)}{2(1-\nu)}$$

INSULATOR MATERIAL	PROPERTIES		END CAP STRESS		
	K $\frac{\text{BTU-IN}}{\text{HR-FR-°F}}$	T_1-T_2 ① °F	σ_T PSI	$\frac{MOR}{\sigma_T}$	R.F.
1. LAS	12.0	157	6540	15.30	1.0
2. "M" BN	55.0	394	16,400	6.10	2.51
3. R.S. Si_3N_4	61.2	412	17,100	5.86	2.62
4. "A" BN	120.0	510	21,200	4.72	3.24
5. H.P. Si_3N_4	155.0	541	22,500	4.44	3.44
6. H.P. SiC	395.0	617	25,700	3.89	3.94

R.F. = RATING FACTOR $= \left(\frac{MOR}{\sigma_T}\right)_{LAS} \div \left(\frac{MOR}{\sigma_T}\right)_{MTL}$ T GAS = 2250°F

① T_1-T_2 FROM 1-D HEAT TRANSFER ANALYSIS T AIR = 650°F

Two-Dimensional Finite Element Analysis of Insulators

The axisymmetric nature of the insulator makes it ammenable to 2-dimensional heat transfer and stress analyses. Figure 6.18 illustrates the finite element model which excludes the end cap cavity for the sake of simplicity. The heat transfer model includes the effect of conduction through the elements (zero gradient across the interface is assumed) and convection and radiation at all boundary locations. Seventeen heat transfer coefficients, seven fluid temperatures, and six external body temperatures versus time are specified. All were derived from theoretical considerations or from appropriately scaled experimental results. Thermal properties such as emmisivity, specific heat, and conductivity are utilized with respect to temperature. Fluid temperatures are reduced to compressor discharge levels in 2.5 seconds and decay exponentially thereafter. The heat transfer coefficients are ramped and similarly decayed.

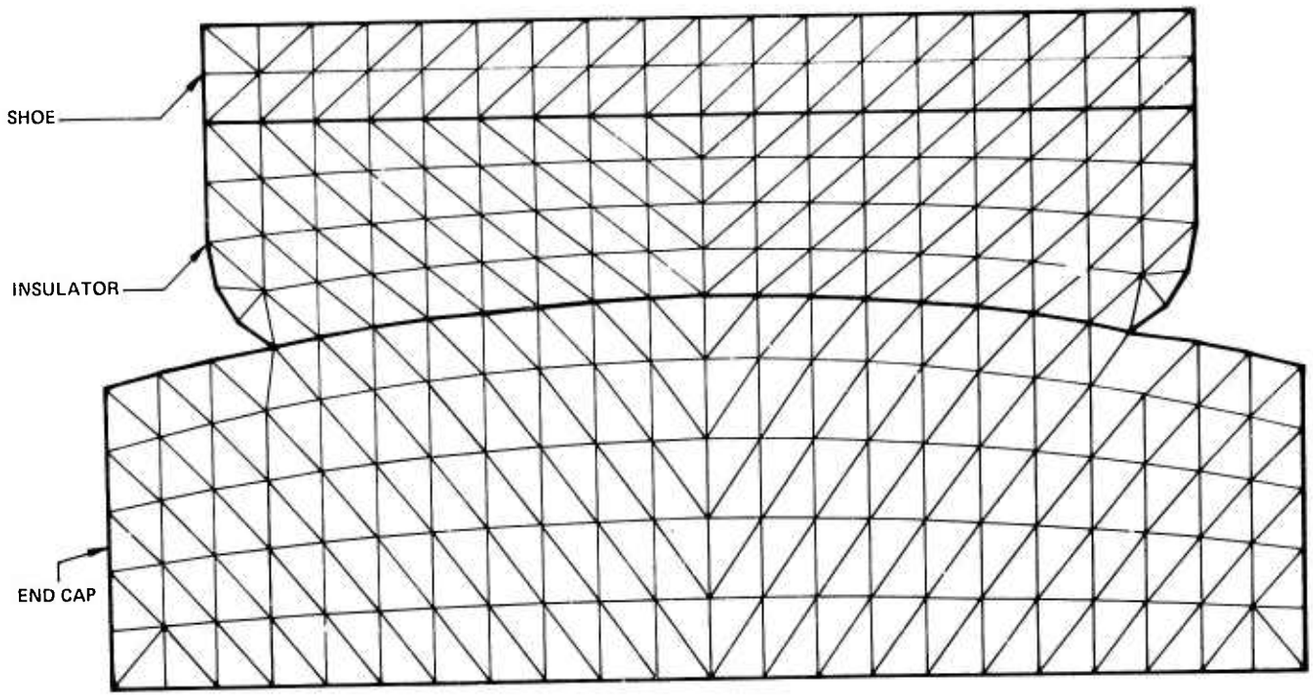

Figure 6.18 Two-Dimensional Finite Element Model Of End Cap - Insulator Combination

The analysis was conducted for the normal condition and the hot gas condition as defined in Figs. 6.19 and 6.20. The hot gas condition is approximately three times as severe as the normal one. Steady state is defined as five minutes after start up. The results are presented for the upstream half of the insulator only. The temperature-time history for the gas/air boundary fluid and the convective heat transfer coefficients versus time are plotted in Figs. 6.19 and 6.20, respectively. High heat transfer coefficients tend to force the surface temperature toward the impinging gas temperature, thus maximizing the stresses.

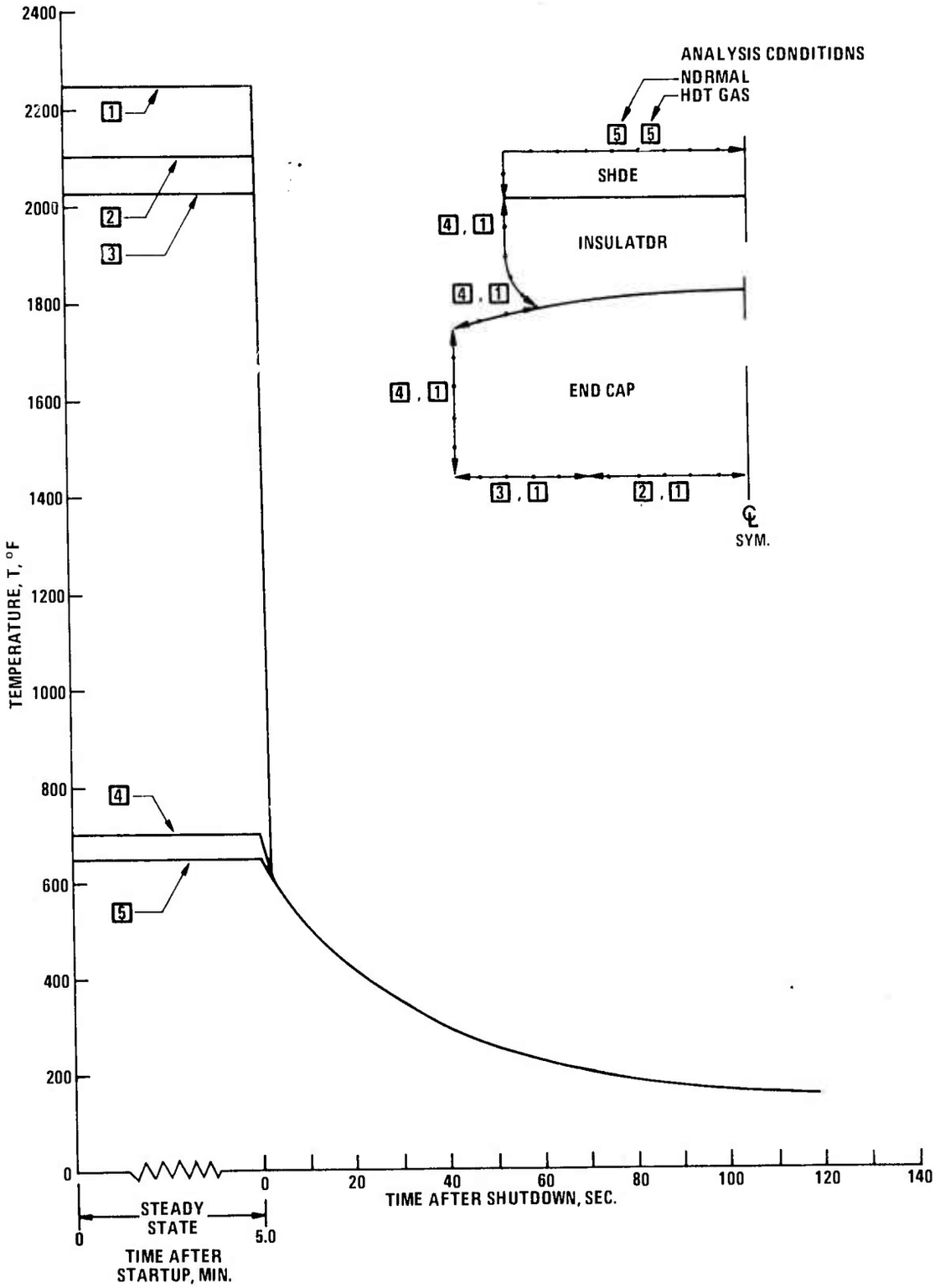

Figure 6.19 Gas/Air Temperature vs Time Profile For Insulator - End Cap Combination

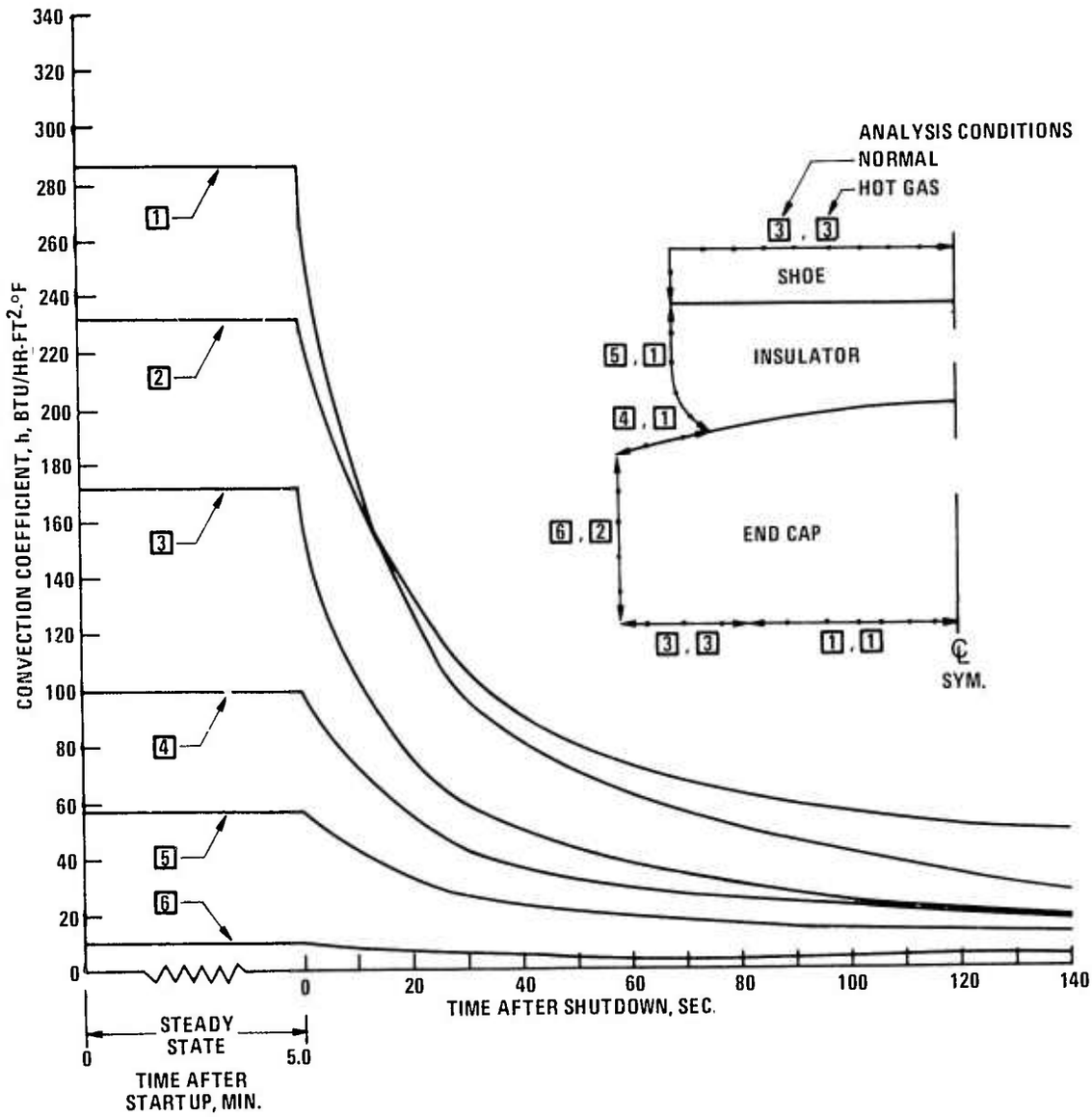

Figure 6.20 Convection Coefficients vs Time Profiles For Shoe, Insulator, End Cap Combinations

The 2-D temperature and stress responses were performed for two materials, LAS and hot-pressed Si_3N_4 because a large amount of temperature-dependent data was available. Furthermore, these materials represent the upper and lower bounds of temperature and stress response. Only the most severe hot gas condition is presented. The transient temperature responses for LAS and hot-pressed Si_3N_4 are given in Figs. 6.21 and 6.22, respectively. LAS insulator surface nodal points 120, 139, and 177 demonstrate clearly that 1800°F design limit has been exceeded. As expected, surface nodal points 139 and 177 (and others not shown) respond rapidly to the gas/air boundary transient of Fig. 6.19, whereas internal points such as 127, 167 and 204 are hardly affected. In general, the response of the hot-pressed Si_3N_4 insulator, as shown in Fig. 6.22, is not as drastic in terms of temperature, time response and gradients. For the LAS insulators, temperatures near the end cap interface (points 120 and 127) are hotter, whereas temperatures near the shoe (points 205 and 215) are cooler. These results reflect the relatively lower thermal conductivity of LAS. It is interesting to note that even for the severe

hot gas condition, points away from direct hot gas impingement are at temperatures below the design limit of 1800°F.

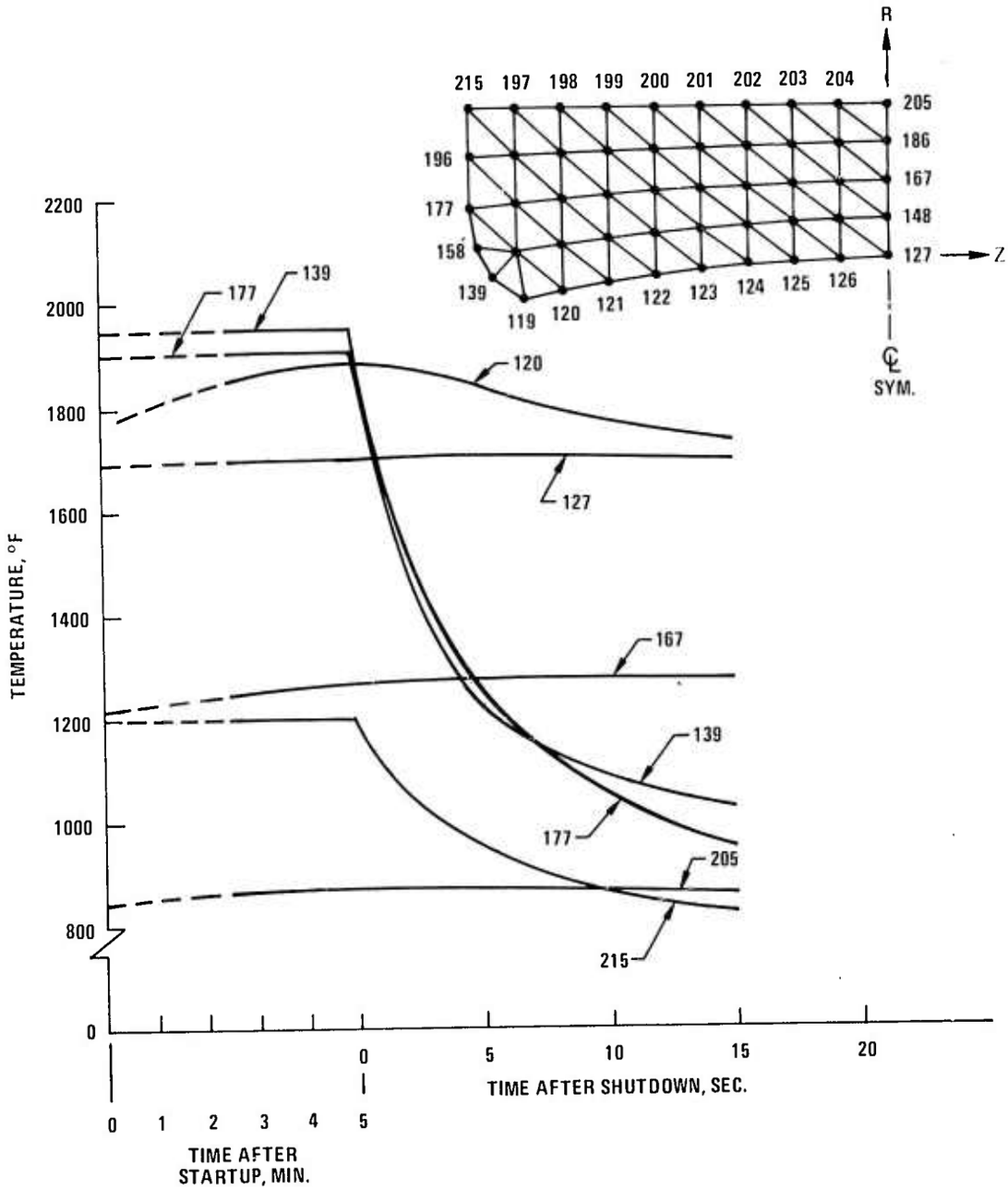

Figure 6.21 Insulator Hot Gas Transient Thermal Response Of LAS

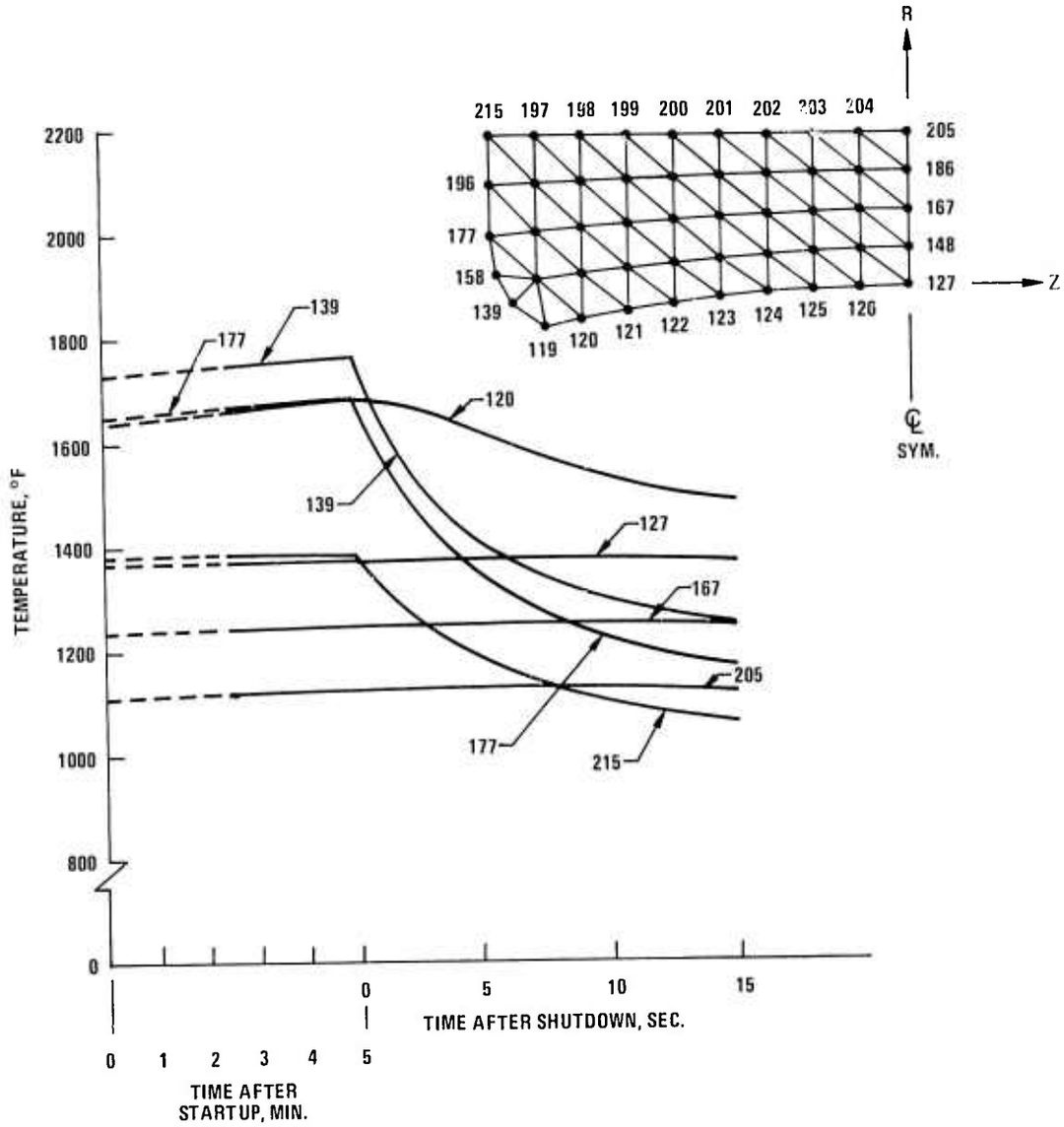

Figure 6.22 Insulator Heat Gas Transient Thermal Response Of Hot-Pressed Si_3N_4

The output from the 2-D heat transfer model was utilized to compute the transient (and steady state) in-plane stresses as defined by the insulator stress model of Fig. 6.23. Z and R denote the longitudinal (flow) direction and the radial direction, respectively. The stress response for an LAS insulator appears in Fig. 6.24, while Fig. 6.25 is characteristic of hot-pressed Si_3N_4. The stresses presented are the maximum tensile principal values (σ_{max}) representing vectorial combinations of σ_R, σ_Z, and δ_{RZ} with the principal contributing stress indicated in parenthesis. As expected from the temperature response, the maximum transient stresses occur at the points (139, 158) from hot gas impingement. For LAS, point 158 attains the maximum transient value of 600 psi, 7 seconds after shutdown, for hot-pressed Si_3N_4; point 139 attains the maximum transient value of 3000 psi, 2 seconds after shutdown. The overall temperature condition of the insulator tends to result in steady state σ_Z (plate bending) type stresses at points away from hot gas impingement (e.g., points 148, 215), whereas the local temperature condition tends to result in transient σ_R type stress at points of impingement. The transient condition has a greater

(but delayed) effect on LAS than on hot-pressed Si_3N_4, because of the relatively low thermal conductivity and higher specific heat of LAS. As a result, the maximum principal stress in the LAS insulator is transient while that in hot-pressed Si_3N_4 is steady state. In addition, the analysis indicates that hot gas impingement point 158 operates under a compression-tenson reverse cyclic mode.

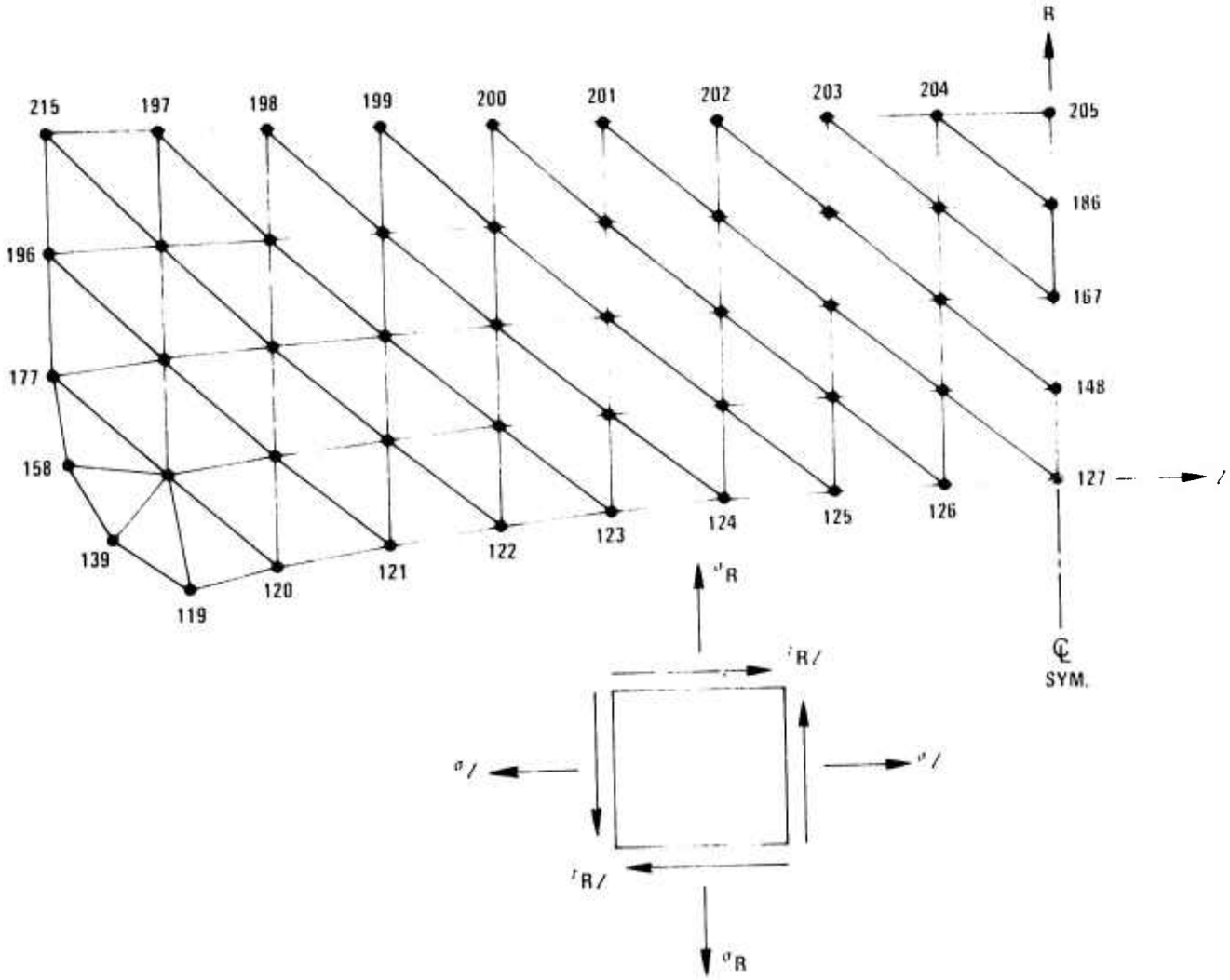

Figure 6.23 Insulator Two-Dimensional Stress Model

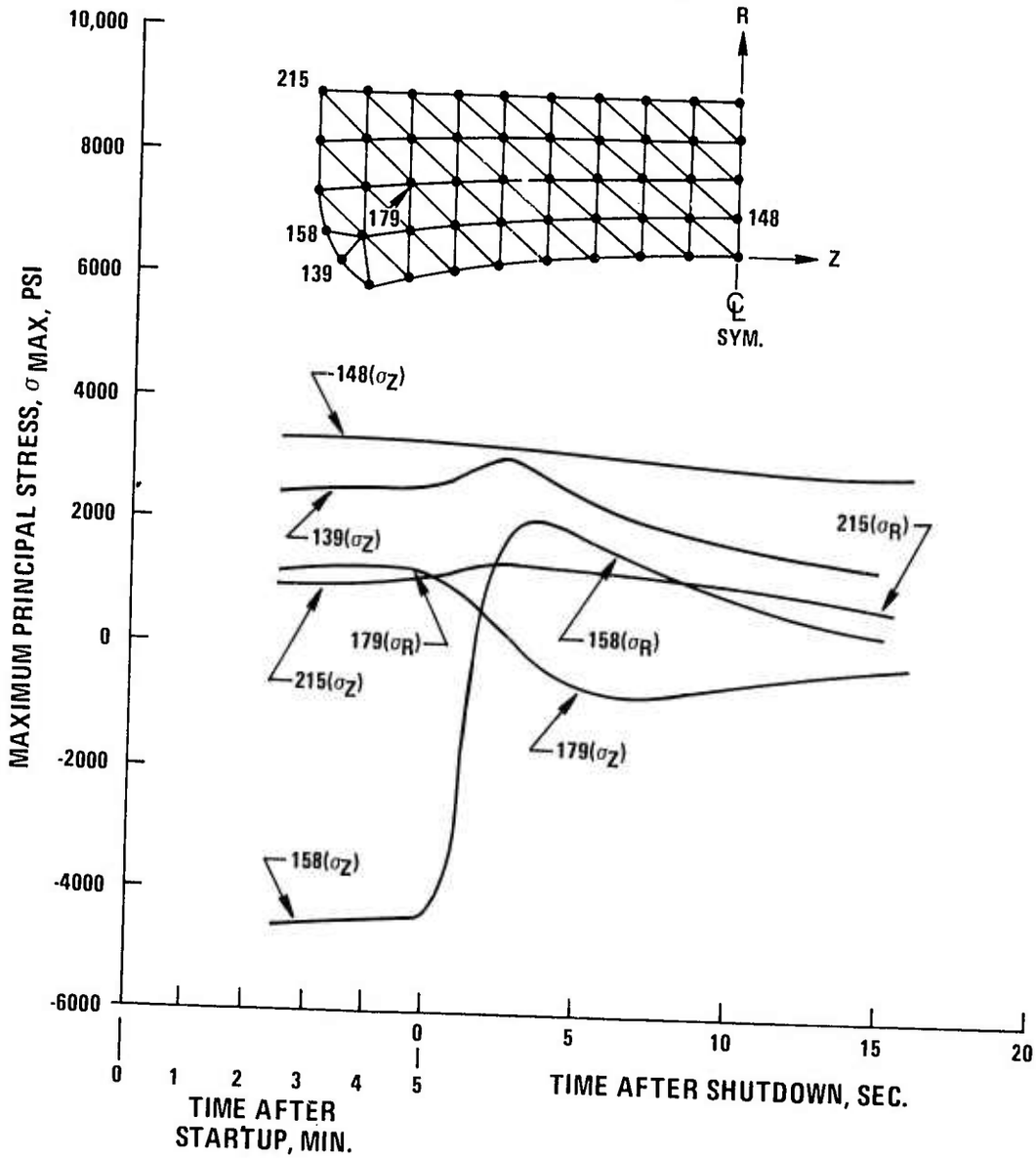

Figure 6.24 Insulator Hot Gas Two-Dimensional In Plane Maximum Stress Response For LAS

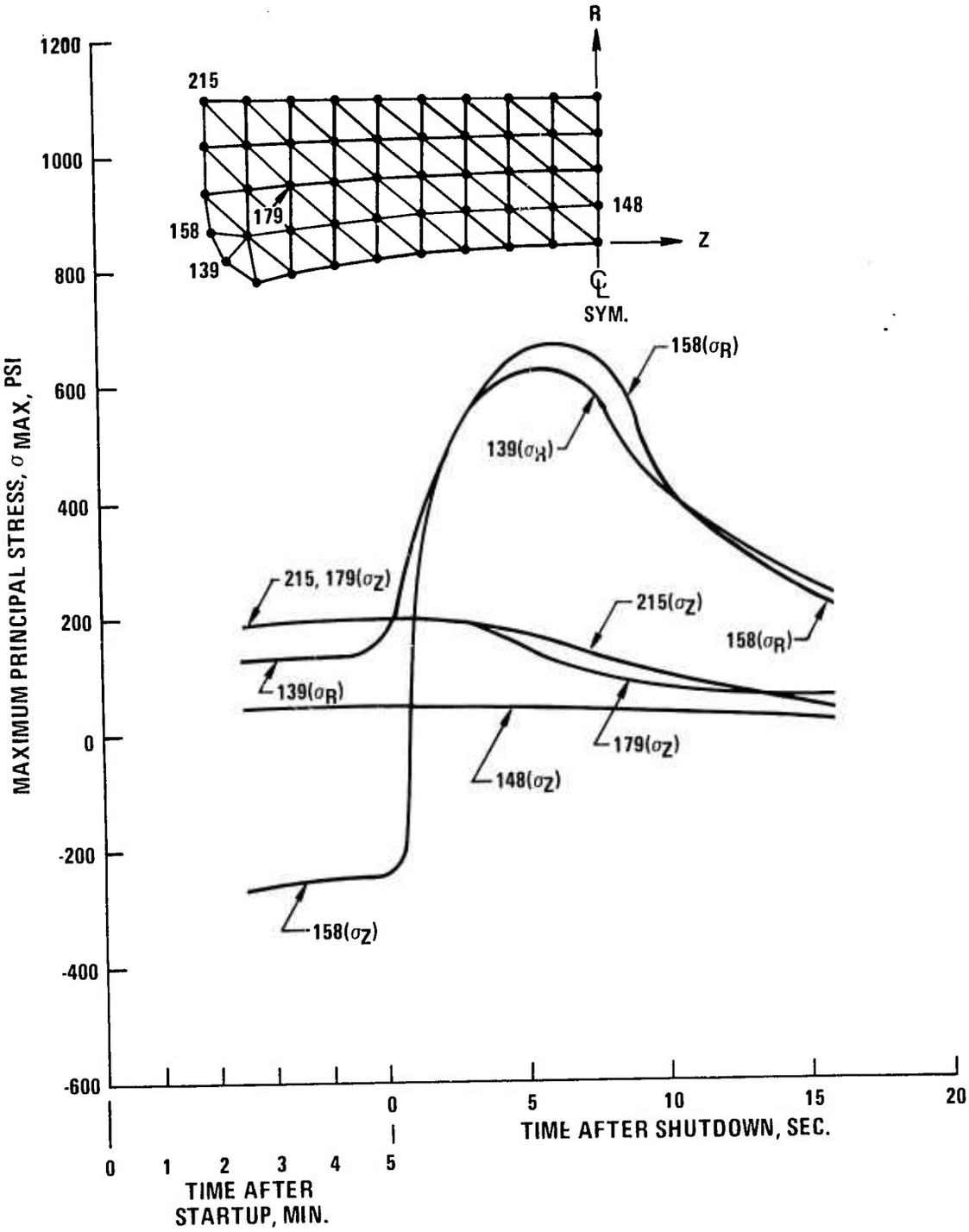

Figure 6.25 Insulator Hot Gas Two-Dimensional Maximum Stress Response Of Hot-Pressed Si_3N_4

Within the range of parameters studied, all of the calculated stresses are within the design allowable stress of the materials studied assuming that they don't exceed 1900°F. Since hot gas impingement does cause hot locations in the insulator above 1800°F, as observed in static rig tests, LAS will no longer be used. "Combat M" boron nitride has been selected for exclusive insulator use when static rig testing at 2500°F is resumed.

6.1.4 STATIC RIG TESTS

Introduction

The static rig was repaired following performance evaluation and calibration runs which were terminated after five cycles at 2300°F[6] when the exhaust ceramic duct cracked discharging debris downstream to damage the ceramic mixer section. A new silicon nitride bonded silicon carbide duct was installed to permit the resumption of cyclic testing at 2500°F. The results of testing, after five cycles, are reported. Silicon nitride vanes remained functional. Silicon carbide stator vane assemblies failed catastrophically. The static rig itself had to be rebuilt to include a redesigned combustor, a water-cooled exhaust duct, and water spray mixer section.

2500°F Static Rig Test Results

- Test Conditions -- After the test assembly consisting of four hot-pressed silicon nitride and four hot-pressed silicon carbide vanes was installed in the static rig (Fig. 6.26), seven additional calibration runs were made with aspirating thermocouple rakes to (1) establish gas temperature profiles at 1200°F, 1800°F, and 2300°F, and (2) correlate rake temperature data with radiation pyrometer readings. Ramp rates were also established using the Veritrak Data Acquisition System.

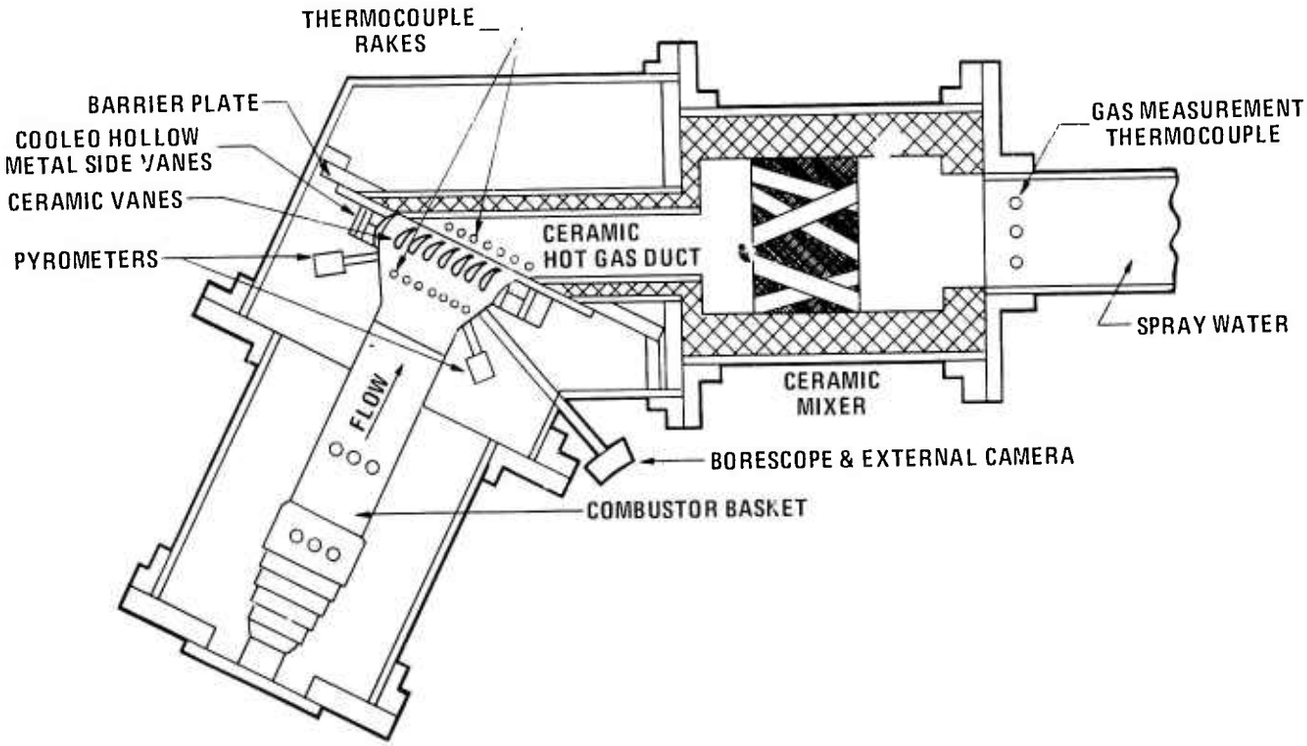

Figure 6.26 Static Test Rig For 2500°F Test Of Ceramic Vanes

Gas temperature profiles are presented in Figs. 6.27, 6.28, and 6.29. These data, together with radiation pyrometry, were used to extrapolate a representative gas temperature profile for 2500°F (Fig. 6.30). The resultant profile is somewhat asymmetric with the peak temperature shifted toward the left because cooling air discharged from the boroscope enters the gas passage from the right.

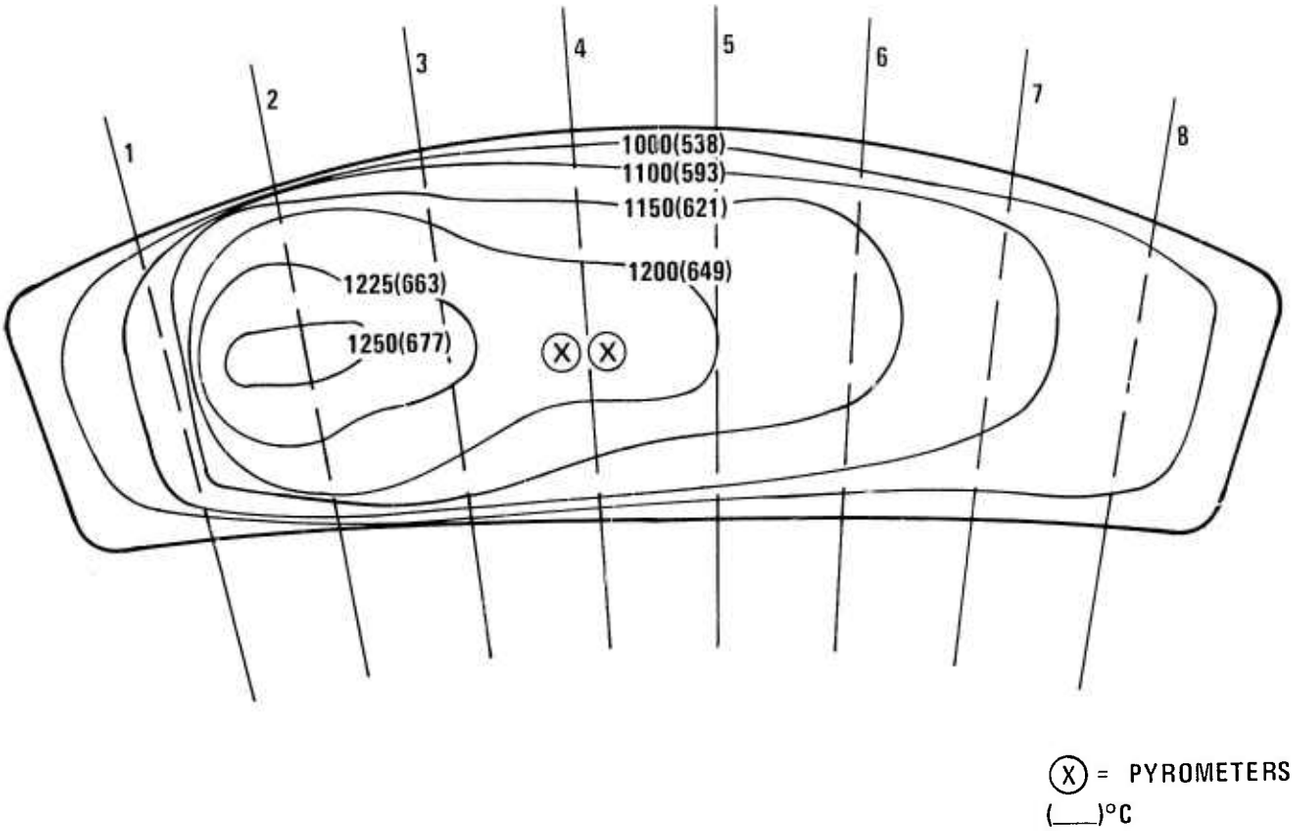

Figure 6.27 Temperature Profile At 1200°F, Idle

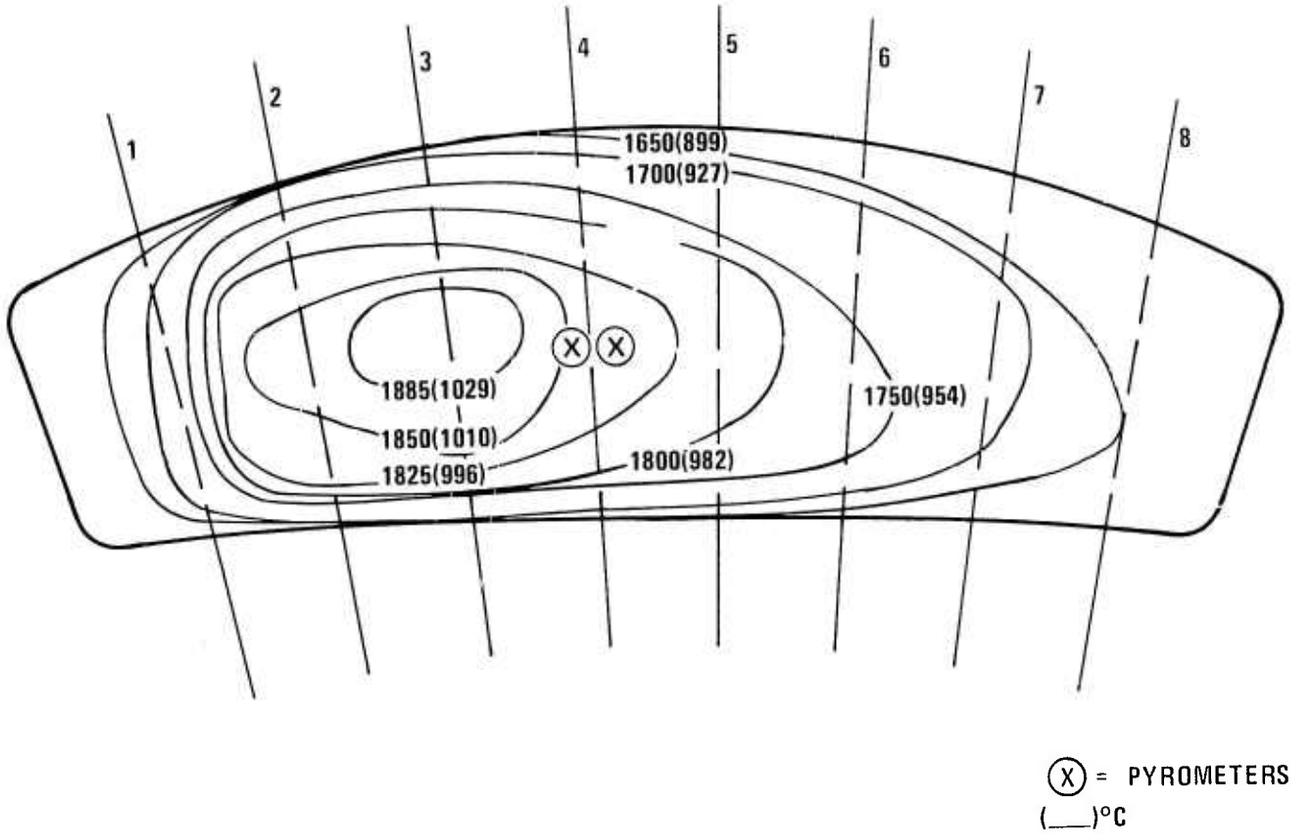

Figure 6.28 Temperature Profile At 1800°F

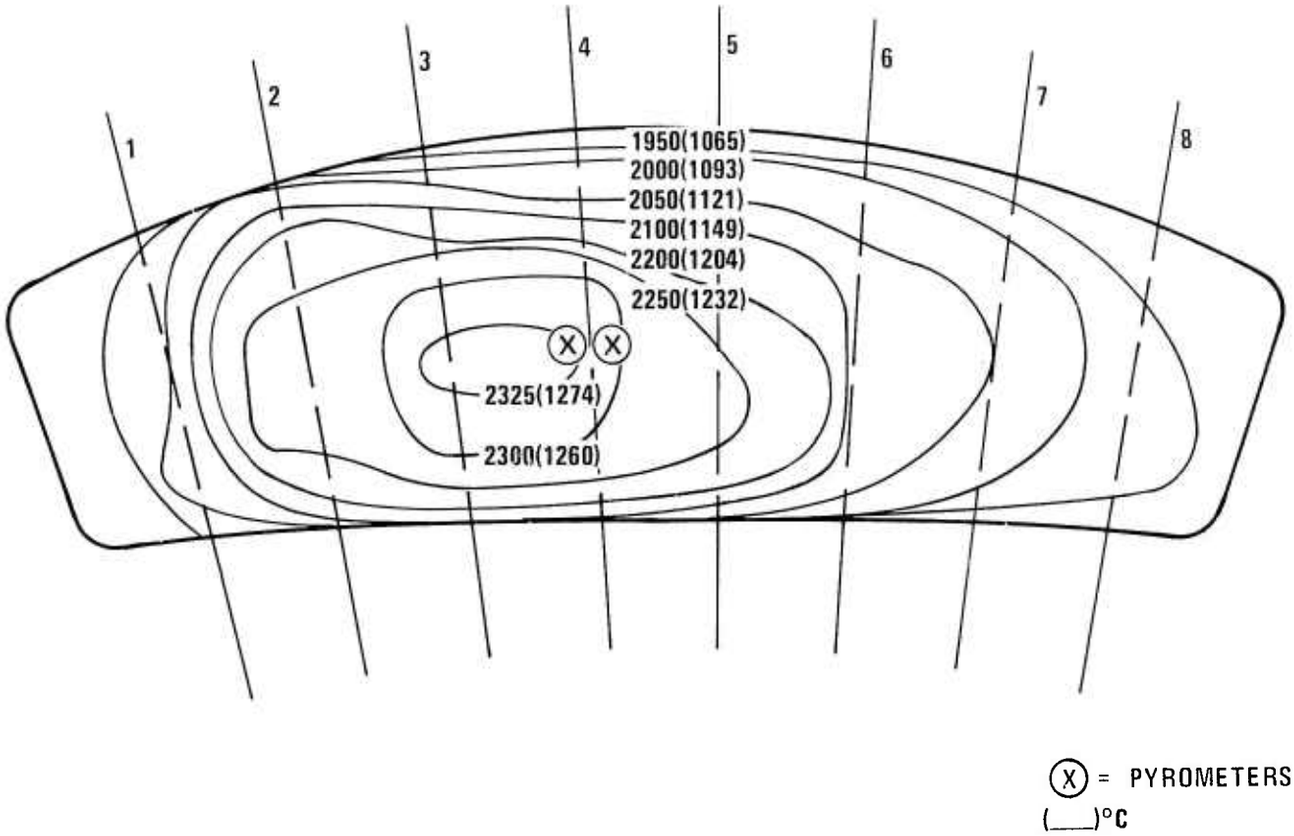

Figure 6.29 Temperature Profile At 2300°F

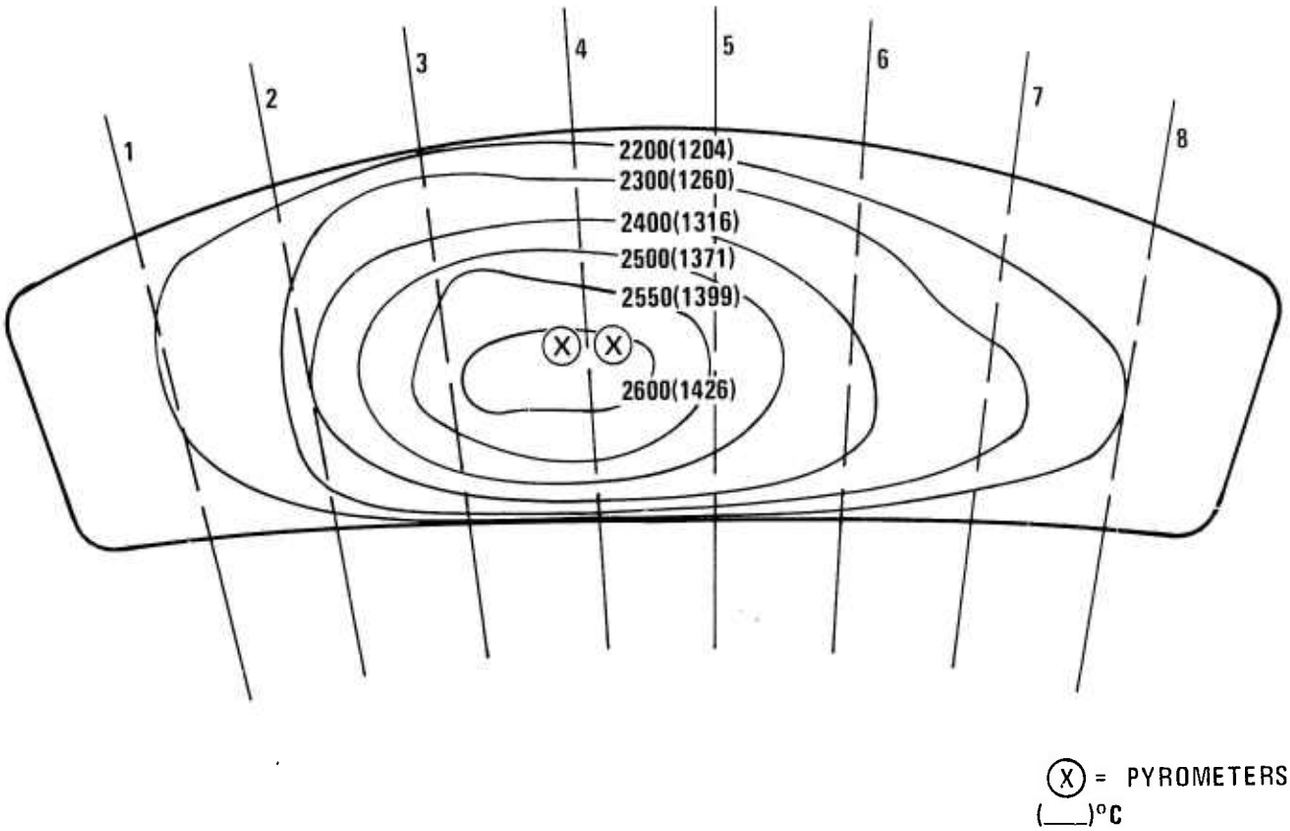

Figure 6.30 Temperature Profile At 2500°F

Other operating conditions were specified as follows:

Airflow	:	31.5 lb/sec
Air Preheat Temp.	:	600°F
Fuel Flow	:	0.85 lb/sec
Fuel Temp.	:	70°F
Shell Pressure	:	105 psig

The maximum heat transfer coefficient on the vane airfoil was about 500 BTU/hr/ft^2/°F. The cycles were similar to those of the 2200°F static rig testing with an increase in peak temperature to 2500°F as shown in Fig. 6.31. The heat-up rate remained 10°F/sec from 1200°F. Cool down represented a ramp to 2000°F (from 2500°F), the 45 second hold, and controlled temperature decay from 2000°F to 1200°F at 25°F/sec. The oscillating temperature condition at 2500°F (Fig. 6.31) apparently resulted from oscillation in the fuel pressure caused by an interaction of the pressure relief valve with an undersized fuel nozzle. While an average temperature of 2500°F was achieved, fluctuations from 2450 to 2600°F were observed.

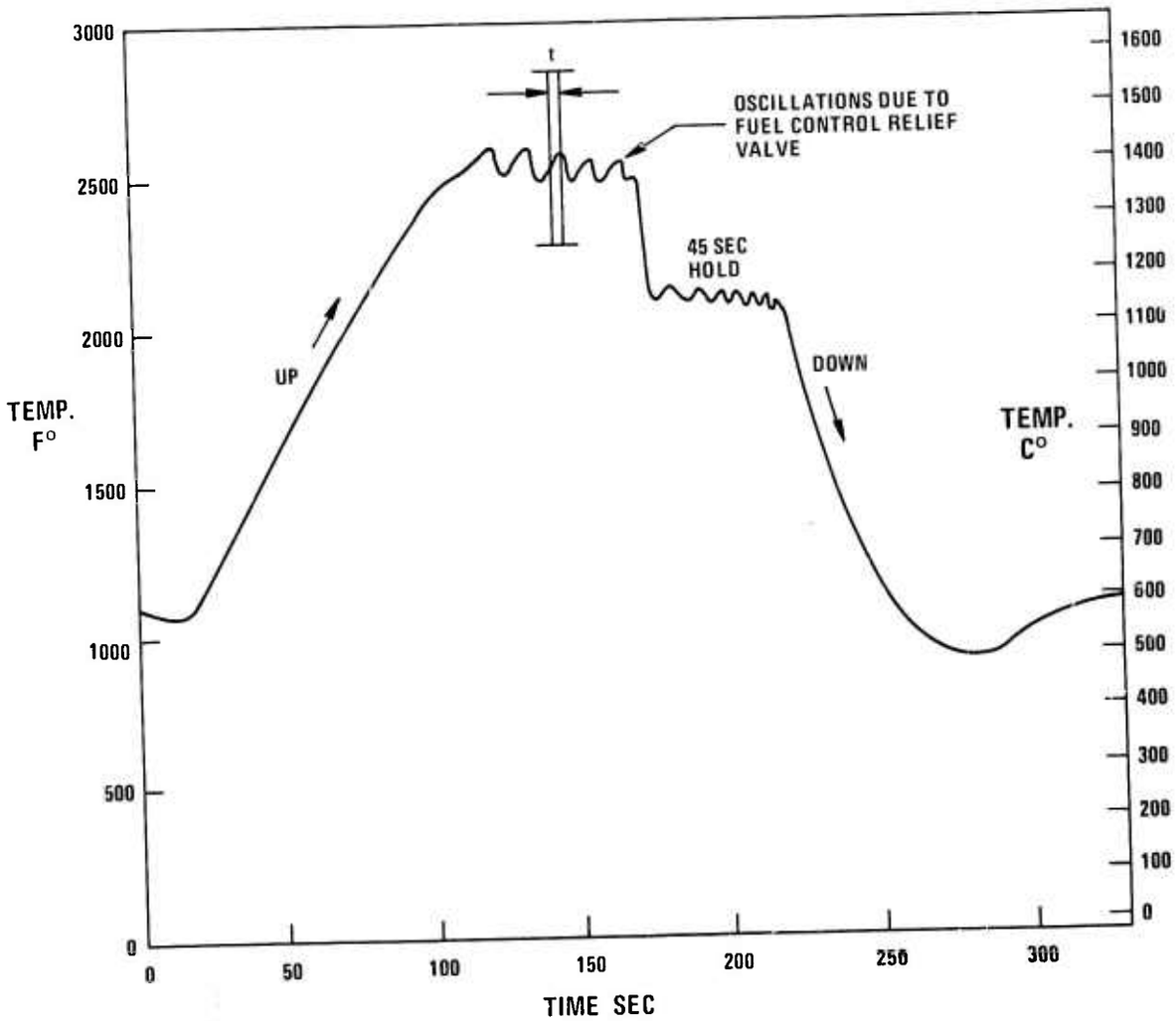

t = TIME AT TEMPERATURE, A VARIABLE

Figure 6.31 Typical Cycle For 2500°F Testing

• Test Configuration -- As stated previously,[6] the test configuration contained four silicon nitride stator vane assemblies in positions 1-4 and four silicon carbide stator vane assemblies in positions 5-8. Three insulator combinations were also employed (Fig. 6.32). Hot-pressed silicon nitride occupied insulator position 1 which protects and supports stator vane positions 1 and 2. LAS Cervit C140 insulators were used in positions 2 and 3 covering vane positions 3-6. The LAS insulator at position 2 was of modified design in that the longitudinal edges were contoured to a 0.250 in. radius to provide edge relief. The LAS insulator at position 3 was of the standard design which failed in 2200°F static rig testing. The fourth insulator position, capping vane locations 7 and 8, was filled with Combat M boron nitride.

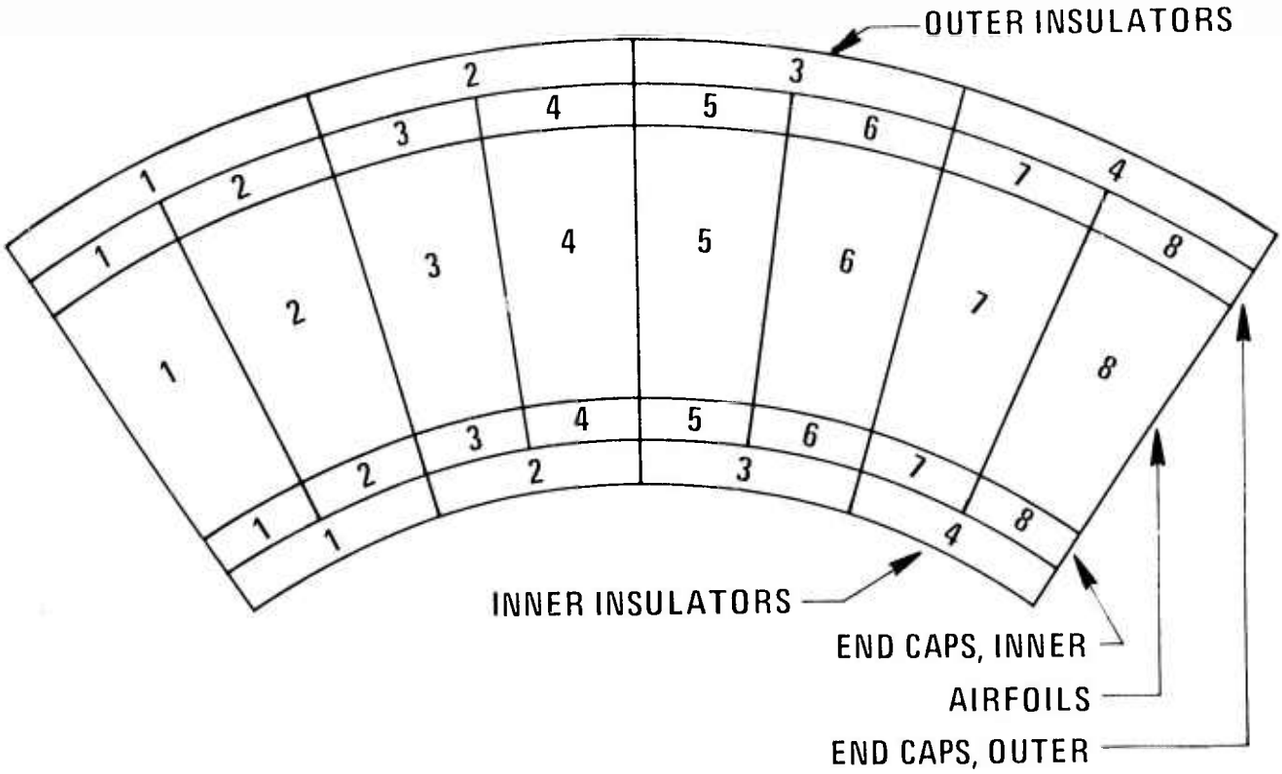

POSITION	END CAPS & AIRFOILS	INSULATORS
1	Si_3N_4	Si_3N_4 HOT PRESSED
2	Si_3N_4	LAS CERVIT C 140
3	Si_3N_4	LAS CERVIT C 140
4	Si_3N_4	BORON NITRIDE TYPE M
5	SiC	
6	SiC	
7	SiC	
8	SiC	

Figure 6.32 Location Of Parts In 2500°F Static Rig Test Assembly

• Test Observations -- Sixteen millimeter Ektachrome color movies were made during the first cycle of static rig testing at 2500°F. It was also possible to observe the concave surfaces of four silicon nitride and two silicon carbide vanes (positions 1-6) visually through the wide angle boroscope as succeeding cycles progressed.

Flames were observed at the vane location from the outset. The amount of flame bathing increased with temperature and completely obscured the vanes at 2500°F. The luminous flame should not and apparently did not affect the radiation pyrometer response to airfoil temperatures, since visible yellow light constitutes only a small part of the spectrum influencing the thermal response. Over 80% of the pyrometric response is attributed to infra-red wavelengths beyond the visible region.

The first and second cycle were run without incident. Cracks were observed in two silicon carbide vanes during the third cycle. These cracks apparently started near the leading edge and propagated roughly parallel to the leading edge. A chip dislodged from the concaveside of one airfoil near the leading edge. All silicon nitride parts appeared undamaged. No significant changes occurred during the fourth cycle.

On the fifth cycle, after reaching steady state at 2500°F, a temperature excursion to 3000°F was noted. The rapid temperature rise invoked automatic emergency procedures which stopped the fuel supply terminating the test. Compressor air continued under conditions of choked flow quenching the vanes to 600°F. The compressor did not stall, but was rapidly unloaded manually using air by-pass valving in the system. Events occurred too rapidly to identify any pressure increase from these effects and the steady state computerized data acquisition system had not yet started to function. The pyrometers and the supervisory thermocouple did record the 3000°F reading.

Inspection of the rig after cool down disclosed:

(1) The combustor basket (Fig. 6.33) had buckled and imploded (creep rupture) sending molten metal and sheet metal debris downstream.

(2) The silicon nitride vanes in positions 1-4 from the left in Fig. 6.34 remained in place and apparently intact. Some metal debris from the combustor is shown against them implying impact. The vanes were heavily coated on the pressure side with metallic splatter and other oxide combustion deposits.

(3) All of the silicon carbide vanes in positions 5-8 were shattered (Fig. 6.34). Airfoils and outer (upper) end caps at positions 7 and 8 had been discharged downstream. The inner (lower) end caps from vane locations 7 and 8 had been displaced but at the test location. The airfoils at positions 5 and 6 were damaged extensively. These components remained under compressive spring load with end caps in place, however.

(4) The metal debris from the combustor and dislodged silicon carbide vane fragments apparently passed through the entire rig since only a few pebble-sized (1 to 3 cm diameter) pieces were reclaimed.

(5) Evidently, the passage of metal and carbide pieces triggered the failure of the ceramic lining of the hot gas duct, pieces of which then slammed into the mixer section. Duct lining fragments literally

blasted a hole through fifteen inches of cast alumina barrier wall before coming to rest. The mixer inlet and exit are shown in Figs. 6.35 and 6.36, respectively.

(6) All control thermocouples were bent back nearly flat either by creep or the passage of debris.

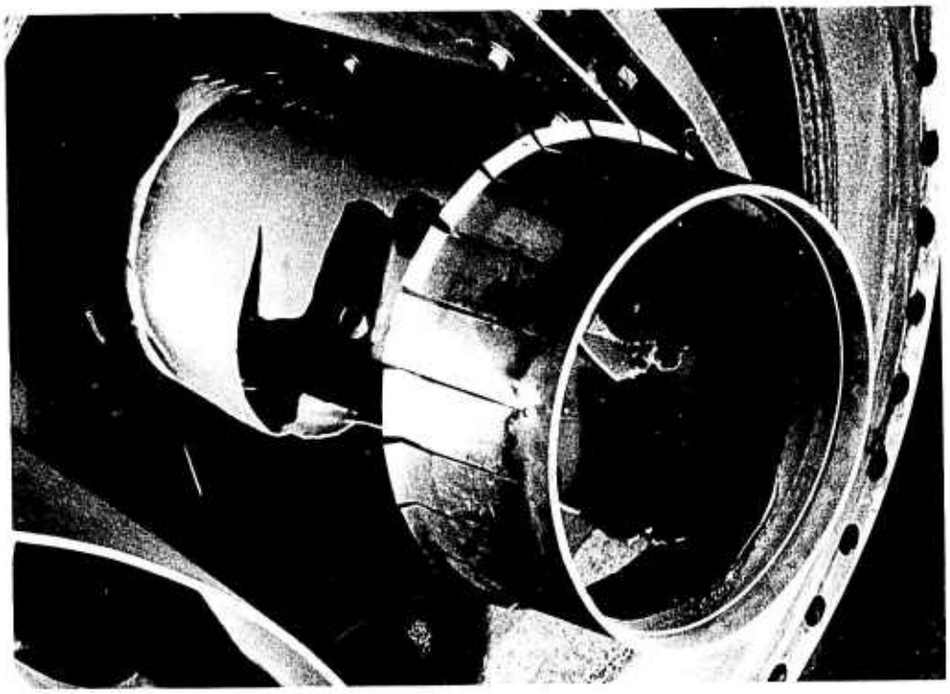

Figure 6.33 Combustor Failure From 2500°F Static Rig Tests

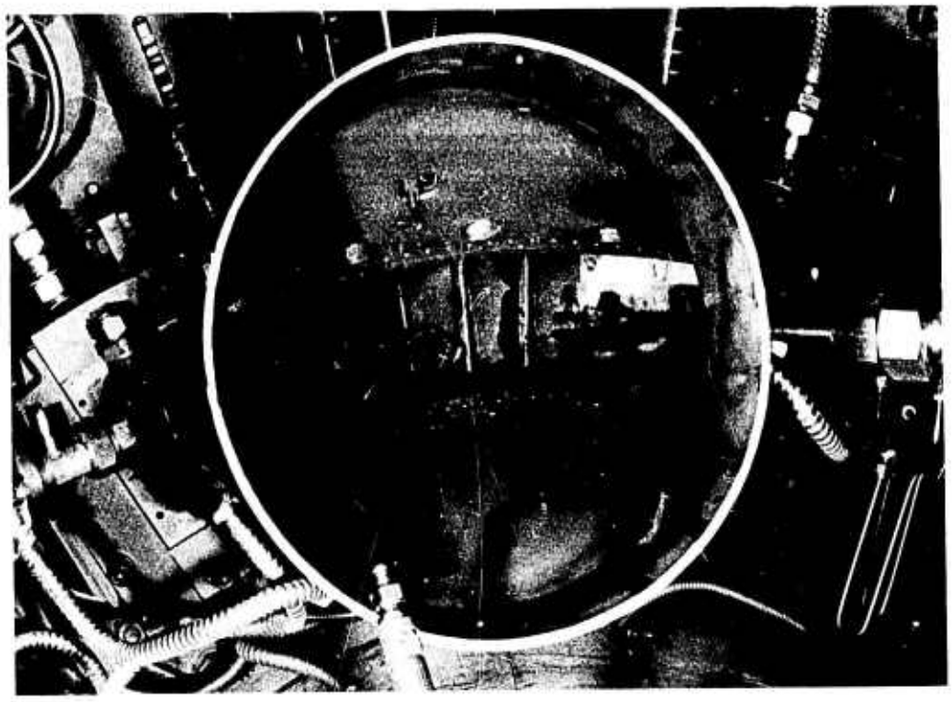

Figure 6.34 Silicon Nitride (Left) And Silicon Carbide (Right) Stator Vane Assemblies After 2500°F Static Rig Test (5 Cycles)

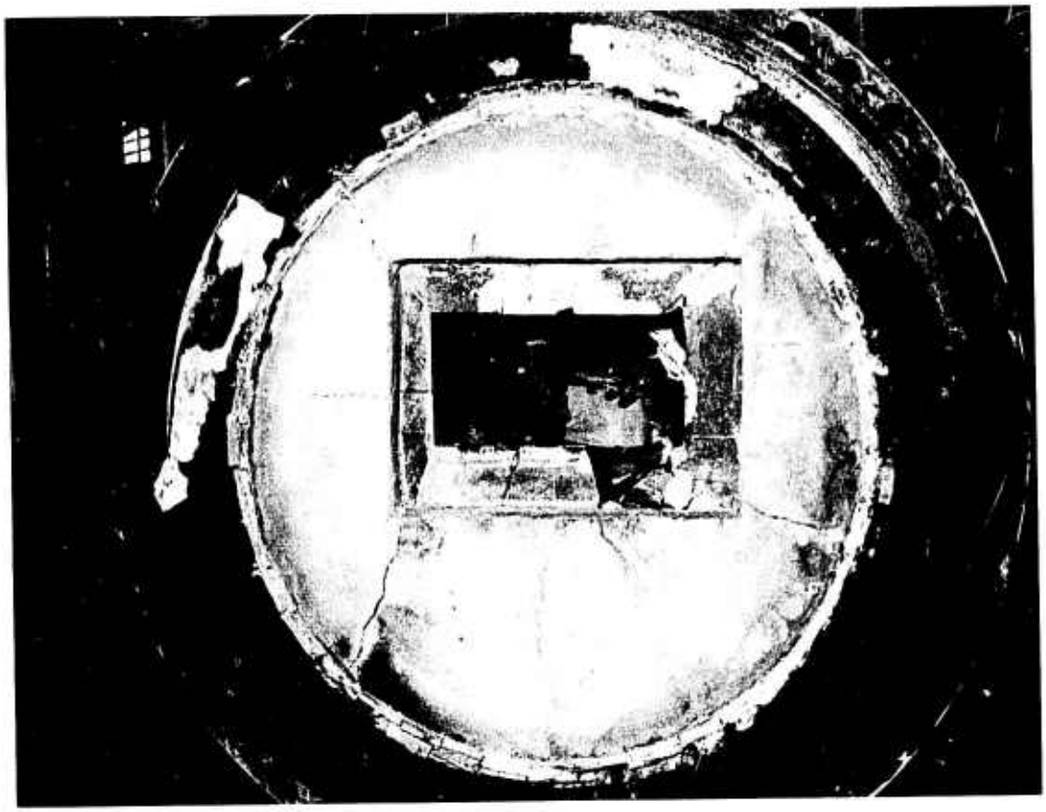

Figure 6.35 Ceramic Mixer-Inlet Side - 2500°F Static Rig Test

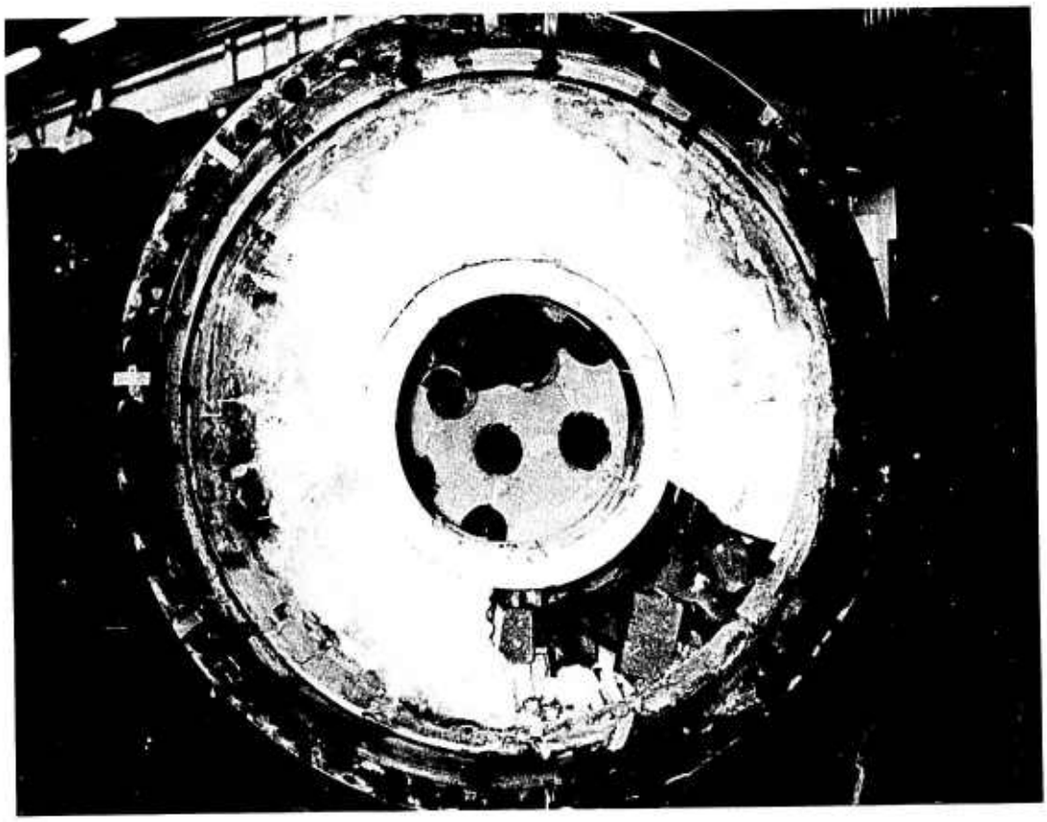

Figure 6.36 Ceramic Mixer-Outlet Side - 2500°F Static Rig Test

One can only deduce that the temperature surge occurred after the implosion, either because combustion shifted to a zone near the combustor failure or because the burner flame was heating up less air as a result of a flow blockage. The open area in the mixer was reduced to half its original size. The heat transfer coefficients would be decreased due to low flow in the 3000 to 600°F (1649 to 316°C) transient, thereby moderating the effect.

Failure Analysis of Stator Vane Components

A more detailed examination of the sandblasted and cleaned airfoils and end caps has been done since the test. Figure 6.37 is typical of the Si_3N_4 components surviving the test. One silicon nitride airfoil and two end caps were cracked. All carbide pieces were badly shattered or cracked. Figure 6.38 illustrates the crack pattern identified by dye penetrant techniques on airfoil #1 made of Si_3N_4. There are three points of crack initiation, marked O_A, O_B and O_C, respectively. The major crack initiated at O_A, from which most of the branching proceeded. X-ray radiography and ultrasonic "A" scanning was conducted to determine whether a foreign object or other defects was associated with point O_A. X-ray radiography did not show any foreign particles, nor did a comparison of X-ray radiographs prepared before and after testing indicate any defect in the proximity of point O_A. The area between branches O_A and O_C were ultrasonically scanned to determine whether the O_B and O_C initiation points could be associated with planar cracks extending from the O_A branch. No conclusive evidence was found. It, therefore, seems that all three points of crack origin in airfoil #1 are associated with transient thermal stress.

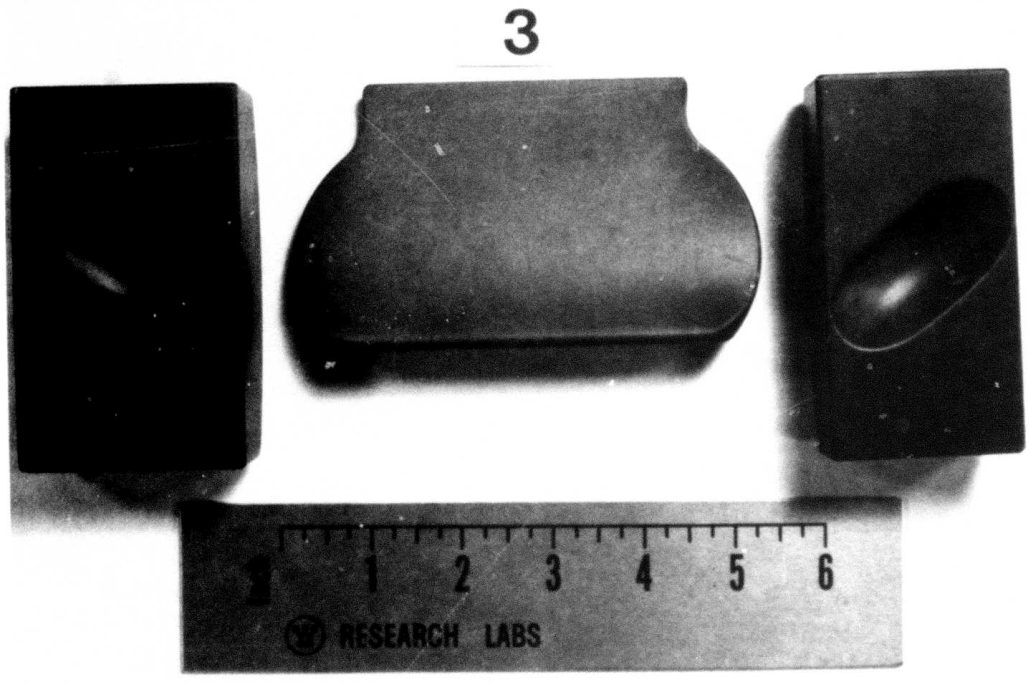

Figure 6.37 Typical Si_3N_4 Stator Vane Assembly After 2500°F Test (Cleaned)

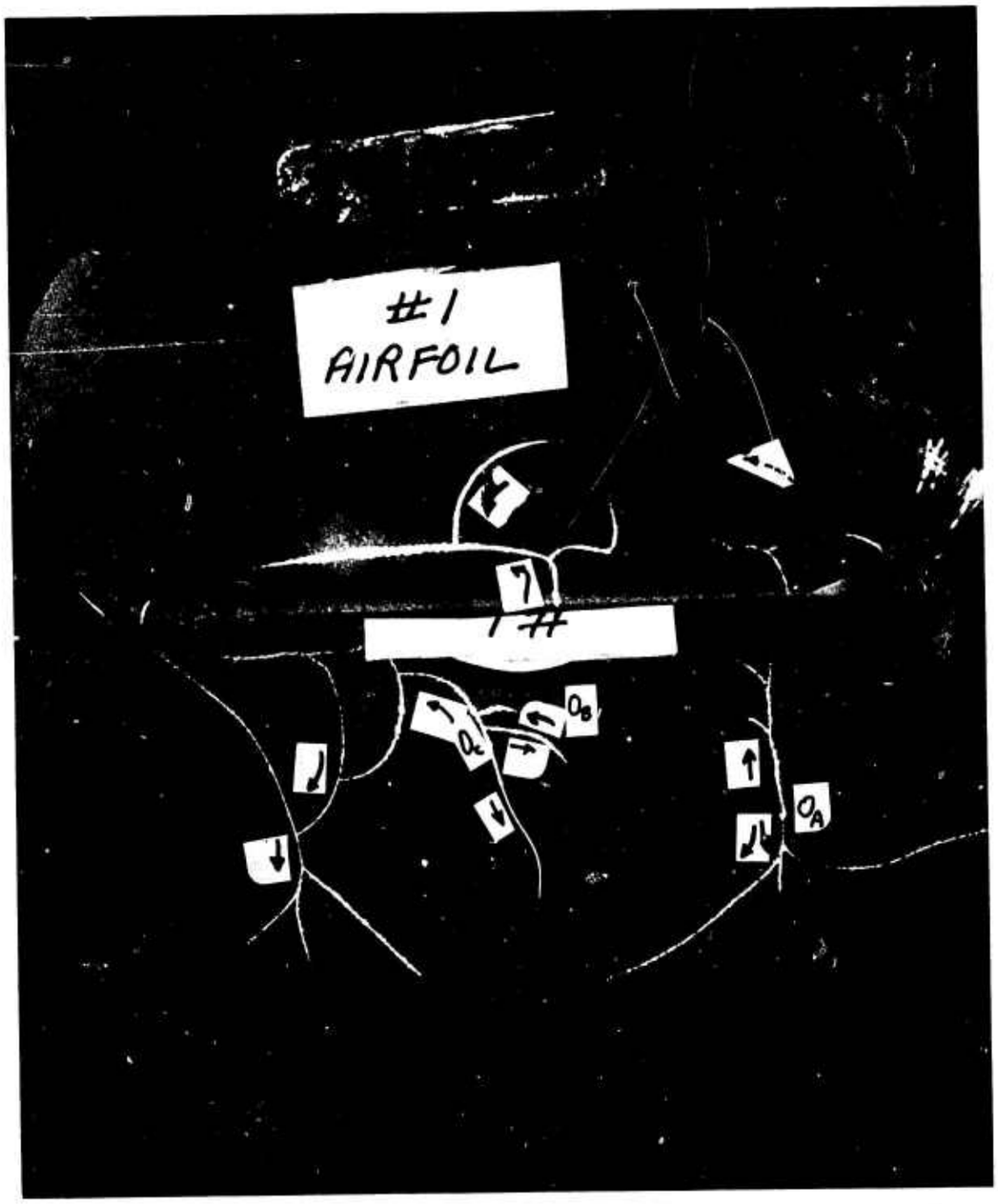

Figure 6.38 Silicon Nitride Airfoil With Thermal Cracks After 2500°F Test

The crack pattern on Si_3N_4 end cap #2 is shown in Fig. 6.39. There is a well defined origin at "O" which is associated with the edge of the torroidal cavity. Cracks were also observed in Si_3N_4 end cap #4 (Fig. 6.40). Here, the major crack branching originated at point O_A which is at the lower edge of the end cap. Two other points of origin were identified at O_B and O_C as indicated. Since there is no possibility of edge loading at either the specific point of crack origin in end cap #2 or at any of the origins in end cap #4, failures must be attributed to transient thermal stress. Stress concentrations may be associated with rough grinding marks along irregularly finished edges.

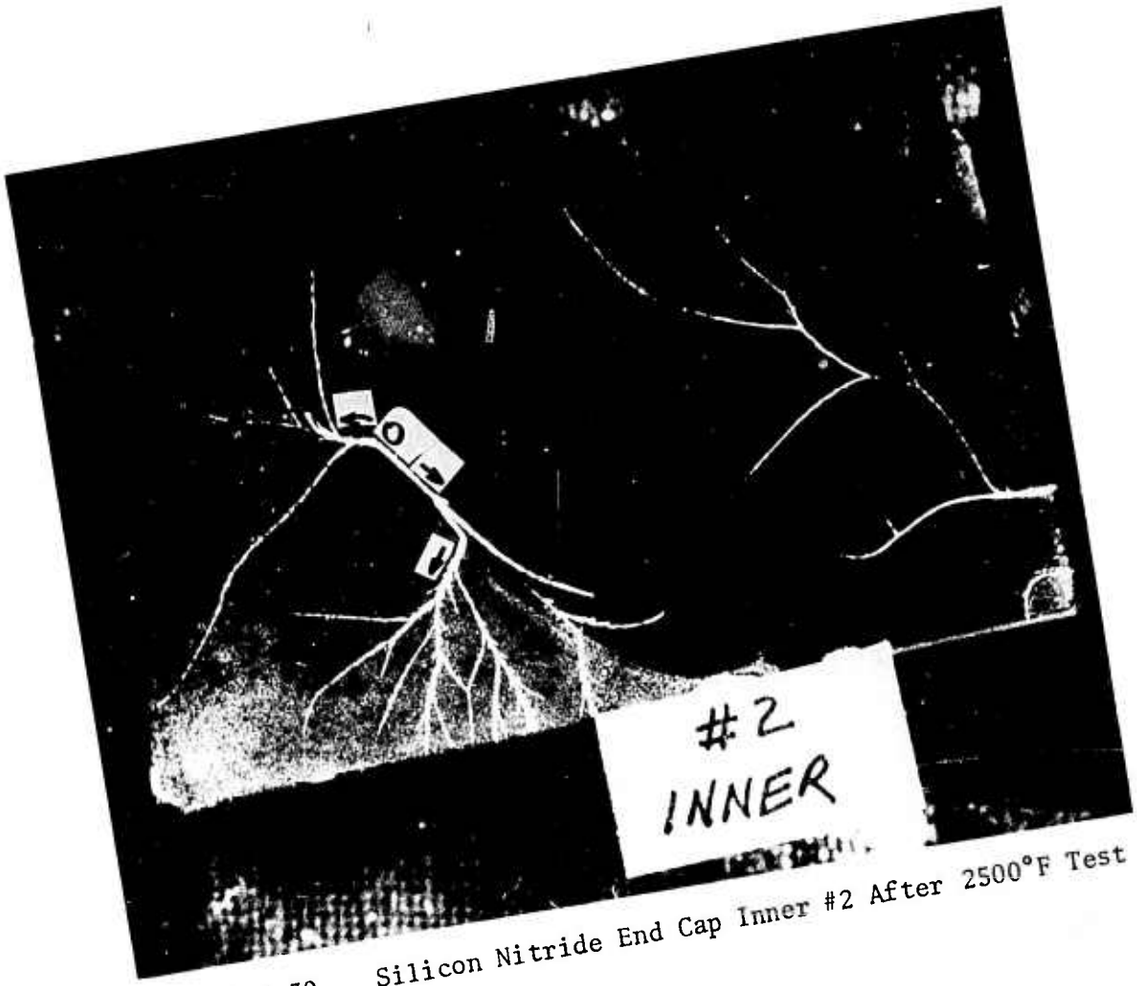

Figure 6.39 Silicon Nitride End Cap Inner #2 After 2500°F Test

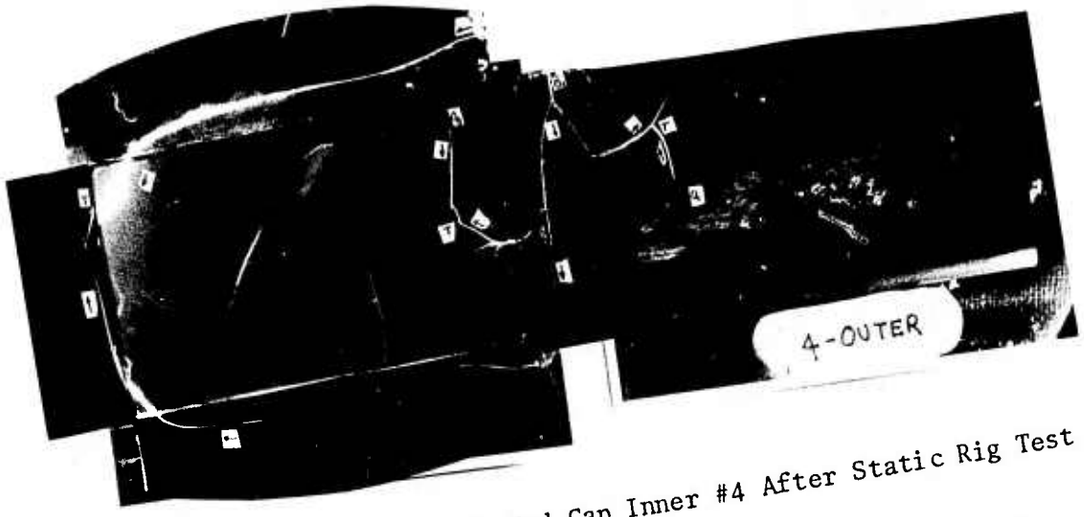

Figure 6.40 Silicon Carbide End Cap Inner #4 After Static Rig Test At 2500°F

Crack patterns in two of the SiC end caps appear in Figs. 6.41 and 6.42. There are two points of origin in end cap #5. O_A is located at the rim of the torroidal cavity at a position where edge loading as a result of airfoil tenon contact is impossible. O_B is located at the edge of the inner plane. The prolific branching at the left half of the front plane indicates the strong effect of thermal gradients.

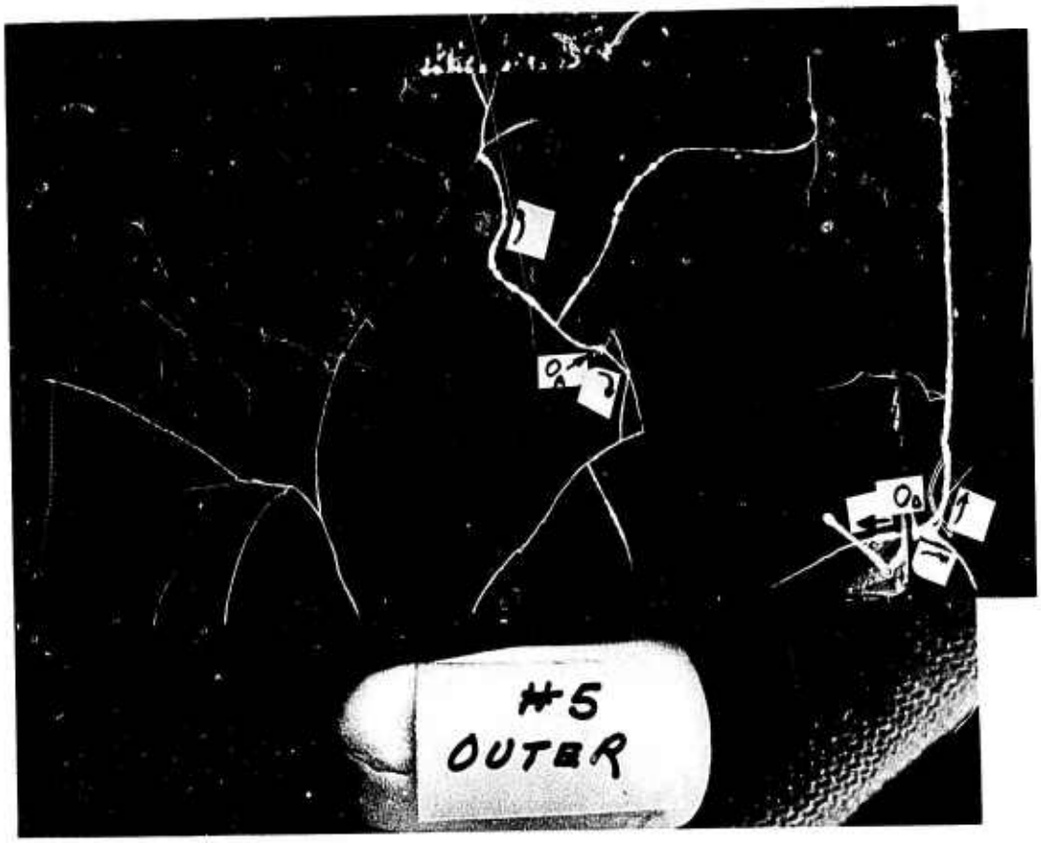

Figure 6.41 Silicon Carbide End Cap Outer #5 After Static Rig Test At 2500°F

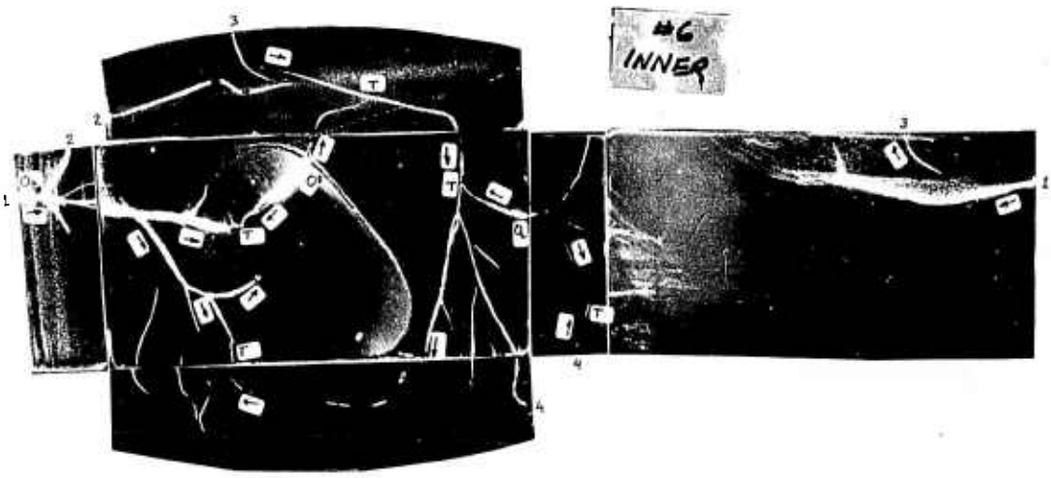

Figure 6.42 Silicon Carbide End Cap Inner #6 After Static Rig Test At 2500°F

End cap #6, Fig. 6.42, shows three points of crack initiation. O_A, the origin of the major crack pattern, is associated with the bottom edge of the end cap. Point O_B has not been located, but it is probably associated with a point at the edge of the torroidal cavity. O_C appears at the edge of the front face. Again, all failures originate at edge locations but none are associated with edge loading.

In summary:

(1) Cracking of the one Si_3N_4 airfoil was attributed to thermal stresses.

(2) Most of the cracked end caps showed multiple failure origins, all associated with edges. Since edge loading was considered impossible in all cases, failures are attributed to thermal stresses.

(3) It was impossible to tell anything further about the failure of silicon carbide vane components because mixing of fragments and missing pieces made reconstruction impossible. However, the airfoil failures occurred prior to impact from metal debris.

Insulator Evaluation After Test

Insulator pairs from the first five cycles of static rig testing at 2500°F are shown in Fig. 6.43. The LAS insulators developed thermal cracks as predicted. Local points of fusion were also identified. Failure occurred by edge loading principally at the left downstream position. The design change creating edge relief did not improve LAS insulator performance appreciably.

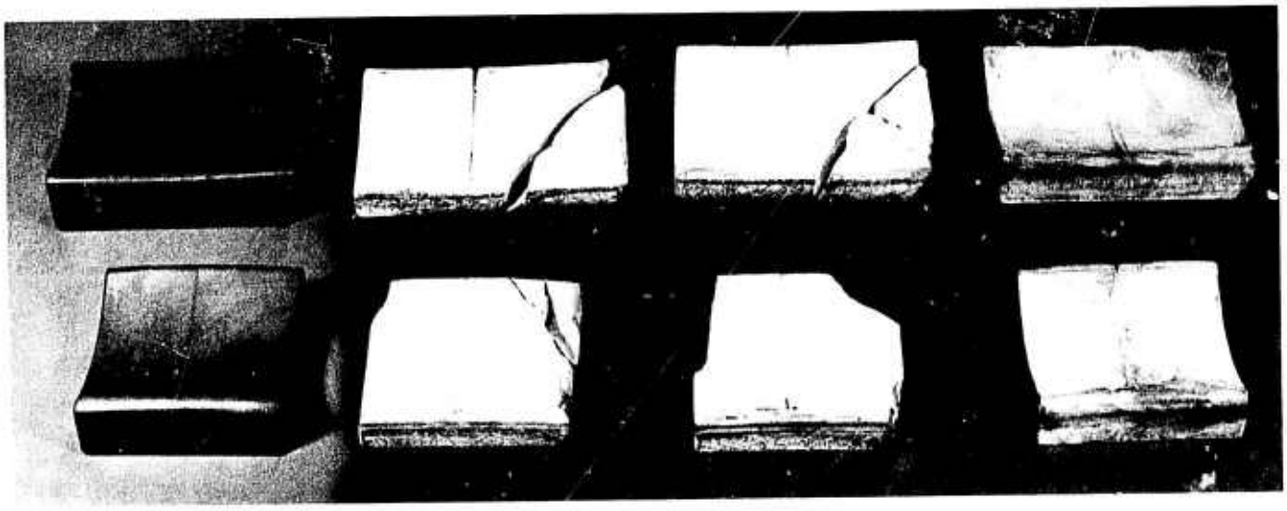

Figure 6.43 Insulators From 2500°F Static Rig Test (5 Cycles)

The hot-pressed silicon nitride and Type M boron nitride insulator survived without apparent damage. Type M boron nitride will be used exclusively in the continuation of static rig testing at 2500°F since it appears to be the best alternative to LAS according to data presented in Tables 6.1 and 6.2 and it is not limited to temperatures below 1800°F.

6.1.5 VANE FABRICATION

Introduction

The Norton Company continues as the sole source of hot-pressed materials for the fabrication of stator vane assemblies. No new hardware has been delivered during the report period, but silicon nitride vanes are being fabricated in production quantities. Billets of silicon nitride hot-pressed with yttria have been ordered for initial evaluation.

Vanes for Advance Turbine Testing

Norton is currently fabricating one hundred silicon nitride stator vane assemblies for the Advanced Turbine Test from their NC 132 material. The design is that of a tapered-twisted airfoil with two end caps in which the cavity depth has been reduced from that of the first generation design.[5,6] Fabrication differs from that employed previously in that production methods ammenable to large quantities rather than individual pieces will be employed. For example, Norton has engaged Ex Cello Corporation to grind the airfoils using a modified version of their drum-cam milling process which is competitive with the forging of compressor and turbine blading.

Prototype airfoils have been produced. Westinghouse has approved the processing steps and accepted the qualification standards and guillotine guaging required for airfoil inspection.

Originally scheduled for delivery for the end of June 1975, Norton agreed to produce the first ten stator vane assemblies by March 1, 1975 so that these could be used for the resumption of static rig testing in April, 1975. As things now stand, airfoils and end caps will become available after May 1, 1975 with airfoils to be delivered by April 25, 1975.

A vendor problem is cited as the cause of delay. An original source could not complete the airfoil tenon machining job as contracted. Ex Cello has accepted the committment to produce the entire airfoil with tenon ends but changes in the machining process made the re-order of small formed grinding wheels mandatory. Problems with the end cap machining process were also encountered.

Yttria Hot-Pressed Si_3N_4

The development of yttria hot-pressed silicon nitride by AMMRC[33] provides a new, creep-resistance material with exceptional high temperature strength for turbine vane evaluation. Norton has accepted a purchase order to produce six 6" x 6" x 1/2" billets; 2 each containing 13.0%, 16.5% and an optimum composition within six weeks for initial property evaluation. The best of three compositions will be selected for vane fabrication and eventual test if properties warrant it.

6.1.6 WATER-COOLED STATIC RIG FOR 2500°F TESTING

Introduction

Rig failure during the fifth cycle of static rig testing at 2500°F necessitated the complete rebuilding of the static rig. Only the outer shell and test configuration were retained. A redesigned combustor was installed. Water and spray cooling are being employed for the exhaust duct and mixer sections, respectively.

Static Rig Modification

The static rig has been completely rebuilt after the catastrophic failure during the fifth cycle of testing at 2500°F. A schematic drawing of the modification is presented in Fig. 6.44. The combustor was redesigned and fabricated with a new secondary section. Two rows of smaller diameter scoops, two extra corrugations (for additional wall cooling), and a conical portion between the corrugations were added without changing the downstream diameter. The exchange of dillution air for the extra cooling air was designed for no overall change in pressure drop. Six thermocouples were installed to measure secondary section wall temperatures.

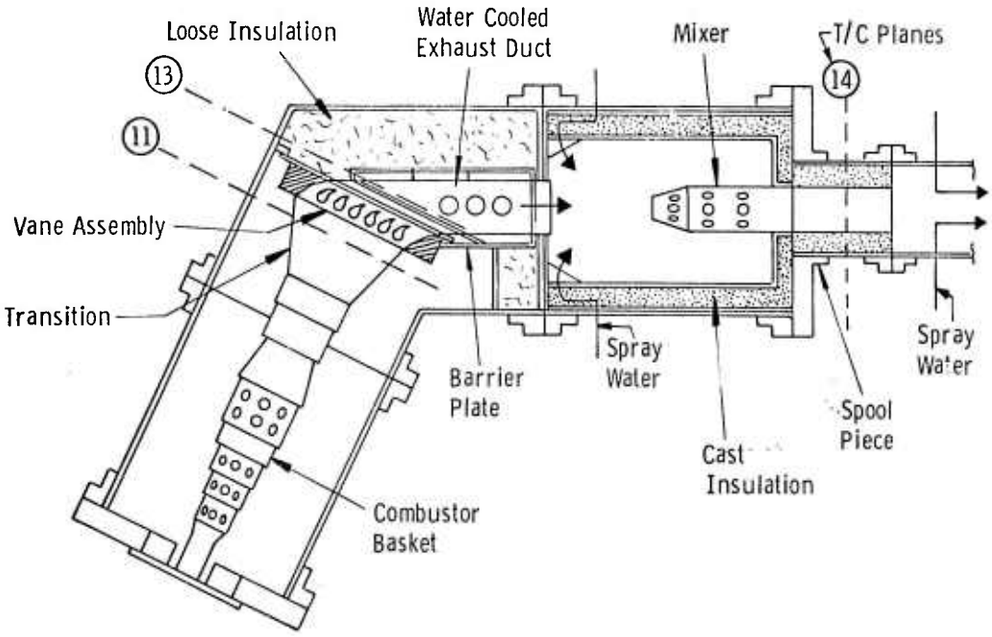

Figure 6.44 Water Cooled Rig For 2500°F Test of Ceramic Vanes

The ceramic exhaust duct was replaced with the water-cooled component shown in Fig. 6.45. Three separate cooling sections are supplied with three separate inlets and outlets. Fifteen thermocouples were provided to monitor the metal wall temperatures during operation. The miter shell section was modified to permit entry and exit of cooling water for the exhaust duct.

The mixer section was redesigned to provide an insert containing six water spray nozzles upstream and a metallic mixer downstream. The insert was cast into the shell using castable alumina with fiberfoam liners. The spray water will cool the gas to 2000°F maximum at the mixer inlet when the vanes are operating at 2500°F.

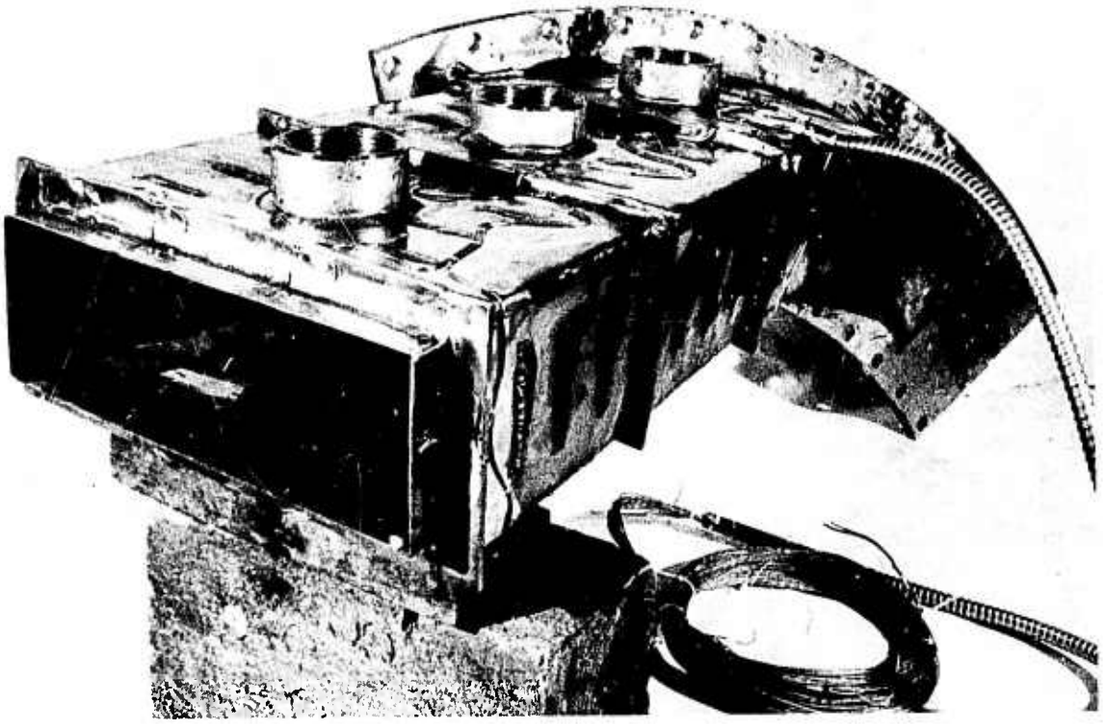

Figure 6.45 Water Cooled Exhaust Duct

The alumina castable liner of the spool piece was repaired in the upstream portion. Only 5 thermocouples were installed to measure exiting gas temperatures because control will be moved upstream using Pt/Pt-Rh thermocouples and the radiation pyrometers at the vane inlet location.

Test Plan

The static rig testing at 2500°F will be resumed in June when silicon nitride stator vane assemblies of the advanced test turbine design are made available. This hardware will have the tapered-twisted airfoil but will not exhibit the enlarged tenon ends to fill the end cap cavities. Test results are expected at the end of the next report period.

Heat Transfer Tests

The static rig will be used to conduct low temperature heat transfer tests and make strain measurements in the interim period before the silicon nitride vanes of advanced turbine design are delivered and installed for the resumption of 2500°F testing. Metal vanes, instrumented with tehrmocouples and strain guages, will be used to obtain data to check the accuracy and reliability of stress analyses conducted on ceramic vane assemblies. Heat transfer coefficients will be generated for an actual three piece vane configuration.

Tests are planned in two temperature regimes: (1) RT to 1050°F with strain guages and thermocouples attached, and (2) RT to 2000°F with only thermocouples. Data extrapolation from 2000°F to 2500°F should produce small errors only because the film coefficient of heat transfer does not change rapidly as a function of temperature at high temperature. To date, the metal vane assemblies have been fabricated and are being instrumented with thermocouples and strain guages.

7. PROGRESS ON MATERIAL TECHNOLOGY-STATIONARY TURBINE PROJECT

7.1 MATERIAL ENGINEERING DATA

SUMMARY

In the stationary turbine project, commercially produced hot-pressed silicon nitride and silicon carbide have been under intensive investigation so that physical, mechanical and thermal property data would be available to the design engineers and stress analysists, as required. This work is expected to continue throughout the program in order to up-date properties as material improvements evolve and to verify billet properties. The latter helps assure reliability of test components fabricated from the hot-pressed billets. This section deals with this continuing acquisition of property information.

Tensile testing of hot-pressed silicon nitride at high temperatures was continued during this report period with emphasis on the acquisition of stress-strain data. These data are being used for 3-dimensional finite element stress analysis that takes into account non-elastic material behavior.

Tensile creep experiments were conducted to determine the possibility of beneficial effects of pre-oxidation on the stress rupture life of hot-pressed silicon nitride in both inert atmospheres and air.

Because LAS insulators have not performed well under static rig testing conditions, the flexural strength of this material was examined to determine the effects of machining and heat treatment.

The flexural creep test has been analyzed to explain differences that are found when flexural and tensile creep data are compared The latest results of low cycle fatigue testing are presented. Erratic behavior appears to be associated with billet to billet variability.

7.1.1 TENSILE TESTS OF Si_3N_4

Introduction

Previous reports have presented statistical tensile strength data for Norton HS-130 silicon nitride.[2-6] In this report period, a closer examination has been made of the non-elastic response of this material from 1800° to 2500°F. The data are of interest for 3-dimensional finite element stress analyses that take into account the non-elastic behavior of materials.

Results

Eight 2-1/4" x 1/4" guage tensile specimens[3] were pulled to failure at 2500°F (strain rate 0.001 in/in/min). The results are plotted in Fig. 7.1. Failure occurred between 20,000 and 25,000 psi in all cases at strains between 0.0023 and 0.0018, respectively. A definite yield point can be detected at ∿ 0.0008 in/in strain (16,000 psi).

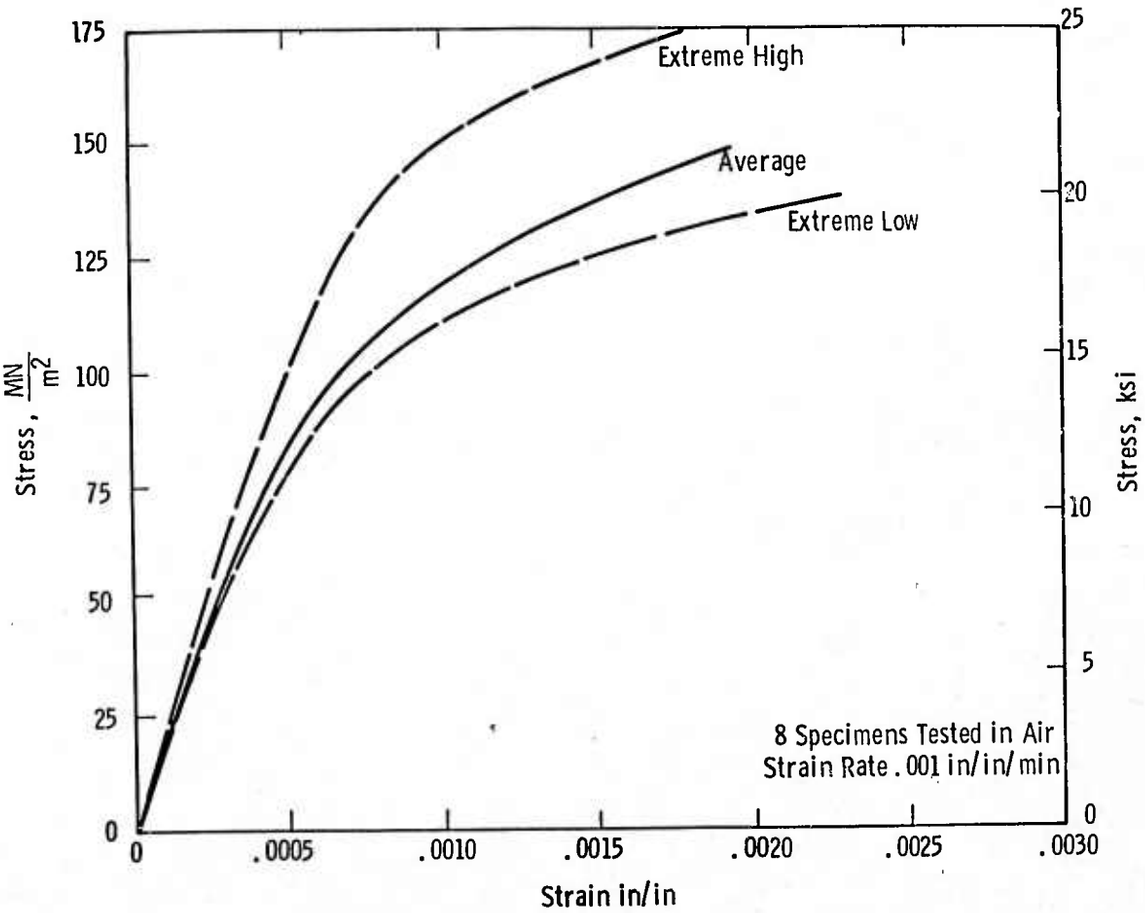

Figure 7.1 Average Stress Strain Curve For Silicon Nitride At 2500°F

7.1.2 FLEXURAL TESTS OF LAS

Introduction

LAS insulators of the 8.00 inch radius configuration were tested in both the 2200°F and 2500°F static rig tests. All LAS insulators developed cracks, caused principally by transient thermal stresses at the upstream circumferential edge or by edge loading at the downstream circumferential edge. As a part of the evaluation of the failed insulators, 4-point loading flexure tests at room temperature were conducted on both untested insulator remnant material and material removed from one of the failed insulators at an apparently undamaged location (2200°F static rig tests[5]). Specimens which had been heat treated to 2000°F for 2 hours to permit the healing of machining damage and specimens ground in both the longitudinal (lengthwise) and transverse (widthwise) directions were also tested.

All specimens were 1.125" x 0.125" x 0.25" ground approximately to the specification used for the insulators tested in the static rig. The results are given in Fig. 7.2. Transverse grinding lowered the average strength ∿ 15% below that of the material ground longitudinally. Heat treatment had very little effect. The insulator that was exposed in the 2200°F static rig tests degraded to 46% of the materials virgin transverse strength.

One can only conclude that temperatures in the static rig at insulator locations did exceed 2000°F locally and this condition contributed to the insulator failure observed.

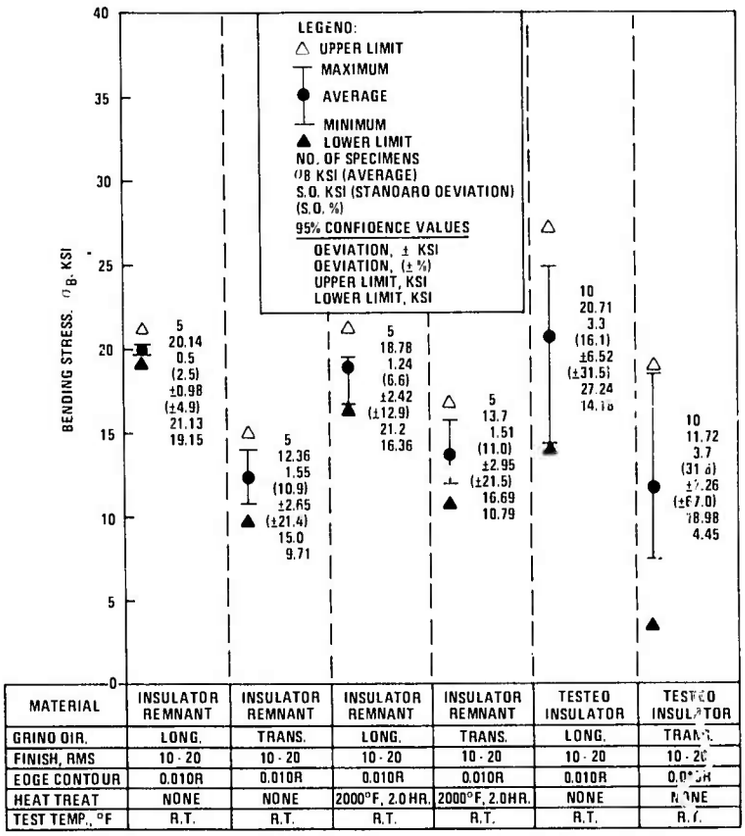

MATERIAL	INSULATOR REMNANT	INSULATOR REMNANT	INSULATOR REMNANT	INSULATOR REMNANT	TESTED INSULATOR	TESTED INSULATOR
GRIND DIR.	LONG.	TRANS.	LONG.	TRANS.	LONG.	TRANS.
FINISH, RMS	10 - 20	10 - 20	10 - 20	10 - 20	10 - 20	10 - 20
EDGE CONTOUR	0.010R	0.010R	0.010R	0.010R	0.010R	0.010R
HEAT TREAT	NONE	NONE	2000°F, 2.0 HR.	2000°F, 2.0 HR.	NONE	NONE
TEST TEMP., °F	R.T.	R.T.	R.T.	R.T.	R.T.	R.T.

Figure 7.2 Flexural Test Results For Cervit C140 LAS Insulator Material At Room Temperature

7.1.3 CREEP IN Si_3N_4

Introduction

It has been shown in previous reports[4-6] and a pending publication[34] that the stress rupture life of Si_3N_4 tested in air exceeds that of specimens tested in an inert atmosphere, i.e., helium. Silicate glass that forms rapidly on the surface as a product of oxidation is thought to provide an effective mechanism for smoothing surface imperfections and healing crack type defects. Experiments were conducted to test this hypothesis and to see whether pre-oxidizing heat treatments would increase the stress rupture life of silicon nitride in a turbine environment.

Results

Several specimens were pre-oxidized in air at 2500°F for tensile creep tests in helium and in air at 15,000 psi stress. The results are summarized in Table 7.1. It is clear that pre-oxidation increases the stress rupture life of Si_3N_4 in He by the accommodation of more strain to failure. Total creep strain is highest in air because the supply of fresh oxide is continuous.[34] In helium, some oxide is lost as a result of the low oxygen partial pressure of the system.

TABLE 7.1. CREEP OF PRE-OXIDIZED Si_3N_4[a] (HS-130)

	No Treatment	Pre-oxidized 200 hr, 2500°F
Rupture life hrs.	75, 44	503
Total Strain %	0.8 0.7	1.17

(a) Tested in He at 2300°F, 15,000 psi tensile stress

7.1.4 FLEXURAL CREEP ANALYSIS

Introduction

The flexural test is commonly used to determine creep properties of ceramic materials. Often, there is a discrepancy between creep values determined by this test and those determined by uniaxial tensile testing. For apparently equivalent initial stress levels, the flexural test produces both lower strains and steady state strain rates than does the uniaxial test. The differences can be attributed to the fact that whereas the constant load applied to a tensile specimen translates into constant stress, a constant load on a flexural specimen creates a constant moment. The stresses throughout the flexural specimens respond so as to maintain this moment. In fact, they change for all cases except for those materials having a linear stress-strain response. The lower strains and strain rates observed for the flexural test result from decreases in outer fiber stresses from those initially imposed.

Analyses have been presented previously.[5,6, 35-39] The analysis to be presented here considers creep in bending for a material having an arbitrary time dependent law of deformation. Methods for calculating outside fiber stresses from measurable quantities will be given. Also, the results of several exemplary calculations are shown to illustrate the methods.

Analysis of Flexural Creep

For a bar with rectangular cross-section, loaded by forces directed perpendicular to its longitudinal axis, having cross-sections which remain planar during bending, the general equation relating the outer fiber stresses to the moment, time and strain is:

$$\frac{\sigma_t \sigma_c}{\sigma_t + \sigma_c} = \Phi = \frac{1}{bh^2}\left[2M + \frac{\varepsilon^*}{d\varepsilon^*/dt}\left(\frac{dM}{dt} - \frac{dM}{dt}\bigg|_{\varepsilon^*}\right)\right] \qquad (1)$$

where σ_t is the outer fiber tensile stress, σ_c is the outer fiber compressive stress, b is the specimen width, h is the specimen thickness, M is the applied moment, ε^* is the total strain difference between the tensile and compressive outer fibers and t is the time. The instantaneous total strain rate $d\varepsilon^*/dt$ is the rate of applied moment change, and $dM/dt|_{\varepsilon^*}$ is the rate of moment change due to stress relaxation at constant total strain.[5,6] For a constant moment creep test, dM/dt is zero. Therefore, the generation equation for flexural creep is:

$$\frac{\sigma_t \sigma_c}{\sigma_t + \sigma_c} = \Phi_c = \frac{1}{bh^2}\left[2M - \frac{\varepsilon^*}{d\varepsilon^*/dt} \cdot \frac{dM}{dt}\bigg|_{\varepsilon^*}\right] \qquad (2)$$

Equation (2) relates the unknown values of σ_t and σ_c on the left to the measurable quantities on the right. M is the applied moment. In four-point loading:

$$M = \frac{P}{2} a \qquad (3)$$

where P is the load and a is the moment arm. The ε^* is linearly proportional to the deflection, the proportionality constant being a function of the loading fixture geometry and the specimen thickness. Over a

region of constant moment (the inner span, c, of a four point loaded specimen):

$$\varepsilon^* = hD/c^2 \tag{4}$$

where D is the deflection at the center with respect to the inner loading points. The $d\varepsilon^*/dt$ is the tangent to the creep curve, ε^* versus t, for the particular ε^* being considered.

The values of $dM/dt|_{\varepsilon^*}$ can be obtained in a variety of ways. The simplest, from an experimental standpoint, is to run multiple creep tests at three or more moment levels. On a M versus t plot, iso-strain (moment relaxation) curves can be drawn. Tangents to these curves at the particular moment magnitudes determine the $dM/dt|_{\varepsilon^*}$ values.

An alternative method of obtaining these moment relaxation rates with a single test requires equipment that can be switched from a constant load mode to a constant deflection mode. Intermittently, the creep test is interrupted and moment relaxation curves are determined over a period just sufficient to establish the slope. This method is particularly useful if the material has a strong history dependence where multiple tests may not produce the proper moment relaxation data. If the times of creep test interruptions are small in comparison to the total time, the interruption should have little effect on the material structure.

As with the constant deflection rate test previously reported,[5,6] it is necessary to have another function relating σ_t to σ_c in order to exactly solve Eq. (2). Lacking that function, boundary conditions can be established. The creep responses of most materials will fall within these boundaries, and, generally, depending on the nature of the deformation, will fall closer to one or the other.

This is illustrated in the tensile stress-tensile strain-time plot of Fig. 7.3. A material will respond so as to remain on the surface bordered by OABCDE. For the creep test, the material is initially loaded elastically along line OA at time zero. Three types of creep (ε_t versus t) curves are illustrated. Curve AB is the constant stress curve calculated from uniaxial tensile testing. Curves AC and AD are calculated for constant moment flexural creep tests. Curve AC is for a material whose non-linear, time dependent deformation response is the same in tension and compression. This would be the case for most metals and some ceramics. Curve AD is for a material which is resistant to compressional deformation, as are numerous ceramics. It is calculated by allowing the compressional side of the flexural specimen to deform only elastically. The creep deformation of most real materials would, therefore, fall between the boundaries of curves AC and AD.

It should be noted from Fig. 7.3 that the tensile stresses of bars flexed under conditions of constant applied moment decreases with time for a material which undergoes creep and has a non-linear stress-strain response. Also, the total strains and strain rates are less than for uniaxial creep.

After experimentally determining the value of the right hand side of Eq. (2), the outside fiber stresses for materials which have equivalent deformation in tension and compression are given by:

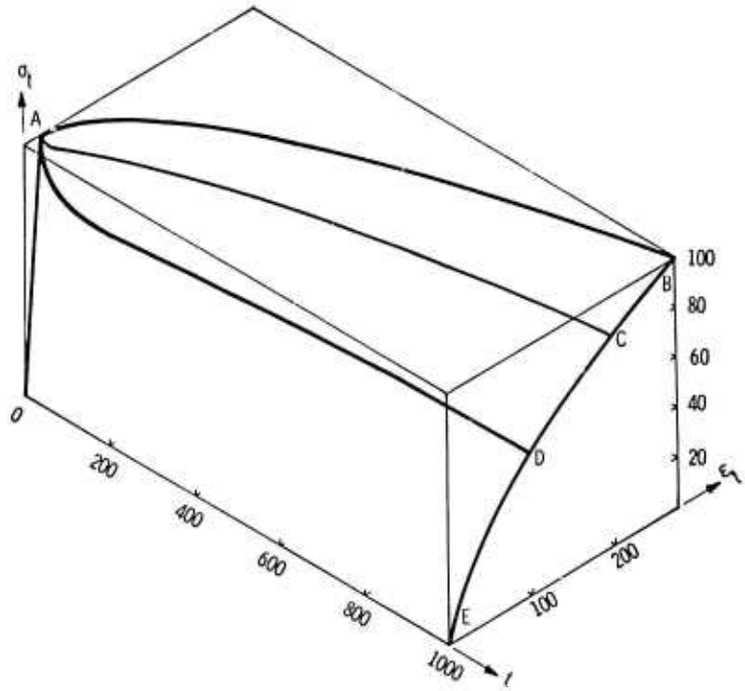

Figure 7.3 Tensile Stress-Strain-Time Deformation Surface, Intersected By Lines Of Constant Stress (AB) And Constant Moment (AC And AD)

$$\sigma_t = \sigma_c = 2\ \phi_c \tag{5}$$

where $\varepsilon_{t_{i-1}}$ and $\varepsilon_{c_{i-1}}$ are the previous maximum tensile and compressive strains, ε_i^* is the total measured strain, and A is the elastic compliance. Initially, both stresses and strains are considered to be applied elastically and are, therefore, easily determined. The compressive strain, ε_{c_i}, and stress, σ_{c_i}, are given by:

$$\varepsilon_{c_i} = \varepsilon_i^* - \varepsilon_{t_i} \tag{8}$$

and

$$\sigma_{c_i} = \varepsilon_{c_i}/A \tag{9}$$

together with the measured strains

$$\varepsilon_t = \varepsilon_c = \varepsilon^*/2 \tag{6}$$

and times, t, curve AC can be calculated.

For materials that are resistant to flow in the compressive mode; the stress-strain-time curves can be incrementally determined using the methods previously developed for constant deflection rate tests.[5,6] The tensile strain, ε_{t_i}, at a given time is the smallest root of the quadratic equation:

$$\varepsilon_{t_i}^2 + (\varepsilon_{c_{i-1}} - 2\ \varepsilon_i^*)\ \varepsilon_{t_i} = [A\ \phi_{c_i}\ \varepsilon_{t_{i-1}} + (\varepsilon_i^* - A\ \phi_{c_i})\ (\varepsilon_i^* - \varepsilon_{c_{i-1}})] = 0 \tag{7}$$

Finally, the tensile stress, σ_{t_i}, can be determined from:

$$\sigma_{t_i} = \sigma_{c_i} (\varepsilon_{c_i} - \varepsilon_{c_{i-1}})/(\varepsilon_{t_i} - \varepsilon_{t_{i-1}}) \qquad (10)$$

for small increments. Together with the times, t_i, the tensile curve AD in Fig. 7.3, as well as a similar compressive curve, may be constructed.

Examples of Analysis

Examples of each boundary type will now be given using calculated deformation data. Flexural creep data were first calculated using the following equation of material deformation:

$$\varepsilon_t = A\,\sigma_t + B\,\sigma_t^{\,n}\,t^m \qquad (11)$$

where σ_t = tensile stress

ε_t = tensile strain

A = elastic compliance = 0.2

$B = 8 \times 10^{-4}$

$n = 2$

$m = 1/2$

For the case of equivalent time dependent deformation in tension and compression:

$$\varepsilon_c = \varepsilon_t \qquad (12)$$

For the case in which the material resists deformation in the compressive mode:

$$\varepsilon_c = A\,\sigma_c \qquad (13)$$

at all times.

The resulting creep data were then analyzed using the methods previously described.[5,6]

Equivalent Time Dependent, Non-Linear Deformation in Tension and Compression

The creep data presented in Figs. 7.4 and 7.5 were calculated from Eqs. (11) and (12) for a constant moment of 100 $bh^2/6$ where the bar width, b, and the bar thickness, h, were both unity. This is equivalent to initially applying an elastic stress at the outside fibers of 100 units. Moment relaxation data were also calculated and are represented by the dashed curves in Fig. 7.4. The data on these two figures can be determined experimentally on real materials.

The values required for the analysis of flexural creep (those on the right side of Eq. (2)) are contained in Figs. 7.4 and 7.5. An example is given. Equation (5) was applied and the results are plotted in Fig. 7.6. The solid lines represent the stress-strain distributions within the bar at the given times. The dashed lines and circles are the outer fiber values. Initially, there is a rapid drop in stress and then a slower but continual stress decrease with time.

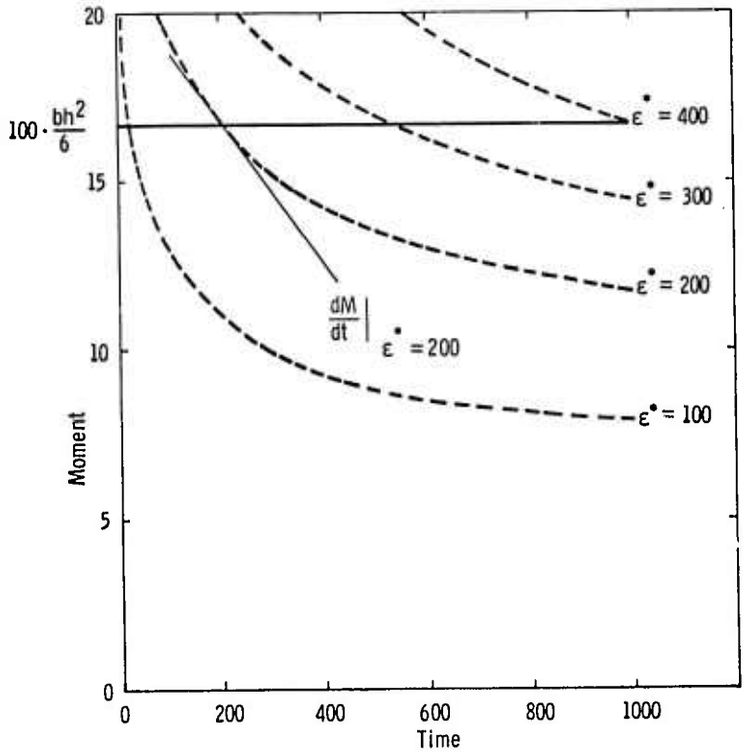

Figure 7.4 Constant Moment Line And Moment Relaxation Curves For A Calculated Example Where Deformation In Tension And Compression Are Equal, Time Dependent And Non-Linear

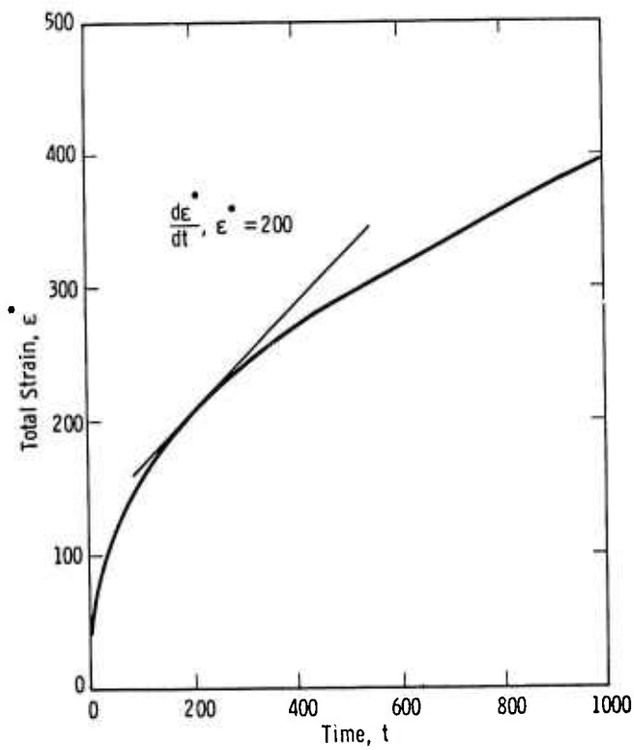

Figure 7.5 Total Strain Versus Time For A Calculated Example Where Deformation In Tension And Compression Are Equal, Time Dependent And Non-Linear

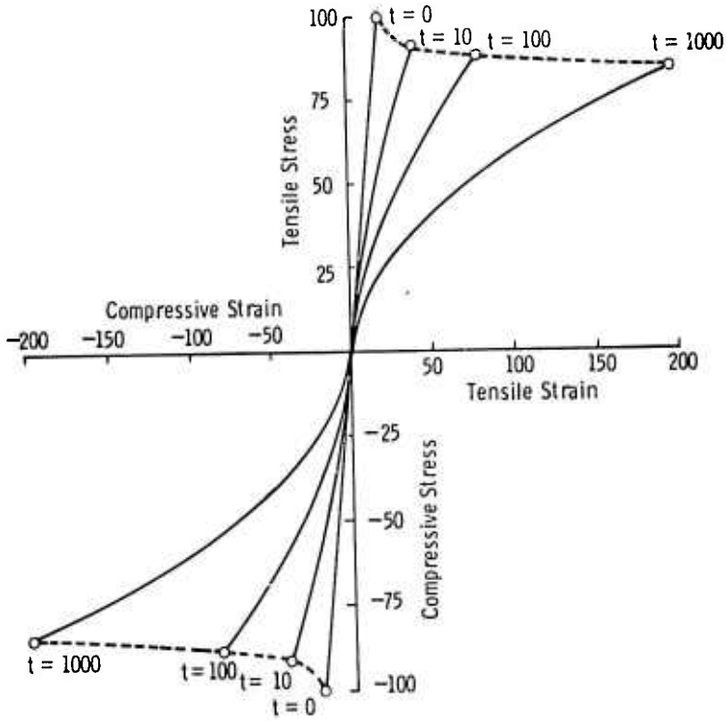

Figure 7.6 Stress-Strain Distributions At Various Times During A Constant Moment Flexural Creep Test For A Calculated Example Where Deformation In Tension And Compression Are Equal, Time Dependent And Non-Linear

In Fig. 7.7, a comparison is made between creep for this constant moment flexural test and that which would be expected for a constant stress uniaxial test. Each was elastically stressed initially to the same value. Note that both the strains and strain rates differ considerably.

Time Dependent, Non-Linear Deformation in Tension and Linear Elastic Deformation in Compression

The creep and stress relaxation data presented in Figs. 7.8 and 7.9 were calculated from Eqs. (11) and (13) for a constant moment of $100\ bh^2/6$ for a bar width and thickness of unity. The values of M, $dM/dt|_{\varepsilon^*}$, ε^*, and $d\varepsilon^*/dt$ at various times were determined as before.

These data were analyzed incrementally using the procedures associated with Eqs. (7) through (10). The results are plotted on Fig. 7.10 and represent the stress-strain distribution within the bar at the given times. The dashed line and circles are the outer fiber values. In this case, the diagram in tensile stress with time is much greater than in the previous case even though the same tensile deformation equation was used.

In Fig. 7.11, a comparison is made between creep for this example of constant moment flexural test and that for the constant stress uniaxial test. The flexural test for the present case results in even lower tensile strains and strain rates than for the previous case. The increase in flexural compressive strain over the constant uniaxial compressive strain is due to the necessity of the bar to maintain a force balance between the tensile and compressive sides. The curve for $\varepsilon^*/2$ versus time

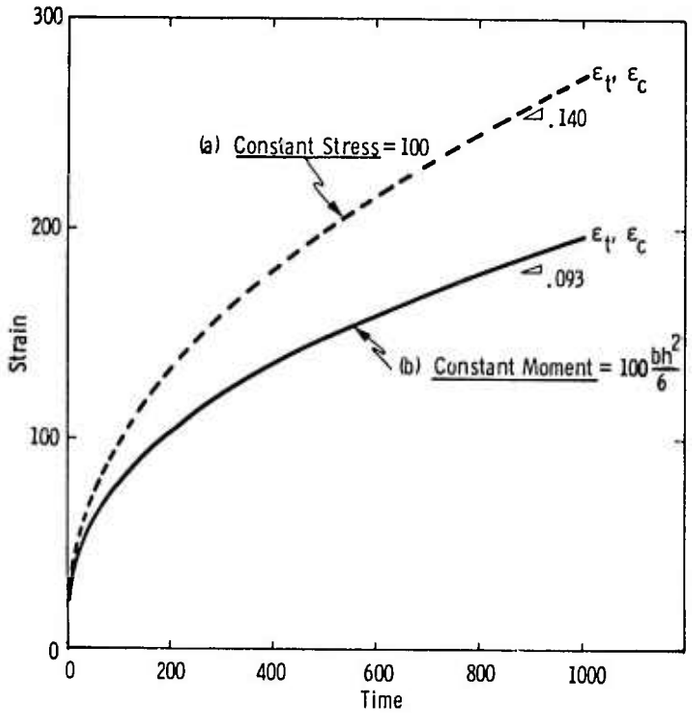

Figure 7.7 Creep Curves For The Uniaxial Constant Stress Test And The Flexural Constant Moment Test For A Calculated Example Where Deformation In Tension And Compression Are Equal, Time Dependent And Non-Linear

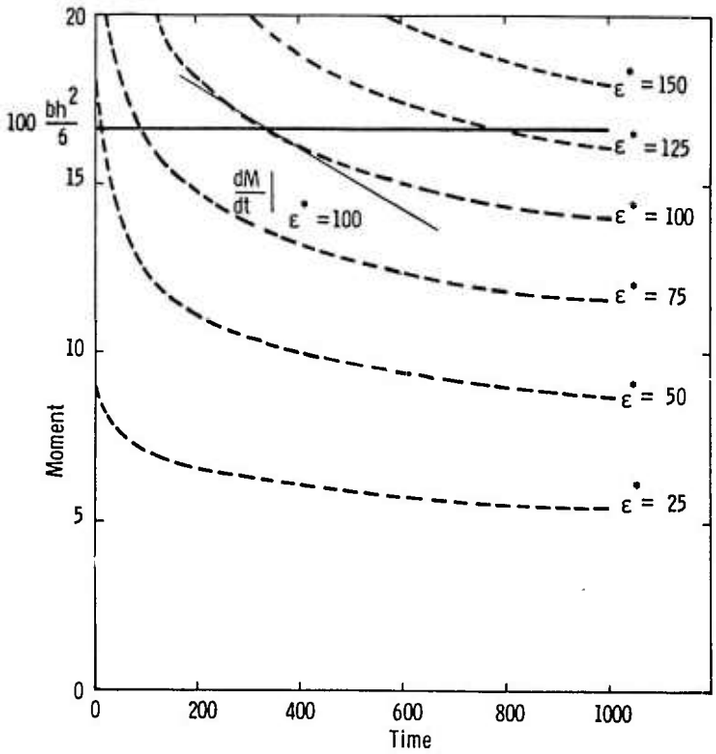

Figure 7.8 Constant Moment Line And Moment Relaxation Curves For A Calculated Example Where Deformation In Tension Was Time-Dependent And Non-Linear, And Deformation In Compression Was Linear Elastic

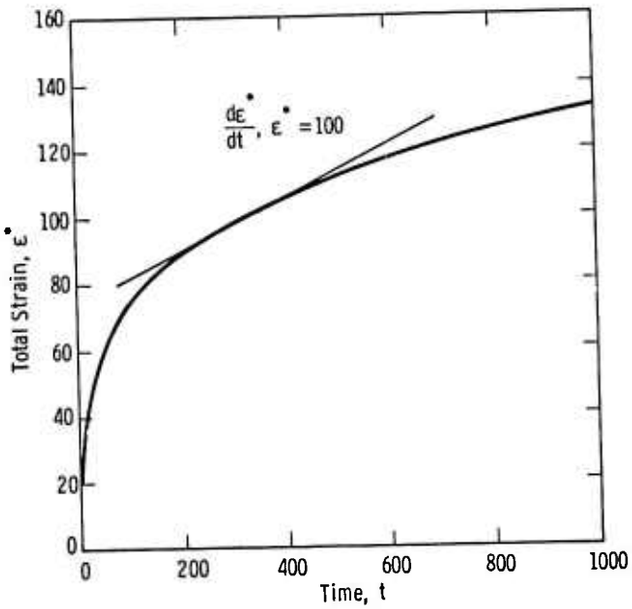

Figure 7.9 Total Strain Versus Time For A Calculated Example Where Deformation In Tension Was Time Dependent And Non-Linear And Deformation In Compression Was Linear Elastic

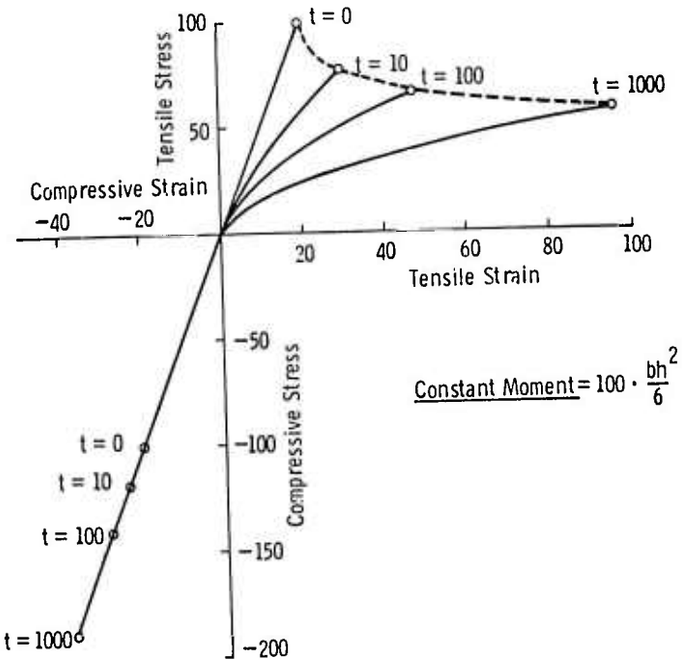

Figure 7.10 Stress-Strain Distributions At Various Times During A Constant Moment Flexural Creep Test For A Calculated Example Where Deformation In Tension Was Time Dependent And Non-Linear, And Deformation In Compression Was Linear Elastic

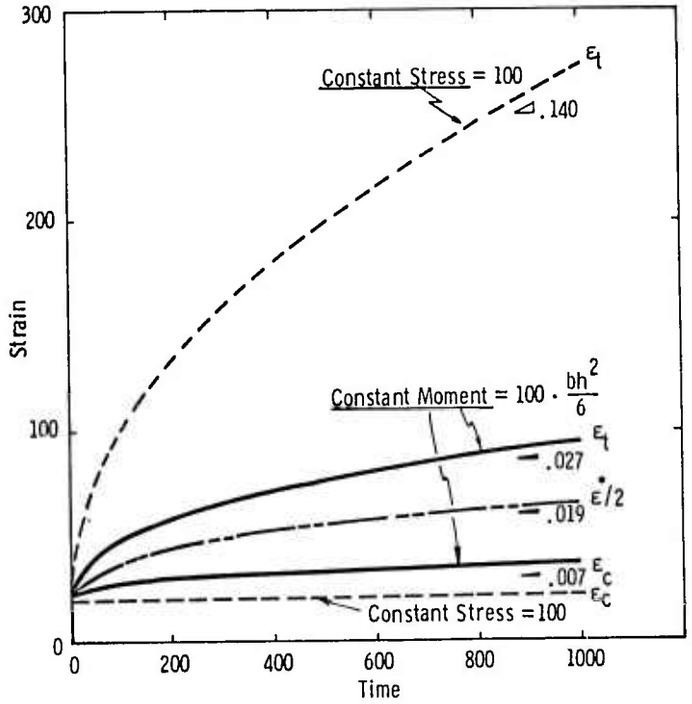

Figure 7.11 Creep Curves For The Uniaxial Constant Stress Test And The Flexural Constant Moment Test For A Calculated Example Where Deformation In Tension Was Time Dependent And Non-Linear, And Deformation In Compression Was Linear Elastic

was also included in Fig. 7.11 because this is the flexural creep curve normally reported. For materials that resist flow in compression it only represents an average.

The results of the two analyses were actually used to construct Fig. 7.3. Reference to that figure clearly shows the relationship between these and uniaxial creep.

7.1.5 LOW CYCLE FATIGUE IN HOT-PRESSED Si_3N_4

Introduction

High cycle fatigue results for hot-pressed silicon nitride were reported early in the program [1,2] Tests up to 2350°F indicated no apparent problem. Preliminary low cycle fatigue tests, however, point to the possibility of adverse affects from thermal fatigue, a condition chronic to superalloy applications in gas turbines. Seventeen fully reversible low cycle fatigue tests in the flexural mode have now been completed on hot-pressed silicon nitride.

Results

Low cycle fatigue data are tabulated in Table 7.2. Results for billets 10 and 7 are erratic and indicate relatively short fatigue life. Billet 2, for which there are only two values, performed in a significantly superior manner indicating that the low cycle fatigue properties of the material are sensitive to some, as yet undefined, characteristic of microstructure and composition. This test will continue.

TABLE 7.2. LOW CYCLE FATIGUE PROPERTIES OF SILICON NITRIDE AT 2300°F

Test	Billet	Hold* stress, psi	Hold* time, sec.	Cycles to Failure	Remarks
1	10	none	none	139	stopped
2	10	none	none	1190	stopped
3	10	20,000	30	107	
4	10	20,000	30	14	not explained
5	10	20,000	30	640	
6	10	20,000	30	78	
7	10	20,000	30	9	flaw indication
8	10	20,000	30	5	flaw indication
9	10	20,000	30	-	
10	10	20,000	30	22	flaw indication
11	10	20,000	30	82	not explained
12	7	20,000	30	293	
13	7	20,000	30	155	
14	7	20,000	15	213	
15	15	20,000	15	338	
16	2	30,000	30	606	
17	2	30,000	30	2095	

* See Reference 6 for cycle description

7.2 MATERIALS SCIENCE

SUMMARY

The purpose of detailed investigations into material sciences is to develop an understanding of material behavior which will lead to improved materials through better control of composition, processing, and fabrication. This is of particular importance since the ceramic materials being utilized in turbine engines are relatively new and appear capable of considerable improvement. Various phases of the material sciences investigation will be continued throughout the life of the program.

The impurities in eight billets of Norton NC 203 hot-pressed SiC have been determined and are reported. The most significant impurities are aluminum and boron at concentrations of $\geq$ 1 w/o and < 0.001-0.060 w/o, respectively.

Thermochemical considerations in the use of Si_3N_4 and SiC in gas turbines are discussed.

PRECEDING PAGE BLANK-NOT FILMED

7.2.1 MICROSTRUCTURE OF HOT PRESSED SILICON NITRIDE AND SILICON CARBIDE

Introduction

The microstructural characterization of Norton HS-130 silicon nitride and Norton hot-pressed silicon carbide, now identified as NC 203, is essentially complete as reported.[1-5] Remnant material from the fabrication of vane assemblies has been examined and found to be consistent generally with previously established microstructural features. Norton NC 132 silicon contains far fewer low density inclusions, however, which apparently accounts for its superior low temperature strength.[4,5] New data include additional chemical analyses of silicon carbide.

The Chemical Composition of Norton NC 203 Silicon Carbide

Quantitative spectrographic analyses have been obtained on the last eight billets of Norton NC 203 silicon carbide. Tungsten content is typically < 0.3 w/o and, therefore, is not shown. Results are reported in Table 7.3.

The aluminum concentration is reasonably uniform at a concentration slightly greater than 1.0 w/o in most cases. This is significant because it does represent a standard of quality control in the blending process where alumina is apparently the hot-press additive employed. Boron which is low in billet 050873, is shown to rise significantly from 300 to 800 ppm. We can only speculate that boron in some form was deliberately added during the fabrication of these later billets.

The calcium content has been reduced to levels approaching the alkali metals. Again it is impossible to comment on the significance at this time.

Twenty-eight elements were identified in the analyses. Most of these represent trace impurities whose role in affecting the performance of SiC has not been ascertained.

TABLE 7.3 CHEMICAL ANALYSIS OF NORTON NC 203 SILICON CARBIDE

Sample/Element	Al	Na	B	Ca	Cr	Fe	Ti	K	Li
050873	≥ 1	< 0.003	< 0.001	0.02	< 0.003	0.1	0.02	< 0.001	< 0.001
050873	≥ 1	< 0.003	< 0.001	0.02	< 0.003	0.1	0.02	< 0.001	< 0.001
3B	≥ 1	< 0.003	0.04	0.003	< 0.003	0.1	0.02	< 0.001	< 0.001
3B	≥ 1	< 0.003	0.03	0.004	< 0.003	0.1	0.02	< 0.001	< 0.001
4B	≥ 1	< 0.003	0.03	0.005	< 0.003	0.1	0.02	< 0.001	< 0.001
4B	≥ 1	< 0.003	0.06	0.007	< 0.003	0.1	0.02	< 0.001	0.001
2A	≥ 1	< 0.003	0.08	0.007	< 0.003	0.1	0.02	< 0.001	0.001
2A	≥ 1	< 0.003	0.06	0.007	< 0.003	0.1	0.02	< 0.001	< 0.001
5B	≥ 1	< 0.003	0.06	0.007	< 0.003	0.1	0.02	< 0.001	< 0.001
5B	≥ 1	< 0.003	0.02	0.005	< 0.003	0.1	0.01	< 0.001	< 0.001
3A	≥ 1	< 0.003	0.02	0.004	< 0.003	0.1	0.01	< 0.001	< 0.001
3A	≥ 1	< 0.003	0.02	0.005	< 0.003	0.1	0.01	< 0.001	< 0.001
2B	≥ 1	< 0.003	0.03	0.004	< 0.003	0.1	0.01	< 0.001	< 0.001
2B	≥ 1	< 0.003	0.02	0.003	< 0.003	0.1	0.01	< 0.001	< 0.001
6B	≥ 1	< 0.003	0.03	0.006	< 0.003	0.1	0.01	< 0.001	< 0.001
6B	≥ 1	< 0.003	0.03	0.004	< 0.003	0.1	0.01	< 0.001	< 0.001
032073 A-1	≥ 1	< 0.003	0.04	0.01	< 0.003	0.1	0.01	< 0.001	< 0.001
032073 A-1	≥ 1	< 0.003	0.03	0.003	< 0.003	0.1	0.01	< 0.001	< 0.001
33841 B	≥ 1	< 0.003	0.04	< 0.001	< 0.003	0.1	0.01	< 0.001	< 0.001
33841 B	≥ 1	< 0.003	0.04	< 0.001	< 0.003	0.1	0.01	< 0.001	< 0.001
433836 A	≥ 1	< 0.003	0.1	0.01	< 0.003	0.1	0.01	< 0.001	< 0.001
433836 A	≥ 1	< 0.003	0.04	0.01	< 0.003	0.1	0.01	< 0.001	< 0.001

7.2.2 GAS-SOLID REACTIONS - THERMOCHEMICAL CONSIDERATIONS IN THE USE OF Si_3N_4 AND SiC IN GAS TURBINES

Introduction

The kinetic processes involved in the static-oxidation and sulfidation of silicon nitride and silicon carbide have been discussed.[1-6] Further thermochemical analyses have been performed to assess the effect of the turbine environment on the decomposition of Si_3N_4 and SiC. The stability of the SiO_2 layer on the formation of SiO (gas) are considered.

Composition of Combustion Gases in a Stationary Gas Turbine

The diesel fuel used in stationary gas turbines has a carbon to hydrogen ratio of approximately 1:1·78. In turbine operations at 10 atm total pressure, air to fuel ratio approximates 50:1 (by weight). The partial pressure of various species in the combustion gases, assuming complete combustion of the fuel and ignoring any sulfur therein, may be calculated in accordance with the following reaction:

$$CH_{1.78} + 1.445\ O_2 + N_2 \rightarrow CO_2 + 0.89\ H_2O + N_2 \qquad (1)$$

The partial pressures for the various species calculated from this reaction are listed below:

Species	Partial Pressure, atm
Nitrogen (N_2)	7.75
Oxygen (O_2)	1.47
Carbon dioxide (CO_2)	0.41
Water vapor (H_2O)	0.36

It is clear that the combustion gases in a stationary gas turbine are highly oxidizing. However, any carbon deposition on turbine components may promote localized reducing conditions. These reducing conditions may play an important role in the oxidation of silicon nitride and silicon carbide.

Decomposition of Si_3N_4

The decomposition of Si_3N_4 takes place according to the reaction:

$$Si_3N_4 \rightarrow 3\ Si\ (s,\ell) + 2\ N_2 \qquad (2)$$

Figure 7.12 shows the decomposition pressure of nitrogen over Si_3N_4 at different temperatures.[25] JANAF Tables list the decomposition temperature of Si_3N_4 (the temperature at which the decomposition pressure of nitrogen reaches 1 atm) $\sim$ 2151°K (3414°F). In stationary gas turbines, the nitrogen pressure is about 7.75 atm. Therefore, the decomposition of Si_3N_4 should not occur at temperatures of 3400°F and above in the gas turbine environment.

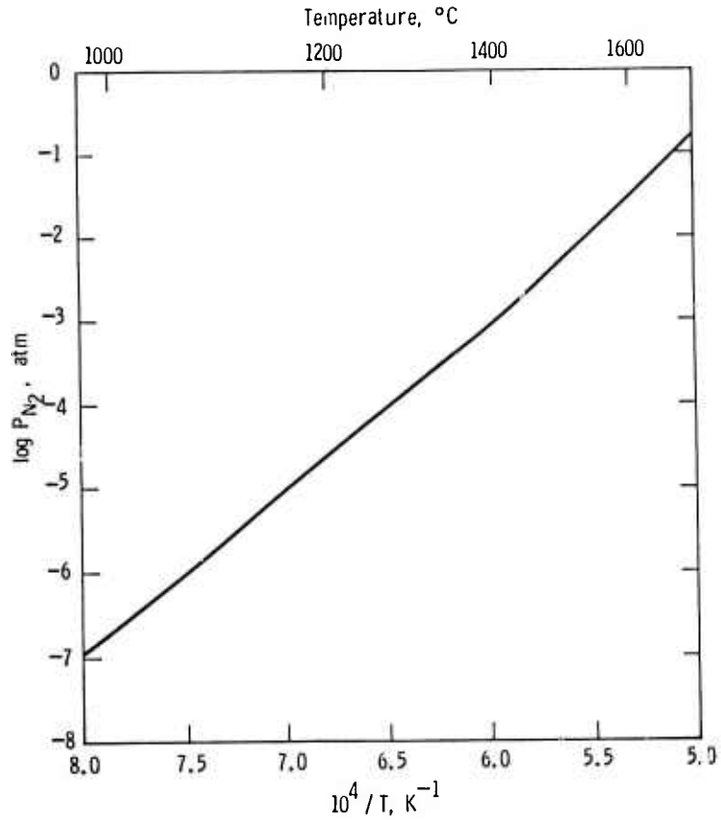

Figure 7.12 Decomposition Pressure Of Nitrogen Over $Si_3N_4(s)$

However, various volatile species, e.g., SiN(g), $Si_2N(g)$, Si(g), $Si_2(g)$, $Si_3(g)$, can form over bare Si_3N_4 (this, at best, will be a localized condition since a layer of SiO_2 should form over Si_3N_4 in the highly oxidizing atmospheres of gas turbines). The partial pressures of these volatile species at different temperatures at nitrogen pressures of 1 atm and 7.75 atm are shown in Figs. 7.13 and 7.14. The predominant volatile species at a nitrogen pressure of 7.75 atm at 2550°F is SiN(g) with a partial pressure of about 10^{-9} atm. Only at about 3000°F does the partial pressure of Si(g) become significant with the partial pressure of both SiN(g) and Si(g) being about 10^{-6} atm.

Decomposition of SiC

Various investigators have reported conflicting decomposition temperatures and decomposition species for SiC. According to the JANAF Tables, silicon carbide decomposes at 3259°K. This temperature is calculated as the point at which the total pressure reaches 1 atm for vapor consisting of $SiC_2(g)$, Si(g), $Si_2C(g)$, $Si_2(g)$, SiC(g) and $Si_3(g)$.

Figures 7.15 and 7.16 show the partial pressures of various volatile species over SiC at 1400 and 2000°K, respectively. Si(g) is the predominant vapor species formed by the decomposition of SiC(s). At 1600°K, the partial pressure of Si(g) at the SiC/C interface is only about 10^{-9} atm, which is very small and should not be significant even if any carbon deposits on the surface of bare SiC. However, at 2000°K, the partial pressure of Si(g) at The SiC/C interface is about 10^{-5} atm, and therefore localized carbon deposits at such high temperatures might cause excessive decomposition of silicon carbide.

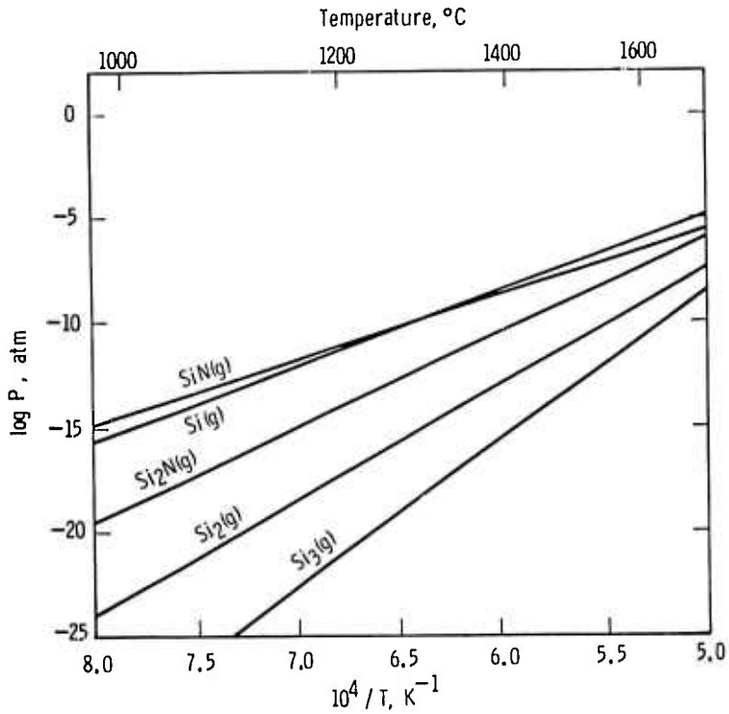

Figure 7.13 Partial Pressures Of Various Volatile Species Over $Si_3N_4(s)$ In Nitrogen At 1 atm Pressure

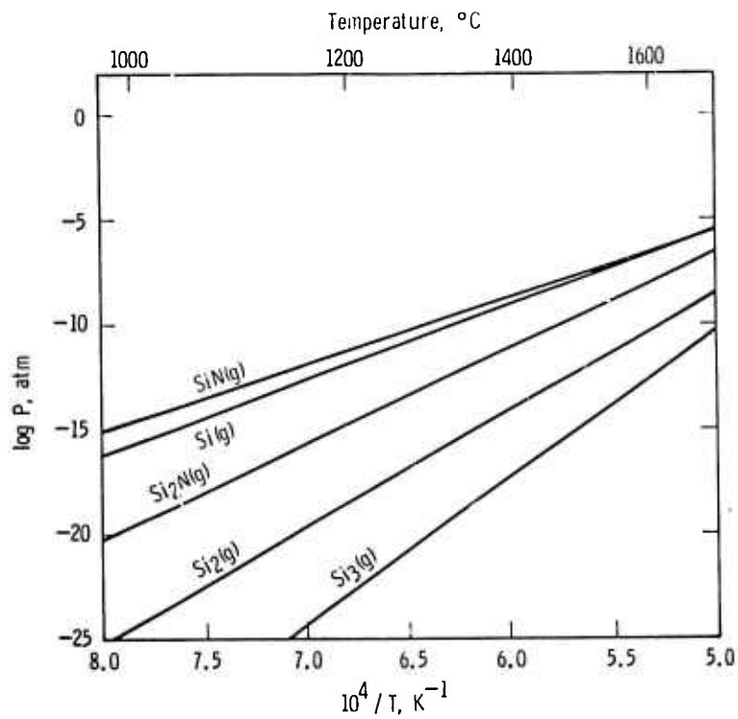

Figure 7.14 Partial Pressure Of Various Volatile Species Over $Si_3N_4(s)$ In Nitrogen At 7.75 atm Pressure

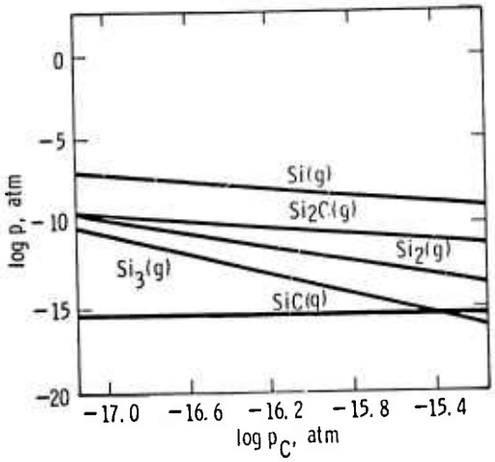

Figure 7.15 Partial Pressures Of Various Volatile Species Over SiC(s) At 1600°K

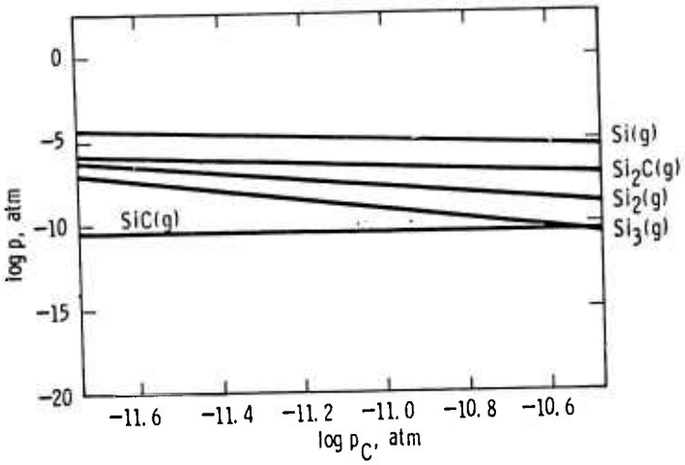

Figure 7.16 Partial Pressures Of Various Volatile Species Over SiC(s) At 2000°K

Stability of SiO_2 Formed Over Si_3N_4 and SiC

When silicon nitride and silicon carbide are exposed to oxidizing atmospheres at elevated temperatures, a passive layer of $SiO_2(s)$ is formed on their surfaces according to reactions:

$$Si_3N_4(s) + 3\ O_2 \rightarrow 3\ SiO_2(s) + 2\ N_2 \qquad (3)$$

$$SiC(s) + 2\ O_2 \rightarrow SiO_2(s) + CO_2 \qquad (4)$$

The volatilization and/or decomposition of this surface silica can result in the formation of various volatile species, e.g., $SiO_2(g)$, $SiO(g)$, $Si(g)$, $Si_2(g)$ and $Si_3(g)$. The partial pressures of these volatile species over $SiO_2(s)$ at 1400, 1600, 1800 and 2000°K as a function of oxygen partial pressure in the ambient are shown in Figs. 7.17 through 7.20. It is clear from these figures that $SiO_2(g)$ is the predominant vapor species at low oxygen pressures. Figure 7.21 shows the partial pressures of these volatile species formed over $SiO_2(s)$ in 1 atm oxygen pressure

as a function of temperature. Under normal conditions, the oxygen pressure in gas turbines is usually greater than 1 atm, and, therefore, the predominant vapor species over $SiO_2(s)$ will be $SiO_2(g)$ with a partial pressure of about 10^{-10} atm at 2550°F. However, if localized reducing conditions surround the Si_3N_4 and SiC parts, then oxygen partial pressure over $SiO_2(s)$ formed on their surfaces can become quite low. Under such reducing conditions, $SiO_2(s)$ can decompose through the formation of $SiO_2(g)$. This is exemplified in Fig. 7.22, where the partial pressures of various volatile species over $SiO_2(s)$ in oxygen at 10^{-8} atm pressure are shown as a function of temperature. At this low oxygen pressure, the partial pressure of SiO(g) at 2550°F is only about 10^{-8} atm.

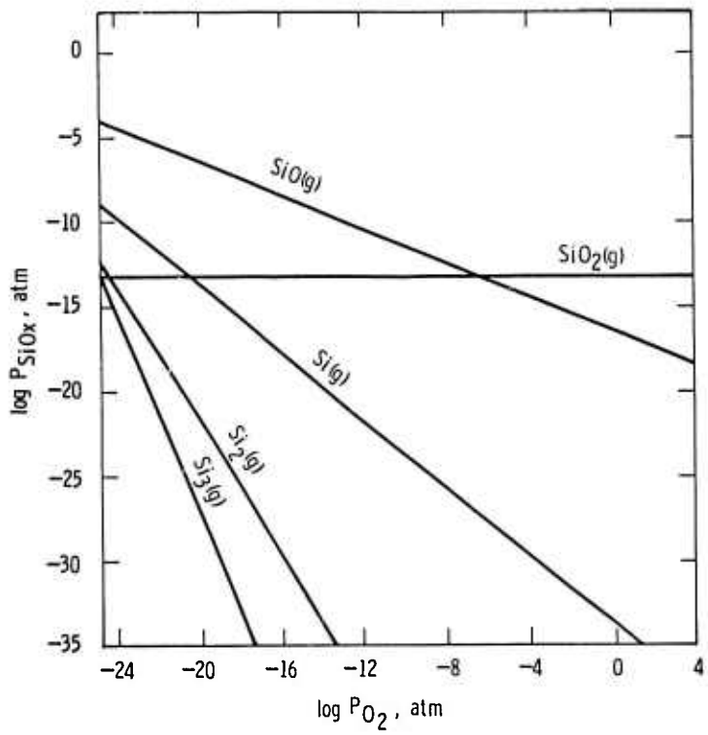

Figure 7.17 Partial Pressures Of Various Volatile Species Over $SiO_2(s)$ At 1400°K (1127°C)

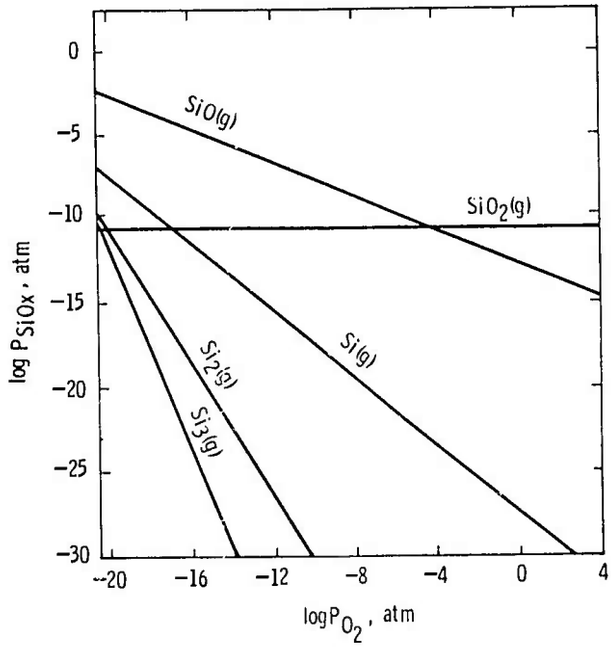

Figure 7.18 Partial Pressure Of Various Volatile Species Over SiO_2(s) At 1600°K

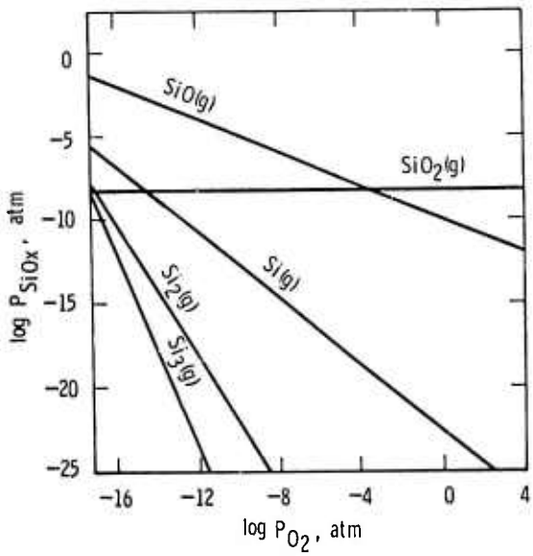

Figure 7.19 Partial Pressures Of Various Volatile Species Over SiO_2(s) At 1800°K (1527°C)

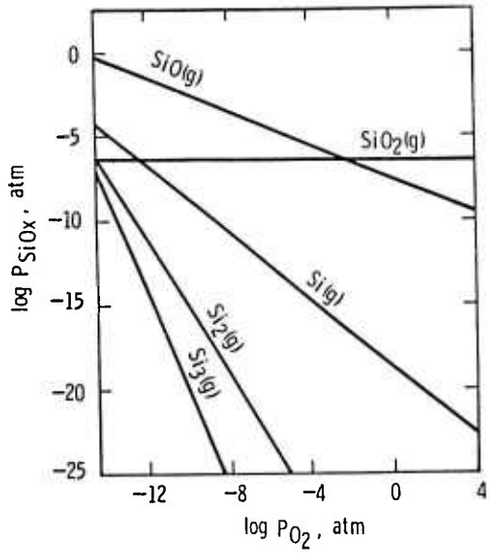

Figure 7.20 Partial Pressures Of Various Volatile Species Over $SiO_2(\ell)$ At 2000°K (1727°C)

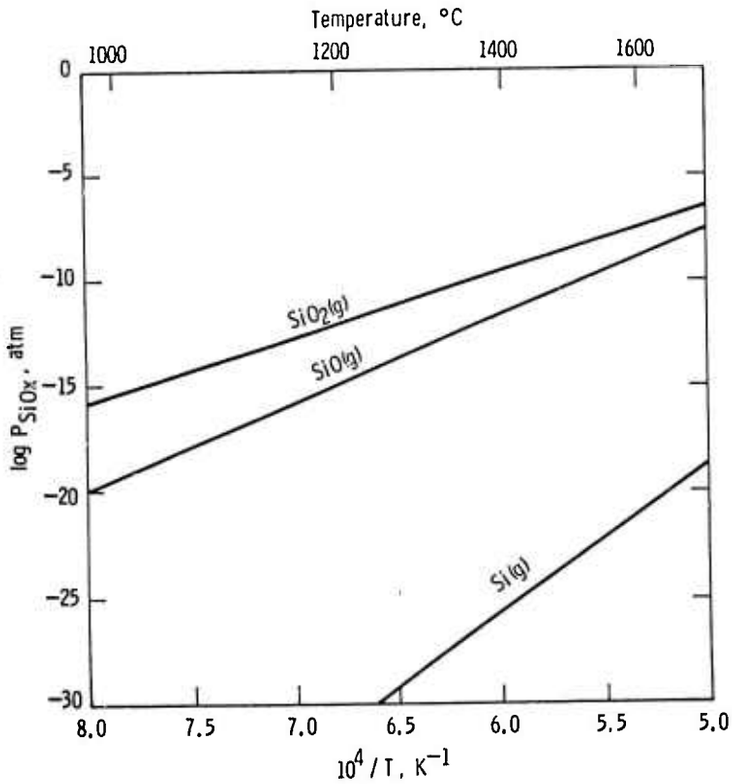

Figure 7.21 Partial Pressures Of Various Volatile Species Over $SiO_2(s,\ell)$ In Oxygen At 1 atm Pressure

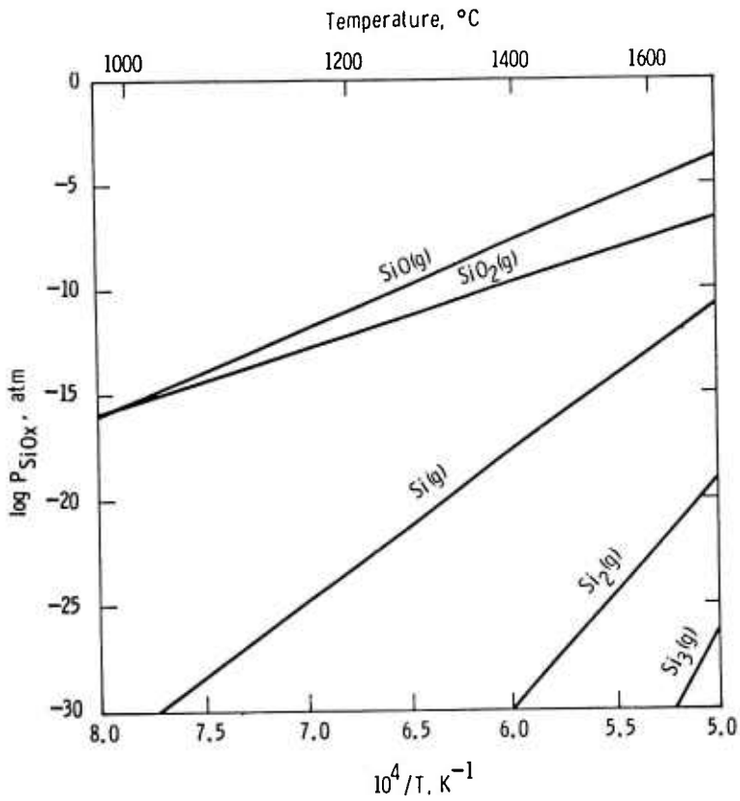

Figure 7.22 Partial Pressures Of Various Volatile Species Over $SiO_2(s,\ell)$ In Oxygen At 10^{-8} atm Pressure

Formation of SiO(g) at Si_3N_4(s)-SiO(s) and SiC(s)-SiO_2(s) Interfaces

The SiO_2(s) formed at the surfaces of Si_3N_4 or SiC can react at the Si_3N_4-SiO_2 or SiC-SiO_2 interface to produce SiO(g) according to reactions:

$$Si_3N_4(s) + 3\ SiO_2(s) \rightarrow 6\ SiO(g) + 2\ N_2(g) \qquad (5)$$

$$SiC(s) + 2\ SiO_2(s) \rightarrow 3\ SiO(g) + CO(g) \qquad (6)$$

The equilibrium partial pressures of SiO(g) thus formed are shown in Fig. 7.23 as a function of temperature. It is clear from this figure that at ∿ 2908°C, SiO(g) pressures for both Si_3N_4 and SiC are of the order of 0.1 atm and this high SiO(g) pressure can cause catastrophic rupture of the protective SiO_2 layer at these high temperatures.

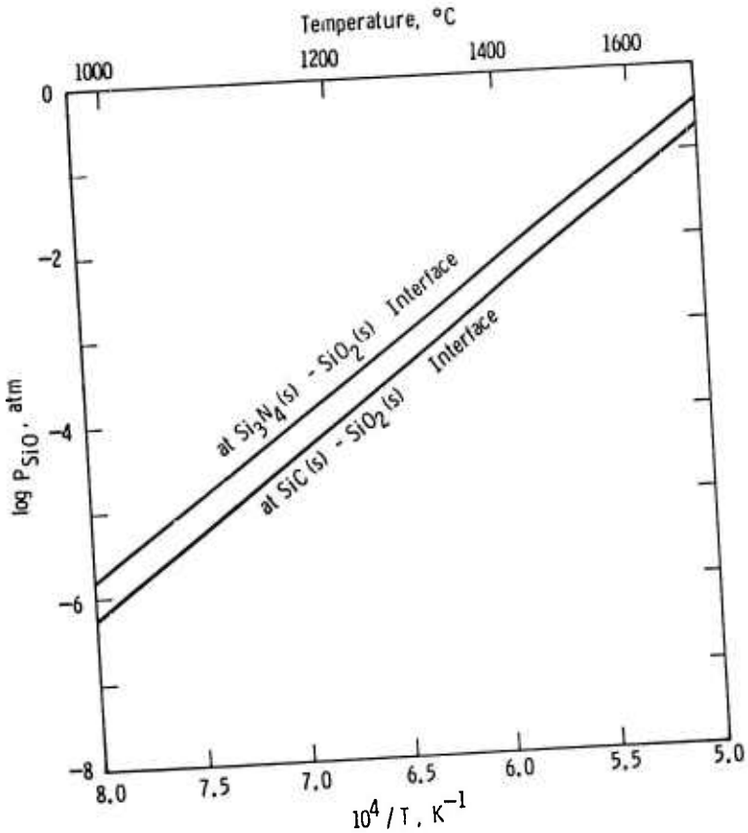

Figure 7.23 Pressures Of SiO(g) At The $Si_3N_4(s)$ - $SiO_2(s)$ And SiC(s) - $SiO_2(s)$ Interfaces

7.2.3 NON-DESTRUCTIVE EVALUATION OF MATERIALS - STATIONARY TURBINE PROJECT

The value of non-destructive method of material evaluation and component inspection cannot be over-emphasized. Westinghouse continues to employ dye penetrant techniques, ultrasonic scanning and radiography for material characterization and component certification. During this report period, however, nothing was done to advance the "state-of-the-art". All results apply to component failure analysis and, therefore, are discussed in Section 6.1.4 as part of static rig testing.

8. REFERENCES

1. McLean, A. F., Fisher, E. A., Harrison, D. E., "Brittle Materials Design, High Temperature Gas Turbine". AMMRC-CTR-72-3, Interim Report, March, 1972.

2. McLean, A. F., Fisher, E. A., Bratton, R. J., "Brittle Materials Design, High Temperature Gas Turbine". AMMRC-CTR-72-19, Interim Report, September, 1972.

3. McLean, A. F., Fisher, E. A., Bratton, R. J., "Brittle Material Design, High Temperature Gas Turbine". AMMRC-CTR-73-9, Interim Report, March, 1973.

4. McLean, A. F., Fisher, E. A., Bratton, R. J., "Brittle Materials Design, High Temperature Gas Turbine". AMMRC-CTR-73-32, Interim Report, September, 1973.

5. McLean, A. F., Fisher, E. A., Bratton, R. J., "Brittle Materials Design, High Temperature Gas Turbine". AMMRC-CTR-74-26, Interim Report, April, 1974.

6. McLean, A. F., Fisher, E. A., Bratton, R. J., "Brittle Materials Design, High Temperature Gas Turbine". AMMRC-CTR-74-59, Interim Report, September, 1974.

7. McLean, A. F., Fisher, E. A., Bratton, R. J. Miller, D. G., "Brittle Materials Design, High Temperature Gas Turbine". AMMRC-CTR-75-8, Interim Report, April, 1975.

8. Wilson, E. L. "SAP 3, A Static Analysis Program For Three Dimensional Structures". Revised August 1972, Bureau of Mines Open File Report 27-73. Contract No. H0110231.

9. Zienkiewicz, O. C., "On the Principle of Repeatability and its Application in Analysis of Turbine and Pump Impellers", International Journal for Numerical Methods in Engineering, Volume 4, pp 445-452 (1972).

10. Swanson Analysis System Inc., "ANSYS Users Manual", Structural Dynamics Research Corporation, 5729 Dragon Way, Cincinnati, Ohio, 45227.

11. Surana, K. S., "NISA Users Manual", Engineering Mechanics Research Corporation, 24001 Southfield Road, Southfield, Michigan 48075.

12. Wilson, E. L. et. al., "Incompatible Displacement Models", International Symposium on Numerical and Computer Methods in Structure Mechanics, Office of Naval Research, Section I-3 (September 8-10, 1971).

13. Zysina-Molozhen, L. M. and Uskov, I. B., "Experimental Investigation of the Heat Transfer on the End Wall of a Blade Channel (in Turbines)", Translated from Russian for NASA by the Israel Program for Scientific Translations (date - late 60's).

14. Ainley, D. C. and Mathieson, G. C. R., "A Method of Performance Estimation for Axial - Flow Turbines", Reports and Memoranda No. 2974, December, 1951, Her Majesty's Stationary Office

15. Katsanis, T., "Fortran Program for Calculating Transonic Velocities on a Blade-to-Blade Turbomachine Stream Surface", NASA TND-5427, Lewis Research Center, Cleveland, Ohio, September, 1969.

16. McNally, W. D., "Fortran Program for Calculating Compressible Laminar and Turbulent Boundary Layers in Arbitrary Pressure Gradients", NASA TND-5681, Lewis Research Center, Cleveland, Ohio, May, 1970.

17. Reshotko, E. & Cohen, C. B., "Heat Transfer at the Forward Stagnation Point of Blunt Bodies", NACA TN-3513, Lewis Flight Propulsion Laboratory, Cleveland, Ohio, July, 1955.

18. Barnes, J. F. and Edwards, J. P., "Cooled Gas Turbine Blades", Cranfield International Symposium Series Vol. II, Proceedings of an International Propulsion Symposium held at the College of Aeronautics, Cranfield, April, 1969, pp 167-177, Pergamon Press, New York, 1971.

19. Schlichting, Hermann (J. Kestin, trans.) "Boundary Layer Theory", sixth ed., McGraw-Hill, 1968.

20. Schlichting, H. and Ulrich, A.,"Zur Berechnung des Umschlages Laminar-Turbulent", Jahrbuch d. dt. Luftfahrtforschung, No. 1, 1942, pp. 8-35.

21. Granville, Paul S., "The Calculation of the Viscous Drag of Bodies of Revolution". Rep. 849, David Taylor Model Basin, July 1953

22. Fitzroy, N. D., "Heat Transfer and Fluid Flow Data Book", General Electric Company, Schenectady, New York, 1970.

23. Hydrodynamic Foil Bearings, U.S. Patent 3,809,443

24. Farris, R. J., "Prediction of the Viscosity of Multimodal Suspensions From Unimodal Viscosity Data", Trans of the Soc. of Rheology, 12:2, pp 281-301 (1968).

25. JANAF Thermochemical Tables, 2nd Edition, National Bureau of Standards, June, 1971.

26. Kinsman, K. R., Govila, R. K., and Beardmore, P., "Plastic Deformation of Ceramic Materials", Penn. State Univ., Plenum Press, 1974, in press.

27. Andersson, C. A., Wei, D. P., and Kossowsky, R., Ibid.

28. Lange, F. F., MCIC Rev. Ceram. Tech., No. 29, 1 (1974).

29. Charles, R. J., J. Appl. Phys., 29, 1657 (1958).

30. Shaffer, P. T. B. and Jun, C. K., "Elastic Modulus of Dense Polycrystalline Silicon Carbide", Mater. Res. Bull. 7 (1) pp 63-70 (1972).

31. Jack, K. H. and Wilson, W. I., "Ceramics Based on the Si-Al-O-N and Related Systems", Nature Physical Sciences 238, pp 28-29 (1972).

32. Oyama, Y., "Solid Solution in the System Si_3N_4 - Ga_2O_3-Al_2O_3", Japanese J. Appl. Phys., 12, pp 500-508 (1973).

33. U. S. Patent 3,830,652, G. E. Gazza, Hot-Pressed, High Strength Silicon Nitride, August 20, 1974.

34. R. Kossowsky, D. G. Miller, E. S. Diaz, Tensile and Creep Strengths of Hot-Pressed Silicon Nitride, J. Materials Sciences, in press.

35. E. A. Davis, Creep of Metals at High Temperature in Bending, J. Appl. Mech., March 1938, pp. A29-A31.

36. E. P. Popov, Bending in Beams with Creep, J. Appl. Phys. 20, 1949, pp. 251-256.

37. J. Marin, Y. Pao and G. Cuff, Creep Properties of Lucite and Plexiglass for Tension, Compression, Bending and Torsion, Trans. ASME, July 1951, pp. 705-719.

38. W. N. Findley and J. J. Poczatek, Prediction of Creep-Deflection and Stress Distribution in Beams from Creep in Tension, J. Appl. Mech., June 1955, pp. 165-171.

39. L. W. Hu and N. H. Triner, Bending Creep and Its Application to Beam-Column, J. Appl. Mech., March 1956, pp. 35-42.

40. W. N. Findley, J. J. Poczatek and P. N. Mather, Prediction of Creep Data When Creep Coefficients are Unequal, Trans. ASME, August, 1958, p. 1294.

ARMY MATERIALS AND MECHANICS RESEARCH CENTER
WATERTOWN, MASSACHUSETTS 02172

TECHNICAL REPORT DISTRIBUTION

No. of Copies	To
1	Office of the Director, Defense Research and Engineering, The Pentagon, Washington, D.C. 20301
12	Commander, Defense Documentation Center, Cameron Station, Building 5, 5010 Duke Street, Alexandria, Virginia 22314
1	Metals & Ceramics Information Center, Battelle Memorial Institute, 505 King Avenue, Columbus, Ohio 43201
2	Dr. James I. Bryant, Office of the Chief of Research, Development and Acquisition, ATTN: DAMA-CSS, The Pentagon, Washington, D.C. 20310
1	Commanding Officer, Army Research Office (Durham), Bx CM, Duke Station Durham, North Carolina 27706 ATTN: Dr. H. M. Davis
1	Commanding General, U.S. Army Material Command, Washington D.C. 20315 ATTN: AMCRD-TC (Dr. El-Bisi)
1	ATTN: ANCDL (Dr. Dillaway)
1	Commanding General, U.S. Army Missile Command, Redstone Arsenal, Alabama 35809 ATTN: Technical Library
4	Commanding General, U.S. Army Tank-Automotive Command, Warren, Michigan 48090, ATTN: AMSTA-BSL, Research Library Br, ATTN: AMSTA-RKM (Mr. C. Green), ATTN: AMSTA-RGR (Mr. Engel), ATTN: AMSTA (Dr. Banks)
1	Commanding General, U.S. Army Weapons Command, Research and Development Directorate, Rock Island, Illinois 61201, ATTN: AMSWE-RDR
1	Commanding Officer, Aberdeen Proving Ground, Maryland 21005, ATTN: Technical Library, Building 313
1	Commanding Officer, U.S. Army Aviation Material Laboratories, Fort Eustis, Virginia 23604
1	Librarian, U.S. Army Aviation School Library, Fort Rucker, Alabama 36360 ATTN: Bldg. 5907
1	Commanding Officer, USACDC Ordnance Agency, Aberdeen Proving Ground, Maryland 21005 ATTN: Library, Building 350

PRECEDING PAGE BLANK-NOT FILMED

ARMY MATERIALS AND MECHANICS RESEARCH CENTER
WATERTOWN, MASSACHUSETTS 02172

TECHNICAL REPORT DISTRIBUTION

No. of Copies	To
1	U.S. Army Air Mobility Research and Development Laboratory ATTN: J. White, Assistant Technical Director, Eustis Directorate, Ft. Eustis, Virginia 23604
1	U.S. Army Air Mobility Research and Development Laboratory ATTN: R. Berrisford, Chief, Structures Division, Eustis Directorate, Ft. Eustis, Virginia 23604
1	U.S. Army Air Mobility Research and Development Laboratory ATTN: T. Coleman, Director, Langley Directorate, Langley Research Center, Langley Field, VA 23365
2	U.S. Army Air Mobility Research and Development Laboratory ATTN: J. Accurio, Director, Lewis Directorate, NASA, Lewis Research Center, 21000 Brookpark Road, Cleveland, Ohio 44135
1	Commanding General, U.S. Army Aviation Systems Command, ATTN: R. Long, Deputy Director RD&E, P.O. Box 209, St. Louis, MO 63166
1	Office Chief Research & Development, Department of Army, ATTN: Col. J. Barnett, Physical & Engineering Sciences Division, Washington, D.C. 20315
1	Commanding General, Army Missile Command, ATTN: AMCDL, Webb Taylor, 5001 Eisenhower Avenue, Alexandria, VA 22304
1	Commanding General, Army Missile Command, ATTN: AMCRD-F, J. Beebe, Washington, D.C. 20315
1	Office, Chief Research & Development, Department of the Army, ATTN: R. Ballard, Physical & Engineering Sciences Division, Washington, D.C. 20315
1	Commander, USA Foreign Science & Technology Center, ATTN: AMXST-SD3, Mr. C. Petschke, 220 7th Street NE, Charlottesville, VA 22901
1	Mr. Irving Machlin, High Temperature Materials Div., Materials and Processes Branch, (NAIR-52031D), Naval Air Systems Command, Department of the Navy, Washington, D.C. 20360

ARMY MATERIALS AND MECHANICS RESEARCH CENTER
WATERTOWN, MASSACHUSETTS 02172

TECHNICAL REPORT DISTRIBUTION

No. of Copies	To
1	Commanding Officer, U.S. Army Engineer Waterways Experiment Station, Vicksburg, Mississippi 39180 ATTN: Research Center Library
	Commanding Officer, U.S. Army MERDEC, Fort Belvoir, Virginia 22060
2	ATTN: STSFB-EP (Mr. James Horton)
1	ATTN; STSFB-EP (Mr. W. McGovern)
1	ATTN: AMCPM-FM (Mr. Allen Elkins)
	Director, Army Materials and Mechanics Research Center, Watertown, Massachusetts 02172
2	ATTN: AMXMR-PL
1	AMXMR-PR
1	AMXMR-CT
1	AMXMR-AP
1	AMXMR-X (Dr. Gorum)
1	AMXMR-EO (Dr. Katz)
2	AMXMR-TM (Dr. Lenoe)
2	AMXMR-D (Dr. Priest)
1	AMXMR-EO (Dr. Messier)
2	AMXMR-P (Dr. Burke)
1	AMXMR-MS (Mr. MacDonald)
1	AMXMR-E (Dr. Larson)
	Advanced Research Projects Agency, 1400 Wilson Blvd., Arlington, Virginia 22209
2	ATTN: Director
1	Dep Director
1	Director of Materials Sciences - Dr. Stickley
1	Dep. Director Materials Sciences - Dr. van Reuth
1	Tech. Information Office - Mr. F. A. Koether
1	Mr. R. M. Standahar, Office of the Director of Defense, Research and Engineering, Room 3D1085, Pentagon, Washington, D.C. 20301
1	Mr. Charles F. Bersch, Department of the Navy, Naval Air Systems Command, Washington, D.C. 20360
1	Dr. A. M. Diness, Metallurgy Branch, Code 471, Office of Naval Research, 800 N. Quincy Street, Arlington, Virginia 22217
2	U.S. Army Air Mobility Research and Development Laboratory, Advanced Systems Research Office, Ames Research Center, Moffett Field, California 94035 ATTN: F. Immen, J. Wheatly

ARMY MATERIALS AND MECHANICS RESEARCH CENTER
WATERTOWN, MASSACHUSETTS 02172

TECHNICAL REPORT DISTRIBUTION

No. of Copies	To
1	Mr. Keith Ellingsworth, Office of Naval Research, Power Program, Arlington, VA 22217
1	Mr. John Fairbanks, Naval Ships Engineering, Prince George Center, Hyattsville, Maryland 20782
1	Capt. D. Zabierek, Air Force Aeropropulsion Lab, Wright-Patterson Air Force Base, Ohio 45433
1	Capt. Smyth, Air Force Materials Laboratory, Wright-Patterson Air Force Base, Ohio 45433
1	Mr. S. Lyons, Wright-Patterson Air Force Base, Ohio 45433
4	Aerospace Research Laboratory, ATTN: ARL-LL, Wright-Patterson Air Force Base, Ohio 45433 ATTN: Dr. Henry Graham ATTN: Dr. James Wimmer ATTN: Maj. L. Jacobson ATTN: Mr. Larry Hjelm
4	NASA Lewis Research Center, 21000 Brookpark Road, Cleveland, Ohio 44135 ATTN: Mr. W. Sanders Dr. Hubert Probst Dr. Robert C. Bill Mr. Donald Guentert
1	Dr. G. C. Deutsch, Ass't Director of Research (Materials), Code RR-1 NASA, Washington, D.C. 20546
1	Mr. George Staber, Office of Coal Research, U.S. Department of the Interior, Washington, D.C. 20240
1	Dr. S. Wiederhorn, Physical Properties Section, Institute for Materials Research, National Bureau of Standards, Washington, D.C. 20234
1	Mr. R. Reynik, Director, Div. of Materials Research, National Science Foundation, 1800 G. Street, N.W., Washington, D.C. 20550
1	Dr. Robb Thomson, Senior Research Scientist, Rm B109, Bld. 225, National Bureau of Standards, Washington, D.C. 20234
1	Mr. H. Morrow, Eustis Directorate, AMRDL, Fort Eustis, VA 23604
1	Dr. R. Warren, Contact Officer, Defense Research & Development Staff, British Embassy, 3100 Massachusetts Avenue N.W., Washington, D.C. 20008

ARMY MATERIALS AND MECHANICS RESEARCH CENTER
WATERTOWN, MASSACHUSETTS 02172

TECHNICAL REPORT DISTRIBUTION

No. of Copies	To
3	Environmental Protection Agency, Division of Advanced Automotive Systems, 2565 Plymouth Road, Ann Arbor, Mi 48105 ATTN: Mr. George Thur Mr. Robert Schultz Mr. Thomas Sebestyen
1	Dean Daniel C. Drucker, Engineering College, University of Illinois, Urbana, Illinois 61801
1	Professor Merton Flemings, Massachusetts Institute of Technology, Cambridge, Massachusetts 02139
1	Professor Edward E. Hucke, Materials and Metallurgical Engineering, The University of Michigan, Ann Arbor, MI 48104
1	Professor Frank A. McClintock, Department of Mechanical Engineering, Massachusetts Institute of Technology, Cambridge, Massachusetts 02139
1	Dr. R. M. Spriggs, Assistant to the President, Lehigh University, Bethlehem, Pennsylvania 18015
1	Mr. J. D. Walton, Jr., EES, Georgia Tech., Atlanta, Georgia 30332
1	Mr. Y. Baskin, Manager Inorganic Chemical Research, Technical Center, Ferro Corporation, 7500 East Pleasant Valley Road, Independence, Ohio 44131
3	Mr. Robert Beck, Dept. Head, Development Materials, Teledyne CAE, 1330 Laskey Road, Toledo, Ohio 43601 Dr. Eli Benstien, Director of Engineering Mrs. Marlene S. Dowdell, Librarian
1	Dr. J. E. Burke, General Electric Company, Corporate Research & Development, P.O. Box 8, Schenectady, New York 12301
1	Dr. C. A. Bruch, Manager, Advanced Studies, General Electric Company, Aircraft Engine Group, Cincinnati, Ohio 45215
1	Mr. A. R. Canady, Caterpillar Tractor Company, Technical Center Building F, Peoria, Illinois 61602
1	Mr. Seymour Bortz, IIT Research Institute, 10 West 35th Street, Chicago, Illinois 43601

ARMY MATERIALS AND MECHANICS RESEARCH CENTER
WATERTOWN, MASSACHUSETTS 02172

TECHNICAL REPORT DISTRIBUTION

No. of Copies	To
1	Mr. L. M. Donley, Owens Illinois Glass, 1900 North Westwood Avenue, Toledo, Ohio 43601
1	Mr. E. J. Dulis, President, Colt Industries, Materials Research Center, Box 88, Pittsburgh, PA 15230
1	Mr. O. Prachar, Passenger Car Turbine Department, Engineering Staff, General Motors Technical Center, Warren, MI 48090
1	Mr. Winston Duckworth and Mr. Lewis E. Hulbert, Battelle Columbus Laboratories, 505 King Avenue, Columbus, Ohio 43201
1	Energy Research Corporation, Bethel, Connecticut 06801
1	Dr. Peter L. Fleischner, National Beryllia Corp., Haskell, New Jersey 07420
1	Mr. O. I. Ford, Technical Manager, Combustor Systems, Aerojet Liquid Rocket Company, P.O. Box 18222, Sacramento, Calf. 95813
1	Mr. Chester T. Sims, Manager, Advanced Materials General, Electric Company, Gas Turbine Products Div., Schenectady, N.Y. 12301
1	Mr. E. W. Hauck, Market Manager, Engine Components, Norton Company, 1 New Bond Street, Worcester, Massachusetts 01606
1	Mr. M. Herman, Detroit Diesel Allison Division, General Motors Corporation, Indianapolis Operations, P.O. Box 894, Indianapolis, Indiana 46206
1	Mr. J. B. Mann, Director of Research, Chrysler Corporation, P.O. Box 1118, Detroit, MI 48231
1	Mr. James F. Holloway, Materials Project Engineer, Pratt & Whitney Corporation, 400 Main Street, E. Hartford, Connecticut 06108
1	Dr. Paul Jorgensen, Associate Director, Materials Laboratory, Stanford Research Institute, Menlo Park, California 94025
1	Dr. A. V. Illyn, Technical Director, Refractories Division, Babcock & Wilcox, Old Savannah Road, Augusta, Georgia 30903
1	Mr. Paul F. Jahn, Vice President, Fiber Materials, Inc., Broadway and Main Streets, Graniteville, Massachusetts 01829

ARMY MATERIALS AND MECHANICS RESEARCH CENTER
WATERTOWN, MASSACHUSETTS 02172

TECHNICAL REPORT DISTRIBUTION

No. of Copies	To
1	Dr. Robert F. Kirby, Materials Engineering Dept. 93-393M, AiResearch Manufacturing Company, Div. of the Garrett Corporation, Sky Harbor Airport, 402 South 36th Street, Phoenix, Arizona 85034
1	Mr. John G. Lanning, Corning Glass Works, Corning, NY 14830
1	Mr. William D. Long, Manager, Product Development, K-Ramics, Kaman Sciences Corporation, Garden of the Gods Road, Colorado Springs, Colorado 80907
1	Mr. James Lynch, Metals & Ceramics Information Center, Battelle Columbus Laboratories, 505 King Avenue, Columbus Ohio 43201
1	Mr. C. H. McMurtry, Project Manager, Research and Development Div., The Carborundum Company, Niagara Falls, New York 14302
1	Mr. Deo Mattoon, Sing Sing Road, Horseheads, New York 14845
1	Mr. G. Kookootsedes, Market Development, Resins and Chemicals, Dow Corning, Midland, Michigan 48640
1	Professor Burton Paul, Dept. of Mechanical Engineering, University of Pennsylvania, Philadelphia, Pennsylvania 19104
1	Mr. Y. K. Pei, Owens Illinois Glass, 1020 North Westwood Avenue, Toledo, Ohio 43607
1	Dr. Jerry D. Plunkett, President, Materials Consultants, Inc., 2150 South Josephine Street, Denver, Colorado 80210
1	Mr. J. A. Rubin, President, Ceradyne Incorporated, 8948 Fullbright Avenue, Chatsworth, California 91311
1	Mr. P. Hansen, Director of Corporate Dev., Kawecki-Berylco Industries, Inc., P.O. Box 1462, Reading, Pennsylvania 19603
1	Mr. Jack W. Sawyer, Gas Turbine International, 4519 Eighteen Street North, Arlington, VA 22207
1	Mr. D. W. McLaughlin, Research & Development Div., Mechanical Technology, Inc., 968 Albany-Shaker Road, Latham, New York 12110

ARMY MATERIALS AND MECHANICS RESEARCH CENTER
WATERTOWN, MASSACHUSETTS 02172

TECHNICAL REPORT DISTRIBUTION

No. of Copies	To
1	Mr. A. R. Stetson, Chief, Process Research Laboratories, Mail Zone R-1, Solar Div. of Int. Harvester Company, 2200 Pacific Highway, San Diego, California 92112
1	Dr. M. L. Torti, Norton Company, 1 New Bond Street, Worcester Massachusetts 01606
1	Dr. T. Vasilos, Applied Technology Division, Avco Corp., Lowell Industrial Park, Lowell, Massachusetss 01851
1	Mr. Francis L. VerSnyder, Manager, Materials Engineering and Research Lab, Pratt & Whitney Corporation, 400 Main Street, E. Hartford, Connecticut 06108
1	Mr. McCoy, Materials Engineering, Garrett-AiResearch Dept. 93-393M, 412 South 36th Street, Phoenix, Arizona 85034
1	Mr. Donald E. Weyer, Dow Corning Corporation, Midland, MI 48640
1	Dr. Michael Guinan, B. Div./L-24, P.O. Box 808, Lawrence Livermore Laboratory, Livermore, California 94550
1	Dr. Mark Wilkins, B Div./L-24, P.O. Box 808, Lawrence Livermore Laboratory, Livermore, California 94550
1	Dr. Charles J. McMahon, Jr., Assoc. Prof. Materials Science, School of Metallurgy & Materials Science, University of Pennsylvania, 3231 Walnut Street, Philadelphia, Pennsylvania
1	Mr. Gaylord D. Smith, The International Nickel Co., Inc., 1 New York Plaza, New York, New York 10004
1	Mr. H. R. Schelp, Garrett Corporation, 9851 Sepulveda Blvd., Los Angeles, California 90009
1	Dr. Robert Widmer, President, Industrial Materials Technology 19 Wheeling Avenue, Woburn, Massachusetts
1	Prof. R. P. Kroon, University of Pennsylvania, Philadelphia, Pennsylvania
1	Dr. Paul G. Shewmon, D212, Argonne National Laboratory, 9700 South Cass Avenue, Argonne, Illinois 60439

ARMY MATERIALS AND MECHANICS RESEARCH CENTER
WATERTOWN, MASSACHUSETTS 02172

TECHNICAL REPORT DISTRIBUTION

No. of Copies	To
1	Dr. Thomas D. McGee, Professor of Ceramic Engineering, Iowa State University, Ames, Iowa 50010
1	Mr. Joe Glotz, Department of the Navy, Naval Air Propulsion Test Center, Trenton, New Jersey 08628
1	Mr. John Miguel, Naval Underwater System Center, Newport, Rhode Island
1	Mr. Robert Benham, AEP-22, U.S. Naval Air Propulsion Test Center (AE), Philadelphia, PA 19112
1	Mr. R. Barry Strachan, Williams Research Corp., Walled Lake, Michigan 48088
1	Mr. S. Walosin, Curtis-Wright Corp. One Passaic Street, Woodridge, N.J. 07075
1	Prof. Marc Richman, Engineering Division, Brown University, Providence, Rhode Island 02912
1	Mr. R. Rice, Naval Research Laboratory, Washington, D.C. 20390
1	Mr. George A. Wacker, Head Metal Physics Br., Naval Ships Research & Development Center, Annapolis, Md. 21402, ATTN: Code 2812
1	Dr. R. Charles, Manager Ceramics Branch, General Electric Co., Corporate R & D Center, P.O. Box 8, Schenectady, New York 12301
1	Mr. C. F. Cline, Manager, Strength Physics Department, Allied Chemical Corporation, P.O. Box 1021R, Morristown, New Jersey 07960
1	Dr. J. T. Bailey, American Lava Corp., Chattanoga, Tennessee 37405
1	Mr. S. T. Wlodek, Cabot Corp. Stellite Div., 1020 West Park Avenue, Kokomo, Indiana 46901
2	Cummins Engine Company, Inc., Columbus, Indiana 47201 Mr. R. Kano, Mr. K. J. Mather
1	Mr. J. D. Mote, EF Industries, Inc., 1301 Courtesy Rd. Louisville, Colorado 80027
1	Mr. William E. Gurwell, Eaton Corporation, Research Center 26201 Northwestern Highway, Southfield, MI 48076

ARMY MATERIALS AND MECHANICS RESEARCH CENTER
WATERTOWN, MASSACHUSETTS 02172

TECHNICAL REPORT DISTRIBUTION

No. of Copies	To
1	Mr. Robert W. Gibson, Jr., Head, Library Dept. General Motors Corporation GM Technical Center, Warren, MI 48090
1	Mr. R. L. Lormand, Lawrence Radiation Lab, P.O. Box 808, Livermore, California 94550
2	Ms. Bolick, National Aeronautics and Space Adminstration Goddard Space Flight Center, Greenbelt, Maryland 20771
1	Mr. Neil T. Saunders, Ch. Mat'ls Appl'n Branch, National Aeronautics and Space Administration, Lewis Research Center, Cleveland, Ohio 44135
1	Ms. Rayna Lee Caplan, Librarian, Northern Research and Engineering Corp., 219 Vassar Street, Cambridge, Mass. 02139
1	Mrs. Jame Bookmyer, Info. Services Div., PPG Industries, Inc., P.O. Box 11472, Pittsburgh, Pennsylvania 15238
1	Mr. P. W. Parsons, Manager, Commercial Research Dept., Stackpole Carbon Company, St. Marys, Pennsylvania 15857
1	Ms. Lucille Steelman, Order Librarian, Stanford Research Institute ATTN: G-037 Library, Menlo Park, Calif. 94025
1	Technical Library, TRW Equipment, TRW Inc., 23555 Euclid Avenue, Cleveland, Ohio 44117
1	Dr. E. P. Flint, U.S. Department of Interior, Bureau of Mines, Room 4513, Interior Bldg., Washington, D.C. 20240
1	Mr. W. Wheatfall, Naval Ship R & D Lab, Code 2812, Annapolis, Maryland 21402
1	Dr. Joseph E. Motherway, University of Bridgeport, Bridgeport, Connecticut 06602
1	Dr. Soloman Musikant, Manager, Metallurgy & Ceramics Lab General Electric Valley Forge, Valley Forge, PA
1	Mr. Louis J. Fiedler, Mat'ls & Process Technology Lab., Avco Corporation, 550 S. Main Street, Stratford, Connecticut 06497
1	Mr. Donald Lapades, The Aerospace Corporation, P.O. Box 92957, Los Angeles, California 90009

ARMY MATERIALS AND MECHANCIS RESEARCH CENTER
WATERTOWN, MASSACHUSETTS 02172

TECHNICAL REPORT DISTRIBUTION

No. of Copies	To
1	Mr. Thomas J. Ahrens, Assoc. Prof. of Geophysics, California Institute of Technology, Seismological Laboratory, 295 San Rafael Avenue, P.O. Bin 2, Arroyo Annex, Pasadena, California 91109
1	Mr. Victor de Biasi, Editor, Gas Turbine World, P.O. Box 494, Southport, Connecticut 06490
1	SKF Industries, Inc., Engineering & Research Center, 1100 1st Avenue, King of Prussia, PA 19406, ATTN: Warren E. Jameson & Harish Dalal
1	Dr. Edward Reynolds, General Motors Technical Center, Passenger Car Turbine Division, Warren, MI 48090
1	Dr. Wm. R. Freeman, Jr., V. and Technical Director, Howmet Corporation, Superalloy Group, One Misco Drive, Whitehall, Michigan 47461
1	Mr. D. William Lee, Arthur D. Little, Inc. Acorn Park, Cambridge, Massachusetts 02140
1	Dr. L. Kaufman, Project Director, Manlabs, Inc., 21 Erie Street, Cambridge, Massachusetts 02139
1	Prof. Morris E. Fine, Northwestern University, The Technological Institute, Dept. of Materials Science, Evanston, Illinois
1	Prototype Developments Associates, Esplanade I, Suite 204 3001 Red Hill Avenue, Costa Mesa, California 92626, ATTN: Mr. John I. Slaughter, President
1	Raytheon Company, Research Division Library, Foundry Avenue, Waltham, Massachusetts 02154, ATTN: Ms. Madaleine Bennett, Librarian
1	Prof. T. L. Chu, Southern Methodist University, Institute of Technology, Electronic Sciences Center, Dallas, Texas 75222
1	Mr. H. Stuart Starrett, Head, Mechanics Section, Southern Research Institute, 2000 Ninth Avenue South, Birmingham, Alabama 35205

ARMY MATERIALS AND MECHANICS RESEARCH CENTER
WATERTOWN, MASSACHUSETTS 02172

TECHNICAL REPORT DISTRIBUTION

No. of Copies	To
1	Dr. O. Conrad Trulson, Union Carbide Corporation, Carbide Products Division, 270 Park Avenue, New York, New York 10017
1	Prof. Earl R. Parker, University of California, Department of Materials Science and Engineering, 286 Hearst Mining Building, Berkeley, California 94720
1	Mr. Willard H. Sutton Manager, Ceramics Projects, Special Metals Corporation, New Hartford, New York 13413
1	Dr. Maurice J. Sinnott, Department of Chemical & Metallurgical Engineering, The University of Michigan, Ann Arbor, MI 48104
1	Mrs. R. J. Benacquista, R.I.A.S., 9616 Labrador Lane, Cockeysville, MD 21030
1	Prof. M. C. Shaw, Head, Department of Mechanical Engineering, Cornegie-Mellon University, Pittsburgh, Pennsylvania 15213
1	Mr. Gail Eichelman, Manufacturing Processes Div., Air Force Mateials Laboratory, Wright-Patterson AFB, Ohio 45433
1	Dr. J. C. Lewis, Metals & Minerals Economics Div. Battelle Memorial Institute, 505 King Avenue, Columbus, Ohio 43201
1	Massachusetts Institute of Technology, Cambridge, Massachusetts, 02139, ATTN: Prof. D. W. Kingery, Rm. 13-4090
1	Prof. Michael F. Ashby, Gordon McKay Professor of Metallurgy, Pierce Hall, Harvard University, Cambridge, Massachusetts 02138
1	Prof. I. B. Cutler, University of Utah, College of Engineering Division of Materials Science and Engineering, Salt Lake City, Utah 84112
1	Mr. J. A. Alexander, Manager, Materials Research Department, TRW 23555 Euclid Avenue, Cleveland, Ohio 44117
1	Airesearch Manufacturing Company, Sky Harbor Airport, 402 South 36th Street, Phoenix, Arizona 85034, Attn: Supervisor, Propulsion Engine Advanced Technology Dept., 93-12M
1	Mr. M. Blake, Norton Company, One New Bond Street, Worcester, Mass. 01606

ARMY MATERIALS AND MECHANICS RESEARCH CENTER
WATERTOWN, MASSACHUSETTS 02172

TECHNICAL REPORT DISTRIBUTION

No. of Copies	To
1	Dr. H. P. Kirchner, Ceramic Finishing Company, P.O. Box 498, State College, Pennsylvania 16801
1	Dr. Morris Berg, General Motors Corporation, AC Spark Plug Division Flint, Michigan 48556
1	Dr. Michael J. Noone, General Electric Company, Space Sciences Laboratory, Box 8555, Philadelphia, Pennsylvania 19101
1	Dr. Richard Kliener, GTE Sylvania, Tonawanda, Pennsylvania 18848
1	Mr. F. E. Krainess, Rockwell International Corporation, D/391-204 AB70 12214 Lakewood Boulevard, Downey, California 90241
1	Mr. David Cormier, Nuclear Planning Division, Stone & Webster Engineering Corporation, 87 Nash Memorial Road, Abington, Ma. 02351
1	Mr. John F. Burst, Technical Director, General Refractories Company, 1520 Locust Street, Philadelphia, Pennsylvania 19102
1	Mr. V. A. Chase, Chief of Development Laboratory, Whittaker Corporation, Research and Development Division, 3540 Aero Court, San Diego, Cal. 92123
1	Dr. Stanley Waugn, Research Division, Raytheon Corporation, Research Division, 28 Seyon Street, Waltham, Massachusetts 02154
1	Coors Porcelain Company, Research Department, 17750 West 32nd Avenue, Golden, Colorado 80401
1	Professor Robert F. Davis, North Carolina State University, Department of Materials Science, Box 5427, Raleigh, North Carolina 27607
1	Dr. H. von E. Doering, Manager, Fuels/Corrosion Unit, General Electric Company, Gas Turbine Products Division, Building 53-311, Schenectedy, New York 12345
1	Dr. R. Ruh, AFML/LLS, Air Force Materials Laboratory, Wright-Patterson AFB, Ohio 45433
1	Mr. Michael E. Naylor, General Motors Technical Division, Passenger Car Turbine Division, Warren, Michigan 48090
1	Dr. John V. Milewski, ESSO Research and Engineering Company, Government Research Laboratory, P.O. Box 8, Linden, New Jersey 07036
1	Mr. M. J. Klein, Research Staff Specialist, Mail Zone R-1, Solar, 2200 Pacific Highway, P.O. Box 80966, San Diego, California 92138

ARMY MATERIALS AND MECHANICS RESEARCH CENTER
WATERTOWN, MASSACHUSETTS 02172

TECHNICAL REPORT DISTRIBUTION

No. of Copies	To
1	Dr. Frank Galasso, United Aircraft Research Laboratories, East Hartford Conn. 06108
8	Lt. Col. E. E. Chick, Chief, Materials Branch, European Research Office U. S. Army R&D Group, (EUR), Box 15, FPO New York 09510
1	Dr. Joseph Griffo, U. S. Atomic Energy Commission Space Nuclear Systems Division, Century XXI Building, Mail Station F-309, Washington, D.C. 20545
1	Mr. Joseph Simpson, Rohr Industries, Inc., Technical Library P.O. Box 1516, Chula Vista, California 92012
1	Mr. Philip J. Willson, Chemical Research, Chrysler Corporation, Box 1118, CIMS 418-19-18, Detroit, Michigan 48231
1	Mr. William Combs, Battelle Memorial Institute, 2030 M Street N.W. Washington, D.C. 20036
1	Mr. M. A. Schwartz, U.S. Department of the Interior, Bureau of Mines Tuscaloosa Metallurgy Research Laboratory, P.O. Box 1, University, Alabama 35486
1	Turbo Power and Marine Systems, Inc., ATTN: Mr. Carl Merz, Farmington, Connecticut 06032
1	Mr. R. N. Singh, Argonne National Laboratory, Materials Science Division 9700 South Cass Avenue, Argonne, Illinois 60439
1	Mr. Richard E. Engdahl, Deposits & Composites, Inc., 1821 Michael Faraday Drive, Reston, Virginia 22090
1	Mr. Leonard Topper, Office of Energy Policy, National Science Foundation 1800 G Street N. W., Washington, D.C. 20550
1	Mr. Ron Lowrey, U.S. Bureau of Mines, P.O. Box 70, Albany, Oregon 97321
1	Materials Science Corporation, Technical Library, Blue Bell Office Campus, Merion Towle Building, Blue Bell, Pennsylvania 19422
1	Ms. Sharon Wright, Creare Inc., Technical Library, Hanover, New Hampshire 03755

ARMY MATERIALS AND MECHANICS RESEARCH CENTER
WATERTOWN, MASSACHUSETTS 02172

TECHNICAL REPORT DISTRIBUTION

No. of Copies	To
1	Mr. John Polyansky, Gas Turbine Design Engineering, Turbodyne Corporation, 626 Lincoln Avenue S E, St. Cloud, Minnesota 56301
1	Mr. Donald J. Legacy, Turbodyne Corporation, Wellsville, New York 14895
1	Mr. P. R. Miller, NASA Headquarters, Code RPD, 600 Independence Avenue S. W., Washington, D.C. 20546
1	Dr. Charles Berg, Chief Engineer, Federal Power Commission, Room 2100 825 North Capital Street, N.E., Washington, D.C. 20426
1	Mr. Michael Lauriente, Department of Transportation, 400 Seventh Street, S. W., Washington, D.C. 20590
1	Dr. Donald Vieth, National Bureau of Standards, Administration Bldg., Room A1002, Washington, D.C. 20234
1	Dr. Leonard Topper, National Science Foundation, Office of Energy R & D Policy, Room 537, 1800 G Street NW, Washington, D.C. 20550
2	Electric Power Research Institute, P.O. Box 10412, Palo Alto, California 94304 ATTN: Dr. Richard E. Balzhiser, Dr. Arthur Cohn
1	W. C. Christensen, Assistant for Resources, Directorate for Energy, OASD (I&L), Room 2B341 Pentagon, Washington, D.C. 20301
1	Mr. Tyler Port, Special Assistant, OASA (I&L), Room 3E620 Pentagon, Washington, D.C. 20301
1	Major Jose Baca, Hdqtrs., Air Force Systems Comman/DLFP, Propulsion and Power Branch, Andrews Air Force Base, Washington, D.C. 20034
1	Mrs. Patricia Mooney, Office of Management and Budget, Energy R&D Coordination Branch, Room 8001, New Executive Office Bldg., Washington, D.C. 20503
1	James Johnson, Environmental Protection Agency, Air Technology Branch, RD-681, Room 621 W, 401 M Street, N.W., Washington, D.C. 20490
1	Mr. Thomas Gross, Staff Member, Office of Energy Conservation, Federal Energy Office, Room 4234, Columbia Plaza Bldg., Washington, D.C. 20461

ARMY MATERIALS AND MECHANICS RESEARCH CENTER
WATERTOWN, MASSACHUSETTS 02172

TECHNICAL REPORT DISTRIBUTION

No. of Copies	To
1	Dr. John S. Foster, Jr., Vice President for Energy Research and Development, TRW Incorporated, One Space Park, Redondo Beach, California 90278
1	Dr. Raymond Bisplinghoff, Deputy Administrator, National Science Foundation, 1800 G. Street, N.W., Washington, D.C. 20550
1	Dr. Alan Womack, Assistant Director, Gas Cooled Reactors, Atomic Energy Commission, Washington, D.C. 20545
1	Dr. Donald Weidhuner, Chief, Power Division, Research Development & Engineering Directorate, Army Materials Command Headquarters, 5001 Eisenhower Avenue, Alexandria, Virginia 22304
1	Dr. A. Lovelace, Deputy Assistant Secretary (R&D), Office of Assistant Secretary of the Air Force (Research & Development), Room 4E973, Pentagon, Washington, D.C. 20330
1	Dr. Neal Richardson, TRW Incorporated, One Space Park, Redondo Beach, California 90278
1	Mr. Roy Peterson, Chief, Pollution Abatement & Gas Turbine Research, Ship Research & Technology Division, Naval Ship Systems Command Hqtrs., 2531 Jefferson Davis Highway, Arlington, Virginia 20362
1	Dr. Eugene C. Gritton, The Rand Corporation, Physical Sciences Department, 1700 Main Street, Santa Monica, California 90406
1	Mr. C. A. Vassilakis, Turbo Power & Marine Systems, New Britain Ave., Farmington, Conn. 06032
1	Mr. P. E. McConnell, Owens-Corning Fiberglas Corporation, Technical Center, Granville, Ohio 43023
1	Turbodyne Corporation, 711 Anderson Avenue North, St. Cloud, Minnesota 56301, ATTN: Diane Konsor
1	Mr. N. B. Elsner, General Atomics Corporation, Box 81608, San Diego, California 92037
1	Mr. Eldor R. Herrmann, Ceramic Systems, Inc., 11402 Schaefer Highway, Detroit, Michigan 48227
1	Dr. William H. Rhodes, GTE Laboratories, Waltham Research Center, 40 Sylvan Road, Waltham, Massachusetts 02154

ARMY MATERIALS AND MECHANICS RESEARCH CENTER
WATERTOWN, MASSACHUSETTS 02172

TECHNICAL REPORT DISTRIBUTION

No. of Copies	To
1	Anne M. Theil, Avco Everett Research Laboratory, Inc., 2385 Revere Beach Parkway, Everett, Massachusetts, 02149
1	Mr. William Oldfield, Materials Research and Computer Simulation, 634 Berkeley Place, Westerville, Ohio 43081
1	Dr. Wilfred H. Dukes, Assistant Director Engineering for Development Bell Aerospace, P.O. Box 29307, New Orleans, Louisiana 70189
1	Dr. Keith E. McKee, Director of Research Engineering Mechanics Div., IIT Research Institute, 10 West 35th Street, Chicago, Illinois 60616
1	Dr. Donald R. Uhlmann, Associate Professor of Ceramics, Department of Metallurgy and Materials Science, Massachusetts Institute of Tech., Cambridge, Massachusetts 02139
1	Dr. John B. Wachtman, Jr., Division Chief, Inorganic Materials Div. National Bureau of Standards, Room A359, Materials Building, Washington, D.C. 20234
1	Mr. Donald G. Groves, Staff Engineer, National Materials Advisory Board, National Academy of Sciences, 2101 Constitution Ave., N.W., Washington, D.C. 20418
1	Major Roger Austin, Air Force Materials Laboratory, Wright-Patterson Air Force Base, Ohio 45433
1	Mr. James J. Gangler, Advanced Research & Technology Div., Code RRM, Room B556, National Aeronautics and Space Adminstration, Headquarters, Washington, D.C. 20546
1	Dr. W. Bunk, DFVLR - Institut fur Werkstoff-Forshung, 505 Porz-Wahn, Linder Hohe, Germany
1	Mr. Karl Koyama, General Atomic Company, Box 81608, San Diego, Ca 92138
1	Mr. M. Allen Magid, Materials Marketing Engineer, Florida R & D Center Pratt & Whitney Aircraft, P.O. Box 2691, West Palm Beach, Fla 33402
1	Mr. Nelson R. Roth, Bell Aerospace Company, P.O. Box #1, Dept. V70, Buffalo, NY 14240
1	Mr. F. G. Stroke, Asst. Mgr. Mrkt. Dev., PPG Industries, Inc., 1 Gateway Center, Pittsburgh, Pa 15222

ARMY MATERIALS AND MECHANICS RESEARCH CENTER
WATERTOWN, MASSACHUSETTS 02172

TECHNICAL REPORT DISTRIBUTION

No. of Copies	To
1	Mr. Leslie Hypnarowski, Carborundum Co., Carborundum Center, Niagara Falls, Ny 14302
1	Dr. Mike Buckley, AFML - LLP, Wright Patterson AFB, Dayton, Ohio 45433
1	Dr. Don Thompson, Rockwell International Corporation, Science Center, 1049 Camino Dos Rios, Thousand Oaks, Ca 91360
1	Dr. W. Thielbaln, Code 4061, Naval Weapons Center, China Lake, Ca 93555
1	Dr. Arthur Cohn, EPRI, P.O. 10412, 3412 Hillview Avenue, Palo Alto, Ca 94304
1	Mr. A. E. Leach, Mgr., Process Development Engineering, Mail Zone C-33, Bell Aerospace Company, P.O. Box 1, Buffalo, NY 14240
1	Dr. Robert K. Thomas, FA4-4, Reactor Engineering, General Atomic Company, P.O. Box 81608, San Diego, Ca 92138
1	Mr. Arthur L. Ross, Valley Forge Space Center, General Electric Company, P.O. Box 8555, Philadelphia, Pennsylvania 19101
1	Mr. Dennis W. Swain, Department 93-19 M, Airesearch Manufacturing Company, P.O. Box 5217, Pheonix, Arizona 85010
1	Mr. Wayne Everett, Wyman-Gordon Company, Research and Development, North Grafton, MA 01536

3 Authors

304 Total Copies Distributed

Army Materials and Mechanics Research Center,
Watertown, Massachusetts 02172

AD______________

BRITTLE MATERIALS DESIGN
HIGH TEMPERATURE GAS TURBINE

Arthur F. McLean, Eugene A. Fisher, Ford Motor Company, Dearborn, Michigan 48121
Raymond J. Bratton, Donald G. Miller, Westinghouse Electric Corporation, Pittsburgh, Pennsylvania 15235

Technical Report AMMRC CTR 75-8, April, 1975
185 pages, 150 illus, 13 tables, 40 references,
Contract DAAG 46-71-C-0162, ARPA Order Number 1849, Seventh Interim Report, July 1, 1974 to December 31, 1974

Key Words

Gas Turbine Engine
Brittle Design
Ceramics
High Temperature Materials
Silicon Nitride
Silicon Carbide
Non-Destructive Tests
Mechanical Properties

ABSTRACT

The "Brittle Materials Design, High Temperature Gas Turbine" program objective is to demonstrate successful use of brittle materials in demanding high temperature structural applications. A small vehicular gas turbine and a large stationary gas turbine, each using uncooled ceramic components, will be utilized in this iterative design and materials development program. Both the contractor, Ford Motor Company, and the subcontractor, Westinghouse Electric Corporation, have had in-house research programs in this area prior to this contract.

In the vehicular turbine project, a major program milestone, comprising a 100 hour durability test of the stationary ceramic hot flow path components in a engine was completed. In the fabrication of ceramic turbine rotors, significant improvement in bonding the components of the silicon nitride duo density rotor resulted when hot pressing of the shaped hub was combined with press bonding to the blade ring. Spin testing of seven hot pressed silicon nitride rotor hubs, with burst speeds ranging from 102,000 to 120,000 rpm, confirmed that this material was adequate for rotor requirements. A silicon carbide combustor tube has been successfully tested in a combustor rig for a total of 171 hours, including 20 hours at an outlet temperature of 2500°F. A redesigned ceramic flow path, Design D, was conceived using common one piece stators and common rotors in both first and second stage locations. Through variations in particle size distribution, it was found that injection molded reaction sintered silicon nitride of 2.7 gm/cm^3 density (84.5% of T.D.) could be made. The effect of oxidation on lower density forms of reaction sintered silicon nitride was evaluated.

In the stationary turbine project, static rig testing of hot pressed silicon nitride and silicon carbide stator vanes up to 2500°F was initiated. Cracks were observed visually on two of the four silicon carbide vanes during the third cycle, but the vanes remained functional. During the fifth cycle, the metal combustor basket imploded, throwing metal debris into the vanes, followed by a temperature excursion to 3000°F and a rapid quench to 600°F under choked flow conditions. Following this accident, it was found that all four silicon carbide vanes had been shattered. One of the four silicon nitride vanes was cracked, while the remaining three vanes were still intact, an encouraging example of ceramic material survival under unexpected catastrophic conditions. The static test rig is being modified and rebuilt for the continuation of 2500°F testing. Additional tensile strength and creep tests were performed on hot pressed silicon nitride.

Army Materials and Mechanics Research Center,
Watertown, Massachusetts 02172

AD______________

BRITTLE MATERIALS DESIGN
HIGH TEMPERATURE GAS TURBINE

Arthur F. McLean, Eugene A. Fisher, Ford Motor Company, Dearborn, Michigan 48121
Raymond J. Bratton, Donald G. Miller, Westinghouse Electric Corporation, Pittsburgh, Pennsylvania 15235

Technical Report AMMRC CTR 75-8, April, 1975
185 pages, 150 illus, 13 tables, 40 references,
Contract DAAG 46-71-C-0162, ARPA Order Number 1849, Seventh Interim Report, July 1, 1974 to December 31, 1974

Key Words

Gas Turbine Engine
Brittle Design
Ceramics
High Temperature Materials
Silicon Nitride
Silicon Carbide
Non-Destructive Tests
Mechanical Properties

ABSTRACT

The "Brittle Materials Design, High Temperature Gas Turbine" program objective is to demonstrate successful use of brittle materials in demanding high temperature structural applications. A small vehicular gas turbine and a large stationary gas turbine, each using uncooled ceramic components, will be utilized in this iterative design and materials development program. Both the contractor, Ford Motor Company, and the subcontractor, Westinghouse Electric Corporation, have had in-house research programs in this area prior to this contract.

In the vehicular turbine project, a major program milestone, comprising a 100 hour durability test of the stationary ceramic hot flow path components in a engine was completed. In the fabrication of ceramic turbine rotors, significant improvement in bonding the components of the silicon nitride duo density rotor resulted when hot pressing of the shaped hub was combined with press bonding to the blade ring. Spin testing of seven hot pressed silicon nitride rotor hubs, with burst speeds ranging from 102,000 to 120,000 rpm, confirmed that this material was adequate for rotor requirements. A silicon carbide combustor tube has been successfully tested in a combustor rig for a total of 171 hours, including 20 hours at an outlet temperature of 2500°F. A redesigned ceramic flow path, Design D, was conceived using common one piece stators and common rotors in both first and second stage locations. Through variations in particle size distribution, it was found that injection molded reaction sintered silicon nitride of 2.7 gm/cm^3 density (84.5% of T.D.) could be made. The effect of oxidation on lower density forms of reaction sintered silicon nitride was evaluated.

In the stationary turbine project, static rig testing of hot pressed silicon nitride and silicon carbide stator vanes up to 2500°F was initiated. Cracks were observed visually on two of the four silicon carbide vanes during the third cycle, but the vanes remained functional. During the fifth cycle, the metal combustor basket imploded, throwing metal debris into the vanes, followed by a temperature excursion to 3000°F and a rapid quench to 600°F under choked flow conditions. Following this accident, it was found that all four silicon carbide vanes had been shattered. One of the four silicon nitride vanes was cracked, while the remaining three vanes were still intact, an encouraging example of ceramic material survival under unexpected catastrophic conditions. The static test rig is being modified and rebuilt for the continuation of 2500°F testing. Additional tensile strength and creep tests were performed on hot pressed silicon nitride.

Army Materials and Mechanics Research Center,
Watertown, Massachusetts 02172

AD______________

BRITTLE MATERIALS DESIGN
HIGH TEMPERATURE GAS TURBINE

Arthur F. McLean, Eugene A. Fisher, Ford Motor Company, Dearborn, Michigan 48121
Raymond J. Bratton, Donald G. Miller, Westinghouse Electric Corporation, Pittsburgh, Pennsylvania 15235

Technical Report AMMRC CTR 75-8, April, 1975
185 pages, 150 illus, 13 tables, 40 references,
Contract DAAG 46-71-C-0162, ARPA Order Number 1849, Seventh Interim Report, July 1, 1974 to December 31, 1974

Key Words

Gas Turbine Engine
Brittle Design
Ceramics
High Temperature Materials
Silicon Nitride
Silicon Carbide
Non-Destructive Tests
Mechanical Properties

ABSTRACT

The "Brittle Materials Design, High Temperature Gas Turbine" program objective is to demonstrate successful use of brittle materials in demanding high temperature structural applications. A small vehicular gas turbine and a large stationary gas turbine, each using uncooled ceramic components, will be utilized in this iterative design and materials development program. Both the contractor, Ford Motor Company, and the subcontractor, Westinghouse Electric Corporation, have had in-house research programs in this area prior to this contract.

In the vehicular turbine project, a major program milestone, comprising a 100 hour durability test of the stationary ceramic hot flow path components in a engine was completed. In the fabrication of ceramic turbine rotors, significant improvement in bonding the components of the silicon nitride duo density rotor resulted when hot pressing of the shaped hub was combined with press bonding to the blade ring. Spin testing of seven hot pressed silicon nitride rotor hubs, with burst speeds ranging from 102,000 to 120,000 rpm, confirmed that this material was adequate for rotor requirements. A silicon carbide combustor tube has been successfully tested in a combustor rig for a total of 171 hours, including 20 hours at an outlet temperature of 2500°F. A redesigned ceramic flow path, Design D, was conceived using common one piece stators and common rotors in both first and second stage locations. Through variations in particle size distribution, it was found that injection molded reaction sintered silicon nitride of 2.7 gm/cm^3 density (84.5% of T.D.) could be made. The effect of oxidation on lower density forms of reaction sintered silicon nitride was evaluated.

In the stationary turbine project, static rig testing of hot pressed silicon nitride and silicon carbide stator vanes up to 2500°F was initiated. Cracks were observed visually on two of the four silicon carbide vanes during the third cycle, but the vanes remained functional. During the fifth cycle, the metal combustor basket imploded, throwing metal debris into the vanes, followed by a temperature excursion to 3000°F and a rapid quench to 600°F under choked flow conditions. Following this accident, it was found that all four silicon carbide vanes had been shattered. One of the four silicon nitride vanes was cracked, while the remaining three vanes were still intact, an encouraging example of ceramic material survival under unexpected catastrophic conditions. The static test rig is being modified and rebuilt for the continuation of 2500°F testing. Additional tensile strength and creep tests were performed on hot pressed silicon nitride.

Army Materials and Mechanics Research Center,
Watertown, Massachusetts 02172

AD______________

BRITTLE MATERIALS DESIGN
HIGH TEMPERATURE GAS TURBINE

Arthur F. McLean, Eugene A. Fisher, Ford Motor Company, Dearborn, Michigan 48121
Raymond J. Bratton, Donald G. Miller, Westinghouse Electric Corporation, Pittsburgh, Pennsylvania 15235

Technical Report AMMRC CTR 75-8, April, 1975
185 pages, 150 illus, 13 tables, 40 references,
Contract DAAG 46-71-C-0162, ARPA Order Number 1849, Seventh Interim Report, July 1, 1974 to December 31, 1974

Key Words

Gas Turbine Engine
Brittle Design
Ceramics
High Temperature Materials
Silicon Nitride
Silicon Carbide
Non-Destructive Tests
Mechanical Properties

ABSTRACT

The "Brittle Materials Design, High Temperature Gas Turbine" program objective is to demonstrate successful use of brittle materials in demanding high temperature structural applications. A small vehicular gas turbine and a large stationary gas turbine, each using uncooled ceramic components, will be utilized in this iterative design and materials development program. Both the contractor, Ford Motor Company, and the subcontractor, Westinghouse Electric Corporation, have had in-house research programs in this area prior to this contract.

In the vehicular turbine project, a major program milestone, comprising a 100 hour durability test of the stationary ceramic hot flow path components in a engine was completed. In the fabrication of ceramic turbine rotors, significant improvement in bonding the components of the silicon nitride duo density rotor resulted when hot pressing of the shaped hub was combined with press bonding to the blade ring. Spin testing of seven hot pressed silicon nitride rotor hubs, with burst speeds ranging from 102,000 to 120,000 rpm, confirmed that this material was adequate for rotor requirements. A silicon carbide combustor tube has been successfully tested in a combustor rig for a total of 171 hours, including 20 hours at an outlet temperature of 2500°F. A redesigned ceramic flow path, Design D, was conceived using common one piece stators and common rotors in both first and second stage locations. Through variations in particle size distribution, it was found that injection molded reaction sintered silicon nitride of 2.7 gm/cm^3 density (84.5% of T.D.) could be made. The effect of oxidation on lower density forms of reaction sintered silicon nitride was evaluated.

In the stationary turbine project, static rig testing of hot pressed silicon nitride and silicon carbide stator vanes up to 2500°F was initiated. Cracks were observed visually on two of the four silicon carbide vanes during the third cycle, but the vanes remained functional. During the fifth cycle, the metal combustor basket imploded, throwing metal debris into the vanes, followed by a temperature excursion to 3000°F and a rapid quench to 600°F under choked flow conditions. Following this accident, it was found that all four silicon carbide vanes had been shattered. One of the four silicon nitride vanes was cracked, while the remaining three vanes were still intact, an encouraging example of ceramic material survival under unexpected catastrophic conditions. The static test rig is being modified and rebuilt for the continuation of 2500°F testing. Additional tensile strength and creep tests were performed on hot pressed silicon nitride.

UNCLASSIFIED

SECURITY CLASSIFICATION OF THIS PAGE (When Data Entered)

REPORT DOCUMENTATION PAGE

READ INSTRUCTIONS BEFORE COMPLETING FORM

1. REPORT NUMBER
AMMRC CTR 75-8

2. GOVT ACCESSION NO.

3. RECIPIENT'S CATALOG NUMBER

4. TITLE (and Subtitle)
Brittle Materials Design, High Temperature Gas Turbine

5. TYPE OF REPORT & PERIOD COVERED
Interim Report Number 7
7/1/74 to 12/31/74

6. PERFORMING ORG. REPORT NUMBER

7. AUTHOR(s)
A. F. McLean, Ford Motor Company
E. A. Fisher, Ford Motor Company
R. J. Bratton, Westinghouse Electric Corp.
D. G. Miller, Westinghouse Electric Corp.

8. CONTRACT OR GRANT NUMBER(s)
DAAG 46-71-C-0162

9. PERFORMING ORGANIZATION NAME AND ADDRESS
Ford Motor Company, Dearborn, Mi 48121

10. PROGRAM ELEMENT, PROJECT, TASK AREA & WORK UNIT NUMBERS
D/A Project: ARPA Order 1849
Agency Accession: DA OD 4733

11. CONTROLLING OFFICE NAME AND ADDRESS
Army Materials and Mechanics Research Center
Watertown, Massachusetts 02172

12. REPORT DATE
April, 1975

13. NUMBER OF PAGES
185

14. MONITORING AGENCY NAME & ADDRESS (if different from Controlling Office)

15. SECURITY CLASS. (of this report)
Unclassified

15a. DECLASSIFICATION/DOWNGRADING SCHEDULE

16. DISTRIBUTION STATEMENT (of this Report)
Distribution limited to U.S. and NATO Government agencies, ~~and DOD~~ [redacted]rs only: Test and Evaluation data; April, 1975. Other requests for this document must be referred to the Director, Army, Materials and Mechanics Research Center, ATTN: AMXMR-PL, Watertown, Massachusetts 02172

17. DISTRIBUTION STATEMENT (of the abstract entered in Block 20, if different from Report)

18. SUPPLEMENTARY NOTES

19. KEY WORDS (Continue on reverse side if necessary and identify by block number)

Gas Turbine Engine	Silicon Nitride
Brittle Design	Silicon Carbide
Ceramics	Non-Destructive Tests
High Temperature Materials	Mechanical Properties

20. ABSTRACT (Continue on reverse side if necessary and identify by block number)

(See reverse side)

DD FORM 1 JAN 73 1473 EDITION OF 1 NOV 65 IS OBSOLETE

UNCLASSIFIED

SECURITY CLASSIFICATION OF THIS PAGE (When Data Entered)

ABSTRACT

The "Brittle Materials Design, High Temperature Gas Turbine" program objective is to demonstrate successful use of brittle materials in demanding high temperature structural applications. A small vehicular gas turbine and a large stationary gas turbine, each using uncooled ceramic components, will be utilized in this iterative design and materials development program. Both the contractor, Ford Motor Company, and the subcontractor, Westinghouse Electric Corporation, have had in-house research programs in this area prior to this contract.

In the vehicular turbine project, a major program milestone, comprising a 100 hour durability test of the stationary ceramic hot flow path components in an engine was completed. In the fabrication of ceramic turbine rotors, significant improvement in bonding the components of the silicon nitride duo density rotor resulted when hot pressing of the shaped hub was combined with press bonding to the blade ring. Spin testing of seven hot pressed silicon nitride rotor hubs, with burst speeds ranging from 102,000 to 120,000 rpm, confirmed that this material was adequate for rotor requirements. A silicon carbide combustor tube has been successfully tested in a combustor rig for a total of 171 hours, including 20 hours at an outlet temperature of 2500°F. A redesigned ceramic flow path, Design D, was conceived using common one piece stators and common rotors in both first and second stage locations. Through variations in particle size distribution, it was found that injection molded reaction sintered silicon nitride of 2.7 gm/cm^3 density (84.5% of T.D.) could be made. The effect of oxidation on lower density forms of reaction sintered silicon nitride was evaluated.

In the stationary turbine project, static rig testing of hot pressed silicon nitride and silicon carbide stator vanes up to 2500°F was initiated. Cracks were observed visually on two of the four silicon carbide vanes during the third cycle, but the vanes remained functional. During the fifth cycle, the metal combustor basket imploded, throwing metal debris into the vanes, followed by a temperature excursion to 3000°F and a rapid quench to 600°F under choked flow conditions. Following this accident, it was found that all four silicon carbide vanes had been shattered. One of the four silicon nitride vanes was cracked, while the remaining three vanes were still intact, an encouraging example of ceramic material survival under unexpected catastrophic conditions. The static test rig is being modified and rebuilt for the continuation of 2500°F testing. Additional tensile strength and creep tests were performed on hot pressed silicon nitride.